Title	Studies on Water Oxidation Catalysis and Mechanism toward Artificial Photosynthesis
Author(s)	洪, 達超
Citation	大阪大学, 2014, 博士論文
Version Type	VoR
URL	https://doi.org/10.18910/34433
rights	
Note	

Doctoral Dissertation

Studies on Water Oxidation Catalysis and Mechanism toward Artificial Photosynthesis

Dachao Hong

January 2014

Department of Material and Life Science
Division of Advanced Science and Biotechnology
Graduate School of Engineering
Osaka University

Doctoral Dissertation

Department of Material and Life Science
Division of Advanced Science and Biotechnology
Graduate School of Engineering

Contents

General Introduction

The global energy supply and the related environmental issues are the most important technological challenge because the increasing world population and the legitimate aspiration of developing countries to reach higher life standards.[1] Sustainable policies and actions are demanded to limit our dependence of fossil fuel and develop alternative energy supplies such as solar, wind, geothermal, wave or biomass power generation.[1] An attractive candidate for alternative energy is solar energy, which is known as a semi-permanent, abundant and clean energy source.[2] The utilization of solar energy will enable us to accomplish a sustainable society with a high life standard.

In the current technology, solar energy is directly converted into electric energy by photovoltaic cells with an energy conversion efficiency of ~25% using a conventional crystalline Si module.[3] However, storage and transportation of electric energy is generally limited by the capacity of batteries.[4] Thus, generated solar electricity needs to be converted to useful chemical fuels.[4] The conversion of electricity to a chemical fuel can be attained by the electrolysis of water to produce hydrogen and oxygen.[5] The reactions of water electrolysis in an acidic solution are shown in eqs 1 and 2, where

$$\text{Anode:}\quad 2H_2O \rightarrow O_2 + 4H^+ + 4e^- \tag{1}$$

$$\text{Cathode:}\quad 2H^+ + 2e^- \rightarrow H_2 \tag{2}$$

water oxidation and reduction take place in anode and cathode, respectively. Efficient electrolysis of water with low overpotentials requires highly active electrocatalysts, especially in anode electrocatalysts for water oxidation because of slower kinetics and higher overpotentials for water oxidation at anodes than hydrogen evolution at cathods.[6]

Another approach employing direct conversion systems for the production of chemical fuels from sunlight such as photoelectrochemical cells (PECs) will be much more advantageous because the use of separated electrolyzers wired to solar cells results in high costs of fabrication and large energy loss.[7] Water splitting taking place in PECs require semiconductor materials, which support rapid charge transfer, exhibit long-term stability, and harvest a wide range of the solar spectrum.[7] Photocatalytic water splitting using a powdered semiconductor is also an attractive system to produce hydrogen using solar energy.[8] Many semiconductor photoelectrodes and photocatalysts have been reported to splitting water into hydrogen and oxygen by irradiation with UV light[9] and visible light.[10] However, efficient photocatalysts for water splitting into hydrogen and oxygen under visible-light irradiation have remained to be challenging.[11]

In addition, all the systems of electrolysis of water, PECs and photocatalytic water splitting involve the water oxidation (eq 1) because water is aimed to use as the electron source for hydrogen production.[8–11] It is a common subject for all the systems of solar energy conversion to accelerate the reaction of water oxidation.[7]

In contrast to hydrogen production systems described above, photosynthesis in nature succeeds in conversion of solar energy directly to energy-rich compounds of carbohydrate by reduction of CO_2 with water in green plants, algae, and cyanobacteria.[12] Photosynthesis takes place in a common process (Figure 1a); The excitation of a dye pigment called P680 in the central chlorophylls by absorption of sunlight leads to charge separation followed by energy transfer to a reaction center, the captured energy is used to oxidize water that catalyzed by the oxygen evolving complex (OEC) in photosystem II (PSII), and the resulting electrons at the excited P680 ($P680^*$) are employed for reduction of substrates in photosystem I (PSI).[12,13] During this process, the water oxidation in PSII is catalyzed by the OEC composed of a $CaMn_4O_5$ cluster, whose crystal structure has been reported as shown in Figure 2b.[14] Artificial photosynthesis systems mimicking photosynthetic functions have been aimed to directly convert solar energy to chemical fuels, mostly hydrogen gas.[15,16] In addition to hydrogen production, hydrogen peroxide and formic acid as a result of reduction of oxygen and carbon dioxide can be produced by incorporating those catalytic reaction into an artificial photosynthesis.[17] The liquid fuels of hydrogen peroxide and formic acid are more favorable for its storage and transportation. Hydrogen peroxide can also be served as a fuel with a high energy density for fuel cells.[18] To accomplish an artificial photosynthesis system, it is necessary to optimize and combine the several processes, which consist of light harvesting, charge separation, catalytic reactions of water oxidation and reduction, as well as CO_2 fixation.[19] In these processes, water oxidation is considered as the critical bottleneck due to involving four-electron transfer coupled to four-proton removal from water to form O-O bond (eq 1).[20] A standard

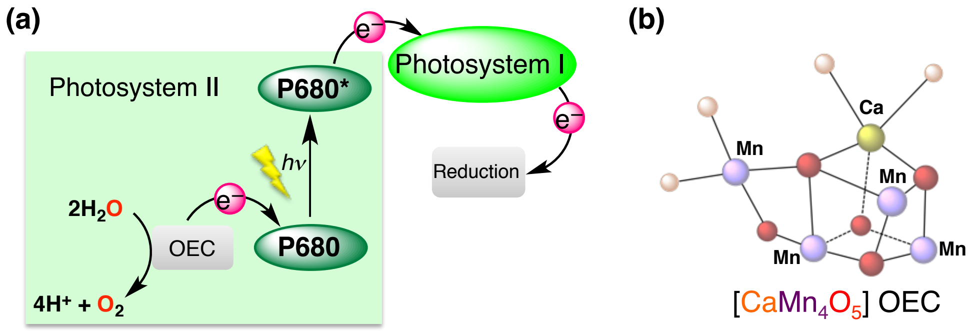

Figure 1. (a) Schematic illustration of electron transfer sequence in photosynthesis and (b) Structure of OEC in PS II.

potential of [$E^o(H_2O/O_2)$ = 1.23 V vs NHE] is also required to drive water reaction. Thus, the development of efficient water oxidation catalysts (WOCs) is the key for building up an artificial photosynthesis system.

Both homogeneous and heterogeneous WOCs mimicking functions of the OEC in PSII have so far been developed for thermal, electrochemical, and light-driven water oxidation.[21-23] The use of homogeneous catalysts, which consist of metal complexes with organic or inorganic ligands, for water oxidation has enabled the identification of reactive intermediates such as high-valent metal-oxo species and detailed kinetic study to provide valuable insights into the catalytic mechanisms.[22] On the other hand, heterogeneous catalysts, which generally consist of metal oxides or hydroxides without organic ligands, are more stable and robust under water oxidation conditions, and they can be easily separated by filtration for repetitive use in practical applications.[23] However, it is quite difficult to identify the reactive intermediates on the surfaces of heterogeneous catalysts, and therefore, the heterogeneous catalytic mechanisms of water oxidation have yet to be clarified.

Water oxidation is normally performed in an aqueous or a pH-adjusted buffer solution with an oxidant and a catalyst to evaluate its catalytic activity and mechanism. For example, cerium ammonium nitrate (CAN, $(NH_4)_2Ce^{IV}(NO_3)_6$) or $[Ru(bpy)_3]^{3+}$ (bpy = 2,2'-bipyridine) is used as a conventional oxidant for thermal water oxidation, whose catalytic cycle is shown in Scheme 1a. Under acidic conditions (pH ≦ 1), CAN possesses an oxidation potential [$E^o(Ce^{3+}/Ce^{4+})$ = 1.61 V vs NHE],[24] which is high enough to oxidize water to evolve oxygen in presence of a WOC with the stoichiometry of eq 3. Under basic conditions, however, CAN is not a suitable oxidant for water

$$4Ce^{4+} + 2H_2O \rightarrow O_2 + 4Ce^{3+} + 4H^+ \qquad (3)$$

oxidation, because hydrolysis of CAN results in reducing its oxidation power.[24] In contrast, $[Ru(bpy)_3]^{3+}$ with the oxidation potential [$E^o(Ru^{2+}/ Ru^{3+})$ = 1.26 V vs NHE][25] acts as an oxidant even under neutral or basic conditions, although the

Scheme 1. Catalytic Cycles of (a) Thermal Water Oxidation and (b) Light-Driven Water Oxidation

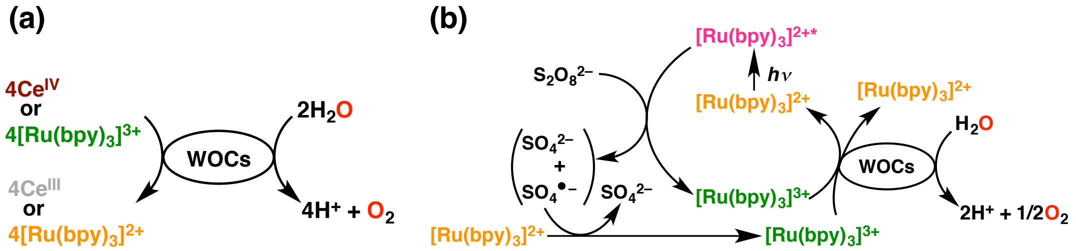

self-decomposition of $[Ru(bpy)_3]^{3+}$ also takes place under neutral or basic conditions by a nucleophilic attack of OH^- or water on $[Ru(bpy)_3]^{3+}$, which competes with electron transfer from a WOC to $[Ru(bpy)_3]^{3+}$.[26] Furthermore, $[Ru(bpy)_3]^{3+}$ can be produced by oxidative quenching of the excited state of $[Ru(bpy)_3]^{2+}$ ($[Ru(bpy)_3]^{2+*}$: * denotes the excited state) by persulfate ($S_2O_8^{2-}$) under visible-light irradiation (Scheme 1b). Photoinduced electron transfer from the $[Ru(bpy)_3]^{2+*}$ to $S_2O_8^{2-}$ affords $[Ru(bpy)_3]^{3+}$, SO_4^{2-}, and $SO_4^{\bullet-}$. The produced $SO_4^{\bullet-}$ is known as a very strong oxidant [E^o ($SO_4^{\bullet-}$/ SO_4^{2-}) = 2.6 V][27] that can oxidize another molecule of $[Ru(bpy)_3]^{2+}$ to produce two equivalents of $[Ru(bpy)_3]^{3+}$ in the overall photoinduced process. In this case, two equivalents of persulfate produce one equivalent of oxygen based on the stoichiometry of light-driven water oxidation as shown in eq 4.

$$2Na_2S_2O_8 + 2H_2O \xrightarrow{h\nu} O_2 + 4H^+ + 4Na^+ + 4SO_4^{2-} \qquad (4)$$

In the case of homogeneous catalysts, ever since Meyer and co-workers reported that a dinuclear ruthenium complexes ($[(bpy)_2(H_2O)RuORu(H_2O)(bpy)_2]^{4+}$), which is called a blue dimer,[28] acts as a catalyst for water oxidation by CAN, there have been extensive studies on water oxidation with ruthenium[29], iridium,[30] cobalt,[31] manganese,[32] iron[33] and nickel[34] complexes in the thermal and light-driven water oxidation. Most of these metal complexes have been reported as homogeneous WOCs. However, there is a question whether metal complexes really act as homogeneous catalysts or only precursors of more active heterogeneous catalysts under water oxidation conditions. A controversial example for the identification of catalytically active species was reported with a tetranuclear cobalt polyoxometalate complex of $[Co^{II}_4(H_2O)_2(\alpha\text{-}PW_9O_{34})_2]^{10-}$ (Co_4POM).[35,36] It was reported that Co_4POM was stable without formation of nanoparticles under catalytic turnover conditions for the light-driven water oxidation with $[Ru(bpy)_3]^{2+}$ and $S_2O_8^{2-}$.[35] However, it was also reported that Co_4POM partially decomposed at pH 8.0 to release Co^{2+} ions under the conditions for electrochemical water oxidation, and this resulted in the formation of active cobalt oxide nanoparticles.[36] Although no definitive conclusions can be drawn regarding the Co_4POM catalyst, because the photochemical and electrochemical conditions are different, more cautions would be required to analyze kinetics and to detect reactive intermediates for molecular metal complexes.

It is important for developing highly efficient and robust WOCs to unveil what is the true catalyst when degradable metal complexes are employed as a catalyst. Nevertheless, there is no work on the identification of catalytically active species when homogeneous metal complexes are employed for the thermal and light-driven water oxidation. It is also becoming more important for the development of efficient WOCs to understand the relationship between homogeneous and heterogeneous catalysts as well as the catalytic mechanism of water oxidation.

The use of homogeneous metal complexes as WOCs merits mechanistic study with various spectroscopic methods. There are two plausible pathways of O-O bond formation in the catalytic reaction of water oxidation reported by using a mononuclear and a dinuclear ruthenium complex as WOCs (Scheme 2).[37–40] Meyer and co-workers reported catalytic water oxidation by CAN with the mononuclear ruthenium complexes $[Ru(tpy)(bpm)(OH_2)]^{2+}$ ($[(L)Ru^{II}(OH_2)]^{2+}$: tpy = 2,2':6',2''-terpyridine, bpm = 2,2'-bipyrimidine), and the catalytic reaction occurred with a mechanism involving Ru(V)-oxo species as shown in Scheme 2a. $[(L)Ru^{II}(OH_2)]^{2+}$ is oxidized by 3 equivalents of CAN to produce Ru(V)-oxo species followed by water nucleophilic attack to form an O-O band. The rate-determined step of water oxidation by CAN with $[(L)Ru^{II}(OH_2)]^{2+}$ was suggested to be the reaction of $[(L)Ru^{IV}(OO)]^{2+}$ with water, which slowly releases O_2 to regenerate $[(L)Ru^{II}(OH_2)]^{2+}$. However, the intermediate of $[(L)Ru^{IV}(OO)]^{2+}$ is suggested by only DFT calculation without any direct detection.

On the other hand, Llobet and co-workers reported that a dinuclear ruthenium complex, $\{[Ru^{II}(tpy)(H_2O)]_2(\mu\text{-bpp})\}^{3+}$ (bpp = 2,6-bis(pyridyl)pyrazolate), catalyzes water oxidation by CAN with the mechanism of intramolecular O-O bond formation (Scheme 2b).[39] The mechanism of intramolecular O-O bond formation was demonstrated by kinetic analysis combined with $^{18}OH_2$ labeling experiments. Although the $^{18}OH_2$ labeling experiments were performed, O-O bond formation by water nucleophilic attack cannot be excluded in the catalytic mechanism if oxygen exchange

Scheme 2. Proposed Mechanisms of Water Oxidation for the Ruthenium Complexes; O-O Bond Formed by (a) Water Nucleophilic Attack to Ru-Oxo and (b) Coupling of Two Ru-Oxo[38,39]

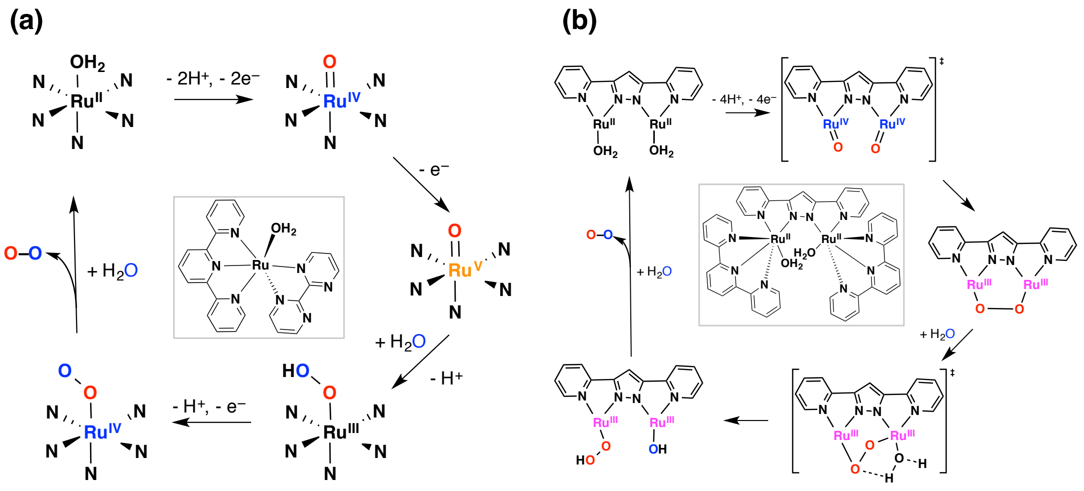

between Ru-oxo species and $^{18}OH_2$ occurs faster than the O-O formation. Thus, the direct detection of reactive intermediates is required to confirm the catalytic mechanism of water oxidation by CAN.

In contrast to homogeneous metal complexes, heterogeneous metal oxides using noble metals such as iridium, ruthenium have been reported as efficient catalysts for water oxidation.[41] However, iridium and ruthenium are precious and expensive metals. Thus, efficient WOCs based on earth-abundant metals, especially the first-row transition metals such as cobalt, nickel, manganese, and iron, are highly required for practical applications. Among them, cobalt-based WOCs have attracted much attention over the years due to their high catalytic activity for water oxidation.[42] Various methods, such as structural controls of size, shape, or phase, have been employed to improve the catalytic activity of cobalt oxide for water oxidation.[43,44] For example, nanosized Co_3O_4 loaded on mesoporous silica exhibited higher activity than micrometer-sized Co_3O_4 particles.[43] A cobalt cluster with a cubic Co_4O_4 core modified by organic ligands can act as a catalyst for the light-driven water oxidation.[44]

In natural systems, the WOC of a $CaMn_4O_5$ cluster composed of binary metals, which are suggested to involve with a core function for water oxidation; The calcium ion is proposed to play a role in the regulation of the redox properties of the manganese cluster, as determined by studies on metal-ion coupled electron transfer.[45] In light of the role of calcium ion in $CaMn_4O_5$ clusters, introduction of other metal ions to metal oxides based on earth abundant metals may be expected to improve the catalytic activity of metal oxides for water oxidation.

Water oxidation employing homogeneous metal complexes with organic ligand request the identification of catalytically active species as well as a mechanistic understanding to improve the catalytic activity. Efficient heterogeneous WOCs based on earth-abundant metals have to be developed toward building up an artificial photosynthesis system.

In this thesis, the author has firstly unraveled the catalytically active species for water oxidation between homogeneous and heterogeneous catalysts when employing metal complexes with organic supporting ligands. Secondly, the catalytic mechanism has been investigated for water oxidation with CAN by using ruthenium complexes possessing inorganic ligands, which are more robust under acidic and oxidative conditions. Finally, the author has provided a valuable method inspired by the OEC, for developing more efficient and robust heterogeneous WOCs based on earth-abundant metals toward artificial photosynthesis. This thesis consists of seven Chapters as follows:

In Chapter 1, mononuclear iridium complexes with a Cp^* ligand and several derivatives of bipyridyl ligand were employed as catalyst precursors for water oxidation by CAN. The catalytically active species for water oxidation by CAN was disclosed by kinetic analysis, O_2 evolution and characterization of the actual catalyst by various spectroscopies.

In Chapter 2, light-driven water oxidation was achieved in the presence of mononuclear cobalt complexes with various organic ligands in basic aqueous solutions containing $[Ru(bpy)_3]^{2+}$ and $Na_2S_2O_8$. The catalytically active species by using a cobalt complex was identified by various spectroscopic measurements.

In Chapter 3, water-soluble mononuclear nonheme iron complexes were employed in thermal and light-driven water oxidation, respectively. The catalytically active species involved in those catalytic systems was disclosed by kinetic analysis and ^{18}O labeling experiments in both thermal and light-driven water oxidation.

The catalytic mechanism of water oxidation by CAN using mononuclear ruthenium complexes with polyoxometalate inorganic ligands employed as WOCs is elucidated in Chapter 4, based on identification of reactive intermediates and kinetic studies by electrochemical and spectroscopic measurements.

In Chapter 5, La^{3+}-ion doped cobalt oxide ($LaCoO_3$) was prepared, and the catalytic activity was examined in the light-driven oxidation with $[Ru(bpy)_3]^{2+}$ and $S_2O_8^{2-}$.

The catalytic activities of Ni^{2+}-ion doped iron oxides ($NiFe_2O_4$) and Ni^{2+}-ion doped manganese oxides ($NiMnO_3$) were evaluated by electrochemical and light-driven water oxidation to investigate the composite effect of binary metals in Chapter 6 and 7, respectively.

References

(1) (a) Hoffert, M. I.; Caldeira, K.; Benford, G.; Criswell, D. R.; Green, C.; Herzog, H.; Jain, A. K.; Kheshgi, H. S.; Lackner, K. S.; Lewis, J. S.; Lightfoot, H. D.; Manheimer, W.; Mankins, J. C.; Mauel, M. E.; Perkins, L. J.; Schlesinger, M. E.; Volk T.; Wigley, T. M. L. *Science*, **2002**, *298*, 981. (b) Lewis, N. S.; Nocera, D. G. *Proc. Natl. Acad. Sci. U. S. A.* **2006**, *103*, 15729. (c) Armaroli, N.; Balzani, V. *Angew. Chem., Int. Ed.* **2007**, *46*, 52. (d) Climate Change 2007: Mitigation of Climate Change, *IPCC Working Group III Fourth Assessment Report*; Intergovernmental Panel on Climate Change: Geneva, **2007**.

(2) (a) Nocera, D. G. *Acc. Chem. Res.* **2012**, *45*, 767. (b) Tran, P. D.; Wong, L. H.; Barber, J.; Loo, J. S. C. *Energy Environ. Sci.* **2012**, *5*, 5902. (c) Fukuzumi, S. *Eur. J. Inorg. Chem.* **2008**, *2008*, 1351.

(3) (a) Green, M. A.; Emery, K.; Hishikawa, Y.; Warta, W. *Prog. Photovolt: Res. Appl.* **2011**, *19*, 84. (b) Zhao, J.; Wang, A.; Green, M. A.; Ferrazza, F. *Appl. Phys. Lett.* **1998**, *73*, 1991.

(4) (a) Grätzel, M. *Nature* **2001***, 414*, 338. (b) Choi, N.-S.; Chen, Z.; Freunberger, S. A.; Ji, X.; Sun, Y.-K.; Amine, K.; Yushin, G.; Nazar, L. F.; Cho, J.; Bruce, P. G. *Angew. Chem., Int. Ed.* **2012**, *51*, 9994. (c) Shui, J.-L.; Karan, N. K.; Balasubramanian, M.; Li, S.-Y.; Liu, D.-J. *J. Am. Chem. Soc.* **2012**, *134*, 16654.

(5) (a) Damjanovic, A.; Dey, A.; Bockris, J. M. *J. Electrochem. Soc.* **1966**, *113*, 739. (b) Park, S.; Shao, Y.; Liu, J.; Wang, Y. *Energy Environ. Sci.* **2012**, *5*, 9331. (c) McCrory, C. C. L.; Jung, S.; Peters, J. C.; Jaramillo, T. F. *J. Am. Chem. Soc.* **2013**, *135*, 16977.

(6) (a) Lyons, M. E. G.; Brandon, M. P. *Int. J. Electrochem. Sci.* **2008**, *3*, 1386. (b) Busch, M.; Ahlberg, E.; Panas, I. *J. Phys. Chem. C* **2012**, *117*, 288. (c) Kanan, M. W.; Surendranath, Y.; Nocera, D. G. *Chem. Soc. Rev.* **2009**, *38*, 109.

(7) (a) Walter, M. G.; Warren, E. L.; McKone, J. R.; Boettcher, S. W.; Mi, Q.; Santori, E. A.; Lewis, N. S. *Chem. Rev.* **2010**, *110*, 6446. (b) Navrotsky, A.; Ma, C.; Lilova, K.; Birkner, N. *Science* **2010**, *330*, 199. (c) Fujishima, A.; Honda, K. *Nature* **1972**, *238*, 37.

(8) (a) Kudo, A.; Miseki, Y. *Chem. Soc. Rev.* **2009**, *38*, 253. (b) Maeda, K.; Domen, K. *J. Phys. Chem. C* **2007**, *111*, 7851.

(9) (a) Kato, H.; Kudo, A. *J. Phys. Chem. B* **2001**, *105*, 4285. (b) Inoue, Y. *Energy Environ. Sci.* **2009**, *2*, 364. (c) Kato, H.; Asakura, K.; Kudo, A. *J. Am. Chem. Soc.* **2003**, *125*, 3082.

(10) (a) Kasahara, A.; Nukumizu, K.; Hitoki, G.; Takata, T.; Kondo, J. N.; Hara, M.; Kobayashi, H.; Domen, K. *J. Phys. Chem. A* **2002**, *106*, 6750. (b) Chen, X.; Liu, L.; Yu, P. Y.; Mao, S. S. *Science* **2011**, *331*, 746. (c) Zhang, F.; Yamakata, A.; Maeda, K.; Moriya, Y.; Takata, T.; Kubota, J.; Teshima, K.; Oishi, S.; Domen, K. *J. Am. Chem. Soc.* **2012**, *134*, 8348.

(11) (a) Sasaki, Y.; Kato, H.; Kudo, A. *J. Am. Chem. Soc.* **2013**, *135*, 5441. (b) Abe, R.; Shinmei, K.; Koumura, N.; Hara, K.; Ohtani, B. *J. Am. Chem. Soc.* **2013**, *135*, 16872.

(12) (a) Lubitz, W.; Reijerse, E. J.; Messinger, J. *Energy Environ. Sci.* **2008**, *1*, 15. (b) Herrero, C.; Lassalle-Kaiser, B.; Leibl, W.; Rutherford, A. W.; Aukauloo, A. *Coord. Chem. Rev.* **2008**, *252*, 456. (c) Dau, H.; Zaharieva, I. *Acc. Chem. Res.* **2009**, *42*, 1861.

(13) (a) Fukuzumi, S. *Bull. Chem. Soc. Jpn.* **2006**, *79*, 177. (b) Fukuzumi, S. *Eur. J. Inorg. Chem.* **2008**, *2008*, 1351.

(14) (a) Amunts, A.; Drory, O.; Nelson, N. *Nature* **2007**, *447*, 58. (b) Umena, Y.; Kawakami, K.; Shen, J.-R.; Kamiya, N. *Nature* **2011**, *473*, 55.

(15) (a) Esswein, A. J.; Nocera, D. G. *Chem. Rev.* **2007**, *107*, 4022. (b) Navarro, R. M.; Alvarez-Galvan, M. C.; Villoria de la Mano, J. A.; Al-Zahrani, S. M.; Fierro, J. L. G. *Energy Environ. Sci.* **2010**, *3*, 1865. (c) Wen, F.; Li, C. *Acc. Chem. Res.* **2013**.

(16) (a) Fukuzumi, S.; Yamada, Y.; Suenobu, T.; Ohkubo, K.; Kotani, H. *Energy Environ. Sci.* **2011**, *4*, 2754. (b) Magnuson, A.; Anderlund, M.; Johansson, O.; Lindblad, P.; Lomoth, R.; Polivka, T.; Ott, S.; Stensjo, K.; Styring, S.; Sundstrom, V.; Hammarstrom, L. *Acc. Chem. Res.* **2009**, *42*, 1899.

(17) (a) Fukuzumi, S.; Yamada, Y.; Karlin, K. D. *Electrochim. Acta* **2012**, *82*, 493. (a) Fukuzumi, S.; Suenobu, T. *Dalton Trans.* **2013**, *42*, 18. (c) Maenaka, Y.; Suenobu, T.; Fukuzumi, S. *Energy Environ. Sci.* **2012**, *5*, 7360. (d) Shibata, S.; Suenobu, T.; Fukuzumi, S. *Angew. Chem., Int. Ed.* **2013**, *52*, 12327.

(18) (a) Yamada, Y.; Fukunishi, Y.; Yamazaki, S.; Fukuzumi, S. *Chem. Commun.* **2010**, *46*, 7334. (b) Yamada, Y.; Yoneda, M.; Fukuzumi, S. *Chem.–Eur. J.* **2013**, *19*, 11733. (c) Yamanaka, I.; Onizawa, T.; Takenaka, S.; Otsuka, K. *Angew. Chem., Int. Ed.* **2003**, *42*, 3653.

(19) (a) Fukuzumi, S.; Ohkubo, K. *J. Mater. Chem.* **2012**, *22*, 4575. (b) Fukuzumi, S. *Phys. Chem. Chem. Phys.* **2008**, *10*, 2283. (c) Fukuzumi, S.; Yamada, Y. *J. Mater. Chem.* **2012**, *22*, 24284. (d) D'Souza, F.; Ito, O. *Chem. Soc. Rev.* **2012**, *41*, 86.

(20) (a) Betley, T. A.; Wu, Q.; Van Voorhis, T.; Nocera, D. G. *Inorg. Chem.* **2008**, *47*, 1849. (b) Eisenberg, R.; Gray, H. B. *Inorg. Chem.* **2008**, *47*, 1697.

(21) (a) Kanan, M. W.; Nocera, D. G. *Science* **2008**, *321*, 1072. (b) Nakagawa, T.; Bjorge, N. S.; Murray, R. W. *J. Am. Chem. Soc.* **2009**, *131*, 15578.

(22) (a) Sala, X.; Romero, I.; Rodríguez, M.; Escriche, L.; Llobet, A. *Angew. Chem., Int. Ed.* **2009**, *48*, 2842. (b) Liu, F.; Concepcion, J. J.; Jurss, J. W.; Cardolaccia, T.; Templeton, J. L.; Meyer, T. J. *Inorg. Chem.* **2008**, *47*, 1727. (c) Cao, R.; Lai, W.; Du, P. *Energy Environ. Sci.* **2012**, *5*, 8134.

(23) (a) Harriman, A.; Pickering, I. J.; Thomas, J. M.; Christensen, P. A. *J. Chem. Soc., Faraday Trans. I* **1988**, *84*, 2795. (b) Fukuzumi, S.; Kato, S.; Suenobu, T. *Phys. Chem. Chem. Phys.* **2011**, *13*, 17960. (c) Morris, N. D.; Mallouk, T. E. *J. Am. Chem. Soc.* **2002**, *124*, 11114.

(24) Wadsworth, E.; Duke, F. R.; Goetz, C. *A. Anal. Chem.* **1957**, *29*, 1824.

(25) Xu, Y.; Fischer, A.; Duan, L.; Tong, L.; Gabrielsson, E.; Åkermark, B.; Sun, L. *Angew. Chem., Int. Ed.* **2010**, *49*, 8934.

(26) (a) Morris, N. D.; Suzuki, M.; Mallouk, T. E. *J. Phys. Chem. A* **2004**, *108*, 9115. (b) Creutz, C.; Sutin, N. *Proc. Natl. Acad. Sci. U. S. A.* **1975**, *72*, 2858.

(27) Kaledin, A. L.; Huang, Z.; Geletii, Y. V.; Lian, T.; Hill, C. L.; Musaev, D. G. *J. Phys. Chem. A* **2010**, *114*, 73.

(28) (a) Gersten, S. W.; Samuels, G. J.; Meyer, T. J. *J. Am. Chem. Soc.* **1982**, *104*, 4029. (b) Gilbert, J. A.; Eggleston, D. S.; Murphy, W. R.; Geselowitz, D. A.; Gersten, S. W.; Hodgson, D. J.; Meyer, T. J. *J. Am. Chem. Soc.* **1985**, *107*, 3855.

(29) (a) Schoonover, J. R.; Ni, J. F.; Roecker, L.; Whiter, P. S.; Meyer, T. J. *Inorg. Chem.* **1996**, *35*, 5885. (b) Yamada, H.; Siems, W. F.; Koike, T.; Hurst, J. K. *J. Am. Chem. Soc.* **2004**, *126*, 9786. (c) Zong, R.; Thummel, R. P. *J. Am. Chem. Soc.* **2005**, *127*, 12802. (d) Geletii, Y. V.; Botar, B.; Koegerler, P.; Hillesheim, D. A.; Musaev, D. G.; Hill, C. L. *Angew. Chem., Int. Ed.* **2008**, *47*, 3896. (e) Duan, L. L.; Fischer, A.; Xu, Y. H.; Sun, L. C. *J. Am. Chem. Soc.* **2009**, *131*, 10397. (f) Romain, S.; Bozoglian, F.; Sala, X.; Llobet, A. *J. Am. Chem. Soc.* **2009**, *131*, 2768. (g) Duan, L.; Bozoglian, F.; Mandal, S.; Stewart, B.; Privalov, T.; Llobet, A.; Sun, L. *Nat. Chem.* **2012**, *4*, 418. (h) Wada, T.; Tsuge, K.; Tanaka, K. *Inorg. Chem.* **2001**, *40*, 329.

(30) (a) McDaniel, N. D.; Coughlin, F. J.; Tinker, L. L.; Bernhard, S. *J. Am. Chem. Soc.* **2008**, *130*, 210. (b) Blakemore, J. D.; Schley, N. D.; Balcells, D.; Hull, J. F.; Olack, G. W.; Incarvito, C. D.; Eisenstein, O.; Brudvig, G. W.; Crabtree, R. H. *J. Am. Chem. Soc.* **2010**, *132*, 16017. (c) Lalrempuia, R.; McDaniel, N. D.; Muller-Bunz, H.; Bernhard, S.; Albrecht, M. *Angew. Chem., Int. Ed.* **2010**, *49*, 9765.

(31) (a) Brunschwig, B. S.; Chou, M. H.; Creutz, C.; Ghosh, P.; Sutin, N. *J. Am. Chem. Soc.* **1983**, *105*, 4832. (b) Yin, Q. S.; Tan, J. M.; Besson, C.; Geletii, Y. V.; Musaev, D. G.; Kuznetsov, A. E.; Luo, Z.; Hardcastle, K. I.; Hill, C. L. *Science* **2010**, *328*, 342. (c) Tanaka, S.; Annaka, M.; Sakai, K. *Chem. Commun.* **2012**, *48*, 1653. (d) Nakazono, T.; Parent, A. R.; Sakai, K. *Chem. Commun.* **2013**, *49*, 6325.

(32) (a) Limburg, J.; Vrettos, J. S.; Chen, H. Y.; de Paula, J. C.; Crabtree, R. H.; Brudvig, G. W. *J. Am. Chem. Soc.* **2001**, *123*, 423. (b) Poulsen, A. K.; Rompel, A.; McKenzie, C. J. *Angew. Chem., Int. Ed.* **2005**, *44*, 6916. (c) Gao, Y.; Akermark, T.; Liu, J. H.; Sun, L. C.; Akermark, B. *J. Am. Chem. Soc.* **2009**, *131*, 8726. (d) Yamazaki, H.; Igarashi, S.; Nagata, T.; Yagi, M. *Inorg. Chem.* **2012**, *51*, 1530.

(33) (a) Ellis, W. C.; McDaniel, N. D.; Bernhard, S.; Collins, T. J. *J. Am. Chem. Soc.* **2010**, *132*, 10990. (b) Fillol, J. L.; Codolà, Z.; Garcia-Bosch, I.; Gómez, L.; Pla, J. J.; Costas, M. *Nat. Chem.* **2011**, *3*, 807. (c) Codolà, Z.; Garcia-Bosch, I.; Acuña-Parés, F.; Prat, I.; Luis, J. M.; Costas, M.; Lloret-Fillol, J. *Chem.–Eur. J.* **2013**, *19*, 8042.

(34) Zhu, G.; Glass, E. N.; Zhao, C.; Lv, H.; Vickers, J. W.; Geletii, Y. V.; Musaev, D. G.; Song, J.; Hill, C. L. *Dalton Trans.* **2012**, *41*, 13043.

(35) (a) Huang, Z.; Luo, Z.; Geletii, Y. V.; Vickers, J. W.; Yin, Q.; Wu, D.; Hou, Y.; Ding, Y.; Song, J.; Musaev, D. G.; Hill, C. L.; Lian, T. *J. Am. Chem. Soc.* **2011**, *133*, 2068. (b) Vickers, J. W.; Lv, H.; Sumliner, J. M.; Zhu, G.; Luo, Z.; Musaev, D. G.; Geletii, Y. V.; Hill, C. L. *J. Am. Chem. Soc.* **2013**, *135*, 14110.

(36) (a) Stracke, J. J.; Finke, R. G. *J. Am. Chem. Soc.* **2011**, *133*, 14872. (b) Stracke, J. J.; Finke, R. G. *ACS Catal.* **2014, *4*,** 79.

(37) Romain, S.; Vigara, L.; Llobet, A. *Acc. Chem. Res.* **2009**, *42*, 1944.

(38) (a) Concepcion, J. J.; Jurss, J. W.; Templeton, J. L.; Meyer, T. J. *J. Am. Chem. Soc.* **2008**, *130*, 16462. (b) Concepcion, J. J.; Tsai, M. K.; Muckerman, J. T.; Meyer, T. J. *J. Am. Chem. Soc.* **2010**, *132*, 1545. (c) Masaoka, S.; Sakai, K. *Chem. Lett.* **2009**, *38*, 182.

(39) Bozoglian, F.; Romain, S.; Ertem, M. Z.; Todorova, T. K.; Sens, C.; Mola, J.; Rodríguez, M.; Romero, I.; Benet-Buchholz, J.; Fontrodona, X.; Cramer, C. J.; Gagliardi, L.; Llobet, A. *J. Am. Chem. Soc.* **2009**, *131*, 15176.

(40) (a) Concepcion, J. J.; Jurss, J. W.; Brennaman, M. K.; Hoertz, P. G.; Patrocinio, A. O. T.; Murakami Iha, N. Y.; Templeton, J. L.; Meyer, T. J. *Acc. Chem. Res.* **2009**, *42*, 1954. (b)Hetterscheid, D. G. H.; Reek, J. N. H. *Angew. Chem., Int. Ed.* **2012**, *51*, 9740.

(41) (a) Hara, M.; Waraksa, C. C.; Lean, J. T.; Lewis, B. A.; Mallouk, T. E. *J. Phys. Chem. A* **2000**, *104*, 5275. (b) Minero, C.; Lorenzi, E.; Pramauro, E.; Pelizzetti, E. *Inorg. Chim. Acta* **1984**, *91*, 301.

(42) (a) Brunschwig, B. S.; Chou, M. H.; Creutz, C.; Ghosh, P.; Sutin, N. *J. Am. Chem. Soc.* **1983**, *105*, 4832. (b) Jiao, F.; Frei, H. *Energy Environ. Sci.* **2010**, *3*, 1018. (c) Artero, V.; Chavarot-Kerlidou, M.; Fontecave, M. *Angew. Chem., Int. Ed.* **2011**, *50*, 7238.

(43) Jiao, F.; Frei, H. *Angew. Chem., Int. Ed.* **2009**, *48*, 1841.

(44) Dismukes, G. C.; McCool, N. S.; Robinson, D. M.; Sheats, J. E. *J. Am. Chem. Soc.* **2011**, *133*, 11446.

(45) (a) Fukuzumi, S.; Morimoto, Y.; Kotani, H.; Naumov, P.; Lee, Y. M.; Nam, W. *Nat. Chem.* **2010**, *2*, 756. (b) Park, J.; Morimoto, Y.; Lee, Y. M.; Nam, W.; Fukuzumi, S. *J. Am. Chem. Soc.* **2011**, *133*, 5236. (c) Morimoto, Y.; Kotani, H.; Park, J.; Lee, Y. M.; Nam, W.; Fukuzumri, S. *J. Am. Chem. Soc.* **2011**, *133*, 403.

Chapter 1

Efficient Water Oxidation by Cerium Ammonium Nitrate with $[Ir^{III}(Cp^*)(4,4'\text{-bishydroxy-}2,2'\text{-bipyridine})(H_2O)]^{2+}$ as a Precatalyst

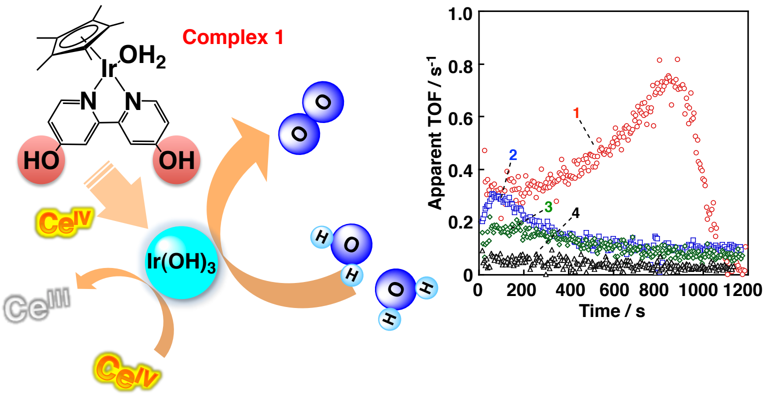

Abstract: Water oxidation by cerium(IV) ammonium nitrate, CAN, with $[Ir^{III}(Cp^*)(4,4'\text{-}R_2\text{-}2,2'\text{-bipyridine})(H_2O)]^{2+}$ (R = OH, OMe, Me or COOH) to evolve oxygen has been investigated together with the possible oxidation of the ligands by CAN. The apparent catalytic activity is highly dependent on the substituent R and the highest catalytic activity was obtained when R = OH. The apparent turnover frequency (TOF) of the catalytic water oxidation by CAN with $[Ir^{III}(Cp^*)\{4,4'\text{-}(OH)_2\text{-}2,2'\text{-bipyridine}\}(H_2O)]^{2+}$, which acts as a precatalyst, gradually increased during the reaction to reach the highest value among the Ir complexes. In the second run, the apparent TOF value was the highest from the beginning of the reaction. ^{1}H NMR and dynamic light scattering measurements for solutions after the first run indicated formation of insoluble nanoparticles, which exhibited a much higher catalytic activity as compared with iridium oxide prepared by a conventional method. The $4,4'\text{-}R_2\text{-}2,2'$-bipyridine ligand was also efficiently oxidized by CAN up to CO_2 only when R = OH. TG/DTA and XPS measurements of nanoparticles produced after the water oxidation suggested that the nanoparticles were composed of iridium hydroxide with a small amount of carbonaceous residue. Thus, iridium hydroxide nanoparticles act as an excellent catalyst for the water oxidation by CAN.

Introduction

In photosynthesis, water is used as an electron source for fixation of carbon dioxide into carbohydrates such as sugar using solar energy. The water oxidation is catalyzed by oxygen-evolving complex (OEC) composed of Mn cluster with one Ca ion in photosystem II.[1–5] The OEC is highly active, however, it is not stable enough to be utilized in artificial photosynthesis systems to generate green chemical fuels such as hydrogen.[6–9] Thus, development of efficient and robust water oxidation catalysts has been highly desired to realize artificial photosynthesis.[10]

Extensive efforts have so far been devoted to develop water oxidation catalysts using transition metal complexes.[11–32] Ever since *cis*,*cis*-$[(\mathrm{bpy})_2(\mathrm{H_2O})\mathrm{Ru^{III}}(\mu\text{-O})\mathrm{Ru^{III}}\text{-}(\mathrm{H_2O})(\mathrm{bpy})_2]^{4+}$ (bpy = 2,2'-bipyridine) was reported as the first molecular catalyst working as a functional model of OEC,[14] the catalytic activity of ruthenium complexes with various ligands for the water oxidation has been extensively studied to elucidate the catalytic mechanism of water oxidation by spectroscopic methods.[20–25] Recently mononuclear ruthenium and iridium complexes have also been shown to act as water oxidation catalysts.[23–31] In particular, a series of mononuclear iridium(III) complexes with η^5-pentamethylcyclopentadienyl ligand ($\mathrm{Cp^*}$) have been reported as efficient water oxidation catalysts, which are more active than ruthenium complexes.[26–31] The ligand of $\mathrm{Cp^*}$ is expected to provide an electron rich environment useful for stabilizing reaction intermediates with a high-valent oxidation state in the catalytic water oxidation by cerium ammonium nitrate, $(\mathrm{NH_4})_2[\mathrm{Ce(NO_3)_6}]$, (CAN). Other than the $\mathrm{Cp^*}$ ligand, the Ir complexes have additional ligands such as phenyl pyridines, bipyridines or phenanthrolines.

On the other hand, iridium oxides are known to act as efficient water oxidation catalysts.[33–42] It was reported that the homogeneous Ir complexes have different catalytic activity from that of heterogeneous iridium oxide nanoparticles, particularly in terms of the kinetic isotope effect.[27] Under the conditions of the catalytic water oxidation by CAN, however, the ligands of Ir complexes are likely to be oxidized to produce Ir containing nanoparticles, which could be actual reactive catalysts.

In Chapter 1, I report the water oxidation by CAN using water-soluble $\mathrm{Ir(Cp^*)}$ complexes, $[\mathrm{Ir^{III}(Cp^*)(4,4'\text{-}R_2\text{-}2,2'\text{-}bpy)(H_2O)}]^{2+}$ (R = OH (**1**), OMe (**2**), Me (**3**) and COOH (**4**)), in Chart 1. The water oxidation rate is quite sensitive to the electron-donating and -withdrawing substituents at the bpy ligand and the fastest water oxidation by CAN was observed using **1**, which acts as a precatalyst. The reactivity of the substituted bpy ligands for the oxidation by CAN has also been examined in comparison with the water oxidation reactivity of the corresponding complexes (**1**–**3**).

The kinetic analysis and the characterization of the catalytically active species have revealed that the precatalyst **1** is converted to iridium hydroxide nanoparticles, which are the actual catalysts for water oxidation, during the catalytic water oxidation by CAN.

Chart 1. Iridium(III) Complexes Used for Water Oxidation by CAN

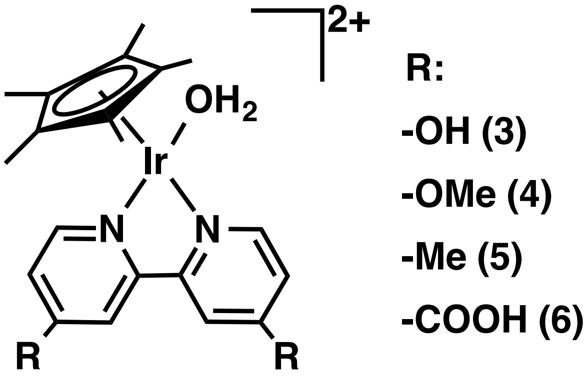

Experimental Section

Materials. All chemicals commercially available were used without further purification unless otherwise noted. H_2IrCl_6 and IrO_2 were purchased from Fukuya Metal Chemical. Pentamethylcyclopentadiene was obtained from Kanto Chemicals. 4,4'-Dimethoxyl-2,2'-bipyridine, 4,4'-dimethyl-2,2'-bipyridine and 2,2'-bipyridine -4,4'-dicarboxylic acid were supplied from Sigma-Aldrich. Cerium(IV) ammonium nitrate (CAN) was purchased from Wako Pure Chemical. Purification of water (18.2 MΩ cm) was performed with a Milli-Q system (Millipore, Direct-Q 3 UV). 4,4'-Dihydroxy-2,2'-bipyridine, $[Ir^{III}(Cp^*)\{4,4'\text{-}(OH)_2\text{-}2,2'\text{-bpy}\}(H_2O)]SO_4$ (**1**), $[Ir^{III}(Cp^*)\{4,4'\text{-}(OMe)_2\text{-}2,2'\text{-bpy}\}(H_2O)]SO_4$ (**2**), $[Ir^{III}(Cp^*)(4,4'\text{-}Me_2\text{-}2,2'\text{-bpy})(H_2O)]\text{-}SO_4$ (**3**) and $[Ir^{III}(Cp^*)\{4,4'\text{-}(COOH)_2\text{-}2,2'\text{-bpy}\}(H_2O)]SO_4$ (**4**) were synthesized according to the literature and characterized by ^1H NMR and mass spectroscopy.[43–46] $[Ir^{III}(Cp^*)(H_2O)_3]SO_4$ was prepared by following the reported method.[43] Iridium hydroxide nanoparticles were prepared by hydrolysis of H_2IrCl_6 in a basic solution and successive calcination.[40]

Synthesis of $[Ir^{III}(Cp^*)\{4,4'\text{-}(OH)_2\text{-}2,2'\text{-bpy}\}(H_2O)]SO_4$ (1). An aqueous solution (30 mL) of [Ir(Cp*)(H2O)3]SO4 (400 mg, 0.84 mmol) and 4,4'-dihydroxy-2,2'-bipyridine (158 mg, 0.84 mmol) was stirred at 40 ºC for 12 h. The formed yellow crystals were collected by filtration to yield **1** (400 mg, 75%). ^1H NMR

(300 MHz, D2O): δ = 1.64 ppm (s, 15H), 7.13 (dd, *J* = 6.4, 2.6 Hz, 2 H), 7.66 (d, *J* = 2.6 Hz, 2H), 8.70 (d, *J* = 6.4 Hz, 2H); ESI-MS: *m/z* = 515 [M–SO4–H2O–H]+.

Synthesis of [Ir^{III}(Cp*){4,4'-(OMe)$_2$-2,2'-bpy}(H$_2$O)]SO$_4$ (2). An aqueous solution (30 mL) of [Ir(Cp*)(H2O)3]SO4 (192 mg, 0.40 mmol) and 4,4'-dimethoxyl-2,2'-bipyridine (86 mg, 0.40 mmol) was stirred at 40 ºC for 12 h. The formed yellow crystals were collected by filtration to yield 2 (223 mg, 85%). ^{1}H NMR (300 MHz, D_2O): δ = 1.67 (s, 15H), 4.11 (s, 6H), 7.41 (dd, *J* = 6.6, 2.2 Hz, 2H), 7.98 (d, *J* = 2.2 Hz, 2H), 8.90 (d, *J* = 6.6 Hz, 2H).

Synthesis of [Ir^{III}(Cp*)(4,4'-Me$_2$-2,2'-bpy)(H$_2$O)]SO$_4$ (3). An aqueous solution (30 mL) of [Ir(Cp*)(H_2O)$_3$]SO_4 (192 mg, 0.40 mmol) and 4,4'-dimethyl-2,2'-bipyridine (74 mg, 0.40 mmol) was stirred at 40 ºC for 12 h. The formed yellow crystals were collected by filtration to yield **3** (202 mg, 81%). ^{1}H NMR (300 MHz, D_2O): δ = 1.67 (s, 15 H), 2.65 (s, 6H), 7.71 (dd, *J* = 5.9, 1.0 Hz, 2H), 8.36 (br, 2H), 8.93 (d, *J* = 5.9 Hz, 2H).

Synthesis of [Ir^{III}(Cp*){4,4'-(COOH)$_2$-2,2'-bpy}(H$_2$O)]SO$_4$ (4). An aqueous solution (30 mL) of [Ir(Cp*)(H_2O)$_3$]SO_4 (192 mg, 0.40 mmol) and 2,2'-bipyridine-4,4'-dicarboxylic acid (98 mg, 0.40 mmol) was stirred at 40 ºC for 12 h. The formed yellow crystals were collected by filtration to yield **4** (205 mg, 75%). ^{1}H NMR (300 MHz, D_2O): δ = 1.70 (s, 15H), 3.7–3.4 (br, 2H), 8.29 (dd, *J* = 5.9, 1.7 Hz, 2H), 9.01 (d, *J* = 1.5 Hz, 2H), 9.27 (d, *J* = 5.9 Hz, 2H).

Synthesis of Iridium Hydroxide (5) and Iridium Oxide (5'). The pH of an aqueous solution of H_2IrCl_6 was adjusted to ~10 by adding 5.0 M NaOH solution with vigorous stirring at 100 ºC. After 1.0 h stirring, precipitates appeared were collected by a centrifugation. Then, the precipitates were washed by water three times and dried *in vacuo* at room temperature and kept at 65 ºC for 10 h (**5**). Iridium oxide (**5'**) was obtained by calcination of iridium hydroxide (**5**) at 600 ºC for 3 h.

Catalytic Oxygen Evolution. An aqueous solution of CAN (10 mM) containing nitric acid (0.10 M, 2.0 mL) in a glass vial (5.0 mL) was sealed with a rubber septum. The solution was carefully deaerated by bubbling Ar gas for ~10 min. To the solution, 10 μL of an aqueous solution of a precatalyst was injected via a syringe piercing through the rubber septum to start the reaction. A small portion (100 μL) of gas in a headspace was sampled with use of a gas-tight syringe and used for gas analysis. The evolved oxygen was separated by passing through a molecular sieve 5A column with an Ar carrier gas and quantified by a TCD detector (Shimadzu GC-17A).

Volumetric gas evolution experiments were also performed by dilatometry in a ~7.0 mL sample vial connected with a Teflon® cannula. An aqueous solution of catalysts (4.0 μmol) containing nitric acid (0.10 M, 1.0 mL) in a vial sealed with a rubber septum was deaerated by bubbling Ar gas. To this solution, a deaerated aqueous solution of CAN (1.0 M, 1.0 mL) was injected to start the reaction. The volume of evolved gas was monitored by transit of a floating bead on water.

Electrochemical Measurements. Cyclic voltammetry (CV) was performed on an ALS 630B electrochemical analyzer using a glassy carbon electrode as a working electrode, a saturated calomel electrode (SCE) as a reference electrode, and Pt wire as an auxiliary electrode. Cyclic voltammograms were obtained in 0.10 M HNO_3 aqueous solutions containing Ir complexes (1.0 mM) at room temperature with scanning rate of 100 mV s^{-1}.

Isotope-Labeled Experiments. An aliquot (10 μL) of a deaerated $H_2{}^{18}O$ solution (88.3% ^{18}O) of **1** (5.0 mM) containing nitric acid (0.10 M) by bubbling He gas was injected to 1.0 mL of a deaerated $H_2{}^{18}O$ solution (88.3% ^{18}O) of CAN (10 mM). After 10 min, 50 μL of the gas in a headspace was sampled by using a gas-tight syringe for gas analysis. The ratio of $^{16}O^{16}O$, $^{16}O^{18}O$ and $^{18}O^{18}O$ was determined based on the intensity of mass spectra (m/z = 32, 34, and 36) obtained by a Shimadzu GC-17A gas chromatograph [He carrier, TC-FFAP column (GL Science, 1010-15242) at 40 ºC] equipped with a mass spectrometer (Shimadzu, QP-5000).

Kinetic Measurements. All kinetic experiments were performed in a 2.0 mL solution in a 1 cm cuvette with a UV-vis spectrometer at 25 °C. UV-vis absorption spectra were recorded on a Hewlett Packard 8453 diode array spectrophotometer. Absorbance at λ = 420 nm (ε_{420} = 1.16 × 10^2 cm^{-1} M^{-1}) due to CAN in an aqueous solution of nitric acid (0.10 M) was monitored during the catalytic water oxidation by CAN and each reaction rate was determined from the decay of absorbance at λ = 420 nm due to CAN.

Determination of CO_2 Produced in Oxidation of Ligands by CAN. A nitric acid solution (0.10 M, 2.0 mL) of CAN (0.12 M) and another nitric acid solution (0.10 M, 1.0 mL) containing ligands (6.0 mM) were deaerated by bubbling N_2 gas for ~10 min. To the solution of ligands, 1.0 mL of the CAN solution was injected with use of a syringe to start the reaction. The amount of CO_2 produced by the oxidation of ligands by CAN was determined by a Shimadzu GC-14B gas chromatograph (N_2 carrier, active carbon with a particle size of 60–80 mesh at 80 °C) equipped with a TCD detector.

Spectroscopic Measurements in Solution. ^{1}H NMR spectra were recorded on a JEOL JNM-AL300 spectrometer in D_2O solutions. The chemical shifts and relative integration of Cp^* signals were referenced by an external standard solution of 5.0 mM 3-(trimethylsilyl)propanoate-2,2,3,3-d_4 acid sodium salt (TSP) in D_2O sealed in a glass capillary. Dynamic light scattering (DLS) measurements were performed with a Zetasizer Nano ZS instrument (Malvern Instruments Ltd., USA) for aqueous solutions containing nitric acid (0.10 M). The DLS instrument used in this study can detect the particle sizes ranging from 0.6 to 6000 nm.

Characterization of Particles. Transmission electron microscope (TEM) images of nanoparticles, which were mounted on a copper microgrid coated with elastic carbon, were observed by a JEOL JEM 2100 operating at 200 keV. X-ray photoelectron spectra (XPS) were measured by a Kratos Axis 165x with a 165 mm hemispherical electron energy analyzer. An incident radiation was Mg $K\alpha$ X-ray (1253.6 eV) at 200 W and a charge neutralizer was turned on for acquisition. Each sample was attached on a stainless stage with a double-sided carbon scotch tape. The binding energy of each element was corrected by C 1s peak (284.6 eV) from residual carbon. TG/DTA data were recorded on an SII TG/DTA 7200 instrument. Each sample (~3.0 mg) was heated from 25 °C to 100 °C (held at 100 °C for 10 min) and from 100 °C to 600 °C with a ramp rate of 2 °C min^{-1}. A certain amount of α-Al_2O_3 was used as a reference for DTA measurements. Nitrogen adsorption-desorption at –196 °C was performed with a Belsorp-mini (BEL Japan, Inc.) within a relative pressure range from 0.01 to 101.3 kPa. A sample mass was used for adsorption analysis after pretreatment at 120 °C for 30 min under vacuum conditions and kept in N_2 atmosphere until N_2-adsorption measurements. The sample was exposed to a mixed gas of He and N_2 with a programmed ratio and adsorbed amount of N_2 was calculated from the change of pressure in a cell after reaching the equilibrium (at least 5 min).

Results and Discussion

Catalytic Water Oxidation by CAN with Ir Complexes as Precatalysts. The catalytic water oxidation by CAN was examined using a series of mononuclear Ir complexes, $[\mathrm{Ir^{III}(Cp^*)(4,4'\text{-}R_2\text{-}2,2'\text{-}bpy)(H_2O)}]\mathrm{SO_4}$ [R = OH (**1**), OMe (**2**), Me (**3**) and COOH (**4**)], which may act as precatalysts in an aqueous solution containing nitric acid (0.10 M). The time course of the reaction was monitored by the UV-vis absorption change due to CAN as shown in Figure 1a. The absorbance change at 420 nm due to CAN is shown in Figure 1b. The apparent turnover frequency (TOF), which was determined from the CAN consumption rate ($-\mathrm{d}[\mathrm{CAN}]/\mathrm{d}t$) divided by amount of catalyst and four, ($-\mathrm{d}[\mathrm{CAN}]/\mathrm{d}t$)/4[catalyst], based on the stoichiometry of the reaction (eq 1, *vide infra*), is plotted in Figure 1c, where the CAN consumption rate was determined by the slope from Figure 1b at 25 s interval. In the cases of **2**–**4**, the apparent TOF values decrease with reaction time to reach constant values. The constant values of apparent TOF are in order of **4** < **3** < **2** with increasing the donor ability of the

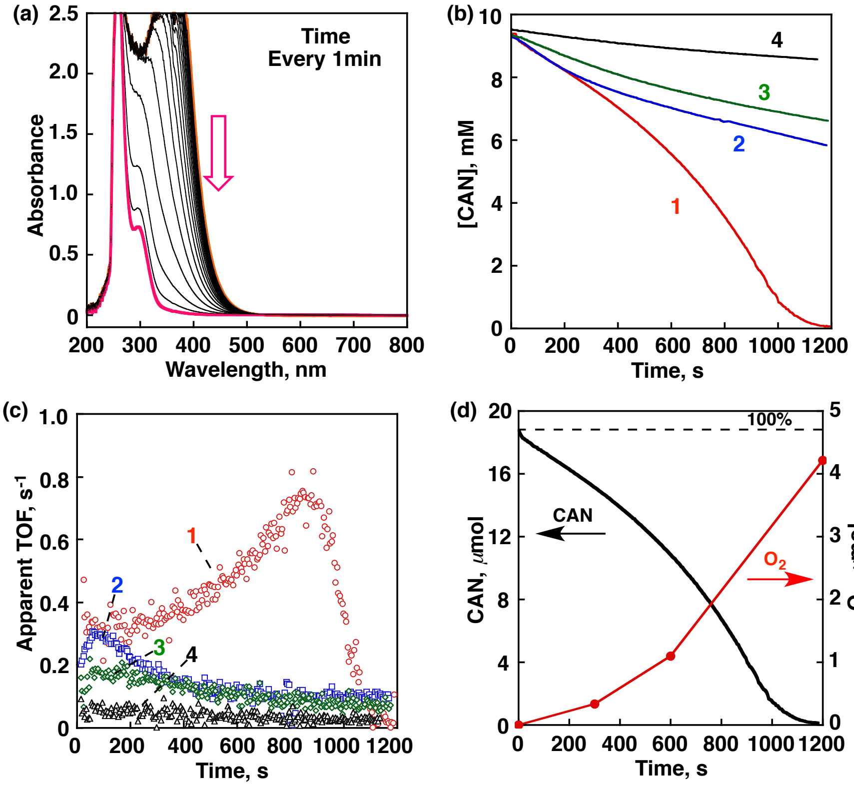

Figure 1. (a) Catalytic water oxidation by CAN with the precatalyst **1** monitored by UV-vis absorption change recorded every 1 min at room temperature. (b) Time courses of concentration of CAN determined from absorbance change at 420 nm in the catalytic water oxidation by CAN using Ir complexes (5.0 μM), [**1** (red), **2** (blue), **3** (green), **4** (black)], in an aqueous solution (2.0 mL) of CAN (10 mM) containing nitric acid (0.10 M). (c) Time courses of apparent TOF of oxygen evolution in the catalytic water oxidation by CAN using Ir complexes, [**1** (red circle), **2** (blue square), **3** (green diamond) and **4** (black triangle)]. (d) Time courses of oxygen evolution and CAN consumption [O_2 was quantified by GC (red) and the consumed CAN was calculated from the absorption change at 420 nm (black) in the catalytic water oxidation by CAN (10 mM) with the precatalyst **1** (5.0 μM) in an aqueous solution (2.0 mL) containing nitric acid (0.10 M)].

substituents, R = COOH < Me < OMe. In contrast to the cases of **2**–**4**, the apparent TOF value with **1** increased with reaction time to reach around a maximum value (0.75 s^{-1}), which is much larger than the values for the reaction systems with **2**–**4** (Figure 1c). At the end of the reaction, the apparent TOF value decreased because most CAN molecules were consumed. Such an increase in the reaction rate with reaction time is also observed for the time dependence of oxygen evolution in Figure 1d, where the rate of oxygen evolution coincides with the rate of consumption of CAN. This indicates that **1** acts as a precatalyst to produce catalytically more active species during the catalytic water oxidation by CAN. The amount of evolved oxygen (4.2 μmol) is nearly one-fourth of the amount of CAN (18.8 μmol) to confirm the stoichiometry in eq 1.

$$2H_2O + 4Ce^{IV} \rightarrow O_2 + 4H^+ + 4Ce^{III} \qquad (1)$$

Table 1 summarizes the apparent TOF values of **1**–**4** for the catalytic water oxidation by CAN with those reported in the literature. The apparent TOF values in Table 1 were calculated on the basis of the number of Ir atoms in a solution, thus, the real TOF normalized by the number of real active sites is larger than the apparent TOF. The maximum apparent TOF of the precatalyst **1** (0.75 s^{-1}) is larger than the TOF (0.60 s^{-1} per one metal center) reported for the catalytic water oxidation by CAN with a dinuclear Ru complex ($[Ru_2Cl(cpp)(4\text{-}MePy)]^+$: cpp = 1,4-bis(6'-COOH-pyrid-2'-yl)-phthalazine),[23] and also the TOF (0.24 s^{-1}) with $[Ir^{III}(Cp^*)(bpy)Cl]Cl$, which afforded the turnover number (TON) of 320 in 8 h.[28] Although $[Fe(taml)(H_2O)]^-$ (taml = tetraamidomacrocyclic ligand) exhibits a higher TOF value (1.7 s^{-1}) than the apparent TOF value with the precatalyst **1**, TON with $[Fe(taml)(H_2O)]^-$ was only 16 and the catalyst was deactivated before the oxidant was consumed.[32] In contrast, the precatalyst **1** kept the high catalytic reactivity for successive 4 times repetitive uses, which were examined by the addition of CAN after each run, indicating that the total TON was more than 1500 (Figure 2).

Additionally, electrocatalytic currents in water oxidation with complexes **1**–**4** (1.0 mM) were recorded against voltage vs saturated calomel electrode (SCE) in 0.10 M

Table 1. Apparent Turnover Frequency (TOF) for Catalytic Water Oxidation by CAN Using $[Ir^{III}(Cp^*)(4,4'\text{-}R_2\text{-}bpy)(H_2O)]^{2+}$ Complexes (R = -OH, -OMe, -Me, -COOH) Compared with Reported TOF Values

compound	apparent TOF / s^{-1}	ref
1	0.75[a]	this work
2	0.27[a]	this work
3	0.16[a]	this work
4	0.05[a]	this work
$[Ru_2Cl(cpp)(4\text{-}MePy)]^{+}$[b]	0.6[c]	21
$[Ir^{III}(Cp^*)(bpy)Cl]Cl$	0.24	28
$[Ir(Cp^*)(OH)_2(Me_2NHC)]$[d]	0.4[e]	31
$[Fe(taml)(H_2O)]^{-}$[f]	1.7[g]	32

[a] Apparent TOF was a maximum value determined from CAN consumption rate divided by amount of catalyst and four, (–d[CAN]/d*t*)/4[catalyst], (Figure 1c). [b] cpp = 1,4-bis(6'-COOH-pyrid-2'-yl)phthalazine. [c] TOF per one metal center. [d] Me_2NHC = *N*-dimethylimidazolin-2-ylidene. [e] Taken from the data for O_2 evolution in ref 31. [f] taml = tetraamidomacrocyclic ligand. [g] TON was as small as 16 (unstable).

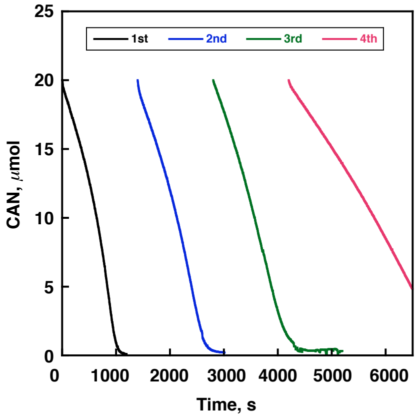

Figure 2. Time courses of CAN consumption determined from the absorbance change at 420 nm in the catalytic water oxidation by CAN with the precatalyst **1** for repeated 4 cycles. The reaction solution (2.0 mL) contained 5.0 μM of **1**, 10 mM CAN and 0.10 M nitric acid.

nitric acid as shown in Figure 3. The anodic currents with **1** started growing around 1.16 V and reached more than 300 μA at 1.5 V. The anodic currents observed with **2** and **3**, which were less active than **1** in water oxidation by CAN, were smaller (around 160 μA at 1.5 V) and the onset potential was 1.21 V. The smallest anodic current of **4** as low as 150 μA (at 1.5 V) was achieved with the onset potential of 1.26 V. The orders of **1**–**4** in both onset potentials and anodic currents completely matched the order of catalytic activity in water oxidation by CAN in Figure 1b. These results demonstrated that the electrochemical water oxidation also took place in the presence of **1**–**4**. The difference of the CV reflects the susceptibilities of the Ir complexes to oxidative degradation (*vide infra*). The lowest onset potential obtained in the presence of **1**, indicates that **1** is most easily converted to other species. Thus, I examined the catalytic water oxidation by CAN with the precatalyst **1** in more detail (*vide infra*).

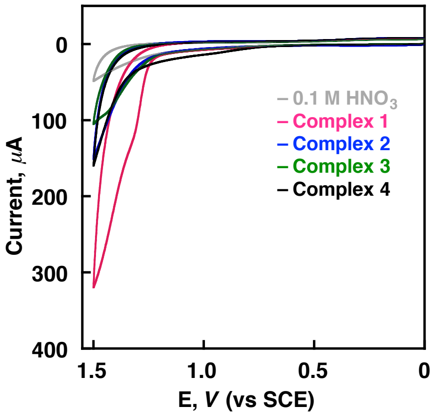

Figure 3. Cyclic voltammograms of complex **1** (red line), **2** (blue line), **3** (green line), **4** (black line) and blank (gray line) with a scan rate of 100 mV s^{-1} in a 0.10 M HNO_3 aqueous solution; the concentration of complexes: 1.0 mM.

Isotope-labeling experiments using ^{18}O-enriched water (88.3%) instead of $H_2{}^{16}O$ were conducted to obtain direct evidence for the catalytic water oxidation by CAN with the precatalyst **1**, in which evolved oxygen comes from water. After the reaction, evolved oxygen in a headspace of a reaction tube was separated by a gas chromatograph equipped with a molecular sieve column and analyzed by a mass spectrometer. Figure 4 compares the relative mass intensities of ^{18}O-labeled and unlabeled oxygen with calculated intensities assuming that all evolved oxygen molecules come from water. If oxygen evolved from the ^{18}O-enriched water (88.3%), the ratio among $^{16}O^{16}O$: $^{16}O^{18}O$: $^{18}O^{18}O$ should be 1.4:21:78. The observed ratio of $^{16}O^{16}O$: $^{16}O^{18}O$: $^{18}O^{18}O$ was 4.0:17:79, which is virtually the same as the calculated ratio within experimental errors (the observed ratio should be 78 ± 2 for $^{18}O^{18}O$), indicating that evolved oxygen comes exclusively from water.

When the concentration of **1** was increased from 5.0 μM to 50 μM, the similar acceleration behavior with reaction time was observed (1st cycle in Figure 5a). The maximum apparent TOF value with 50 μM of the precatalyst **1** was determined to be 0.47 s^{-1} (2nd cycle in Figure 5b), which becomes smaller than the value (0.75 s^{-1}) with 5.0 μM of the precatalyst **1** (Figure 1c). This is consistent with the catalytically reactive species not being a homogeneous catalyst.[47–49] When CAN was added to the resulting solution after the reaction of 1st cycle, the apparent TOF value remained the same as the maximum value in the 1st cycle from the beginning of the 2nd cycle and the 3rd cycle (Figure 5b). This confirms that **1** acts as a precatalyst which was converted to more active species during the 1st cycle of the reaction.

Characterization of Active Species Derived from 1. ^1H NMR measurements

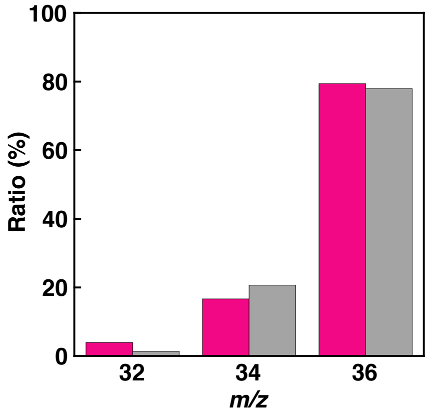

Figure 4. Comparison of relative abundance of ^{18}O-labeled and unlabeled oxygen evolved during the catalytic oxidation of $H_2{}^{18}O$-enriched water (88.3% $H_2{}^{18}O$) by CAN (10 mM) with the precatalyst **1** (50 μM) containing nitric acid (0.10 M) (pink: observed mass intensity, gray: calculated values assuming that evolved oxygen results exclusively from water).

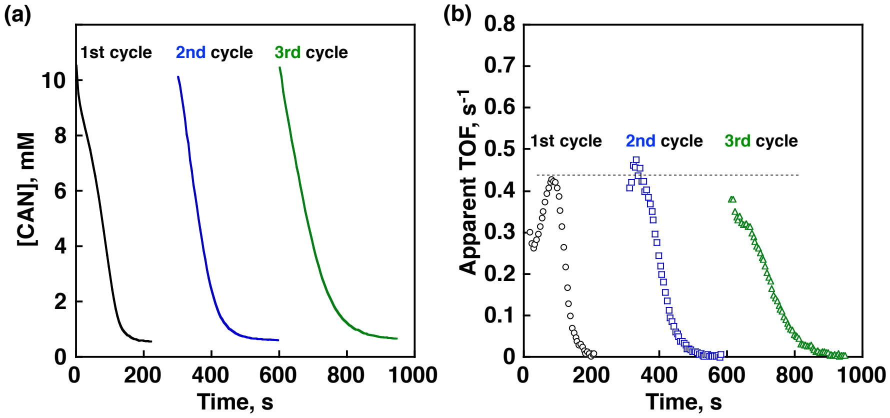

Figure 5. (a) Time courses of concentration of CAN determined from absorbance change at 420 nm in the catalytic water oxidation by CAN (10 mM) with the precatalyst **1** (50 μM) in an aqueous solution (2.0 mL) containing nitric acid (0.10 M) for the 1st, 2nd and 3rd cycles. (b) Time courses of apparent TOF for the 1st, 2nd and 3rd cycles.

were performed for D_2O solutions containing **1** (5.0 mM), CAN (0–50 mM) and DNO_3 (0.10 M) to detect soluble species after the catalytic water oxidation by CAN. Figure 6a (black) indicates the reference spectrum for the solution without CAN where ^{1}H NMR signals from methyl groups of Cp* and bpy groups of 4,4'-$(OH)_2$-bpy appear at 1.7, 7.2, 7.8 and 8.7 ppm. In the presence of CAN, all the ^{1}H NMR signals from the ligands shifted to a lower magnetic field and the intensities decreased significantly as compared with the signal intensity of an external standard (TSP) with increasing CAN concentration (Figures 6a and 7). The decrease in the signal intensity of Cp* with an increase in [CAN]/[**1**] (Figure 6b) suggests that **1** decomposed to insoluble species, which were undetected by ^{1}H NMR measurements.[50]

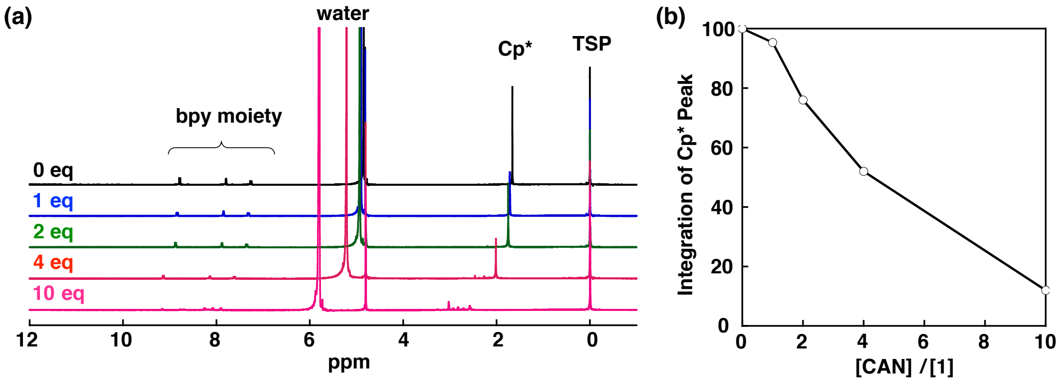

Figure 6. (a) ^{1}H NMR spectra of **1** (5.0 mM) in the absence of CAN (black), and the presence 1.0 (blue), 2.0 (green), 4.0 (red) and 10 (pink) equivalents of CAN using TSP in capillary as internal standard in D_2O solutions containing DNO_3 (0.10 M). (b) Plots of integration of the ^{1}H NMR signal due to the Cp* moiety of **1** in reference to TSP vs [CAN]/[**1**] ratio.

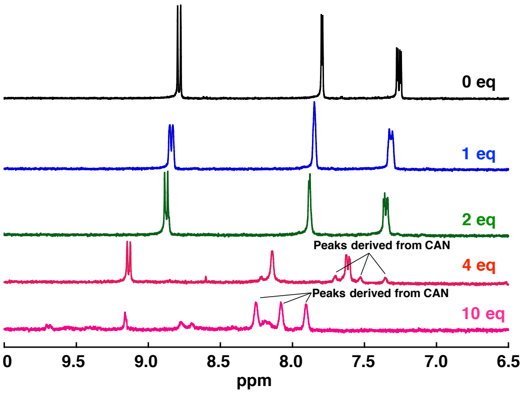

Figure 7. ^{1}H NMR spectra in bpy region of **1** (5.0 mM) in 0.1 M DNO_3 with 0 (black), 1 (blue), 2 (green), 4 (red) and 10 (pink) equiv of CAN. TSP sealed in a glass capillary was used as an external standard.

In order to confirm formation of insoluble particles in the solutions, dynamic light scattering (DLS) measurements were conducted for aqueous solutions after the water oxidation by CAN with the precatalyst **1**. When the solution contained 50 μM of **1** and 10 mM of CAN, the particles with the average size of 348 nm, which is distributed in the range of 180–1000 nm, were detected by the DLS measurements as shown in Figure 8 (black). When the concentration of **1** was increased from 50 μM to 250 or 500 μM, formation of larger particles with the average size of 600 nm distributed from 300 to 1100 nm, was observed (blue: 250μM, red: 500 μM in Figure 8). The formation of larger particles can explain lower TOF values observed for a solution with higher concentration of **1** (*vide supra*).

Change of catalysis from homogeneous to heterogeneous has been often discussed under harsh reaction conditions.[47–53] The electrochemical deposition of insoluble species has also been reported using $[Ir^{III}(Cp^*)(OH_2)_3]SO_4$ as a precursor on an

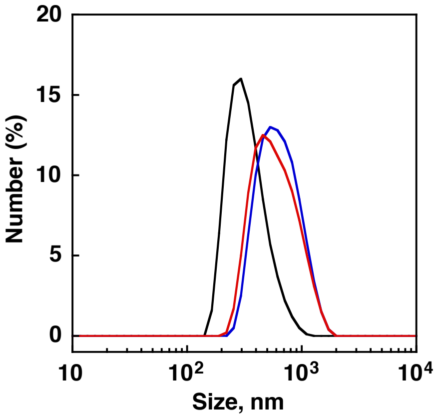

Figure 8. Particles size distribution determined by DLS measurements of aqueous solutions of **1** (black: 50 μM, blue: 250 μM and red: 500 μM) with CAN (10 mM) and nitric acid (0.10 M).

electrode surface with an applying voltage of 1.4 V vs NHE in potassium nitrate.[53] An IR measurement and an elemental analysis of the deposited species indicated that the deposits contained 9% of carbon as organic substances derived from Cp*.[54] When Ir(Cp*) complexes have a chelate ligand, i.e., [Ir(Cp*)(κ^2-2-phenylpyridine)Cl] and [Ir(Cp*)(bpy)Cl], the complexes did not form deposits under the electrochemical reaction conditions.[54] In our experiments, the precatalyst **1** readily decomposed to form catalytically more active nanoparticles in an aqueous solution of CAN containing nitric acid (0.10 M), whereas **2**–**4** showed no acceleration behavior under the same experimental conditions.

The large catalytic activity observed for the precatalyst **1** as compared with **2**–**4** due to formation of nanoparticles in the catalytic water oxidation by CAN suggests that the ligand of **1** is oxidized by CAN. Thus, the oxidation of the ligands of **1**–**3** by CAN was examined to compare the reactivity of the ligands.[55] Time courses of absorbance change of CAN in the oxidation of the ligands of **1**–**3** is shown in Figure 9a, where the ligand of **1** [4,4'-$(OH)_2$-bpy] exhibited the much larger reactivity as compared with other ligands, 4,4'-$(OMe)_2$-bpy and 4,4'-$(Me)_2$-bpy. The initial oxidized products of the ligands were difficult to be characterized, because the polymeric precipitates were obtained after the ligand oxidation. In the presence of excess CAN, CO_2 was detected as a fully oxidized product of ligands. Time courses of CO_2 formation are shown in Figure 9b, where CO_2 is produced much more rapidly for the ligand of **1** as compared with other ligands, in agreement with the apparent catalytic activity in the water oxidation by CAN (Figure 1b). Thus, the substitution of bpy from OMe to OH resulted in remarkable difference in

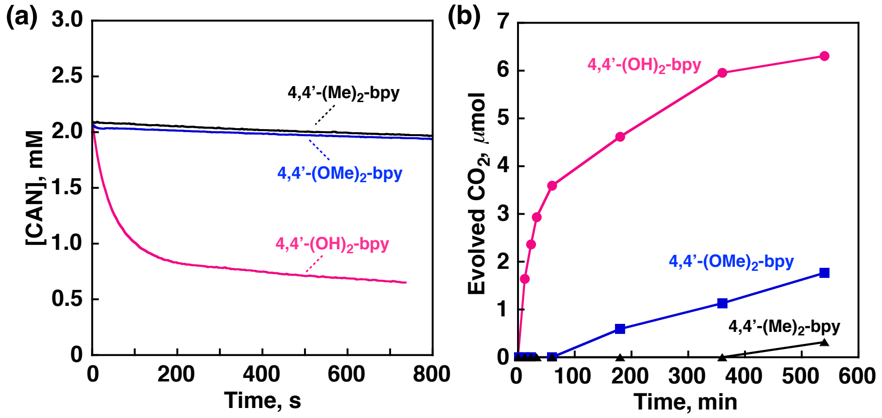

Figure 9. (a) Time courses of concentration of CAN in the oxidation of 4,4'-$(OH)_2$-bpy (pink: 10 mM), 4,4'-$(OMe)_2$-bpy (blue: 10 mM) and 4,4'-$(Me)_2$-bpy (black: 10 mM) with CAN (2.0 mM) in aqueous solutions (2.0 mL) containing nitric acid (0.10 M). (b) Time course of CO_2 evolution in the oxidation of 4,4'-$(OH)_2$-bpy (circle: 3.0 mM), 4,4'-$(OMe)_2$-bpy (square: 3.0 mM) and 4,4'-$(Me)_2$-bpy (triangle: 3.0 mM) with CAN (60 mM) in an aqueous solution (2.0 mL) containing nitric acid (0.10 M).

terms of the oxidation reactivity of the bpy ligands, leading to the largest reactivity of the precatalyst **1** for the catalytic water oxidation by CAN. The easy oxidation of the *phenolic-like* OH (to quinoid-type structures) may be the reason why complex **1** is the most easily oxidized of these complexes.

Nanoparticles Derived from 1 Observed by TEM. ^{1}H NMR and DLS measurements of the solutions after the catalytic water oxidation by CAN with the precatalyst **1** and the ligand oxidation by CAN clearly indicate the decomposition of **1** to produce nanoparticles (**1'**) during the water oxidation.[56] The nanoparticles formed after the water oxidation were separated from the reaction solution by centrifugation, washed with water several times and dried *in vacuo* at room temperature. The obtained precipitates were observed by transmission electron microscopy (TEM). TEM images of **1'** are displayed in Figure 10. The particles **1'** formed secondary particles whose sizes were larger than micron order (Figures 10a and 10b). In the high magnification images of **1'** in Figures 10c and 10d, some primary nanoparticles with the size in the rage of 100–300 nm were observed. TEM images of iridium hydroxide (**5**) prepared by hydrolysis of $H_2Ir^{IV}Cl_6$ with NaOH and iridium oxide (**5'**) are displayed in Figures 11 and 12 indicate that the size of **5** and **5'** is in the rage of 50–200 nm with an undefined shape.

TG/DTA and XPS Measurements of 1'. Thermal behavior of **1'** was investigated by TG/DTA measurements under air-flowing conditions. The particles formed after addition of 10 equivalents of CAN to 2.0 mM of complex **1** in an aqueous solution (2.0 mL) containing 0.10 M nitric acid were separated by centrifugation, washed with water several times and dried *in vacuo* at room temperature. The total amount of the particles was around 3 mg obtained from the 5 solutions and this was

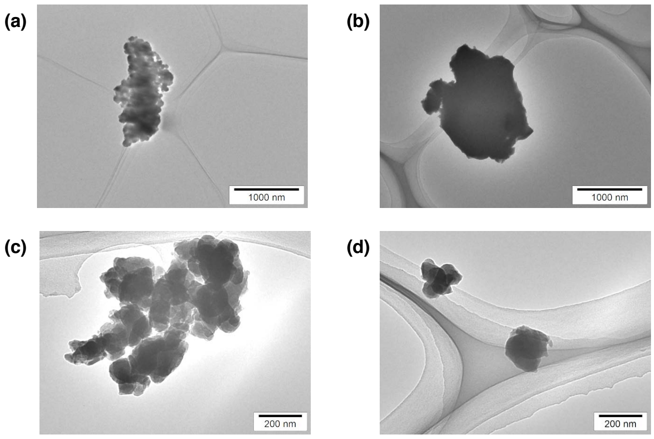

Figure 10. TEM images of nanoparticles (**1'**) formed by the reaction of **1** with CAN at different magnifications (a–d).

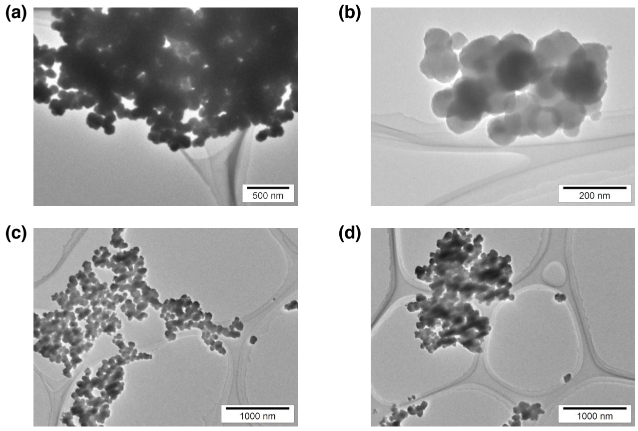

Figure 11. TEM images at different magnifications (a–d) of iridium hydroxide (**5**) prepared by a conventional method.

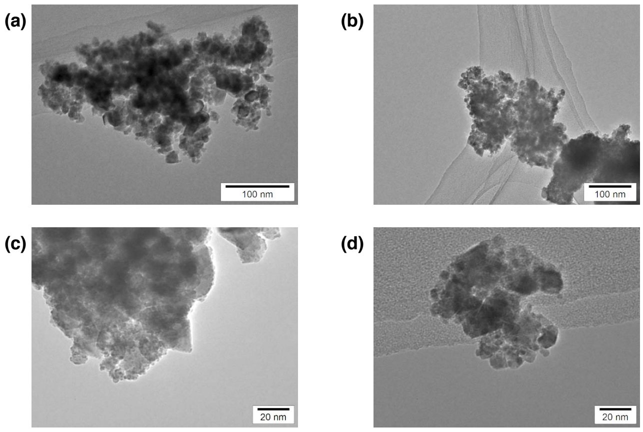

Figure 12. TEM images at different magnifications (a–d) of iridium oxide (**5’**) prepared by a conventional method.

used for the TG/DTA measurement. Figure 13 shows TG/DTA curve of **1’** in which the TG curve can be divided into three consecutive stages with weight loss. The first step of weight loss with an endothermic peak at 120 °C corresponds to the removal of physisorbed water. The second step from about 200 °C to 300 °C accompanied by an exothermic peak was assigned to oxidative removal of carbonaceous residues derived from the ligand because **1** decomposes around 300 °C, which is slightly higher temperature than the observed weight-loss temperature for **1’** as shown in Figure 14. Weight loss observed in this step was ca 5%. The third regular weight loss started at about 430 °C and continued up to about 500 °C is ascribed to dehydration of iridium hydroxide to iridium oxides. Formation of iridium hydroxide species even under highly acidic conditions has been reported previously.[57] The weight loss observed in this step was nearly 8.0%, which is close to 7.8% weight loss expected at the dehydration process from $Ir(OH)_3$ to IrO_2.

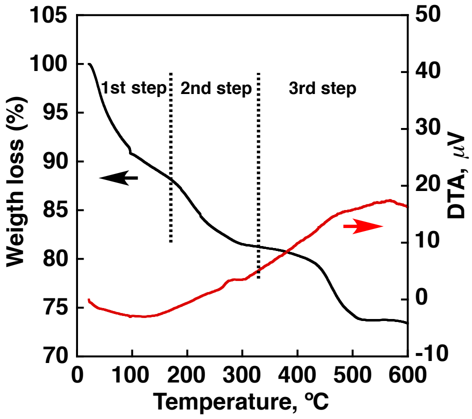

Figure 13. TG/DTA data for **1'** (TG curve: black, DTA curve: red). The temperature increased from 25 °C to 600 °C with a ramp rate of 2 °C/min.

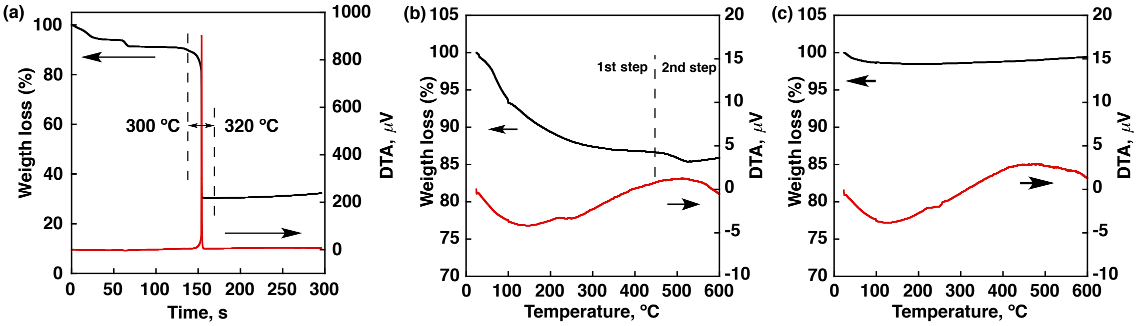

Figure 14. TG/DTA data for (a) the Ir complex **1**, (b) iridium hydroxide (**5**) and (c) iridium oxide (**5'**); TG curve (black) and DTA curve (red). The temperature increased from 25 °C to 100 °C (held at 100 °C for 10 min) and from 100 °C to 600 °C with a ramp rate of 2 °C min^{-1}.

In order to confirm the weight-loss assignment for each step, TG/DTA measurements were performed for iridium hydroxide (**5**). The TG curve of iridium hydroxide in Figure 14b showed only two consecutive steps because of the absence of a step for removal of contaminated organic species observed in the case of **1'**. The weight loss at the second step of iridium hydroxide starting from 450 °C attributed to dehydration of iridium hydroxide was observed as the third step for **1'** around 450 °C. Thus, the thermal analysis of **1'** suggests that **1'** before calcination is mainly composed of $Ir(OH)_3$ with ca 5 % of carbonaceous residues derived from organic ligands of **1**.

To determine surface conditions of the nanoparticles (**1'**) produced in the catalytic water oxidation by CAN with the precatalyst **1**, X-ray photoelectron spectroscopy (XPS) measurements of **1'** were performed for the energy regions of Ir 4f, O 1s and C 1s with reference to commercially available IrO_2 and iridium hydroxide (**5**). As reported previously, the binding energy of Ir $4f_{5/2}$ reflects the valence of Ir ions sensitively where the binding energies of Ir $4f_{5/2}$ for Ir^0, Ir^{III} and Ir^{IV} are reported to be 61.0 eV, 62.0 eV and 63.7 eV, respectively.[58–60] The XPS spectra of Ir 4f and O 1s for **1’, 5** and the IrO_2 are shown in Figure 15. The binding energy of Ir $4f_{5/2}$ of both the IrO_2 and **5** was 61.9 eV, which is close to the reported binding energy of 62.0 eV for Ir(III) species.[58] The Ir $4f_{5/2}$ peak of **1’** appeared at 62.8 eV, which is shifted to higher binding energy by 1.1 eV compared with the Ir $4f_{5/2}$ peak of the IrO_2, but still closer to the reported value for Ir(III) rather than Ir(IV). However, the actual oxidation state of the surface of Ir nanoparticles (**1’**) has yet to be determined because X-ray-induced reduction during XPS measurements may affect the observed oxidation state.[61–64] The O 1s peaks of **1’**, **5** and the IrO_2 appeared at 532.3 eV, 531.3 eV and 530.2 eV, respectively. An increase in the binding energy of O 1s peak of **1’** and **5** results from formation of hydroxide species as often reported previously.[65–67] The larger shift observed for O 1s peak of **1’** than that of **5** may be due to the high valence of Ir species. Formation of iridium hydroxide species in **1’** is also supported by TG/DTA results as described above. Additionally, XPS measurements for the energy region of N 1s was performed for **1’**, however, no peak was detected, indicating no occlusion of bpy ligand in the nanoparticles. Thus, it can be concluded that **1’** derived from **1** after the water oxidation by CAN is composed of $Ir(OH)_3$ and carbonaceous residues.

Catalytic Activity of Iridium Hydroxide for Water Oxidation by CAN. The catalytic activity of **1’** derived from **1** for the water oxidation by CAN was compared

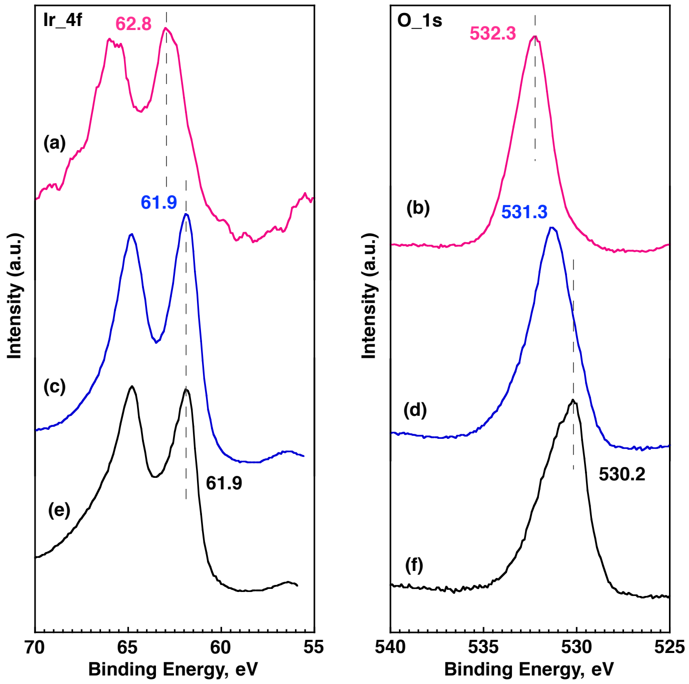

Figure 15. X-ray photoelectron spectra in the binding energy regions of Ir 4f and O 1s for (a and b) **1’**, (c and d) **5** and (e and f) commercially available IrO_2.

with that of $[IrCp^*(OH_2)_3]SO_4$ which contains no organic ligand other than Cp^*. Each catalyst (2.0 mM) was immersed in an aqueous solution containing nitric acid (2.0 mL, 0.10 M). The evolved gas was quantified by dilatometry every minute. As shown in Figure 16 (blue for **1'** and red for $[IrCp^*(OH_2)_3]SO_4$), the TOF in first two minuets observed with $[IrCp^*(OH_2)_3]SO_4$ was more than four times larger than that of **1'**. Particles were also formed when adding CAN to $[IrCp^*(OH_2)_3]SO_4$ in 0.10 M HNO_3 (Figure 17). This result clearly indicates that bpy-ligand is not effective for water oxidation by CAN. Then, the catalytic activity of iridium hydroxide (**5**) and iridium oxide (**5'**), which was obtained by calcination of **5** at 600 °C, were compared with the reactivity of precatalyst **1**, because **5'** has been reported as the most active catalyst for the water oxidation.[33–42] The catalytic water oxidation by CAN with the precatalyst **1**, **5** and **5'** (2.0 mM Ir-basis) was conducted using a large concentration of CAN (0.50 M) in an aqueous solution containing nitric acid (0.10 M). The initial (< 2 min) rate of oxygen evolution with **1'** (0.19 μmol s^{-1}, TOF = 0.048 s^{-1}) was similar to that with **5'** (0.17 μmol s^{-1}, TOF = 0.043 s^{-1}), although the TOF value of **1'** (0.048 s^{-1}) at a high concentration of CAN (0.50 M) is much lower than the value (0.75 s^{-1}) at a low concentration of CAN (10 mM) in Table 1. The overall catalytic activity of **1'** at prolonged reaction time (> 2 min) is significantly higher than that of **5'**, which was deactivated faster as compared with **1'** (Figure 16 blue and black). The difference in catalysis between **5** and **5'** became more obvious when surface-area-corrected TOF values are compared. The catalytic activity of **5** and **5'** are summarized in Table 2. Surface-area-corrected TOF (TOF_s) of **5** is 1.6 s^{-1} is significantly higher than that of **5'** (0.23 s^{-1}). The TOF_s values for **5** and **5'** are estimates because ambiguities exist when

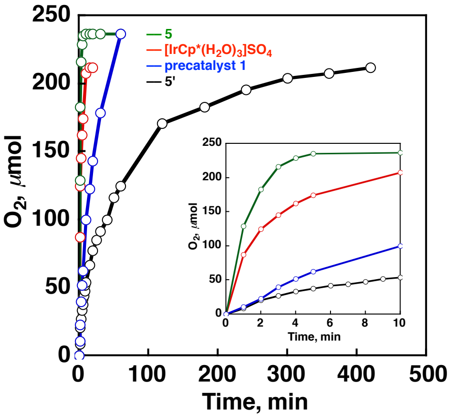

Figure 16. Time courses of oxygen evolution by the catalytic water oxidation by CAN (0.50 M) with the precatalyst **1** (blue: 2.0 mM), $[IrCp^*(H_2O)_3]SO_4$ (red: 2.0 mM), iridium hydroxide **5** (green: 2.0 mM Ir-basis) and iridium oxide **5'** (black: 2.0 mM Ir-basis) in an aqueous solution containing nitric acid (0.10 M) measured by dilatometry. The inset shows the initial time courses.

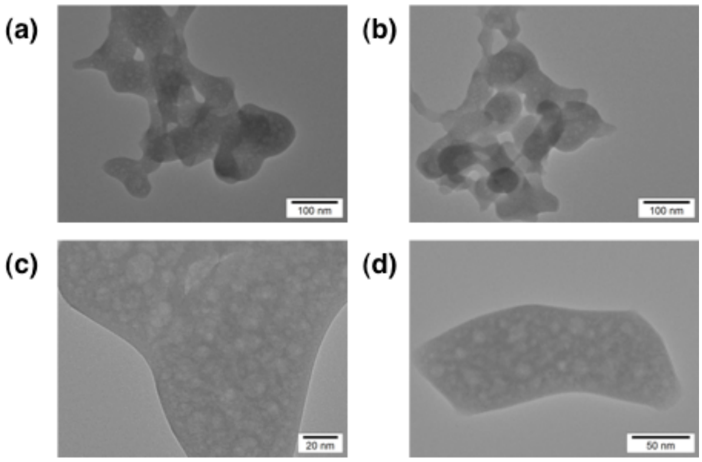

Figure 17. TEM images at different magnifications (a–d) of the particles from [IrCp*(H$_2$O)$_3$]SO$_4$ prepared by adding 10 equivalents of CAN to 2.0 mM of [IrCp*(H$_2$O)$_3$]SO$_4$ in 0.10 M nitric acid.

Table 2. Oxygen Evolution Rates, TOF, BET Surface Area and Surface-Area-Corrected TOF Values (TOF$_s$) of Iridium Hydroxide (5) and Iridium Oxide (5')

	iridium hydroxide (**5**)	iridium oxide (**5'**)
R_{O2} (μmol s^{-1})^a	2.1	0.17
TOF (s^{-1})^b	0.54	0.043
BET (m^2 g^{-1})	88	51
TOF$_s$ (s^{-1})^c	1.6	0.23

[a] See Figure 16 for experimental conditions. O$_2$ evolution rate was obtained from initial rate. [b] Turnover frequency for O$_2$ evolution calculated on the basis of the number of Ir atoms in the reaction solution. [c] Turnover frequency calculated on the basis of the number of Ir atoms on the surfaces of catalytic particles (see Figure 18, *vide infra*).

Calculation of the numbers of Ir atoms on the particles surfaces

The numbers of surface Ir atoms were calculated by following equation.

$N_s = [N_A \times (d / f_w)]^{2/3} \times$ (number of Ir atoms in chemical formula) $\times$ (catalyst weight) $\times$ (SA)

N_s : number of surface Ir atoms
N_A : the Avogadro's number
d : density of Ir-based metal oxide (IrO$_2$ for 11.7 g cm^{-3})
f_w: formula weight of Ir-based metal oxide
SA: BET surface area

	BET surface area (m^2 g^{-1})	number of surface Ir atoms in the reaction solution
Iridium hydroxide (**5**)	88	8.1×10^{17}
Iridium oxide (**5'**)	51	4.6×10^{17}

Figure 18. Calculation of the numbers of Ir atoms on the particles surfaces.

cross-correlating electrochemical active area and BET surface area, particularly for hydrous oxides.[68] Indeed, if there were a slight underestimate of the surface area for the amorphous material, the TOF_s values would be a disparate between **5** and **5'**. However, more than 7 times larger TOF_s value of **5** than that of **5’** implies that **5** is certainly more active than **5’**. Thus, the higher catalytic activity of **1’** was ascribed to formation of iridium hydroxide during the reaction.

Conclusion

Catalytically active nanoparticles for water oxidation by cerium(IV) ammonium nitrate, CAN, were obtained by the reaction of $[Ir^{III}(Cp^*)\{4,4'-(OH)_2-2,2'-bipyridine\}(H_2O)]^{2+}$ (**1**) with CAN in an aqueous solution containing nitric acid. Such catalytically active nanoparticles were hardly produced from iridium Cp^* complexes with other substituted-bpy ligands ($[Ir^{III}(Cp^*)(4,4'-R_2-2,2'-$ bipyridine$)(H_2O)]^{2+}$, R = OMe, Me and COOH) during the water oxidation. The formation of catalytically active nanoparticles from **1** may result from the highest oxidation susceptibility of $4,4'-(OH)_2$-bipyridine, which is the ligand of **1**, among the substituted-bpy ligands. TG/DTA and XPS measurements conducted for the nanoparticles produced from **1** after the water oxidation by CAN indicate that the nanoparticles are composed of iridium hydroxide with a small amount of carbonaceous residues. However, the actual reactive species on the surface of iridium hydroxide nanoparticles during the water oxidation has yet to be clarified. Nevertheless, the present study has demonstrated that the choice of the precursor for generation of the catalytically active nanoparticles is of primary importance to achieve the high catalytic activity and stability for the water oxidation.

References

(1) Amunts, A.; Drory, O.; Nelson, N. *Nature* **2007**, *447*, 58.

(2) Umena, Y.; Kawakami, K.; Shen, J.-R.; Kamiya, N. *Nature* **2011**, *473*, 55.

(3) Magnuson, A.; Anderlund, M.; Johansson, O.; Lindblad, P.; Lomoth, R.; Polivka, T.; Ott, S.; Stensjo, K.; Styring, S.; Sundstrom, V.; Hammarstrom, L. *Acc. Chem. Res.* **2009**, *42*, 1899.

(4) Dau, H.; Zaharieva, I. *Acc. Chem. Res.*, **2009**, *42*, 1861.

(5) Siegbahn, P. E. M. *Acc. Chem. Res.,* **2009**, *42*, 1871.

(6) Gust, D.; Moore, T. A.; Moore, A. L. *Acc. Chem. Res.* **2009**, *42*, 1890.

(7) (a) Lewis, N. S.; Nocera, D. G.; *Proc. Natl. Acad. Sci. U. S. A.* **2006**, *103*, 15729. (b) Kanan, M. W.; Surendranath, Y.; Nocera, D. G. *Chem. Soc. Rev.* **2009**, *38*, 109.

(8) Kudo, A.; Miseki, Y. *Chem. Soc. Rev.* **2009**, *38*, 253.

(9) Liu, F.; Concepcion, J. J.; Jurss, J. W.; Cardolaccia, T.; Templeton, J. L.; Meyer, T. J. *Inorg. Chem.* **2008**, *47*, 1727.

(10) (a) Jiao, F.; Frei, H. *Energy Environ. Sci.* **2010**, *3*, 1018. (b) Eisenberg, R.; Gray, H. B. *Inorg. Chem.* **2008**, *47*, 1697.

(11) Murakami, M.; Hong, D.; Suenobu, T.; Yamaguchi, S.; Ogura, T.; Fukuzumi, S. *J. Am. Chem. Soc.* **2011**, *133*, 11605.

(12) Deng, Z. P.; Tseng, H. W.; Zong, R. F.; Wang, D.; Thummel, R. *Inorg. Chem.* **2008**, *47*, 1835.

(13) Sala, X.; Ertem, M. Z.; Vigara, L.; Todorova, T. K.; Chen, W. Z.; Rocha, R. C.; Aquilante, F.; Cramer, C. J.; Gagliardi, L. Llobet, A. *Angew. Chem., Int. Ed.* **2010**, *49*, 7745.

(14) Gersten, S. W.; Samuels, G. J.; Meyer, T. J. *J. Am. Chem. Soc.* **1982**, *104*, 4029.

(15) Yagi, M.; Narita, K. *J. Am. Chem. Soc.* **2004**, *126*, 8084.

(16) Poulsen, A. K.; Rompel, A.; McKenzie, C. J. *Angew. Chem., Int. Ed.* **2005**, *44*, 6916.

(17) Tseng, H. W.; Zong, R.; Muckerman, J. T.; Thummel, R. *Inorg. Chem.* **2008**, *47*, 11763.

(18) Geletii, Y. V.; Huang, Z. Q.; Hou, Y.; Musaev, D. G.; Lian, T. Q.; Hill, C. L. *J. Am. Chem. Soc.* **2009**, *131*, 7522.

(19) Yin, Q. S.; Tan, J. M.; Besson, C.; Geletii, Y. V.; Musaev, D. G.; Kuznetsov, A. E.; Luo, Z.; Hardcastle, K. I.; Hill, C. L. *Science* **2010**, *328*, 342.

(20) Duan, L. L.; Fischer, A.; Xu, Y. H.; Sun, L. C. *J. Am. Chem. Soc.* **2009**, *131*, 10397.

(21) Xu, Y.; Fischer, A.; Duan, L.; Tong, L.; Gabrielsson, E.; Akermark, B.; Sun, L. *Angew. Chem., Int. Ed.* **2010**, *49*, 8934.

(22) Chen, Z. F.; Concepcion, J. J.; Luo, H. L.; Hull, J. F.; Paul, A.; Meyer, T. J. *J. Am. Chem. Soc.* **2010**, *132*, 17670.

(23) Sala, X.; Ertem, M. Z.; Vigara, L.; Todorova, T. K.; Chen, W. Z.; Rocha, R. C.; Aquilante, F.; Cramer, C. J.; Gagliardi, L.; Llobet, A. *Angew. Chem., Int. Ed.* **2010**, *49*, 7745.

(24) Wada, T.; Muckerman, J. T.; Fujita, E.; Tanaka, K. *Dalton Trans.* **2010**, *40*, 2225.

(25) Wasylenko, D. J.; Ganesamoorthy, C.; Henderson, M. A.; Koivisto, B. D.; Osthoff, H. D.; Berlinguette, C. P. *J. Am. Chem. Soc.* **2010**, *132*, 16094.

(26) McDaniel, N. D.; Coughlin, F. J.; Tinker, L. L.; Bernhard, S. *J. Am. Chem. Soc.* **2008**, *130*, 210.

(27) Hull, J. F.; Balcells, D.; Blakemore, J. D.; Incarvito, C. D.; Eisenstein, O.; Brudvig, G. W.; Crabtree, R. H. *J. Am. Chem. Soc.* **2009**, *131*, 8730.

(28) Blakemore, J. D.; Schley, N. D.; Balcells, D.; Hull, J. F.; Olack, G. W.; Incarvito, C. D.; Eisenstein, O.; Brudvig, G. W.; Crabtree, R. H. *J. Am. Chem. Soc.* **2010**, *132*, 16017.

(29) Lalrempuia, R.; McDaniel, N. D.; Muller-Bunz, H.; Bernhard, S.; Albrecht, M. *Angew. Chem., Int. Ed.* **2010**, *49*, 9765.

(30) Savini, A.; Bellachioma, G.; Ciancaleoni, G.; Zuccaccia, C.; Zuccaccia, D.; Macchioni, A. *Chem. Commun.* **2010**, *46*, 9218.

(31) Hetterscheid, D. G. H.; Reek, J. N. H. *Chem. Commun.* **2011**, *47*, 2712.

(32) Ellis, W. C.; McDaniel, N. D.; Bernhard, S.; Collins, T. J. *J. Am. Chem. Soc.* **2010**, *132*, 10990.

(33) Brunschwig, B. S.; Chou, M. H.; Creutz, C.; Ghosh, P.; Sutin, N. *J. Am. Chem. Soc.* **1983**, *105*, 4832.

(34) Harriman, A.; Pickering, I. J.; Thomas, J. M.; Christensen, P. A. *J. Chem. Soc., Faraday Trans. I* **1988**, *84*, 2795.

(35) Nakamura, R.; Frei, H. *J. Am. Chem. Soc.* **2006**, *128*, 10668.

(36) Nakagawa, T.; Bjorge, N. S.; Murray, R. W. *J. Am. Chem. Soc.* **2009**, *131*, 15578.

(37) Hara, M.; Mallouk, T. E. *Chem. Commun.* **2000**, 1903.

(38) Tilley, S. D.; Cornuz, M.; Sivula, K.; Gratzel, M. *Angew. Chem., Int. Ed.* **2010**, *49*, 6405.

(39) Kwon, S. J.; Fan, F. R. F.; Bard, A. J. *J. Am. Chem. Soc.* **2010**, *132*, 13165.

(40) Hoertz, P. G.; Kim, Y. I.; Youngblood, W. J.; Mallouk, T. E. *J. Phys. Chem. B* **2007**, *111*, 6845.

(41) Yagi, M.; Tomita, E.; Kuwabara, T. *J. Electroanal. Chem.* **2005**, *579*, 83.

(42) Nahor, G. S.; Hapiot, P.; Neta, P.; Harriman, A. *J. Phys. Chem.* **1991**, *95*, 616.

(43) Ogo, S.; Makihara, N.; Watanabe, Y. *Organometallics* **1999**, *18*, 5470.

(44) Himeda, Y.; Onozawa-Komatsuzaki, N.; Miyazawa, S.; Sugihara, H.; Hirose, T.; Kasuga, K. *Chem. –Eur. J.* **2008**, *14*, 11076.

(45) McFarland, J. M.; Francis, M. B. *J. Am. Chem. Soc.* **2005**, *127*, 13490.

(46) Hong, Y. R.; Gorman, C. B. *J. Org. Chem.* **2003**, *68*, 9019.

(47) Widegren, J. A.; Finke, R. G. *J. Mol. Catal. A* **2003**, *198*, 317.

(48) Widegren, J. A.; Bennett, M. A.; Finke, R. G. *J. Am. Chem. Soc.* **2003**, *125*, 10301.

(49) Stracke, J. J.; Finke, R. G. *J. Am. Chem. Soc.* **2011**, *133*, 14872.

(50) Savini, A.; Belanzoni, P.; Bellachioma, G.; Zuccaccia, C.; Zuccaccia, D.; Macchioni, A. *Green. Chem.* **2011**, *13*, 3360.

(51) Whitesides, G. M.; Hackett, M.; Brainard, R. L.; Lavalleye, J. P. P. M.; Sowinski, A. F.; Izumi, A. N.; Moore, S. S.; Brown, D. W.; Staudt, E. M. *Organometallics* **1985**, *4*, 1819.

(52) (a) Anton, D. R.; Crabtree, R. H. *Organometallics* **1983**, *2*, 621. (b) Crabtree, R. H. *Acc. Chem. Res.* **1979**, *12*, 331.

(53) Schley, N. D.; Blakemore, J. D.; Subbaiyan, N. K.; Incarvito, C. D.; D'Souza, F.; Crabtree, R. H.; Brudvig, G. W. *J. Am. Chem. Soc.* **2011**, *133*, 10473.

(54) Brudvig, G. W.; Blakemore, J. D.; Schley, N. D.; Olack, G. W.; Incarvito, C. D.; Crabtree, R. H. *Chem. Sci.* **2011**, *2*, 94.

(55) The reactivity of 4,4'-$(COOH)_2$-2,2'-bpy could not be examined because of the poor solubility in water.

(56) Similar formation of iridium oxide materials by the electrochemical oxidation of $Ir(Cp^*)(H_2O)_3$ has been reported in ref 54.

(57) Castilloblum, S. E.; Richens, D. T.; Sykes, A. G. *Inorg. Chem.* **1989**, *28*, 954.

(58) Hara, M.; Asami, K.; Hashimoto, K.; Masumoto, T. *Electrochim. Acta* **1983**, *28*, 1073.

(59) Hall, H. Y.; Sherwood, P. M. A. *J. Chem. Soc., Faraday Trans. I* **1984**, *80*, 135.

(60) Wei, G. Q.; Wang, Y. X.; Huang, C. D.; Gao, Q. J.; Wang, Z. T.; Xu, L. *Int. J. Hydrogen Energy* **2010**, *35*, 3951.

(61) Mercier-Bion, F.; Drot, R.; Ehrhardt, J. J.; Lambert, J.; Roques, J.; Simoni, E. *Surf. Interface Anal.* **2010**, *43*, 777.

(62) Feibelman, P. J.; Knotek, M. L. *Phys. Rev. B* **1978**, *18*, 6531.

(63) Knotek, M. L.; Feibelman, P. J. *Surf. Sci.* **1979**, *90*, 78.

(64) Cazaux, J. *Appl. Surf. Sci.* **1985**, *20*, 457.

(65) Yang, J.; Liu, H.; Martens, W. N.; Frost, R. L. *J. Phys. Chem. C* **2010**, *114*, 111.

(66) Mathew, T.; Shiju, N. R.; Sreekumar, K.; Rao, B. S.; Gopinath, C. S. *J. Catal.* **2002**, *210*, 405.

(67) Yamada, Y.; Yano, K.; Xu, Q. A.; Fukuzumi, S. *J. Phys. Chem. C* **2010**, *114*, 16456.

(68) Trasatti, S.; Petrii, O. A. *Pure Appl. Chem*. **1991**, *63*, 711.

Chapter 2

Water-Soluble Mononuclear Cobalt Complexes with Organic Ligands Acting as Precatalysts for Efficient Photocatalytic Water Oxidation

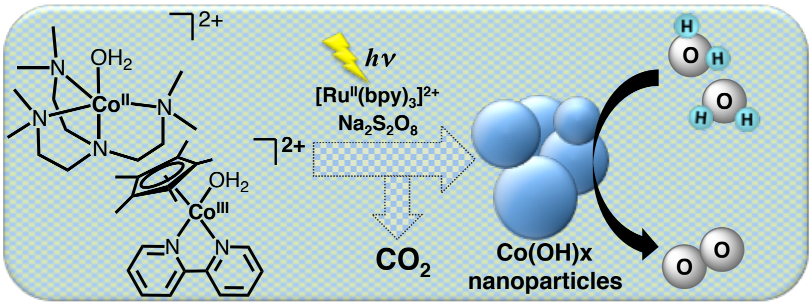

Abstract: The photocatalytic water oxidation to evolve O_2 was performed by photoirradiation ($\lambda > 420$ nm) of an aqueous solution containing $[Ru(bpy)_3]^{2+}$ (bpy = 2,2'-bipyridine), $Na_2S_2O_8$ and water-soluble cobalt complexes with various organic ligands as precatalysts in the pH range of 6.0–10. The turnover numbers (TONs) based on the amount of Co for the photocatalytic O_2 evolution with $[Co^{II}(Me_6tren)(OH_2)]^{2+}$ (**1**) and $[Co^{III}(Cp^*)(bpy)(OH_2)]^{2+}$ (**2**) [Me_6tren = tris(*N*,*N'*-dimethylaminoethyl)amine, Cp^* = η^5-pentamethylcyclopentadienyl] at pH 9.0 reached 420 and 320, respectively. The evolved O_2 yield increased in proportion to concentrations of precatalysts **1** and **2** up to 0.10 mM. However, the O_2 yield dramatically decreased when the concentration of precatalysts **1** and **2** exceeded 0.10 mM. When the concentration of $Na_2S_2O_8$ was increased from 10 mM to 50 mM, CO_2 evolution was observed during the photocatalytic water oxidation. These results indicate that a part of the organic ligands of **1** and **2** were oxidized to evolve CO_2 during the photocatalytic reaction. The degradation of complex **2** under photocatalytic conditions and the oxidation of Me_6tren ligand of **1** by $[Ru(bpy)_3]^{3+}$ were confirmed by ^{1}H NMR measurements. Dynamic light scattering (DLS) experiments indicate the formation of particles with the diameter of around 20 ± 10 nm and 200 ± 100 nm during the photocatalytic water oxidation with **1** and **2**, respectively. The particle sizes determined by DLS agreed to those of the secondary particles observed by TEM. The XPS measurements of the formed particles suggest that the surface of the particles is covered with cobalt hydroxides, which could be converted to active species containing high-valent cobalt ions during the photocatalytic water oxidation. The recovered nanoparticles produced from **1** act as a robust catalyst for the photocatalytic water oxidation.

Introduction

Solar energy is used efficiently to produce high-energy chemicals such as sugar by photosynthesis, in which an oxygen-evolving complex composed of a manganese-oxo cluster with a calcium ion oxidizes water to extract electrons and protons.[1–6] In order to mimic the photosynthesis artificially, light-harvesting and charge-separation units as well as catalytic units for water oxidation and CO_2 fixation should be developed.[7–17] To date, the development of efficient water oxidation catalysts (WOCs) is a bottleneck to attain the artificial photosynthesis because water oxidation is a challenging process including multi-electron transfer coupled with multi-proton transfer.[18–22]

For the past few decades, extensive efforts have been devoted to develop WOCs using various metal complexes.[23–50] Many multi- or mononuclear ruthenium complexes with organic ligands have been demonstrated to act WOCs since the finding of a binuclear ruthenium complex, so-called "*blue dimer*", which catalyzes the water oxidation by an oxidant such as ammonium cerium nitrate.[51–66] Iridium complexes have also been demonstrated as effective WOCs in late years, such as mononuclear iridium complexes with a Cp^* (Cp^* = η^5-pentamethylcyclopentadienyl) ligand.[67–74] However, the drawbacks of these precious metals are high prices and limited stocks for any practical applications.

Recently, cobalt-based compounds have attracted many researchers, because cobalt is much more abundant and less expensive than ruthenium and iridium.[75–86] For example, a thin film of cobalt phosphate prepared by electrodeposition exhibits low overpotential and high catalytic reactivity for the water oxidation.[81,82] Co_3O_4 has also been reported to act as an active catalyst in the heterogeneous photocatalytic water oxidation with $[Ru(bpy)_3]^{2+}$ (bpy = 2,2'-bipyridine) as a photosensitizer and $Na_2S_2O_8$ as a sacrificial electron acceptor.[16,76] Besides the electrochemical and the photocatalytic water oxidation, the thermal water oxidation can be catalyzed by WOCs containing Co(II) ions with a one-electron oxidant such as $[Ru(bpy)_3]^{3+}$.[77–80] Thus, cobalt-containing materials are promising candidates for WOCs in developing the artificial photosynthesis.

On the perspective of cobalt complexes, mononuclear cobalt complexes with organic ligands are attractive candidates, because catalytically active cobalt ions can be isolated in the atomic level and their reactivity can be controlled by changing the chemical structure of ligands as far as they are stable under highly oxidative conditions. A tetranuclear cobalt polyoxometalate complex of $[Co^{II}_4(H_2O)_2(\alpha\text{-}PW_9O_{34})_2]^{10-}$, which contains no organic ligand, has been reported to act as an efficient catalyst in the homogenous photocatalytic system using $[Ru(bpy)_3]^{2+}$ and $Na_2S_2O_8$.[83] Although it has recently been reported that the tetranuclear cobalt polyoxometalate complex decomposed at pH 8.0 in the electrochemical water oxidation,[85] no evidence has shown that such decomposition undergoes in the homogenous water oxidation. It is important for developing highly active water oxidation catalysts to unveil what is the true catalyst when degradable catalytic complexes are employed as a catalyst.

In Chapter 2, I report the photocatalytic water oxidation using $[Ru(bpy)_3]^{2+}$ as a photosensitizer and $Na_2S_2O_8$ as a sacrificial electron acceptor in the presence of a water-soluble mononuclear cobalt complex with an organic ligand, $[Co^{II}(Me_6tren)(OH_2)]^{2+}$ (**1**), $[Co^{III}Cp^*(bpy)(OH_2)]^{2+}$ (**2**), $[Co^{II}(12\text{-TMC})]^{2+}$ (**3**) or $[Co^{II}(13\text{-TMC})]^{2+}$ (**4**) (12-TMC = 1,4,7,10-tetramethyl-1,4,7,10-tetraazacyclododecane and 13-TMC = 1,4,7,10-tetramethyl-1,4,7,10-tetraazacyclotridecane) (Chart 1). The catalytic reactivity in water oxidation using **1**–**4** as precatalysts was compared with that using $Co(NO_3)_2$ possessing no organic ligands but reported to catalyze water oxidation.[77–80] The kinetic analysis and the characterization of the actual reactive catalyst together with oxidation of the ligands have revealed that both **1** and **2** were converted to nanoparticles during the photocatalytic water oxidation and that the nanoparticles composed of $Co(OH)_x$ are the active catalysts for the water oxidation reactions.

Chart 1. Chemical Structures of Mononuclear Water-Soluble Cobalt Complexes Used as Precatalysts (a) $[Co^{II}(Me_6tren)(OH_2)]^{2+}$ (1), (b) $[Co^{III}(Cp^*)(bpy)(OH_2)]^{2+}$ (2), (c) $[Co^{II}(12\text{-TMC})]^{2+}$ (3) and (d) $[Co^{II}(13\text{-TMC})]^{2+}$ (4). (e) A Scheme Showing the Overall Catalytic Cycle for Photocatalytic Water Oxidation with $[Ru(bpy)_3]^{2+}$, $Na_2S_2O_8$ and a Cobalt-Containing Catalyst

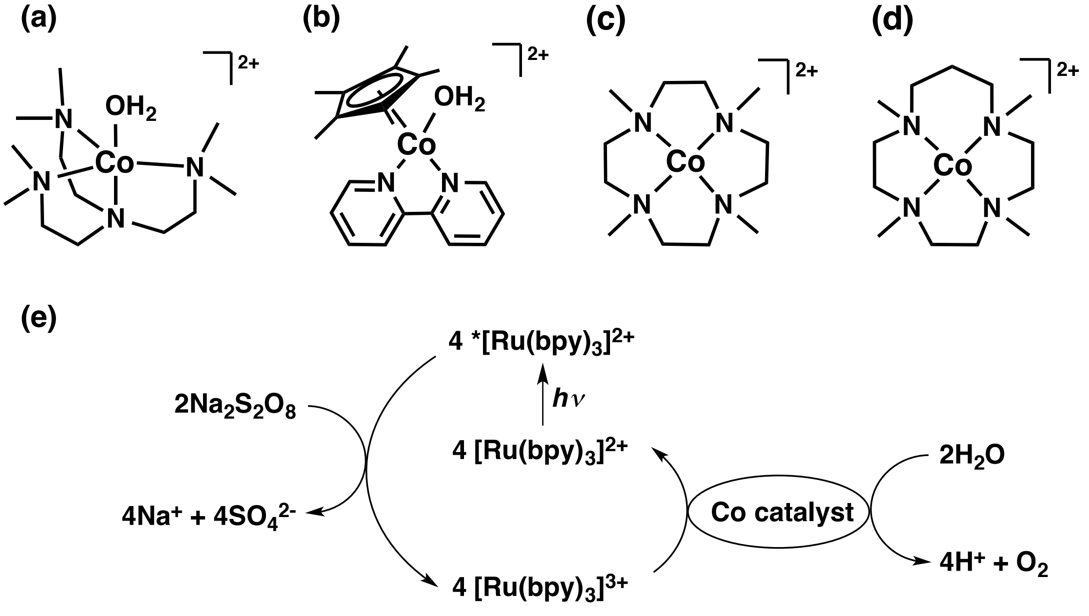

Experimental Section

Materials. All chemicals commercially available were used without further purification unless otherwise noted. $Co(NO_3)_2$ and 2,2'-bipyridine were purchased from Wako Pure Chemical Industries Ltd. Pentamethylcyclopentadiene was obtained from Kanto Chemical Co., Inc. $[Ru(bpy)_3]Cl_2$ was obtained from Tokyo Chemical Industry Co., Ltd. $Co(ClO_4)_2$ and tris(2-ethylamino)amine were supplied from Sigma-Aldrich Co. Purified water (18.2 MΩ cm) was obtained using a Milli-Q system (Millipore, Direct-Q 3 UV). $[Ru(bpy)_3](ClO_4)_2$ was synthesized by adding an aqueous solution of $HClO_4$ to an aqueous solution of $[Ru(bpy)_3]Cl_2$. $[Co^{II}(Me_6tren)(OH_2)](ClO_4)_2$ (**1**),[87–89] $[Co^{III}(Cp^*)(bpy)(OH_2)](PF_6)_2$ (**2**),[90,91] $[Ru(bpy)_3](ClO_4)_3$[78] were synthesized according to the literature procedures and characterized by electrospray ionization mass spectroscopy and ^1H NMR. Authentic Co_3O_4 was synthesized according to previous reports.[92,93] $[Co^{II}(12\text{-}TMC)](ClO_4)_2$ and $[Co^{II}(13\text{-}TMC)](ClO_4)_2$ were synthesized according to a previous report.[94]

Synthesis of Tris(*N, N'*-(dimethylamino)ethyl)amine (Me_6tren). Me_6tren was prepared according the reported procedure (M. Ciampoli, *et al. Inorg. Chem.* 1966, **5**, 41). ^1H NMR (300 MHz, $CDCl_3$): $\delta = 2.16$ ppm (s, 18H), 2.30 (m, 6 H), 2.54 (m, 6 H).

Synthesis of $[Co(Me_6tren)(OH_2)](ClO_4)_2$ (1). $Co(ClO_4)_2{\cdot}6H_2O$ (1.83 g) was dissolved in a 30 mL of CH_3CN solution containing Me_6tren (1.15 g). The solution was stirred for 2 h at room temperature. Et_2O (150 mL) was added to the mixture to yield pale purple precipitate, which was filtered and dried *in vacuo*. The purple powder was recrystallized from CH_3CN-Et_2O. Yield: 72% (1.89 g). ESI-MS in CH_3CN: $m/z = 342.2$ for $[Co(Me_6tren)Cl]^+$ and $m/z = 388.1$ for $[Co(Me_6tren)(ClO_4)]^+$.

Synthesis of $[Co(Cp^*)(bpy)(OH_2)](PF_6)_2$ (2). Pentamethylcyclopentadiene (Cp^*, 25 mL) and *tert*-butyllithium (~1.7 M in *n*-pentane, 90 mL) were combined in an equimolar amount (1:1) in *n*-pentane at 203 K. The solution was stirred and slowly allowed to warm up to room temperature. After stirring for further 24 h at room temperature, a white suspension was filtered as pentamethylcyclopentadienyllithium (Cp^*Li) by an inert gas frit. The anhydrous $CoCl_2$ (1.32 g) was added to the solution of Cp^*Li (1.42 g) in 20 mL of tetrahydrofuran. The mixture was stirred for 3 h at room temperature until the brown solution became green-brown. Afterwards the solution was concentrated to a smaller volume under reduced pressure and extracted with 100 mL of *n*-pentane. The brown extractions were bubbled by CO gas for 30 min through the solution. Di-*μ*-chloro-bis[chloro(pentamethylcyclopentadienyl)cobalt] ($[(\mu\text{-}Cl)(Co\text{-}Cp^*Cl)]_2$) was obtained as green powder. The $[(\mu\text{-}Cl)(CoCp^*Cl)]_2$ (100 mg) in 20 mL of water was stirred with the stoichiometric amount of $AgPF_6$ (191 mg) for 4 h at the room temperature. After filtering off AgCl as precipitates, 2,2'-bipyridine (65 mg) was added to the filtrate. The reaction was completed in 15 min at 313 K. An aqueous solution of NH_4PF_6 was added to the reaction solution to obtain crystalline product. ^1H NMR (300 MHz, D_2O): $\delta = 1.27$ ppm (s, 15H), 8.04 (t, 2 H), 8.36 (t, 2 H), 8.44 (d, 2 H), 9.78 (d, 2 H).

Photocatalytic Water Oxidation. Photocatalytic water oxidation was performed as follows. A cobalt complex or $Co(NO_3)_2$ (0.0050–2.5 mM) was added to a buffer solution (50 mM, pH 7.0 and 8.0 for phosphate buffer and 100 mM, pH 9.0 and 10 for borate buffer) containing $Na_2S_2O_8$ (10 or 50 mM) and $[Ru(bpy)_3](ClO_4)_2$ (0.50 mM) purged with Ar gas for 10 min in a vial (i.d. ~1 cm) sealed with a rubber septum. The reactions were started by irradiating the solution with a Xe lamp (500 W) through a transmitting glass filter ($\lambda > 420$ nm) at room temperature. After each irradiation time, 100 μL of Ar was injected into the vial and then the same volume of the gas in the headspace of the vial was sampled by a gas tight syringe and used for gas chromatography (GC) analysis. The O_2 in the sampled gas was separated by passing through a molecular sieve 5A column with an Ar carrier gas and quantified by a thermal conductivity detector (TCD, Shimadzu GC-17A). The total amount of evolved O_2 was calculated from the concentration of O_2 in the headspace gas.

Water oxidation with $[Ru(bpy)_3]^{3+}$ was performed as follows. A buffer solution (pH 8.0) containing a Co species (50 μM) in a vial sealed with a rubber septum was carefully deaerated by Ar gas for 10 min. The solution was withdrawn (2.0 mL) by a syringe and injected to 3.0 μmol (1.5 mM) of $[Ru(bpy)_3]^{3+}$ in another vial sealed with a rubber septum with flowing Ar gas. After the solution was injected completely and Ar gas was stopped, the solution was stirred vigorously for 10 min. A small portion (100 μL) of the gas in the headspace of the vial was sampled by a gas-tight syringe and used for gas analysis by GC.

The quantum yields of O_2 evolution were determined for the photocatalytic water oxidation under the following conditions. A square quartz cuvette (light path length: 10 mm), which was filled with a buffer solution (50 mM, pH 8.0 phosphate buffer) containing $Na_2S_2O_8$ (10 mM), $[Ru(bpy)_3](ClO_4)_2$ (0.50 mM) and **1** or **2** (50 μM), was irradiated with monochromatized light of $\lambda = 450 \pm 10$ nm from a Shimadzu RF-5300PC fluorescence spectrophotometer. The total number of incident photons was measured by a standard method using an actinometer (potassium ferrioxalate, $K_3[Fe^{III}(C_2O_4)_3]$) in an aqueous solution at room temperature where photon flux was determined to be 3.67×10^{-8} einstein s^{-1}. The evolved O_2 in a headspace of the cuvette was quantified by GC.

Isotope-Labeling Experiments. An $H_2{}^{18}O$ (44.9% ^{18}O) solution of phosphate buffer (25 mM, pH 8.0) containing **1** (50 mM), $[Ru(bpy)_3](ClO_4)_2$ (0.25 mM) and $Na_2S_2O_8$ (5.0 mM) was irradiated by a Xe lamp ($\lambda > 420$ nm) in a vial sealed with a rubber septum after bubbling He gas. After 10 min, a small portion (50 mL) of the gas in a headspace was sampled by using a gas-tight syringe for gas analysis. The ratio of $^{16}O^{16}O$, $^{16}O^{18}O$ and $^{18}O^{18}O$ was determined based on the intensity of mass spectra (m/z = 32, 34, and 36) obtained by a Shimadzu GC-17A gas chromatograph [He carrier, TC-FFAP column (GL Science, 1010-15242) at 40 ºC] equipped with a mass spectrometer (Shimadzu, QP-5000).

CO_2 Detection. A buffer solution (pH 9.0, 2.0 mL) containing $Na_2S_2O_8$ (50 mM), $[Ru(bpy)_3](ClO_4)_2$ (0.50 mM) and cobalt catalysts (0–2.5 mM) was sealed in a vial with a rubber septum. The solution was carefully deaerated by bubbling N_2 gas for 10 min. After photoirradiation of the solution by a Xe lamp ($\lambda > 420$ nm), a small portion (50 μL) of the gas in the headspace was extracted by a gas-tight syringe and analyzed by a Shimadzu GC-14B gas chromatograph (N_2 carrier, active carbon with a particle size of 60 – 80 mesh at 80 ºC) equipped with a TCD.

Spectroscopic Measurements. ^1H NMR spectra were recorded on a JEOL JNM-AL300 spectrometer in CD_3CN or D_2O solutions. Dynamic light scattering (DLS) measurements were performed with a Zetasizer Nano ZS instrument (Malvern Instruments Ltd., USA) for reaction solutions. The DLS instrument used in this study can detect the particle sizes ranging from 0.6 to 6000 nm. UV-vis absorption spectra were recorded on a Hewlett Packard 8453 diode array spectrophotometer.

Electrochemical Measurements. Cyclic voltammetry (CV) was performed on an ALS 630B electrochemical analyzer using a glassy carbon electrode as a working electrode, a saturated calomel electrode (SCE) as a reference electrode, and a Pt wire as an auxiliary electrode. Cyclic voltammograms were obtained in buffer solutions (pH 8.0, 2.0 mL) containing ligands (4.0 mM) at room temperature with a scanning rate of 100 mV s^{-1}.

Characterization of Particles. Transmission electron microscope (TEM) images of nanoparticles, which were mounted on a copper microgrid coated with elastic carbon, were observed by a JEOL JEM-2100 operating at 200 keV. X-ray photoelectron spectra (XPS) were measured by a Kratos Axis 165x with a 165 mm hemispherical electron energy analyzer. An incident radiation was Mg $K\alpha$ X-ray (1253.6 eV) at 200 W and a charge neutralizer was turned on for acquisition. Each sample was attached on a stainless stage with a double-sided carbon scotch tape. The binding energy of each element was corrected by C 1s peak (284.6 eV) from residual carbon. TG/DTA data were recorded on an SII TG/DTA 7200 instrument. Each sample was heated from 25 °C to 100 °C (held at 100 °C for 10 min) and from 100 °C to 300 °C with a ramp rate of 2 °C/min. A certain amount of α-Al_2O_3 was used as a reference for DTA measurements. Powder X-ray diffraction (XRD) patterns were recorded by a Rigaku Ultima IV. Incident X-ray radiation was produced by Cu X-ray tube, operating at 40 kV and 40 mA with Cu $K\alpha$ radiation of 1.54 Å. A scanning rate was 4° min^{-1} from 10° to 80° in 2θ.

Results and Discussion

Photocatalytic Water Oxidation with Cobalt Complexes as Precatalysts. The reaction was executed by photoirradiation (λ > 420 nm) of a buffer solution (2.0 mL, initial pH 8.0) containing 0.50 mM $[Ru(bpy)_3]^{2+}$, 10 mM $Na_2S_2O_8$ and a cobalt complex, $[Co^{II}(Me_6tren)(OH_2)]^{2+}$ (**1**), $[Co^{III}(Cp^*)(bpy)(OH_2)]^{2+}$ (**2**), $[Co^{II}(12\text{-TMC})]^{2+}$ (**3**) or $[Co^{II}(13\text{-TMC})]^{2+}$ (**4**) (see Chart 1), or $Co(NO_3)_2$ (50 μM) as a precatalyst. The time courses of O_2 evolution in the headspace of a vial are shown in Figure 1. No O_2 evolution was confirmed from a reaction solution without cobalt species. O_2 evolution was observed with all cobalt species, indicating cobalt species are an effective precatalyst for the photocatalytic water oxidation. As previously reported, $Na_2S_2O_8$ acts as a two-electron acceptor (eq 1).[83] In such a case, the stoichiometric amount of O_2

$$2H_2O + 2Na_2S_2O_8 \rightarrow O_2 + 4H^+ + 4Na^+ + 4SO_4^{2-} \qquad (1)$$

evolution should be 10 μmol in the present reaction system. Among the reaction systems with Co species, the largest amount of evolved O_2 was obtained with precatalyst **1** (5.4 μmol), where the amount of evolved O_2 increases in the order of **1** ~ $Co(NO_3)_2$ > **3** > **2** > **4**.

Table 1 summarizes the turnover numbers (TONs) in 10 min based on Co in a solution and O_2 yields of the reaction systems containing cobalt complexes **1**–**4** as precatalysts in the photocatalytic water oxidation together with those of $Co(NO_3)_2$ and cobalt complexes reported in the literature.[83,86] The direct comparison of catalytic activity reported in the literature is difficult, because catalytic behavior highly depends on a trivial change in reaction conditions. Additionally, coexisting ions such as counter anions influenced on the catalytic behavior of Co species. When $[Ru(bpy)_3]Cl_2$ was employed as a photosensitizer instead of $[Ru(bpy)_3](ClO_4)_2$, the O_2 yield was suddenly decreased from 54% to only 9% in the water oxidation with precatalyst **1** (Figure 2a). However, the TON of 54 obtained with precatalyst **1** is similar to those of $Co(NO_3)_2$ and $[Co^{II}_4(H_2O)_2(PW_9O_{34})_2]^{10-}$.[83] The TON of 29 obtained with precatalyst **2** is higher than

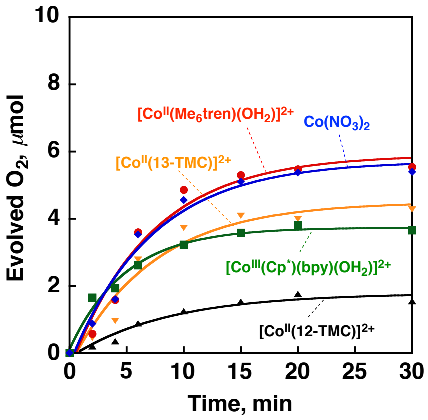

Figure 1. Time courses of O_2 evolution under photoirradiation (Xe lamp, $\lambda > 420$ nm) of a buffer solution (2.0 mL, 50 mM phosphate, pH 8.0) containing $[Ru(bpy)_3]^{2+}$ (0.50 mM), $Na_2S_2O_8$ (10 mM) and a mononuclear cobalt complex (50 μM), $[Co^{II}(Me_6tren)(OH_2)]^{2+}$ (red), $[Co^{III}(Cp^*)(bpy)(OH_2)]^{2+}$ (green), $[Co^{II}(12\text{-}TMC)]^{2+}$ (black), $[Co^{II}(13\text{-}TMC)]^{2+}$ (yellow) or $Co(NO_3)_2$ (50 μM, blue) as a precatalyst.

Table 1. Turnover Numbers (TONs) and O_2 Yields for Photocatalytic Water Oxidation with Cobalt Species (Precatalysts) Compared with Reported TONs and O_2 Yields under the Condition of pH 8.0

Co species (precatalysts)	TON [a]	yield [b] (%)	ref
1	54[c]	54 (62[d])	this work
2	29[c]	29 (60[d])	this work
3	16[c]	16	this work
4	41[c]	41	this work
$Co^{II}(NO_3)_2$	52[c]	52 (22[d])	this work
$[Co^{II}_4(H_2O)_2(PW_9O_{34})_2]^{10-}$	56[e]	45	83
$Co^{III}_4O_4(OAc)_4(py)_4$[f]	10[g]	31	86

[a] TON is defined as the total number of moles of O_2 per mole of precatalyst. [b] Yield is defined as the two times moles of O_2 per mole of $Na_2S_2O_8$. [c] Catalyst concentration was 50 μM. [d] At pH 10. [e] TON per one metal center and concentration of catalysts was 5.0 μM. [f] OAc = acetate, py = pyridine. [g] TON per one metal center and at pH 7.

that of $[Co^{III}_4O_4(OAc)_4(py)_4]$ (TON: 10).[86]

The reaction mechanism in the photocatalytic water oxidation depicted in Chart 1e was evidenced by the two independent experiments, which confirmed the generation of $[Ru(bpy)_3]^{3+}$ by photoirradiation of the solution containing $[Ru(bpy)_3]^{2+}$ and $Na_2S_2O_8$ and the thermal water oxidation by $[Ru(bpy)_3]^{3+}$ in the presence of precatalyst **1** or **2**. Among the Co complexes of **1**–**4**, only complex **2** contains Co(III) species, which allows to observe ^{1}H NMR spectra of the ligands owing to the diamagnetic property of

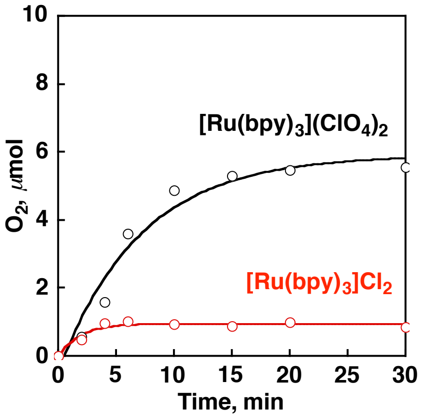

Figure 2. Time courses of O_2 evolution by using $[Ru(bpy)_3](ClO_4)_2$ (black, 0.50 mM) or $[Ru(bpy)_3]Cl_2$ (red, 0.50 mM) in 2.0 mL of phosphate buffer containing **1** (50 μM) and $Na_2S_2O_8$ (10 mM) at initial pH 8.0 to clarify the coexistence effect of Cl^- ion on O_2 evolution.

Co(III). Thus, we examined the photocatalytic water oxidation in detail with precatalyst **1** exhibiting the highest activity, precatalyst **2** containing Co(III) species and $Co(NO_3)_2$ possessing no organic ligand. As shown in Chart 1e and eq 2, photoexcitation of

$$2[Ru^{II}(bpy)_3]^{2+} + Na_2S_2O_8 \xrightarrow{h\nu} 2[Ru^{III}(bpy)_3]^{3+} + 2Na^+ + 2SO_4^{2-} \qquad (2)$$

$[Ru(bpy)_3]^{2+}$ results in generation of $[Ru(bpy)_3]^{3+}$ by the oxidative quenching of the photoexcited state ($^*[Ru(bpy)_3]^{2+}$: * denote the excited state) with $Na_2S_2O_8$. The generation of $[Ru(bpy)_3]^{3+}$ was monitored by the absorption band at 670 nm assigned to $[Ru(bpy)_3]^{3+}$. The time course of $[Ru(bpy)_3]^{3+}$ generation by photoirradiation in the presence of $Na_2S_2O_8$ is shown in Figure 3. The efficiency of $[Ru(bpy)_3]^{3+}$ generation

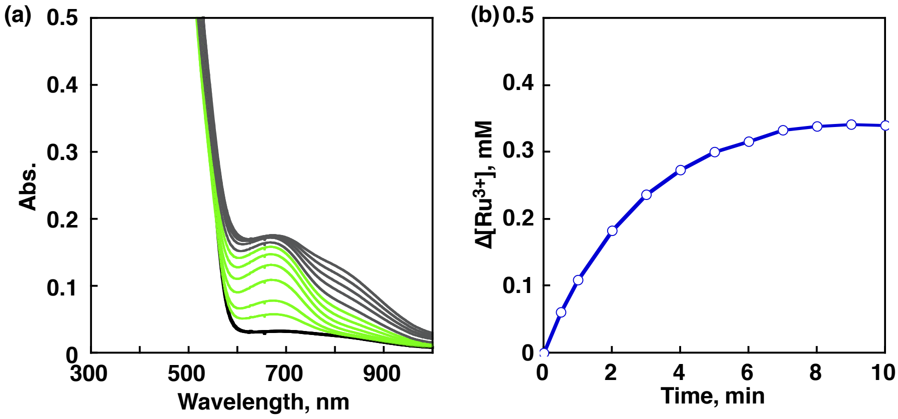

Figure 3. (a) UV-vis spectral changes of $[Ru(bpy)_3]^{2+}$ (0.50 mM) to produce $[Ru(bpy)_3]^{3+}$ in 2.0 mL of phosphate buffer (50 mM, pH 8) containing with $Na_2S_2O_8$ (10 mM) by photoirradiation with a Xe lamp using a band pass filter (440–460 nm). (b) Time course of $[Ru(bpy)_3]^{3+}$ concentration under the photoirradiation determined from the absorbance change at 670 nm under the conditions of (a).

calculated from the absorbance change was around 60% at pH 8.0. The efficiency lower than 100% may result from the low oxidation efficiency of $[Ru^{II}(bpy)_3]^{2+}$ by one electron reduced $Na_2S_2O_8$[95,96] or the ligand oxidation of $[Ru(bpy)_3]^{3+}$ (*vide infra*).

The thermal water oxidation by $[Ru(bpy)_3]^{3+}$ (1.5 mM) in eq 3 was examined in the

$$4[Ru^{III}(bpy)_3]^{3+} + 2H_2O \rightarrow 4[Ru^{II}(bpy)_3]^{2+} + O_2 + 4H^+ \quad (3)$$

presence of precatalyst **1** or **2** (50 μM) in 2.0 mL of a phosphate buffer (pH 8.0). When a buffer solution of **1** or **2** was added to $[Ru(bpy)_3]^{3+}$ at room temperature, the color of the solution was changed from green to orange within 5 min. Evolved O_2 in the headspace was analyzed and quantified by GC after 10 min for each reaction system, where the O_2 yields with precatalysts **1** and **2** were 52 ± 5% and 36 ± 5%, respectively. Thus, the thermal water oxidation by $[Ru(bpy)_3]^{3+}$ was achieved by precatalyst **1** or **2**. Isotope-labeling experiments using ^{18}O-enriched water (44.9%) instead of $H_2{}^{16}O$ were conducted with precatalyst **1** to obtain direct evidence for the water oxidation in which the source of evolved O_2 was water (eq 1). After the reaction, evolved O_2 in a headspace of a reaction vial was separated by a gas chromatograph equipped with a molecular sieve column and quantified by a mass spectrometer. Figure 4 compares the relative mass intensities of ^{18}O-labelled and unlabeled O_2 with calculated intensities assuming that all evolved O_2 molecules derive from water. If O_2 was derived from the ^{18}O-enriched water (44.9%), the ratio of $^{16}O^{16}O$: $^{16}O^{18}O$: $^{18}O^{18}O$ should be 30:50:20. The observed ratio of $^{16}O^{16}O$: $^{16}O^{18}O$: $^{18}O^{18}O$ was indeed 26:51:23, which is virtually the same as the calculated ratio within experimental errors, indicating that evolved O_2

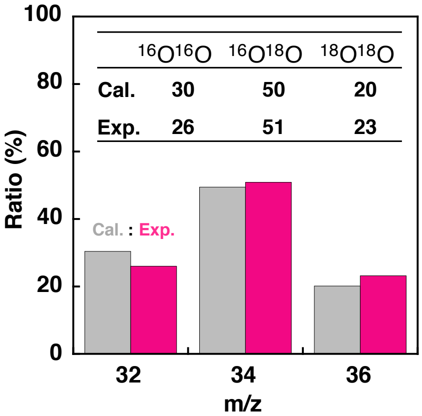

Figure 4. Comparison of relative abundance of ^{18}O-labeled and unlabeled O_2 evolved in the photocatalytic oxidation of a buffer solution (1.0 mL) prepared with ^{18}O-enriched water (44.9% $H_2{}^{18}O$) containing precatalyst **1** (50 μM), $[Ru(bpy)_3]^{2+}$ (0.50 mM) and $Na_2S_2O_8$ (10 mM) (pink, observed mass intensity; grey, calculated values assuming that evolved O_2 results exclusively from water).

comes exclusively from water. These experimental results support the stepwise process of the photocatalytic water oxidation depicted in Chart 1c.

The quantum yields for the photocatalytic water oxidation with precatalysts **1** and **2** at pH 8.0 were determined to be 32% and 30%, respectively (see Experimental Section). These quantum yields were determined by dividing the net values for precatalysts **1** (19%) and **2** (18%) by the efficiency of $[Ru(bpy)_3]^{3+}$ generation (60% at pH 8.0) by photoirradiation in the presence of $Na_2S_2O_8$ (eq 2). The quantum yields normalized by the efficiency of $[Ru(bpy)_3]^{3+}$ generation were as high as that of $[Co^{II}_4(H_2O)_2(PW_9O_{34})_2]^{10-}$ (30%) at pH 8.0.[83] TONs, O_2 yields and quantum yields of precatalysts **1** and **2** in the photocatalytic water oxidation were similar to those of cobalt catalysts previously reported.[83,86]

Effect of pH on Photocatalytic Water Oxidation. The photocatalytic water oxidation was examined under various pH conditions ranging from 6.0 to 10.0. High pH is thermodynamically favorable for the water oxidation. However, a spontaneous reduction of $[Ru(bpy)_3]^{3+}$ to $[Ru(bpy)_3]^{2+}$ accompanied with the oxidation of bpy ligand has also been reported at high pH, leading to degradation of the photosensitizer.[78,79] In order to investigate the effect of pH on the O_2 yield of the photocatalytic water oxidation in the presence of **1**, **2** or $Co(NO_3)_2$ as a precatalyst, the initial pH of the reaction solution was set to be between 6.0 and 10 by employing two buffers, phosphate buffer (pH 6.0–8.0) and borate buffer (pH 9.0–10). Figure 5 shows the time courses of O_2 evolution by photoirradiation (λ > 420 nm) of a buffer solution (2.0 mL) containing $[Ru(bpy)_3]^{2+}$ (0.50 mM), $Na_2S_2O_8$ (10 mM) and precatalyst **1**, **2** or $Co(NO_3)_2$ (50 μM) under various pH conditions. The O_2 yield monotonously increased with increasing the pH from 6.0 to 9.0 in the presence of precatalyst **1**. The O_2 yield obtained under the condition of pH 10 (61%) was comparable to that obtained under the condition of pH 9.0 (62%). Similarly, the higher O_2 yield was obtained at higher pH in the presence of precatalyst **2**. The catalytic activity observed with precatalyst **2** was low compared to that with precatalyst **1** under the condition of pH 8.0. However, the difference in the catalytic activity became smaller at pH 9.0. The O_2 yield increased under the conditions of higher pH, although O_2 evolution ceased in 15 min of photoirradiation at any pHs.

When the photocatalytic water oxidation was conducted with $Co(NO_3)_2$ as a precatalyst under various pH conditions, the O_2 yield reached the maximum value of 52% at pH 8.0 and dramatically decreased to 22% at pH 10 as shown in Figure 5c. This pH-dependent catalytic behavior of $Co(NO_3)_2$ under the conditions of pH higher than 9.0 exhibits sharp contrast to the catalytic behavior observed for precatalysts **1** and **2** where they maintained high catalytic activity under the conditions of pH higher than 9.0.

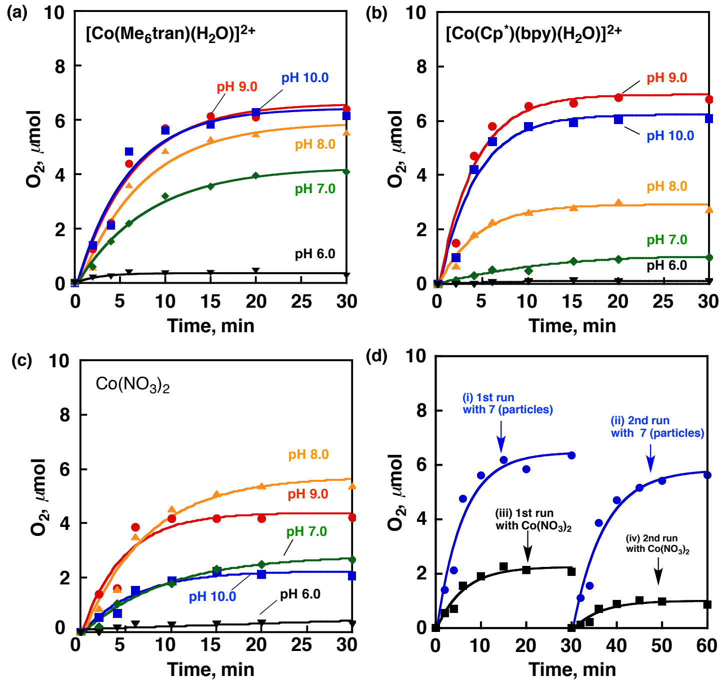

Figure 5. Time courses of O_2 evolution under photoirradiation (Xe lamp, λ > 420 nm) of a buffer solution (2.0 mL) containing $[Ru(bpy)_3]^{2+}$ (0.50 mM) and $Na_2S_2O_8$ (10 mM) with a precatalyst (a) $[Co^{II}(Me_6tren)(OH_2)]^{2+}$ (**1**, 50 μM), (b) $[Co^{III}(Cp^*)(bpy)(OH_2)]^{2+}$ (**2**, 50 μM) or (c) $Co(NO_3)_2$ at an initial pH value of 6.0 (black triangle), 7.0 (green diamond), 8.0 (yellow triangle), 9.0 (red cycle) or 10 (blue square). (d) Time courses of O_2 evolution under photoirradiation (Xe lamp, λ > 420 nm) of a buffer solution (pH 10, 2.0 mL) containing $[Ru(bpy)_3]^{2+}$ (0.50 mM) and $Na_2S_2O_8$ (10 mM) with a precatalyst (i and ii) **1** (50 μM) and (iii and iv) $Co(NO_3)_2$ (50 μM). 2nd run was performed by adding $Na_2S_2O_8$ (5.0 μmol) to the solutions after 1st run.

The robustness of the reaction system with precatalyst **1** in comparison with that with $Co(NO_3)_2$ was examined by the further addition of $Na_2S_2O_8$, which is the sacrificial electron acceptor, to the solution after reactions at pH 10. The catalytic activity of $Co(NO_3)_2$ becomes the maximum at pH 8.0. However, the decrease of pH to 6–7 after 1st run precluded the repetitive examination (Figure 6a). When $Na_2S_2O_8$ (5.0 μmol) was added to the solutions after the reactions at pH 10 for 30 min, successive O_2 evolution was observed from both solutions with precatalysts **1** and $Co(NO_3)_2$ as shown in Figure 5d. However, the O_2 yield of the reaction with $Co(NO_3)_2$ in the 2nd run was only 10%, which is significantly lower than the O_2 yield of 22% in the 1st run, whereas the O_2 yield of the reaction with precatalyst **1** in the 2nd run was 54%, which is similar to that of 1st run (61 %). In the reaction solution used for the 2nd run, the concentration of $[Ru(bpy)_3]^{2+}$ and pH of the solution decreased to ~0.4 mM and ~9.5, respectively, however, these changes do not affect the catalytic behavior significantly (Figures 5, 6b and 6c). These results clearly indicate that the reaction system with precatalyst **1** is more durable than that with $Co(NO_3)_2$. The robustness of the reaction system with precatalyst

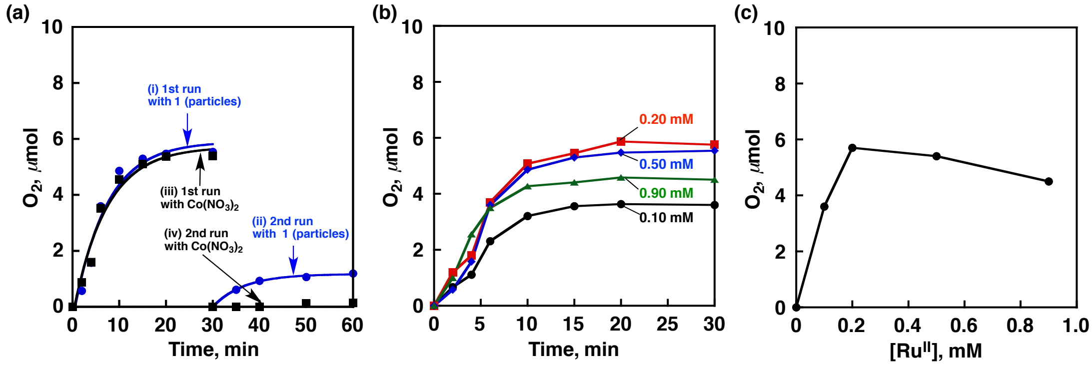

Figure 6. (a) Time courses of O_2 evolution under photoirradiation (Xe lamp, $\lambda > 420$ nm) of a buffer solution (pH 8.0, 2.0 mL) containing $[Ru(bpy)_3]^{2+}$ (0.50 mM) and $Na_2S_2O_8$ (10 mM) with a precatalyst (i and ii) **1** (50 μM) and (iii and iv) $Co(NO_3)_2$ (50 μM). 2nd runs were performed by adding $Na_2S_2O_8$ (5.0 μmol) to the solutions after 1st run and adjusted pH to 8.0 by NaOH (1M, 40 μL). (b) Time courses of O_2 evolution under photoirradiation (Xe lamp, $\lambda > 420$ nm) of a buffer solution (pH 8.0, 2.0 mL) containing precatalyst **1** (50 μM), $Na_2S_2O_8$ (10 mM) and $[Ru(bpy)_3](ClO_4)_2$ [0.10 mM (black cycle), 0.20 mM (red square), 0.50 mM (blue diamond), 0.90 mM (green triangle)]. (c) Dependence of O_2 evolution on concentrations of $[Ru(bpy)_3](ClO_4)_2$ after 20 min photoirradiation (Xe lamp, $\lambda > 420$ nm) of the solution (pH 8.0).

1 can be ascribed to the presence of organic residues (*vide infra*).

Concentration Effect of Cobalt Complexes on Photocatalytic Water Oxidation. The concentration effect of precatalysts **1** and **2** on the O_2 yields at pH 9.0 was compared with $Co(NO_3)_2$. The time courses of O_2 evolution with different concentrations of the cobalt complexes and $Co(NO_3)_2$ are shown in Figure 7, where O_2 was evolved even when the concentration of cobalt species was as low as 5.0 μM. The maximum TON values based on Co were 420 for the reaction system with precatalyst **1**, 320 for that with precatalyst **2** and 315 for that with $Co(NO_3)_2$ at the concentration of 5.0 μM, indicating that **1** provides the most efficient catalyst for the photocatalytic water oxidation. These TON values were much higher than those at pH 8.0 with high concentration of Co species (50 μM) (Table 1). The amount of evolved O_2 increased with an increase of the concentration of precatalyst **1** up to 50 μM with maximum O_2 yield of 62% (Figure 7a). The O_2 yield was gradually decreased by a further increase in concentration of precatalyst **1**. When the concentration of precatalyst **1** was increased to 2.5 mM, no O_2 evolution was observed even at the initial stage of photoirradiation. As compared with precatalyst **1**, similar trend of O_2 evolution was observed with precatalyst **2** (Figure 7b). The O_2 yield was reached to the highest value of 65% when the concentration of precatalyst **2** was 50 μM. On the other hand, the O_2 yield gradually increased by increase in concentration of $Co(NO_3)_2$ as shown in Figure 7c. The highest O_2 yield with $Co(NO_3)_2$ was obtained at the concentration of 0.50 and 2.5 mM. The O_2

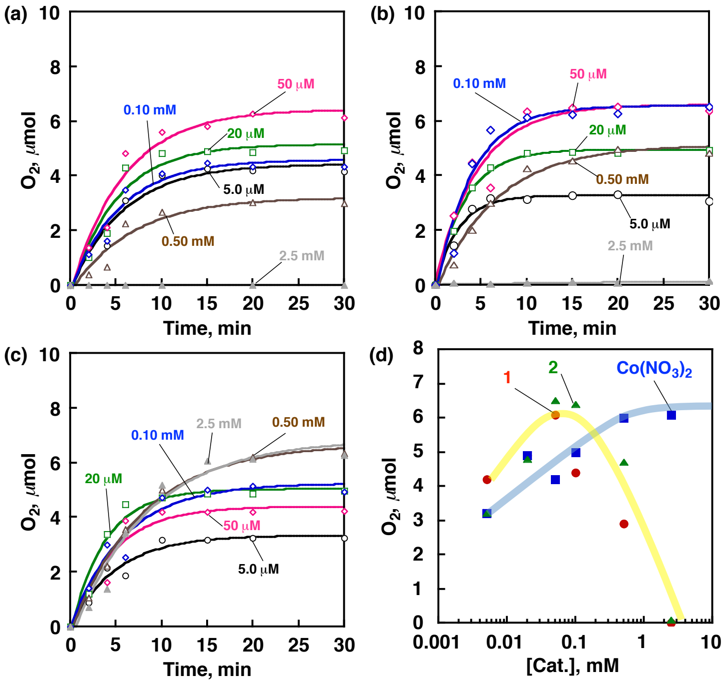

Figure 7. Time courses of O_2 evolution under irradiation with visible light (Xe lamp, $\lambda > 420$ nm) at different concentrations of precatalyst (a) **1**, (b) **2** and (c) $Co(NO_3)_2$ [5.0 μM (black circle), 20 μM (green square), 50 μM (pink diamond) and 0.10 mM (blue diamond), 0.50 mM (blown triangle) and 2.5 mM (grey triangle)] in the solution containing $[Ru(bpy)_3]^{2+}$ (0.50 mM) and $Na_2S_2O_8$ (10 mM) in 2.0 mL of borate buffer (100 mM, pH 9.0). (d) Dependence of O_2 evolution on concentrations of precatalysts, **1** (red circles), **2** (green triangles) and $Co(NO_3)_2$ (blue square) after 20 min photoirradiation (Xe lamp, $\lambda > 420$ nm) of the solution (pH 9.0).

evolution ceased within 15 min from the reaction solution with precatalyst **1**, **2** or $Co(NO_3)_2$ at any concentrations because of degradation of bpy ligand of $[Ru(bpy)_3]^{2+}$ under the present reaction conditions (*vide infra*).

The concentration effects of precatalysts **1** and **2** compared with $Co(NO_3)_2$ on the O_2 evolution at pH 9.0 are summarized in Figure 7d, where the O_2 yields of the photocatalytic water oxidation by photoirradiation of a buffer solution (pH 9.0) containing $[Ru(bpy)_3]^{2+}$, $Na_2S_2O_8$ and various concentrations of precatalysts **1** (red circles), **2** (green triangles) and $Co(NO_3)_2$ (blue squares) are shown. In the presence of $Co(NO_3)_2$, the O_2 yield increased with an increase in concentration of $Co(NO_3)_2$ up to 0.50 mM. The highest O_2 yield obtained with 0.50 mM of $Co(NO_3)_2$ was maintained with higher concentration (2.5 mM) of $Co(NO_3)_2$. On the other hand, peculiar behavior of O_2 yields was observed depending on concentrations of precatalysts **1** and **2**. The O_2 yields were the highest when the concentration of precatalysts **1** and **2** was around 50 μM, and then decreased with an increase in concentrations of precatalysts **1** and **2**. Finally, no O_2 evolution was observed when the concentrations of precatalysts **1** and **2** were 2.5 mM. These results indicate that cobalt complexes **1** and **2** were converted to different species at the concentration > 2.5 mM. Actually, formation of precipitates/particles in the solution was observed after the photocatalytic water oxidation with 2.5 mM of precatalyst **1**.

Photocatalytic Water Oxidation by Particles Derived from Complex 1. The particles/precipitates were used to examine the activity in photocatalytic water oxidation to confirm that the particles are indeed the actual catalysts for the photocatalytic water oxidation. As shown in Figure 8a, no O_2 was evolved with complex **1** (2.5 mM) in the buffer solution containing $Na_2S_2O_8$ and $[Ru(bpy)_3]^{2+}$ under photoirradiation (1st run). The reason for no O_2 evolution at the 1st run may be that the oxidation of the organic ligands of **1** proceeds prior to water oxidation. Particles formed at the 1st run were separated from the reaction solution by centrifugation, washed with water and ethanol successively and dried *in vacuo* at room temperature.

When the particles (~0.12 mg) were employed as a catalyst at the 2nd run, efficient O_2 evolution (yield: 61%) was observed as shown in Figure 8b. The yield obtained with the particles was as high as that obtained with low concentration of precatalyst **1** (50 μM) as shown in Figure 7. The robustness of the collected nanoparticles was confirmed by using them at further reaction cycle. A slightly lower, however, significant amount of O_2 evolution (yield: 47%) was obtained in the 3rd run with the particles collected from the reaction solution of 2nd run as shown in Figure 8c. The lower O_2 yield at 3rd run was due to the recovery loss of catalytic particles. These results clearly demonstrated that the actual catalyst for the photocatalytic water oxidation was the particles derived from **1**. Thus, the transformation of **1** and **2** into true catalysts during

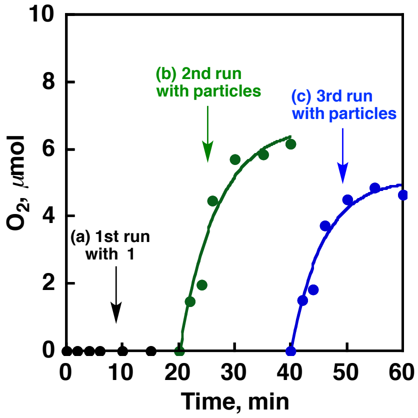

Figure 8. Time courses of O_2 evolution under photoirradiation (Xe lamp, $\lambda > 420$ nm) of a buffer solution (2.0 mL, 100 mM borate, pH 9.0) containing $[Ru(bpy)_3]^{2+}$ (0.50 mM) and $Na_2S_2O_8$ (10 mM) (a) with complex **1** (2.5 mM) (1st run), (b) with nanoparticles (~0.12 mg) derived from **1** in a fresh solution (2nd run) and (c) with the nanoparticles collected after 2nd run with another fresh solution (3rd run).

the photocatalytic water oxidation were investigated in detail by ^{1}H NMR measurements (*vide infra*).

Oxidative Decomposition of Cobalt Complexes. Figure 9 shows the ^{1}H NMR spectra of complex **2** (1.0 mM) in a buffer solution (D_2O, pD 10) containing $[Ru(bpy)_3](ClO_4)_2$ (0.20 mM) and $Na_2S_2O_8$ (10 mM). The lower magnetic fields of the NMR spectra are magnified in Figure 10. Before photoirradiation, two sets of bpy ligands of **2** (black circles) and $[Ru(bpy)_3]^{2+}$ (pink triangles) were observed in the lower magnetic field (7–10 ppm), and only one sharp peak appeared at 1.3 ppm assigned to methyl groups of Cp* as shown in Figure 9a. When the solution was photoirradiated for 30 min, the NMR peak assigned to the Cp* ligand of **2** diminished, and small peaks in the range of 1–2.5 ppm and four peaks, which are in the range of 7–9 ppm, assigned to free bpy appeared (Figure 9b). This NMR spectral changes suggested oxidative decomposition of Cp* ligand and dissociation of bpy ligand from the cobalt ion or the oxidation of the cobalt ion from Co(III) to Co(IV). In order to confirm the possibility of the cobalt ion oxidation, a reducing reagent of dihydronicotineamide adenine dinucleotide (NADH) was added to the solution after photoirradiation to reduce Co(IV) species, which might be formed during the photocatalytic oxidation. As shown in Figure 9c, no significant change in the NMR spectrum was observed. Additionally, the solution was exposed to air for oxidizing Co(II) species, which might be formed by over-reduction of Co(IV) species. However, no NMR spectral change was observed as shown in Figure 9d. Thus, the spectral change caused by photoirradiation resulted from the oxidation of Cp* ligand and dissociation of bpy ligand from the cobalt ion. The

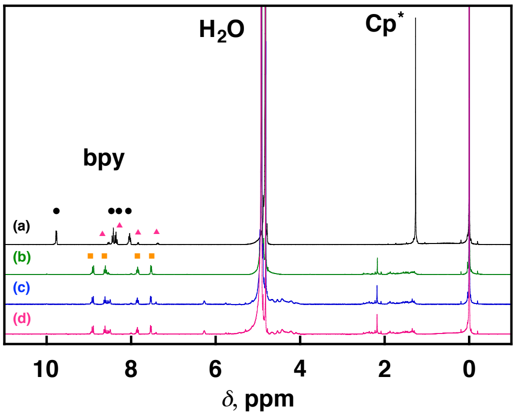

Figure 9. ^{1}H NMR spectra of (a) **2** (2.0 mM) with $[Ru(bpy)_3]^{2+}$ (0.20 mM) and $Na_2S_2O_8$ (10 mM), (b) after photoirradiation of the aqueous solution for 30 min, (c) adding 1.0 mM of NADH to the photoirradiated solution and (d) solution containing NADH exposed to air for 1 h (black circles, bpy of **2**; pink triangles, bpy from $[Ru(bpy)_3]^{2+}$; yellow squares, free bpy) in a D_2O borate buffer (pD 10). Lower magnetic fields of the spectra are magnified in Figure 10.

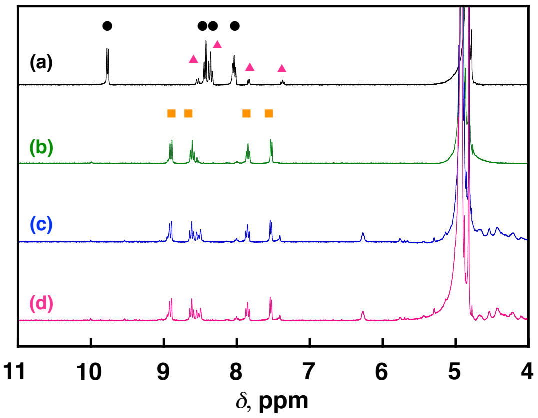

Figure 10. Lower magnetic fields of the ^1H NMR spectra of Figure 9.

oxidation of Cp* ligand has been reported previously for the $[Ir(Cp^*)(H_2O)_3]^{2+}$ complex during the water oxidation by cerium ammonium nitrate.[73] During the reaction, Cp* was oxidized to acetic acid and formic acid. Similar oxidation may occur on the Cp* ligand of **2** during the water oxidation by $[Ru(bpy)_3]^{3+}$.

Because **1** contains a paramagnetic Co(II) ion, ^1H NMR measurements were performed on the ligand of **1** (Me$_6$tren, 5.0 mM) in CD_3CN solution after the oxidation with $[Ru(bpy)_3]^{3+}$ (5.0 mM) to examine the ligand oxidation. Figure 11a indicates the reference spectrum of the solution without $[Ru(bpy)_3]^{3+}$, where ^1H NMR signals from methyl and methylene groups of Me$_6$tren appeared at 2.3 and 2.8 and 3.2 ppm. When 1 equiv. of $[Ru(bpy)_3]^{3+}$ was added to the solution, these NMR peaks became broadened and shifted to the lower magnetic field (2.5–3.0 ppm). The new peaks that appeared in the region of 7–9 ppm were assigned to $[Ru(bpy)_3]^{2+}$ and no peaks assigned to free bpy ligand were observed. No significant spectral change was observed after 1 or 2 h of the addition of $[Ru(bpy)_3]^{3+}$ to the solution at room temperature as shown in Figures 11c

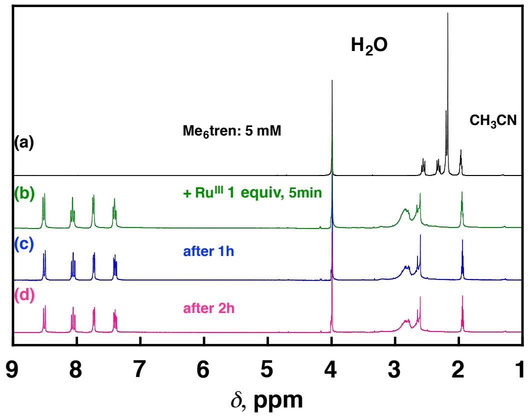

Figure 11. ^1H NMR spectra of (a) Me$_6$tren (5.0 mM) and Me$_6$tren (5.0 mM) after reaction with $[Ru(bpy)_3]^{3+}$ (5.0 mM) for (b) 5 min, (c) 1 h and (d) 2 h in CD_3CN at 298 K.

and 11d, respectively. The ^{1}H NMR spectral change indicates that the oxidation of Me_6tren with $[Ru(bpy)_3]^{3+}$ readily occurred in CD_3CN. These results suggest that the ligand of **1** is oxidized during the photocatalytic water oxidation.

The electrochemical oxidation of the organic ligands of complexes **1**–**4** was performed to compare the reactivity of the ligands. Figure 12 shows the cyclic voltammograms of the ligands (4.0 mM) in a pH 8.0 buffer solution. The anodic current with Me_6tren ligand of **1** started growing around 0.36 V *vs.* saturated calomel electrode (SCE) and reached more than 300 μA at 1.2 V as compared with the smaller anodic currents observed for Cp*H (~50 μA), 12-TMC and 13-TMC (~180 μA), with which precatalyst **2**–**4** were less active than precatalyst **1** in photocatalytic water oxidation. Almost no anodic current was observed for the bpy ligand, while the bpy ligand easily dissociated from complex **2** during the photocatalytic water oxidation (Figure 10). The oxidation of 12-TMC is similar to that of 13-TMC, however, the coordination length of 13-TMC to cobalt ion (Co–N) is longer that that of 12-TMC.[94] The weaker coordination of 13-TMC to cobalt ion may result easy dissociation of 13-TMC from complex **4** as compared with that of 12-TMC. These results indicate that the ligands oxidation and dissociation from complexes result in the susceptibilities of the cobalt complexes to decomposition. Thus, the easier oxidation of Me_6tren ligand is most likely to lead to the higher activity of the formed nanoparticles. Additionally, the oxidation of the organic ligands of complexes **1**–**4** by $[Ru^{III}(bpy)_3]^{3+}$ in a CH_3CN solution was examined as shown in Figure 13, where the Me_6tren, Cp*H, 12-TMC and 13-TMC ligands exhibited much larger reactivity than the bpy ligand in CH_3CN. The bpy ligand was also gradually oxidized by $[Ru^{III}(bpy)_3]^{3+}$ at prolonged reaction time. The ligands oxidation by $[Ru^{III}(bpy)_3]^{3+}$ also matched the order of reactivity in photocatalytic water oxidation.

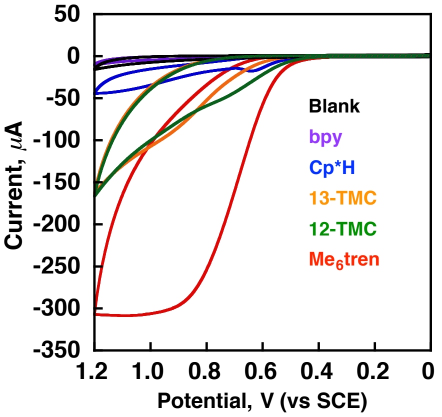

Figure 12. Cyclic voltammograms of a buffer solution (pH 8.0, 50 mM; black line) containing ligands of **1**–**4** (4.0 mM); bpy (purple line), Cp*H (blue line), 13-TMC (yellow line), 12-TMC (green line) and Me_6tren (red line) at a scan rate of 100 mV s^{-1}.

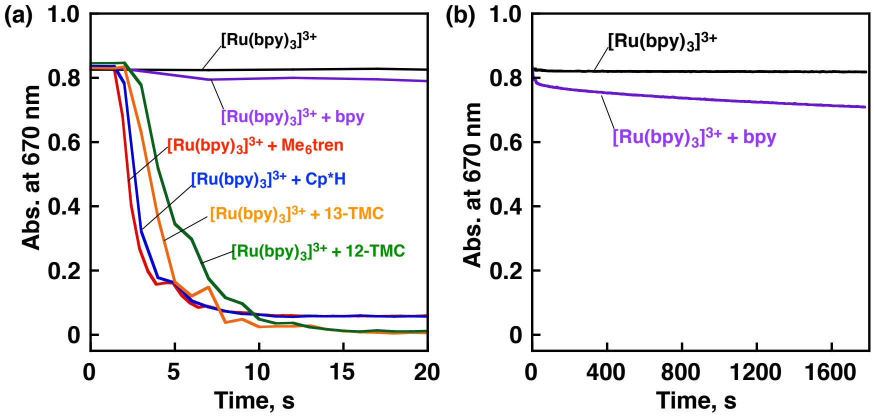

Figure 13. (a) Time courses of absorbance decay at 670 nm of a CH_3CN solution containing $[Ru^{III}(bpy)_3]^{3+}$ (2.0 mM) (black line) with addition of the ligands of complexes **1**–**4** (2.0 mM); bpy (purple line), Cp*H (2.0 mM) (blue line), 13-TMC (yellow line), 12-TMC (green line) and Me_6tren (red line). (b) Prolonged reaction time for (a).

The final products of the ligand oxidation during the photocatalytic water oxidation were examined in more detail (*vide infra)*.

CO_2 Formation with High Concentration of $Na_2S_2O_8$. The complete oxidation of Me_6tren provides water, NO_x and CO_2 as products. Among them, CO_2 can be easily detected and quantified by gas chromatography. The photocatalytic water oxidation was performed with a high concentration of $Na_2S_2O_8$ to fully oxidize the ligand. Figure 14 shows the time courses of CO_2 formation by the photoirradiation of a buffer solution (pH 9.0) containing $Na_2S_2O_8$ (50 mM), $[Ru(bpy)_3]^{2+}$ (0.50 mM) and various concentrations of precatalyst **1** or $Co(NO_3)_2$ (0–2.5 mM). Even without precatalysts **1** and $Co(NO_3)_2$, CO_2 formation was observed after 20 min of the photoirradiation, because the ligand of $[Ru(bpy)_3]^{2+}$ was oxidized to CO_2 after 20 min in the reaction solution (Figure 14a). The rapid degradation of $[Ru(bpy)_3]^{2+}$ can explain the ceasing of the O_2 evolution in 15 min as observed in all the experiments in Figures 1 and 5. The photoirradiation of a buffer solution containing $Na_2S_2O_8$ and $[Ru(bpy)_3]^{2+}$ for 2 h led to evolve 3.2 μmol of CO_2 (Figure 14a). If all bpy ligand of $[Ru(bpy)_3]^{2+}$ in the solution was oxidized to CO_2, 30 μmol of CO_2 should be formed. The amount of 3.2 μmol of CO_2 corresponds to 11%, indicating that all the bpy ligand was not fully oxidized under current reaction conditions. In the presence of $Co(NO_3)_2$ (0.05 mM) in the reaction solution, 8.4 μmol of CO_2 (28%) was formed (Figure 14a), indicating that cobalt species act as a catalyst for the complete oxidation of bpy ligand. The increase in $Co(NO_3)_2$ concentration from 0.050 mM to 2.5 mM resulted in a increase in O_2 evolution as shown in Figure 7.

The presence of precatalyst **1** (0.050 mM) in place of $Co(NO_3)_2$ also resulted in an increase in the amount of evolved CO_2 (7.8 μmol) by photoirradiation for 2 h (Figure

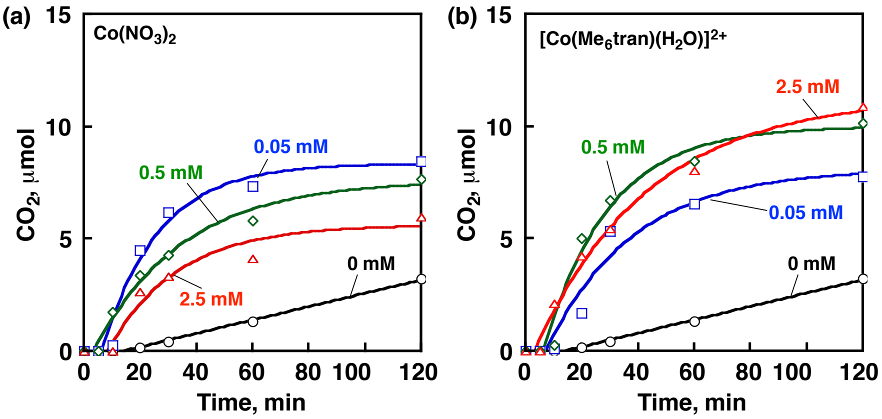

Figure 14. Time courses of CO_2 evolution under photoirradiation (Xe lamp, λ > 420 nm) of a buffer solution (2.0 mL, 100 mM borate, pH 9.0) containing $[Ru(bpy)_3]^{2+}$ (0.50 mM), $Na_2S_2O_8$ (50 mM) and a cobalt precatalyst of (a) $Co(NO_3)_2$ or (b) **1** at concentrations of 0 mM (black circle), 0.050 mM (blue square), 0.50 mM (green diamond) and 2.5 mM (red triangle).

14b). The CO_2 formation may be derived mainly from the bpy oxidation, because only 1.2 μmol of carbon atoms was included in Me_6tren ligand of **1** (0.050 mM). When the concentration of precatalyst **1** increased to 2.5 mM, precipitates were formed in the solution and no O_2 evolution but instead the largest amount of CO_2 evolution (10.9 μmol) was observed as shown in Figure 14b. These results demonstrated that the ligand oxidation occurred prior to the water oxidation. The oxidation of the ligand resulted in the formation of Co cluster species, which are insoluble to water.

Characterization of nanoparticles formed from cobalt complexes by DLS, TEM, XPS and TG/DTA. In order to confirm formation of insoluble nanoparticles during the photocatalytic water oxidation, dynamic light scattering (DLS) measurements were conducted for aqueous solutions containing **1**, **2** or $Co(NO_3)_2$. When a buffer solution (pH 9.0) containing **1** (50 μM), $[Ru(bpy)_3]^{2+}$ (0.50 mM) and $Na_2S_2O_8$ (10 mM) was photoirradiated (λ > 420 nm) for 3 min, particles with the average size of 20 nm were detected as shown in Figure 15a. The size distribution of the particles was 15–60 nm. No further significant change in the particle size was observed by prolonging the photoirradiation time to 30 min. In the reaction solution containing **2**, the size of formed particles ranged from 100 nm to 500 nm with photoirradiation for 3 min (black line) as shown in Figure 15b. When the reaction time was elongated to 10 min, the particle size became a little larger (blue broken line, 150 nm to 500 nm). However, the size became smaller (red dotted line, 80 nm to 200 nm) when the photoirradiation time was further elongated to 30 min. The decrease in the size of nanoparticles resulted from a decrease in pH by generation of protons associated with the water oxidation (eq 1), leading to the partial dissolution of the particles.

The size of particles derived from $Co(NO_3)_2$ (50 μM) increased to an average size of

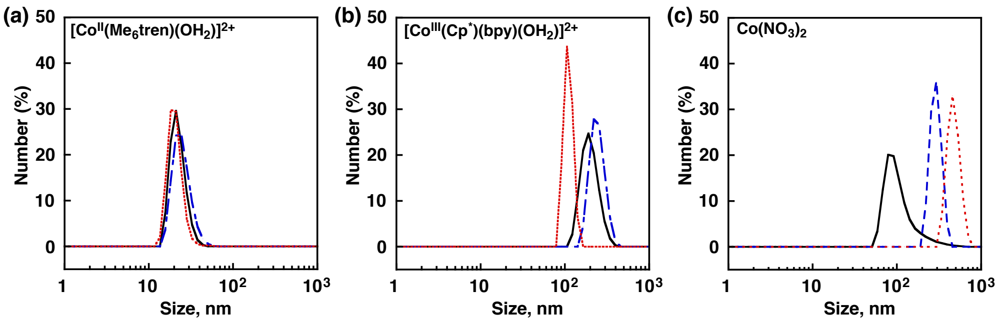

Figure 15. Particles size and their distribution determined by DLS measurements of particles derived from (a) **1**, (b) **2** and (c) $Co(NO_3)_2$. Particles formed by photoirradiation (Xe lamp, $\lambda > 420$ nm) of a buffer solution (2.0 mL, 100 mM borate, pH 9.0) containing **1**, **2** or $Co(NO_3)_2$ (50 μM), $[Ru(bpy)_3]^{2+}$ (0.50 mM) and $Na_2S_2O_8$ (10 mM) for 3 min (black line), 10 min (blue broken line) and 30 min (red dotted line).

500 nm from 50 – 100 nm by prolonging the photoirradiation time to 30 min as shown in Figure 15c in contrast to the case of **2**. The size increase of particles leading to the decrease in the effective surface area can explain why the O_2 yield with $Co(NO_3)_2$ (50 μM) was lower as compared with **1** and **2** (Figure 7). The formed particles were postulated as cobalt hydroxides, which formed due to the high pH. These results revealed that particles derived from **1**, **2** and $Co(NO_3)_2$ were formed even at the initial stage of the photoirradiation.

Judging from the results of ^{1}H NMR, DLS measurements and the ligand oxidation by $[Ru(bpy)_3]^{3+}$ described above, the decomposition of **1** and **2** resulted in the formation of nanoparticles as soon as the photocatalytic water oxidation was started. The particles formed after the photocatalytic water oxidation of a buffer solution (pH 9.0) containing $Na_2S_2O_8$ (10 mM), $[Ru(bpy)_3]^{2+}$ (0.50 mM) with **1**, **2** or $Co(NO_3)_2$ (2.5 mM) were separated from the reaction solution by centrifugation, washed with water several times and dried *in vacuo* at room temperature. The precipitates obtained were then analyzed by transmission electron microscopy (TEM). TEM measurements were performed on the particles derived from **1**, **2** and $Co(NO_3)_2$.

TEM images of the particles derived from **1** are displayed in Figures 16a and 16b. From the low magnification image (Figure 16a), the size of particles ranged from 10 to 50 nm, which is nearly identical to the particles sizes determined by DLS (15–60 nm). From high magnification image of Figure 16b, smaller particles in the size of few nanometers were also formed, indicating that the particles observed in Figure 16a are secondary particles. Figures 16c and 16d show the TEM images of nanoparticles derived from **2**. Judging from these images, the particles are composed of large needle-like-shaped particles and small spherical particles. The size determined for the particles derived from **2** by the DLS measurements ranged from 100 to 300 nm, which agreed to the

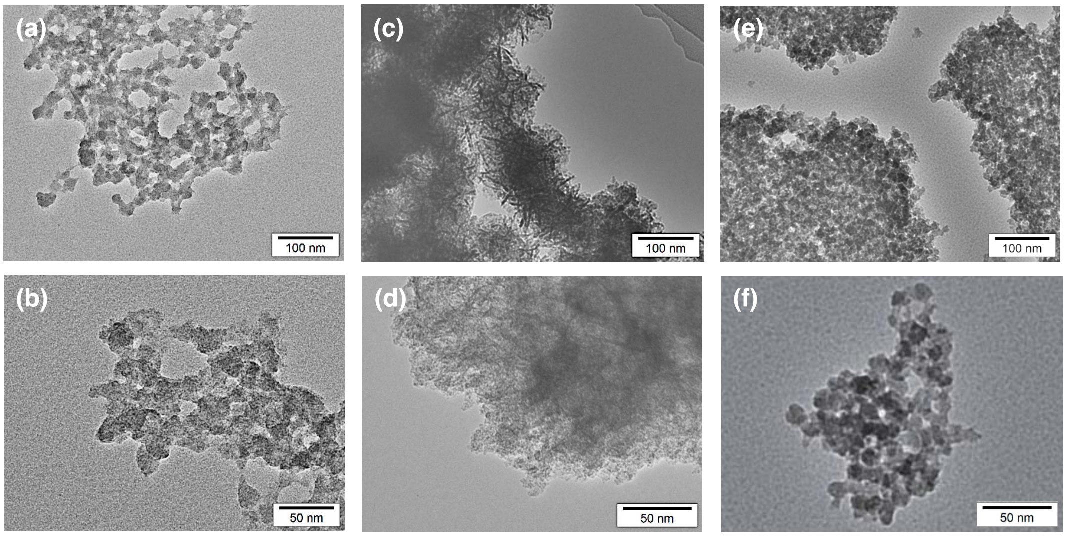

Figure 16. TEM images of nanoparticles formed during the photocatalytic water oxidation with (a and b) **1**, (c and d) **2** and (e and f) $Co(NO_3)_2$ in a buffer solution (pH 9) containing $[Ru(bpy)_3]^{2+}$ (0.50 mM) and $Na_2S_2O_8$ (10 mM).

length of needle-like particles. The size decrease after 30 min observed by DLS resulted from the dissociation of stacking needle-like-shaped particles. The TEM images of particles derived from $Co(NO_3)_2$ indicated that the size of primary particles is around 10 nm as shown in Figure 16f. The particles aggregated to form secondary particles in the size of 100 to 800 nm as shown in Figures 16e and 16f. Thus, the sizes of secondary particles derived from **1**, **2** and $Co(NO_3)_2$ were quite consistent with those determined by DLS. Powder X-ray diffraction measurements were also performed on these particles, however, no peak was observed, suggesting that the particles are amorphous (Figure 17).

In order to determine the surface conditions of the nanoparticles formed in the photocatalytic water oxidation with **1**, X-ray photoelectron spectroscopy (XPS)

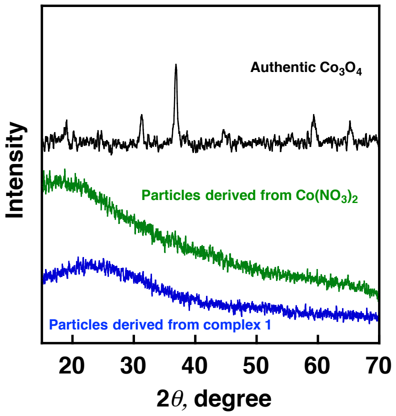

Figure 17. Powder XRD patterns of authentic Co_3O_4 (black), particles derived from $Co(NO_3)_2$ (green) and particles derived from complex **1** (blue).

measurements of the nanoparticles were performed for the energy regions of Co 2p, O 1s, Ru 3d and C 1s, although no peak was observed in the Ru 3d region. Figure 18a displays the XPS spectrum for Co 2p of the nanoparticles derived from **1** together with an authentic sample of Co_3O_4. Co $2p_{1/2}$ and Co $2p_{3/2}$ peaks of the nanoparticles appeared at 780.0 eV and 795.3 eV with weak satellite peaks. Similarly, Co_3O_4 shows two intense peaks at 779.8 eV for Co $2p_{3/2}$ and at 795.1 eV for Co $2p_{1/2}$ with weak satellite peaks. The presence of satellite peaks has been reported to support the presence of Co(II) species.[93,97,98] Slightly intense satellite peaks observed with the nanoparticles are ascribed to the higher ratio of Co(II) species compared with the authentic Co_3O_4 sample, because **1** exclusively contained Co(II) species before the photocatalytic water oxidation.

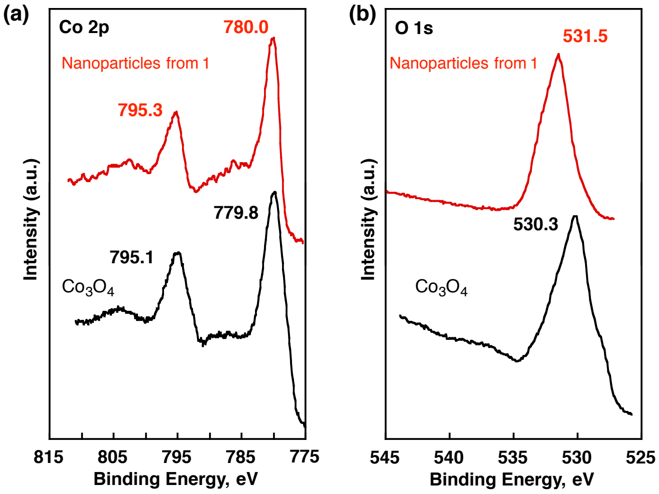

Figure 18. X-ray photoelectron spectra of particles derived from **1** (red) and Co_3O_4 (black) as a reference compound in the energy regions of (a) Co 2p and (b) O 1s. The binding energy of each element was corrected by C 1s peak (284.6 eV).

In Figure 18b, the O 1s peak of the nanoparticles appeared at 531.5 eV, which is in higher binding energy region compared with the O 1s peak of Co_3O_4 (530.3 eV) by 1.2 eV. An increase in the binding energy of the O 1s peak of the nanoparticles has often been observed for metal hydroxide species.[93] Thus, it can be concluded that the surface of the nanoparticles derived from **1** under the photocatalytic water oxidation is mainly composed of $Co(OH)_x$, which can act as the actual catalyst for the photocatalytic water oxidation.

TG/DTA measurements have been preformed to confirm the occlusion of carbonaceous residues in the particles derived from **1**. Figure 19 shows the TG/DTA curve of nanoparticles derived from **1** in which the TG curve can be divided into two consecutive stages with weight loss. The first step of weight loss around 110 ºC corresponds to the removal of physisorbed water. The second step of the weight loss staring from 150 ºC to 220 ºC accompanied by an exothermic peak was assigned to oxidative removal of carbonaceous residues derived from the ligand, because precatalyst **1** thermally decomposes around 250 ºC, which is slightly higher temperature than the observed weight-loss temperature for nanoparticles derived from **1** as shown in Figure 20. The steep weight loss observed in this step was ca 14%. The results indicated that the carbonaceous residues occluded in **1** could prevent particles from aggregation and act as a modifier of catalytic particles. Thus, the easily oxidized ligand may be converted to carbonaceous residues, which can be occluded in the nanoparticles. The carbonaceous residues prevent the aggregation of the nanoparticles during the photocatalytic water oxidation (Figure 15). As compared to the Me$_6$tren ligand of **1**, it

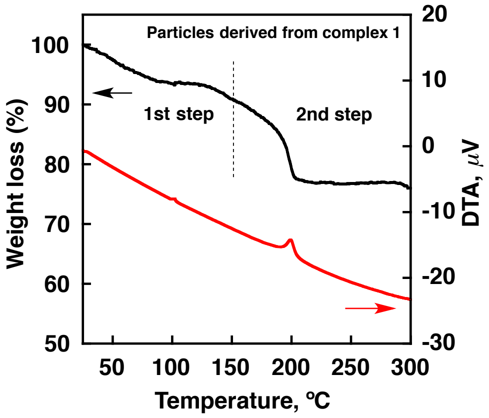

Figure 19. TG/DTA data for nanoparticles derived from complex **1** (TG curve: black, DTA curve: red). The temperature increased from 25 ºC to 300 ºC with a ramp rate of 2 °C min^{-1}.

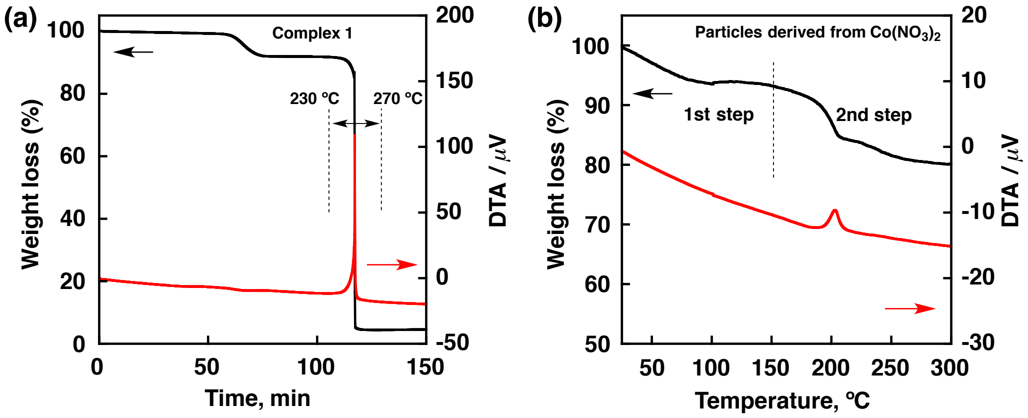

Figure 20. TG/DTA data for (a) complex **1** and (b) nanoparticles derived from Co(NO$_3$)$_2$ (TG curve: black, DTA curve: red). The temperature increased from 25 ºC to 600 ºC with a ramp rate of 2 °C min^{-1}. Comments: The particles derived from Co(NO$_3$)$_2$ contains carbonaceous residue less than 8.7%, which is originated from the ligand of [Ru(bpy)$_3$]$^{2+}$ in the reaction solution.

was more difficult to oxidize the ligand of **2** (Figure 9). The carbonaceous residues were hardly formed on the surface of nanoparticles derived from **2**, because the stable ligands can dissociate from cobalt metal ions before the ligand oxidation. As shown in Figure 9, free bpy ligands were released during the oxidation reaction.

Conclusions

O_2 evolution by the photocatalytic water oxidation was examined with $[Ru(bpy)_3]^{2+}$ as a photosensitizer and $Na_2S_2O_8$ as an electron acceptor in the presence of water-soluble cobalt complexes, $[Co^{II}(Me_6tren)(OH_2)]^{2+}$ (**1**), $[Co^{III}(Cp^*)(bpy)\ (OH_2)]^{2+}$ (**2**) $[Co^{II}(12\text{-TMC})]^{2+}$ (**3**), $[Co^{II}(13\text{-TMC})]^{2+}$ (**4**) and $Co(NO_3)_2$ as precatalysts to evolve O_2 with the yield in order of **1** ~ $Co(NO_3)_2$ > **3** > **2** > **4**. Isotope labeling experiments with $H_2{}^{18}O$ clearly indicate that evolved O_2 derived from water. The O_2 yield in the photocatalytic water oxidation increased with increasing concentrations of precatalysts **1** and **2**, but dramatically decreased when the concentrations of the precatalysts were larger than 0.10 mM. CO_2 was evolved instead of O_2 with increase in $Na_2S_2O_8$ concentration. The observation of the CO_2 formation indicates that the organic ligand oxidation occurred during the photocatalytic water oxidation. Formation of nanoparticles by the decomposition of cobalt complexes was evidenced by the DLS and TEM measurements. The XPS measurements of the nanoparticle products suggest that the surface of the particles is composed of Co(II), Co(III) and OH species. Thus, the present results led us to conclude that the mononuclear cobalt complexes with organic ligands **1** and **2** act as efficient precatalysts, which are oxidized during the photocatalytic water oxidation to produce actual reactive catalysts, i.e., nanoparticles composed of $Co(OH)_x$. Although the organic ligands would not be in their original forms in the catalytic particles, the carbonaceous residues derived from them act as a modifier or capping agent of the nanoparticles. Thus, the choice of the ligand of cobalt complexes is important to obtain an efficient and robust catalytic material for the water oxidation.

References

(1) Lewis, N. S.; Nocera, D. G. *Proc. Natl. Acad. Sci. U. S. A.* **2006**, *103*, 15729.

(2) Dau, H.; Zaharieva, I. *Acc. Chem. Res.* **2009**, *42*, 1861.

(3) Umena, Y.; Kawakami, K.; Shen, J.-R.; Kamiya, N. *Nature* **2011**, *473*, 55.

(4) Gust, D.; Moore, T. A.; Moore, A. L. *Acc. Chem. Res.* **2009**, *42*, 1890.

(5) Siegbahn, P. E. M. *Acc. Chem. Res.* **2009**, *42*, 1871.

(6) Magnuson, A.; Anderlund, M.; Johansson, O.; Lindblad, P.; Lomoth, R.; Polivka, T.; Ott, S.; Stensjo, K.; Styring, S.; Sundstrom, V.; Hammarstrom, L. *Acc. Chem. Res.* **2009**, *42*, 1899.

(7) Fukuzumi, S.; Yamada, Y.; Suenobu, T.; Ohkubo, K.; Kotani, H. *Energy Environ. Sci.* **2011**, *4*, 2754.

(8) Fukuzumi, S. *Eur. J. Inorg. Chem*. ***2008***, 1351.

(9) Kanan, M. W.; Surendranath, Y.; Nocera, D. G. *Chem. Soc. Rev.* **2009**, *38*, 109.

(10) Nocera, D. G. *Chem. Soc. Rev.* **2009**, *38*, 13.

(11) Fukuzumi, S. *Bull. Chem. Soc. Jpn.* **2006**, *79*, 177.

(12) Fukuzumi, S. *Phys. Chem. Chem. Phys.* **2008**, *10*, 2283.

(13) Ohkubo, K.; Fukuzumi, S. *Bull. Chem. Soc. Jpn.* **2009**, *82*, 303.

(14) Eisenberg, R.; Gray, H. B. *Inorg. Chem.* **2008**, *47*, 1697.

(15) Huynh, M. H.; Meyer, T. J. *Chem. Rev.* **2007**, *107*, 5004.

(16) Jiao, F.; Frei, H. *Energy Environ. Sci.* **2010**, *3*, 1018.

(17) Duan, L.; Tong, L.; Xu, Y.; Sun, L. *Energy Environ. Sci.* **2011**, *4*, 3296.

(18) Romain, S.; Vigara, L.; Llobet, A. *Acc. Chem. Res.* **2009**, *42*, 1944.

(19) Sala, X.; Romero, I.; Rodríguez, M.; Escriche, L.; Llobet, A. *Angew. Chem., Int. Ed.* **2009**, *48*, 2842.

(20) Betley, T. A.; Wu, Q.; Van Voorhis, T.; Nocera, D. G. *Inorg. Chem.* **2008**, *47*, 1849.

(21) Youngblood, W. J.; Lee, S.-H. A.; Maeda, K.; Mallouk, T. E. *Acc. Chem. Res.* **2009**, *42*, 1966.

(22) Cape, J. L.; Hurst, J. K. *J. Am. Chem. Soc.* **2008**, *130*, 827.

(23) Brimblecombe, R.; Swiegers, G. F.; Dismukes, G. C.; Spiccia, L. *Angew. Chem., Int. Ed.* **2008**, *47*, 7335.

(24) Najafpour, M. M.; Nayeri, S.; Pashaei, B. *Dalton Trans.* **2011**, *40*, 9374.

(25) Concepcion, J. J.; Jurss, J. W.; Brennaman, M. K.; Hoertz, P. G.; Patrocinio, A. O. T.; Murakami Iha, N. Y.; Templeton, J. L.; Meyer, T. J. *Acc. Chem. Res.* **2009**, *42*, 1954.

(26) hevchenko, D.; Anderlund, M. F.; Thapper, A.; Styring, S. *Energy Environ. Sci.* **2011**, *4*, 1284.

(27) Harriman, A.; Pickering, I. J.; Thomas, J. M.; Christensen, P. A. *J. Chem. Soc., Faraday Trans. I* **1988**, *84*, 2795.

(28) Nakagawa, T.; Beasley, C. A.; Murray, R. W. *J. Phys. Chem. C* **2009**, *113*, 12958.

(29) Nakagawa, T.; Bjorge, N. S.; Murray, R. W. *J. Am. Chem. Soc.* **2009**, *131*, 15578.

(30) Cao, R.; Ma, H. Y.; Geletii, Y. V.; Hardcastle, K. I.; Hill, C. L. *Inorg. Chem.* **2009**, *48*, 5596.

(31) Risch, M.; Khare, V.; Zaharieva, I.; Gerencser, L.; Chernev, P.; Dau, H. *J. Am. Chem. Soc.* **2009**, *131*, 6936.

(32) Duan, L.; Xu, Y. H.; Gorlov, M.; Tong, L. P.; Andersson, S.; Sun, L. C. *Chem.–Eur. J.* **2010**, *16*, 4659.

(33) Xu, Y. H.; Duan, L. L.; Tong, L. P.; Åkermark, B.; Sun, L. C. *Chem. Commun.* **2010**, *46*, 6506.

(34) Duan, L. L.; Fischer, A.; Xu, Y. H.; Sun, L. C. *J. Am. Chem. Soc.* **2009**, *131*, 10397.

(35) Xu, Y. H.; Åkermark, T.; Gyollai, V.; Zou, D. P.; Eriksson, L.; Duan, L. L.; Zhang, R.; Åkermark, B.; Sun, L. C. *Inorg. Chem.* **2009**, *48*, 2717.

(36) Ellis, W. C.; McDaniel, N. D.; Bernhard, S.; Collins, T. J. *J. Am. Chem. Soc.* **2010**, *132*, 10990.

(37) Fillol, J. L.; Codolà, Z.; Garcia-Bosch, I.; Gómez, L.; Pla, J. J.; Costas, M. *Nat Chem* **2011**, *3*, 807.

(38) Hoertz, P. G.; Kim, Y. I.; Youngblood, W. J.; Mallouk, T. E. *J. Phys. Chem. B* **2007**, *111*, 6845.

(39) Morris, N. D.; Suzuki, M.; Mallouk, T. E. *J. Phys. Chem. A* **2004**, *108*, 9115.

(40) Morris, N. D.; Mallouk, T. E. *J. Am. Chem. Soc.* **2002**, *124*, 11114.

(41) Hara, M.; Waraksa, C. C.; Lean, J. T.; Lewis, B. A.; Mallouk, T. E. *J. Phys. Chem. A* **2000**, *104*, 5275.

(42) Yagi, M.; Toda, M.; Yamada, S.; Yamazaki, H. *Chem. Commun.* **2010**, *46*, 8594.

(43) Yagi, M.; Narita, K. *J. Am. Chem. Soc.* **2004**, *126*, 8084.

(44) McDaniel, N. D.; Coughlin, F. J.; Tinker, L. L.; Bernhard, S. *J. Am. Chem. Soc.* **2008**, *130*, 210.

(45) Fukuzumi, S.; Kato, S.; Suenobu, T. *Phys. Chem. Chem. Phys.* **2011**, *13*, 17960.

(46) Poulsen, A. K.; Rompel, A.; McKenzie, C. J. *Angew. Chem., Int. Ed.* **2005**, *44*, 6916.

(47) Gao, Y.; Åkermark, T.; Liu, J. H.; Sun, L. C.; Åkermark, B. *J. Am. Chem. Soc.* **2009**, *131*, 8726.

(48) Geletii, Y. V.; Botar, B.; Koegerler, P.; Hillesheim, D. A.; Musaev, D. G.; Hill, C. L. *Angew. Chem., Int. Ed.* **2008**, *47*, 3896.

(49) Geletii, Y. V.; Besson, C.; Hou, Y.; Yin, Q. S.; Musaev, D. G.; Quiñonero, D.; Cao, R.; Hardcastle, K. I.; Proust, A.; Kögerler, P.; Hill, C. L. *J. Am. Chem. Soc.* **2009**, *131*, 17360.

(50) Sartorel, A.; Carraro, M.; Scorrano, G.; De Zorzi, R.; Geremia, S.; McDaniel, N. D.; Bernhard, S.; Bonchio, M. *J. Am. Chem. Soc.* **2008**, *130*, 5006.

(51) Murakami, M.; Hong, D.; Suenobu, T.; Yamaguchi, S.; Ogura, T.; Fukuzumi, S. *J. Am. Chem. Soc.* **2011**, *133*, 11605.

(52) Gersten, S. W.; Samuels, G. J.; Meyer, T. J. *J. Am. Chem. Soc.* **1982**, *104*, 4029.

(53) Concepcion, J. J.; Tsai, M. K.; Muckerman, J. T.; Meyer, T. J. *J. Am. Chem. Soc.* **2010**, *132*, 1545.

(54) Concepcion, J. J.; Jurss, J. W.; Norris, M. R.; Chen, Z. F.; Templeton, J. L.; Meyer, T. J. *Inorg. Chem.* **2010**, *49*, 1277.

(55) Zong, R.; Thummel, R. P. *J. Am. Chem. Soc.* **2005**, *127*, 12802.

(56) Tseng, H. W.; Zong, R.; Muckerman, J. T.; Thummel, R. *Inorg. Chem.* **2008**, *47*, 11763.

(57) Muckerman, J. T.; Polyansky, D. E.; Wada, T.; Tanaka, K.; Fujita, E. *Inorg. Chem.* **2008**, *47*, 1787.

(58) Chen, Z. F.; Concepcion, J. J.; Jurss, J. W.; Meyer, T. J. *J. Am. Chem. Soc.* **2009**, *131*, 15580.

(59) Concepcion, J. J.; Jurss, J. W.; Templeton, J. L.; Meyer, T. J. *J. Am. Chem. Soc.* **2008**, *130*, 16462.

(60) Wasylenko, D. J.; Ganesamoorthy, C.; Henderson, M. A.; Koivisto, B. D.; Osthoff, H. D.; Berlinguette, C. P. *J. Am. Chem. Soc.* **2010**, *132*, 16094.

(61) Wasylenko, D. J.; Ganesamoorthy, C.; Koivisto, B. D.; Henderson, M. A.; Berlinguette, C. P. *Inorg. Chem.* **2010**, *49*, 2202.

(62) Romain, S.; Bozoglian, F.; Sala, X.; Llobet, A. *J. Am. Chem. Soc.* **2009**, *131*, 2768.

(63) Bernet, L.; Lalrempuia, R.; Ghattas, W.; Mueller-Bunz, H.; Vigara, L.; Llobet, A.; Albrecht, M. *Chem. Commun.* **2011**, *47*, 8058.

(64) D. E. Polyansky, J. T. Muckerman, J. Rochford, R. Zong, R. P. Thummel and E. Fujita, *J. Am. Chem. Soc.*, 2011, **133**, 14649.

(65) Xu, Y.; Fischer, A.; Duan, L.; Tong, L.; Gabrielsson, E.; Åkermark, B.; Sun, L. *Angew. Chem., Int. Ed.* **2010**, *49*, 8934.

(66) Yamada, H.; Siems, W. F.; Koike, T.; Hurst, J. K. *J. Am. Chem. Soc.* **2004**, *126*, 9786.

(67) Hong, D.; Murakami, M.; Yamada, Y.; Fukuzumi, S. *Energy Environ. Sci.* **2012**, *5*, 5708.

(68) Bozoglian, F.; Romain, S.; Ertem, M. Z.; Todorova, T. K.; Sens, C.; Mola, J.; Rodríguez, M.; Romero, I.; Benet-Buchholz, J.; Fontrodona, X.; Cramer, C. J.; Gagliardi, L.; Llobet, A. *J. Am. Chem. Soc.* **2009**, *131*, 15176.

(69) Blakemore, J. D.; Schley, N. D.; Balcells, D.; Hull, J. F.; Olack, G. W.; Incarvito, C. D.; Eisenstein, O.; Brudvig, G. W.; Crabtree, R. H. *J. Am. Chem. Soc.* **2010**, *132*, 16017.

(70) Lalrempuia, R.; McDaniel, N. D.; Muller-Bunz, H.; Bernhard, S.; Albrecht, M. *Angew. Chem., Int. Ed.* **2010**, *49*, 9765.

(71) Savini, A.; Bellachioma, G.; Ciancaleoni, G.; Zuccaccia, C.; Zuccaccia, D.; Macchioni, A. *Chem. Commun.* **2010**, *46*, 9218.

(72) Savini, A.; Belanzoni P.; Bellachioma, G.; Zuccaccia, C.; Zuccaccia, D.; Macchioni, A. *Green Chem.* **2011**, *13*, 3360.

(73) Hetterscheid, D. G. H.; Reek, J. N. H. *Chem. Commun.* **2011**, *47*, 2712.

(74) Blakemore, J. D.; Schley, N. D.; Olack, G. W.; Incarvito, C. D.; Brudvig, G. W.; Crabtree, R. H. *Chem. Sci.* **2011**, *2*, 94.

(75) Shevchenko, D.; Anderlund, M. F.; Thapper, A.; Styring, S. *Energy Environ. Sci.* **2011**, *4*, 1284.

(76) Jiao, F.; Frei, H. *Angew. Chem., Int. Ed.* **2009**, *48*, 1841.

(77) Brunschwig, B. S.; Chou, M. H.; Creutz, C.; Ghosh, P.; Sutin, N. *J. Am. Chem. Soc.* **1983**, *105*, 4832.

(78) Ghosh, P. K.; Brunschwig, B. S.; Chou, M.; Creutz, C.; Sutin, N. *J. Am. Chem. Soc.* **1984**, *106*, 4772.

(79) Creutz, C.; Sutin, N. *P. Natl. Acad. Sci. U. S. A.* **1975**, *72*, 2858.

(80) Elizarova, G. L.; Matvienko, L. G.; Parmon, V. N. *J. Mol. Catal.* **1987**, *43*, 171.

(81) Surendranath, Y.; Kanan, M. W.; Nocera, D. G. *J. Am. Chem. Soc.* **2010**, *132*, 16501.

(82) Gerken, J. B.; McAlpin, J. G.; Chen, J. Y. C.; Rigsby, M. L.; Casey, W. H.; Britt, R. D.; Stahl, S. S. *J. Am. Chem. Soc.* **2011**, *133*, 14431.

(83) Huang, Z. Q.; Luo, Z.; Geletii, Y. V.; Vickers, J. W.; Yin, Q. S.; Wu, D.; Hou, Y.; Ding, Y.; Song, J.; Musaev, D. G.; Hill, C. L.; Lian, T. Q. *J. Am. Chem. Soc.* **2011**, *133*, 2068.

(84) Yin, Q. S.; Tan, J. M.; Besson, C.; Geletii, Y. V.; Musaev, D. G.; Kuznetsov, A. E.; Luo, Z.; Hardcastle, K. I.; Hill, C. L. *Science* **2010**, *328*, 342.

(85) Stracke, J. J.; Finke, R. G. *J. Am. Chem. Soc.* **2011**, *133*, 14872.

(86) Dismukes, G. C.; McCool, N. S.; Robinson, D. M.; Sheats, J. E. *J. Am. Chem. Soc.* **2011**, *133*, 11446.

(87) Ciampoli, M.; Nardi, N. *Inorg. Chem.* **1966**, *5*, 41.

(88) Britovsek, G. J. P.; England, J.; White, A. J. P. *Inorg. Chem.* **2005**, *44*, 8125.

(89) Choi, Y. J.; Cho, K. B.; Kubo, M.; Ogura, T.; Karlin, K. D.; Cho, J.; Nam, W. *Dalton Trans.* **2011**, *40*, 2234.

(90) Kolle, U.; Fuss, B. *Chem. Ber. Recl.* **1984**, *117*, 743.

(91) Dadci, L.; Elias, H.; Frey, U.; Hornig, A.; Koelle, U.; Merbach, A. E.; Paulus, H.; Schneider, J. S. *Inorg. Chem.* **1995**, *34*, 306.

(92) Dong, Y. M.; He, K.; Yin, L.; Zhang, A. M. *Nanotechnology* **2007**, *18*, 435602.

(93) Yamada, Y.; Yano, K.; Xu, Q. A.; Fukuzumi, S. *J. Phys. Chem. C* **2010**, *114*, 16456.

(94) Cho, J.; Sarangi, R.; Kang, H. Y.; Lee, J. Y.; Kubo, M.; Ogura, T.; Solomon, E. I.; Nam, W. *J. Am. Chem. Soc.* **2010**, *132*, 16977.

(95) White, H. S.; Becker, W. G.; Bard, A. J. *J. Phys. Chem.* **1984**, *88*, 1840.

(96) Kaledin, A. L.; Huang, Z.; Geletii, Y. V.; Lian, T.; Hill, C. L.; Musaev, D. G. *J. Phys. Chem. A* **2010**, *114*, 73.

(97) Hu, L. H.; Peng, Q.; Li, Y. D. *J. Am. Chem. Soc.* **2008**, *130*, 16136.

(98) Yang, J.; Liu, H.; Martens, W. N.; Frost, R. L. *J. Phys. Chem. C* **2010**, *114*, 111.

Chapter 3

Water Oxidation Catalysis with Nonheme Iron Complexes under Acidic and Basic Conditions: Homogeneous or Heterogeneous?

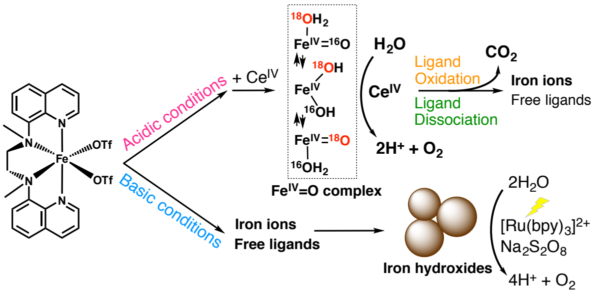

Abstract: Thermal water oxidation by cerium(IV) ammonium nitrate (CAN) was catalyzed by nonheme iron complexes, such as Fe(BQEN)(OTf)$_2$ (**1**) and Fe(BQCN)(OTf)$_2$ (**2**) (BQEN = *N*,*N*'-dimethyl-*N*,*N*'-bis(8-quinolyl)ethane-1,2-diamine, BQCN = *N*,*N*'-dimethyl-*N*,*N*'-bis(8-quinolyl)cyclohexanediamine, OTf = $CF_3SO_3^-$) in a non-buffered aqueous solution; turnover numbers of 80 ± 10 and 20 ± 5 were obtained in the O_2 evolution reaction by **1** and **2**, respectively. The ligand dissociation of the iron complexes was observed under acidic conditions, and the dissociated ligands were oxidized by CAN to yield CO_2. We also observed that **1** was converted to an iron(IV)-oxo complex during the water oxidation in competition with the ligand oxidation. In addition, oxygen exchange between the iron(IV)-oxo complex and $H_2{}^{18}O$ was found to occur at a much faster rate than the oxygen evolution. These results indicate that the iron complexes act as the true homogeneous catalyst for water oxidation by CAN at low pHs. In contrast, light-driven water oxidation using $[Ru(bpy)_3]^{2+}$ (bpy = 2,2'-bipyridine) as a photosensitizer and $S_2O_8{}^{2-}$ as a sacrificial electron acceptor was catalyzed by iron hydroxide nanoparticles derived from the iron complexes under basic conditions as the result of the ligand dissociation. In a buffer solution (initial pH 9.0), formation the iron hydroxide nanoparticles with a size of around 100 nm at the end of the reaction was monitored by DLS *in situ* and characterized by XPS and TEM measurements. We thus conclude that the water oxidation by CAN was catalyzed by short-lived homogenous iron complexes under acidic conditions, whereas iron hydroxide nanoparticles derived from iron complexes act as a heterogeneous catalyst in the light-driven water oxidation reaction under basic conditions.

Introduction

One of the most promising candidates for a sustainable energy cycle is artificial photosynthesis that directly converts solar energy into chemical energy.[1–4] Artificial photosynthetic systems are composed of three functional parts, such as light-harvesting and charge-separation,[4] water oxidation,[5] and water reduction.[6] In these three parts, water oxidation is considered as the most challenging part because the process is an uphill energy transformation involving transfer of four electrons and four protons ($2H_2O \rightarrow O_2 + 4H^+ + 4e^-$).[7,8] Thus, extensive efforts have so far been devoted to developing homogeneous and heterogeneous water oxidation catalysts (WOCs).[9,10]

Many WOCs containing precious metals, such as ruthenium[11–16] and iridium,[17–20] have been reported to exhibit high activity in two major systems, such as thermal water oxidation by cerium(IV) ammonium nitrate (CAN) under acidic conditions and light-driven water oxidation under basic conditions using $[Ru(bpy)_3]^{2+}$ (bpy = 2,2’-bipyridine) and persulfate ($S_2O_8^{2-}$) as a photosensitizer and a sacrificial electron acceptor, respectively. For practical applications, the use of precious metals should be avoided because of its high cost and limited stock. Thus, much attention has been paid to the development of WOCs with earth-abundant metals such as cobalt,[21–24] copper,[25] manganese,[26–28] and iron.[29] Among these metals, iron is the most earth-abundant and environmentally benign metal often used as a catalyst in various oxidation reactions.[30,31] It has been reported recently that a series of homogeneous iron complexes with water coordination sites exhibit high catalytic activity for water oxidation by CAN with a maximum turnover value of 360.[32] Iron complexes have also been employed for light-driven water oxidation under basic conditions using $[Ru(bpy)_3]^{2+}$ and $S_2O_8^{2-}$ as a photosensitizer and a sacrificial electron acceptor, respectively.[33] In the light-driven water oxidation, iron complexes were converted to Fe_2O_3 as the true catalysts that conduct the water oxidation.[33] It has been suggested recently that the active iron catalysts for water oxidation at low and high pHs are different.[33] The oxidative degradation of ligands of metal complexes has been reported to produce metal oxide nanoparticles, which act as the true catalysts for water oxidation.[20,24,28] However, conditions to distinguish homogeneous iron complex catalysts *versus* heterogeneous iron catalysts derived from the iron complexes for the catalytic water oxidation have yet to be scrutinized.[34] The degradation of homogeneous iron complex catalysts due to the ligand oxidation during the catalytic water oxidation has also remained elusive. These issues on the homogeneous *versus* heterogeneous catalysis of iron-based materials as well as the water oxidation catalytic mechanism should be certainly much more clarified judging from the importance of the potential use of earth-abundant iron catalysts in water oxidation.

In Chapter 3, I report thermal and light-driven water oxidation reactions by employing two water-soluble mononuclear nonheme iron complexes, Fe(BQEN)(OTf)$_2$ (**1**) and Fe(BQCN)(OTf)$_2$ (**2**) (BQEN = *N*,*N*'-dimethyl-*N*,*N*'-bis(8-quinolyl)ethane-1,2-diamine, BQCN = *N*,*N*'-dimethyl-*N*,*N*'-bis(8-quinolyl)cyclohexanediamine, OTf = $CF_3SO_3^-$) (Chart 1), to disclose the true catalysts involved in those catalytic systems. Under acidic conditions, water oxidation by CAN was catalyzed by **1** and **2** in competition with the ligand oxidation. Under basic conditions, light-driven water oxidation by **1** showed the formation of iron hydroxide nanoparticles as the true catalyst. Thus, the true catalysts in the thermal and light-driven water oxidation reactions are shown to be different depending on pH conditions.

Chart 1. Iron Complexes Used in Thermal and Light-Driven Water Oxidation Reactions

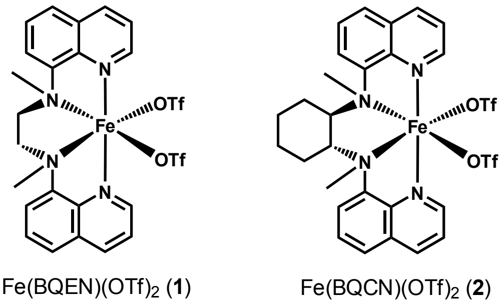

Fe(BQEN)(OTf)$_2$ (**1**)   Fe(BQCN)(OTf)$_2$ (**2**)

Experimental Section

Materials. All chemicals obtained from Aldrich Chemical Co. were the best available purity and used without further purification unless otherwise noted. Cerium(IV) ammonium nitrate (CAN), $Na_2S_2O_8$, and iron(II) sulphate were purchased from Wako Pure Chemical Industries Ltd. $H_2{}^{18}O$ (98% ^{18}O-enriched) was purchased from Taiyo Nippon Sanso Co. [Ru(bpy)$_3$]Cl$_2$ was obtained from Tokyo Chemical Industry Co., Ltd. [Ru(bpy)$_3$]SO$_4$ was synthesized by adding one equiv of Ag_2SO_4 to an aqueous solution of [Ru(bpy)$_3$]Cl$_2$. Purification of water (18.2 MΩ cm) was performed with a Milli-Q system (Millipore, Direct-Q 3 UV). Fe(OTf)$_2$·2CH$_3$CN, Fe(BQEN)(OTf)$_2$ (**1**), and Fe(BQCN)(OTf)$_2$ (**2**) were synthesized according to the literature procedures.[35,36]

Oxygen Evolution Quantified by Manometry. On-line manometric measurements were carried out on a Testo 521 differential pressure manometer with an operating range of 0.1–10 kPa and accuracy within 0.5% of the measurements. The manometer was coupled to thermostatic reaction vessels for dynamic monitoring of the headspace pressure above each reaction solution. The manometer's secondary ports were connected to thermostatic reaction vessels containing the same solvents and headspace volumes as the sample vials. Each measurement for a reaction solution (2.0 mL) was performed at 298 K.

Oxygen Evolution Quantified by GC. A vial (5.0 mL) containing an aqueous solution of an iron complex (1.0 mM or 12.5 μM, 2.0 mL) and another vial containing CAN (0.20 mmol or 0.25 mmol) were sealed with a rubber septum. The two vials were carefully deaerated by bubbling Ar gas for 10 min. The aqueous solution of the iron complex (2.0 mL) in the vial was taken and injected into the vial containing CAN via a syringe piercing through the rubber septum to start the reaction with vigorous stirring. After each reaction time, 100 μL of Ar gas was injected into the vial, and then the same volume of gas in the headspace of the vial was sampled by a gas tight syringe and quantified by a Shimadzu GC-17A gas chromatograph (GC) [Ar carrier, a capillary column with molecular sieves (Agilent Technologies, 19095PMS0, 30 m × 0.53 mm) at 313 K] equipped with a thermal conductivity detector (TCD).

The stoichiometric and repetitive experiments were performed as follows: An aqueous solution of CAN (0.20 M, 1.0 mL) containing HNO_3 (0.10 M) was prepared. An aliquot (40 μL) of the CAN solution (8.0 μmol) was injected to a non-buffered aqueous solution of **1** (1.0 mM, 2.0 mL) in a vial deaerated by bubbling Ar gas to start the reaction (first run). Evolved oxygen gas in the headspace of the vial was quantified by GC. After 30 min, another aliquot (40 μL) of the CAN solution was injected to the solution of first run deaerated again by bubbling Ar gas (second run), and the same procedure was applied for the third run.

Light-driven water oxidation was performed as follows: An iron complex (5.0 μM) was added to a borate buffer solution (100 mM, pH 8.0, 8.5 or 9.0, 2.0 mL) containing $Na_2S_2O_8$ (5.0 mM) and $[Ru(bpy)_3]SO_4$ (0.25 mM) deaerated by bubbling Ar gas. The solution was then irradiated with a xenon lamp (Ushio Optical, Model X SX-UID 500X AMQ) through a color filter glass (Asahi Spectra Co., Ltd.) transmitting $\lambda > 420$ nm at room temperature. Evolved oxygen gas in the headspace of the reaction vial was quantified by GC.

CO_2 Detection. Samples were prepared with the same procedures for the O_2 evolution measurements except for bubbling N_2 gas. After each reaction time, 50 μL of gas in the headspace was sampled and quantified by a Shimadzu GC-14B gas chromatograph (N_2 carrier, active carbon with a particle size of 60–80 mesh at 353 K) equipped with a TCD.

ESI-MS Measurements. Electrospray ionization mass spectra (ESI-MS) were collected on a Thermo Finnigan (San Jose, CA, USA) LCQTM Advantage MAX quadrupole ion trap instrument, by infusing samples directly into the source at 20 μL min^{-1} using a syringe pump. The spray voltage was set at 4.7 kV and the capillary temperature at 353 K.

^{18}O-labeling Experiments. A volume of an aqueous solution (20 μL, $H_2{}^{16}O$) containing CAN (0.20 M) and HNO_3 (0.10 M) was injected into an aqueous solution (0.46 mL, $H_2{}^{16}O$) of **1** (2.0 μmol) in a vial (2.0 mL) deaerated by bubbling He gas for 20 min. A deaerated $H_2{}^{18}O$ solution (0.50 mL) was then added to the $H_2{}^{16}O$ solution followed by the additional injection of the CAN solution (20 μL, 4.0 μmol). After 10 min, 100 μL of gas in the headspace of the vial was sampled for gas analysis. The ratio of $^{16}O^{16}O$, $^{16}O^{18}O$ and $^{18}O^{18}O$ was determined based on the intensities of mass peaks (m/z = 32, 34, and 36) obtained by a Shimadzu GC-17A gas chromatograph [He carrier, a capillary column with molecular sieves (Agilent Technologies, 19095PMS0, 30 m × 0.53 mm) at 313 K] equipped with a Shimadzu QP-5000 mass spectrometer.

Spectroscopic Measurements. UV-vis absorption spectra were recorded on a Hewlett Packard 8453 diode array spectrophotometer. Dynamic light scattering (DLS) measurements were performed with a Zetasizer Nano ZS instrument (Malvern Instruments Ltd., USA). The DLS instrument used in this study can detect the particle sizes ranging from 0.6 to 6000 nm.

Electrochemical Measurements. Cyclic voltammetry (CV) and Differential pulse voltammetry (DPV) measurements were performed on a CH Instruments 630B potentiostat using a glassy carbon electrode (3.0 mm diameter) as a working electrode, a saturated calomel electrode (SCE) as a reference electrode, and a Pt wire as an auxiliary electrode. Analyte concentrations (iron complexes or ligands) were 0.50 mM in water containing 0.10 M $NaNO_3$. The pH of a solution was adjusted using aqueous HNO_3 or NaOH solutions. All electrochemical measurements were carried out under nitrogen at room temperature with the scan rate of 100 mV s^{-1} for CV and amplitude of 50 mV and the pulse period of 0.2 s for DPV.

Characterization of Particles. Transmission electron microscope (TEM) images of nanoparticles, which were mounted on a copper micro grid coated with elastic carbon, were observed by a JEOL JEM 2100 operating at 200 keV. X-ray photoelectron spectra (XPS) were measured by a Kratos Axis 165x with a hemispherical electron energy analyzer. An incident radiation was Mg $K\alpha$ X-ray (1253.6 eV) at 200 W, and a charge neutralizer was turned on for acquisition. Each sample was attached on a stainless stage with a double-sided carbon scotch tape. The binding energy of each element was corrected by the C 1s peak (284.6 eV) from the residual carbon.

Results and Discussion

Water Oxidation by CAN Catalyzed by Iron Complexes. The catalytic water oxidation by CAN was investigated by adding an iron complex (12.5 μM) to an aqueous solution (2.0 mL) containing CAN (125 mM). The time courses of O_2 evolution quantified by gas chromatography (GC) are shown in Figure 1 (see GC charts in Figure S1 in Supporting Information (SI)). When **1** and **2** were used as catalysts, O_2 evolution was observed with turnover numbers (TONs) of 80 ± 10 and 20 ± 5 at 60 min determined by GC. No O_2 evolution was observed in the absence of the iron complexes, indicating that the iron complexes catalyzed water oxidation. However, the O_2 yield in the reaction by **1** was less than 3.2% based on the stoichiometry of the reaction eq 1,

$$2H_2O + 4Ce^{IV} \rightarrow O_2 + 4Ce^{III} + 4H^+ \quad (1)$$

in which one molecule of O_2 evolves from 4 equiv of CAN. The O_2 evolution was also quantified by manometry (Figure 2), however, a slight amount of CO_2 was also evolved under the catalytic conditions (Figure 1b and see CG charts in Figure S2 in SI). Thus, TONs of O_2 evolution should be determined based on the direct detection of O_2 by GC together with the manometry.[32]

CAN is a strong oxidant ($E_{1/2}$ = 1.61 V vs NHE),[37] and it has been reported to oxidize ligands of metal complexes and also to evolve CO_2 during the water oxidation reaction.[16,20,24,28] For this reason we analyzed the integrity of the BQEN ligand at the end of the water oxidation by CAN. ^{1}H NMR spectroscopy clearly demonstrated that

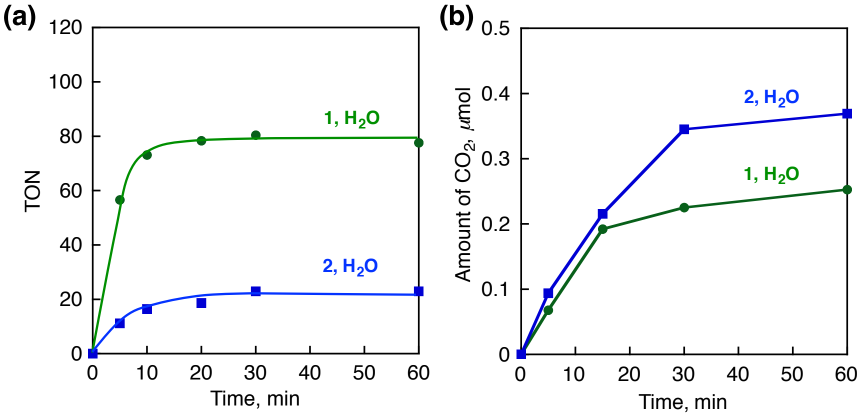

Figure 1. (a) Time courses of O_2 evolution in the catalytic water oxidation by CAN (125 mM) with **1** and **2** (12.5 μM) in a non-buffered aqueous solution (2.0 mL). O_2 was quantified by GC. TON is defined as the total number of mole of O_2 per mole of the complex. (b) Time courses of CO_2 evolution with **1** (green cycles) and **2** (blue squares) in the reaction.

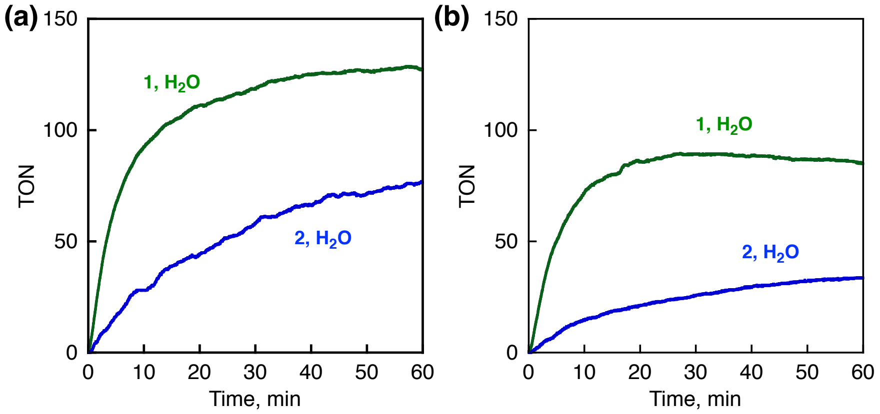

Figure 2. Time courses of O_2 evolution quantified by manometry in the catalytic water oxidation by CAN (125 mM) with **1** and **2** (12.5 μM) in a non-buffered aqueous solution (2.0 mL). (a) Addition of CAN into iron complexes; CAN (250 μmol) was dissolved in 0.20 mL water and added into 1.8 mL of iron complex solution (b) Addition of iron complexes into CAN; CAN (250 μmol) was dissolved in 1.95 mL water in the reaction vial. The reaction was started by adding 50 μL of iron complex solution into CAN solution.

the BQEN ligand was completely oxidized in the water oxidation reaction (Figure 3). I also carried out CO_2 analysis by GC under the same conditions using a high concentration of iron complexes (1.0 mM). Figure 4 shows the time courses of CO_2 and O_2 evolution with **1**, **2**, and $FeSO_4$ performed in a non-buffered aqueous solution and in an aqueous solution containing 0.10 M HNO_3. CO_2 evolution was observed with both **1**

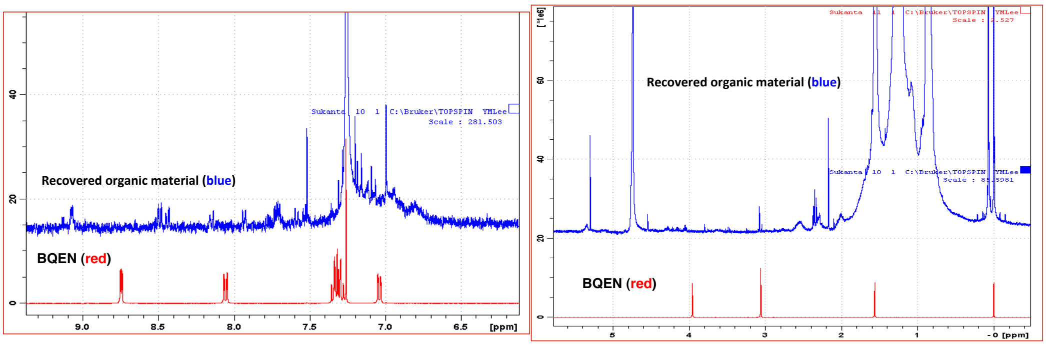

Figure 3. ^{1}H NMR spectra (in $CDCl_3$) of BQEN ligand (red line) and the organic material (blue line) obtained from the water oxidation reaction by CAN (0.10 M) with **1** (1.0 mM) in a non-buffered aqueous solution after 1 h. The organic compounds were collected as follows: H_2SO_4 was added to the resulting solution to remove the precipitates (cerium sulphate) formed in the solution by centrifugation, and a yellow-brown solution was obtained. Addition of excess KCN into the yellow-brown solution (to remove iron ions) generated brown precipitates along with a red solution. The precipitates were separated from the red solution by centrifugation. The precipitates and the red solution were washed separately with CH_2Cl_2. Then the combined CH_2Cl_2 solutions were washed with water and dried over Na_2SO_4. Finally, the yellow oily residue was obtained by removal of CH_2Cl_2.

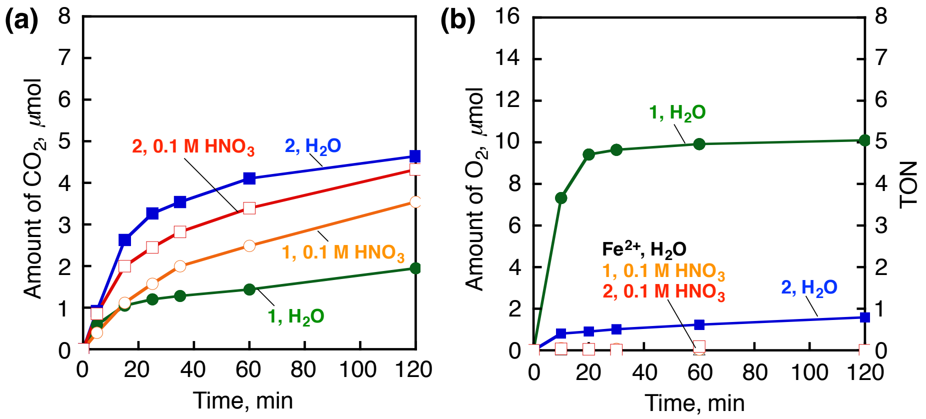

Figure 4. Time courses of (a) CO_2 evolution and (b) O_2 evolution in the catalytic water oxidation by CAN (0.10 M) with **1**, **2** and $FeSO_4$ (1.0 mM) in a non-buffered aqueous solution and in an aqueous solution containing 0.10 M HNO_3 (2.0 mL). The product yields were determined using GC.

and **2** even at the initial reaction stage either in the non-buffered solution or in the 0.10 M HNO_3 aqueous solution (Figure 4a, see GC charts in Figure S3 in SI). This result clearly demonstrates that the ligands of **1** and **2** are completely degraded to CO_2 by CAN. The amount of CO_2 evolution observed with **2** (4.1 μmol) after 60 min is ~3 times larger than that observed with **1** (1.4 μmol), indicating BQCN ligand is more easily oxidized by CAN. The CO_2 evolution in the ligand oxidation of **1** and **2** competes with the O_2 evolution in the water oxidation by CAN. As shown in Figure 4b, O_2 evolution was also observed with **1** and **2** at the high concentration in the non-buffered solution. The O_2 evolution with **1** was stopped at 20 min with a small TON of 5 and with an O_2 yield of 20% in the non-buffered solution. The total amounts of O_2 and CO_2 evolution obtained with **1** agreed with the amount of evolved gas quantified by manometry (Figure 5). The smaller amount of O_2 evolution with **2** could be ascribed to the larger amount of CO_2 evolution resulted from the ligand oxidation. The CO_2

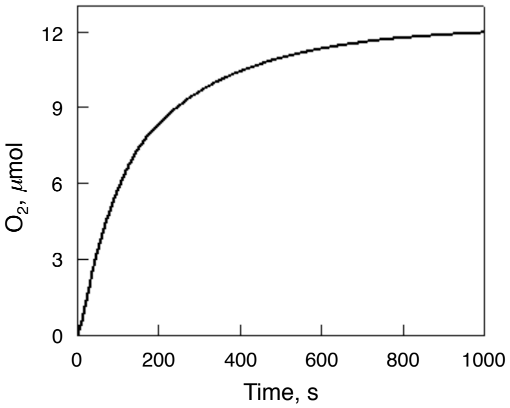

Figure 5. Time courses of O_2 evolution monitored by manometry in the catalytic water oxidation by CAN (0.10 M) with **1** (1.0 mM) in a non-buffered aqueous solution (2.0 mL).

evolution continued even after the O_2 evolution ceased in 20 min suggests that the deactivation of the water oxidation catalyst resulted from the ligand oxidation of the iron complexes by CAN.

When the reaction of **1** with CAN was performed in an aqueous solution in the presence of 0.10 M HNO_3, the amount of CO_2 evolution was twice larger than that in an aqueous solution without HNO_3 (Figure 4a). On the other hand, no O_2 evolution was observed with **1** and **2** in the presence of 0.10 M HNO_3 in water (Figure 4b). The ligand oxidation of **1** and **2** was accelerated, whereas the water oxidation was decelerated under highly acidic conditions. The ligands may be dissociated from iron complexes at low pHs to generate free iron ions, which have no catalytic activity for the water oxidation as no O_2 evolution was observed from the reaction solution containing $FeSO_4$ (Figure 4b).

The ligand dissociation of **1** was examined with various concentrations of HNO_3 in an aqueous solution containing 1.0 mM of **1** as shown in Figure 6, where the absorption band at 450 nm due to **1** decreased with increasing concentration of HNO_3, accompanied by an increase in the absorption band at 365 nm due to free BQEN ligand (Figure 7a). The addition of NaOH to the resulting solution resulted in no recovery of the absorption band at 450 nm (Figure 7b). Thus, the ligand dissociation by HNO_3 is an irreversible process. The absorbance at 365 nm was plotted against the pH values together with the absorbance change at 450 nm as shown in Figure 6b. The BQEN ligand was started to dissociate from **1** around pH 3.5 and completely dissociated at pH 1.5. This result explains why no O_2 was evolved with **1** in the presence of 0.10 M HNO_3 (Figure 4b).

The ligand dissociation of **1** at different pHs was also examined by differential pulse voltammetry in an aqueous solution containing **1** (0.50 mM) as shown in Figure 8 and

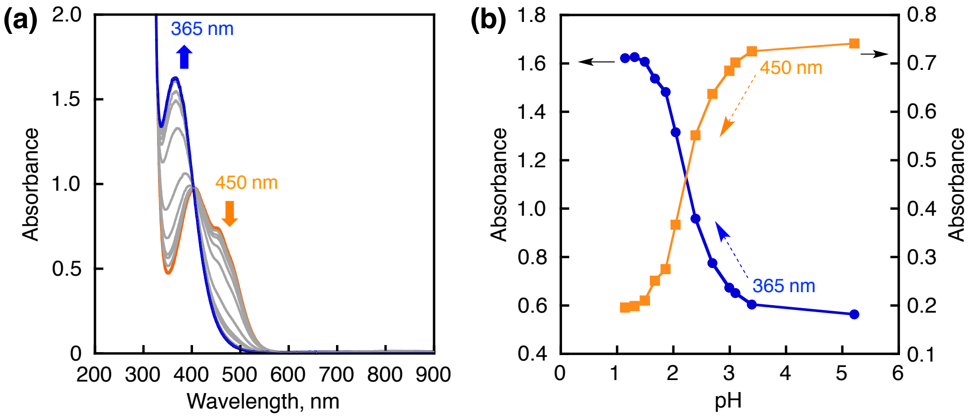

Figure 6. (a) UV-vis spectral changes by titration of nitric acid to a non-buffered solution (2.0 mL) containing **1** (1.0 mM). (b) The absorbance changes at 450 nm and 365 nm observed with the titration.

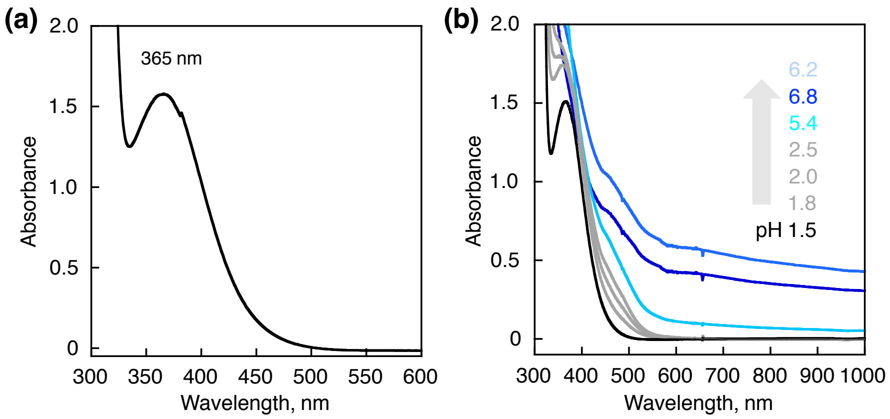

Figure 7. (a) UV-vis spectra of an aqueous solution (2.0 mL) containing BQEN (1.0 mM) and HNO_3 (0.10 M). (b) UV-vis spectral changes observed for the titration of an aqueous solution (2.0 mL) of **1** (1.0 mM) in HNO_3 (0.10 M) with NaOH.

Figure S4 in SI. Under the acidic conditions (e.g., pH 2.4), the oxidation peaks due to both **1** and free BQEN ligand were observed (Figure 8a). The pH dependence of the ratio on the oxidation peaks due to **1** (~0.5 V vs SCE) and free BQEN ligand (~0.75 V vs SCE) is shown in Figure 8b, which agrees with the absorbance changes depending on pH in Figure 3b. A cyclic voltammogram of **1** at pH 3.4, where the BQEN ligand is not dissociated significantly, exhibits the catalytic current for O_2 evolution in addition to the small oxidation peaks due to **1** and free BQEN ligand (Figure 9).

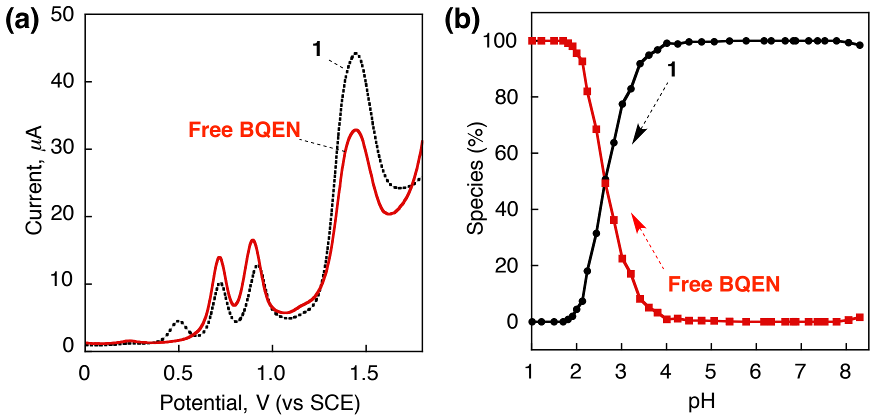

Figure 8. (a) Differential pulse voltammetry (DPV) of **1** (0.50 mM, dotted line) or free BQEN ligand (0.50 mM, red line) in an aqueous solution (pH 2.4, 0.10 M $NaNO_3$). (b) pH dependence of distribution of **1** (black circles) and dissociated BQEN ligand (red square) determined by DPV measurements. The speciation curves were calculated by considering an equilibrium in aqueous medium: $Fe(BQEN)(OTf)_2$ $\rightleftharpoons$ "$Fe(OTf)_2$" + "BQEN" [% complex = {area of Fe^{III}/Fe^{II} curve/(area of Fe^{III}/Fe^{II} curve + area of first-step ligand oxidation curve)} × 100]. The areas of DPV curves were calculated by using software built in a CHI630b Electrochemical Analyzer. See Figure S4 in SI for DPV data obtained under different pH conditions.

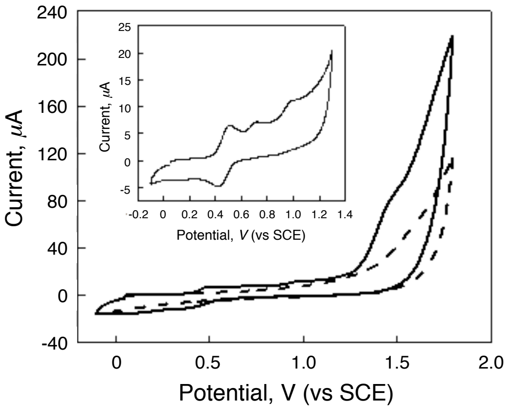

Figure 9. CVs of glassy carbon background (black dashed) and complex **1** (0.50 mM, black solid) in an aqueous solution (pH 3.4, 0.10 M $NaNO_3$) with scan rate of 100 mV s^{-1}. Inset shows the CV of **1** up to potential 1.3 V with a reversible $Fe^{III/II}$ couple at $E_{1/2}$ = 0.47 V followed by two dissociated BQEN ligand centered irreversible oxidation waves.

The pH of a 0.10 M CAN aqueous solution was 0.80, which enabled the BQEN ligand to dissociate completely from **1** as shown in Figures 3b and 4b. However, O_2 was evolved in water oxidation by 0.10 M CAN with **1** in a non-buffered aqueous solution (Figure 4b). This indicates that the catalytic water oxidation by CAN with **1** occurs in competition with the ligand dissociation of **1**. Indeed, the ligand dissociation by an acid was observed to occur within several seconds (Figure 10), however, high-valent iron complexes formed in the presence of CAN prohibited the ligand dissociation because of the strong binding of the ligands to the high-valent metal center, which resulted from the strongly electron-withdrawing ability of the high-valent iron. The oxidation of **1** by CAN resulted in rapid production of a high-valent iron complex, which is continuously formed by excess CAN during the water oxidation (*vide infra*). The O_2 evolution was stopped at 20 min, since the ligand was completely dissociated from **1**. Thus, the use

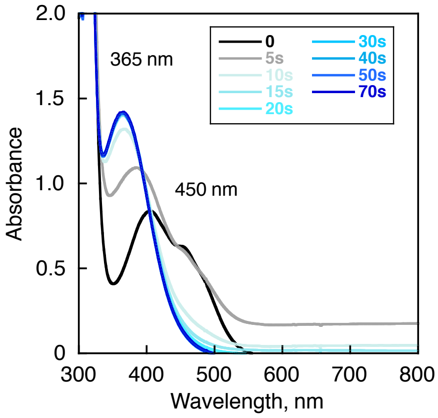

Figure 10. UV-vis spectral changes observed by adding HNO_3 (70 wt%, 20 μL) to **1** (1.0 mM) in a non-buffered aqueous solution (2.0 mL).

of a non-buffered aqueous solution is important to achieve the catalytic water oxidation with **1** to evolve O_2, because the ligand was dissociated in a buffered acid solution before the addition of CAN.

DLS measurements were performed to examine the formation of nanoparticles during the O_2 evolution as shown in Figure 11; no formation of nanoparticles was observed. Generally, particles of iron oxides are rarely derived from iron ions under acidic conditions at ambient temperature.[38]

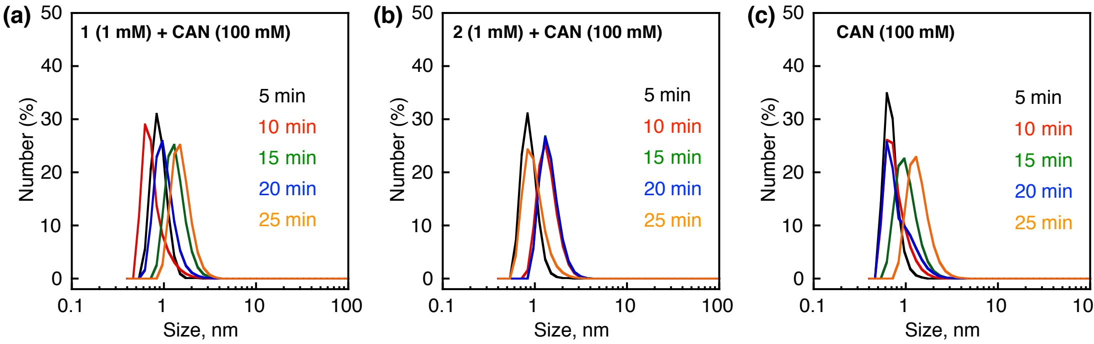

Figure 11. Particle size distribution determined by dynamic light scattering (DLS) measurements of non-buffered aqueous solutions of (a) **1** (1.0 mM) plus CAN (0.10 M), (b) **2** (1.0 mM) plus CAN (0.10 M), and (c) only CAN (0.10 M) at reaction times of 5.0 min (black line), 10 min (red line), 15 min (green line), 20 min (blue line), and 25 min (orange line).

Intermediates for Water Oxidation by 1 and CAN. The stoichiometric oxidation of **1** by CAN was investigated in a non-buffered aqueous solution to detect the intermediate(s) formed in the catalytic water oxidation. When 2 equiv of CAN were added to the solution, an absorption band at 760 nm appeared (Figure 12a). The same absorption band was observed when excess CAN (0.10 M) was used (Figure 13). The absorption band at 760 nm can be assigned to $[Fe^{IV}(BQEN)(O)]^{2+}$ ($Fe^{IV}=O$) by comparison with that of $[Fe^{IV}(BQEN)(O)]^{2+}$ prepared independently by the reported method, in which **1** was reacted with peracetic acid in MeCN.[39–41] The ESI-MS peak due to $[Fe^{IV}(BQEN)(^{16}O)(OTf)]^{+}$, which was produced by the reaction of **1** with peracetic acid in MeCN in the presence of $H_2{}^{16}O$, was observed at $m/z = 563.0$, which was shifted to $m/z = 565.0$ when the reaction was performed in MeCN in the presence of $H_2{}^{18}O$ (Figure 12b). The latter result is in line with our recent result that an intermediate containing oxygen atom exchanges its oxygen with $H_2{}^{18}O$ to produce $[Fe^{IV}(BQEN)(^{18}O)(OTf)]^{+}$.[40] The absorption band observed at 740 nm due to $[Fe^{IV}(BQEN)(O)]^{2+}$ in MeCN was shifted to 760 nm upon addition of H_2O (Figure 12c), probably because of the coordination of H_2O or protonation, in agreement with the absorption band observed in the oxidation of **1** by two equiv of CAN (Figure 12a).

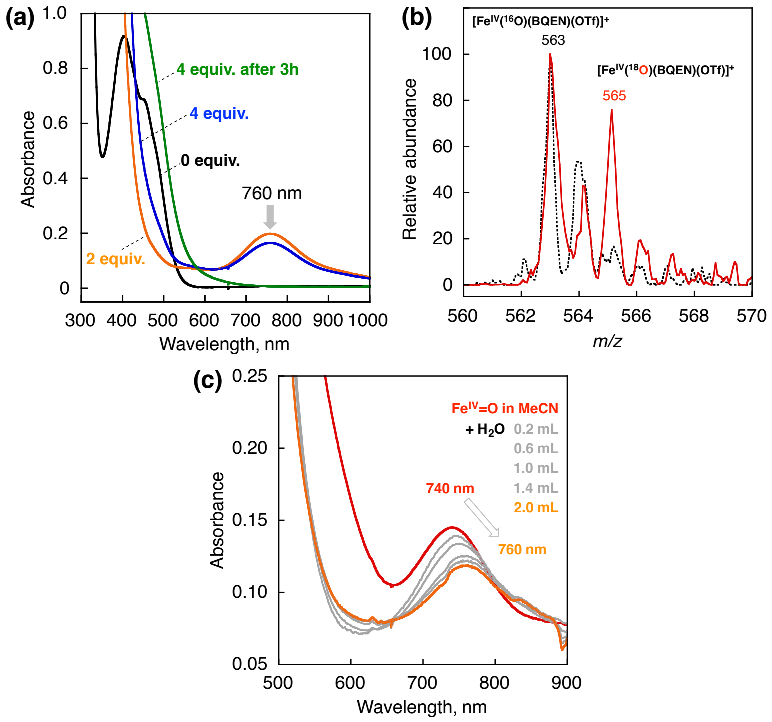

Figure 12. (a) UV-vis spectral changes observed in the stoichiometric water oxidation by **1** (1.0 mM) upon addition of different amounts of CAN (1.0–4.0 mM) in a non-buffered aqueous solution (2.0 mL). (b) ESI-MS spectra of $[Fe^{IV}(BQEN)(O)(OTf)]^+$ formed in the reaction of **1** (1.0 mM) with peracetic acid (1.2 mM) in the presence of $H_2{}^{16}O$ (20 μL, black dots) and $H_2{}^{18}O$ (20 μL, red line) in MeCN (2.0 mL). The peaks at m/z 563.0 and 565.0 correspond to $[Fe^{IV}(BQEN)(^{16}O)(OTf)]^+$ and $[Fe^{IV}(BQEN)(^{18}O)(OTf)]^+$ (calcd m/z = 563.1 and 565.1, respectively). (c) UV-vis spectral changes of Fe^{IV}=O (1.0 mM, red line) upon addition of various amounts of H_2O (grey lines: 0.20 mL, 0.60 mL, 1.0 mL, 1.4 mL, and orange line: 2.0 mL) into an MeCN solution (2.0 mL) of Fe^{IV}=O at 273 K. Fe^{IV}=O intermediate was generated in the reaction of **1** (1.0 mM) with peracetic acid (4.0 mM) in MeCN at 273 K.

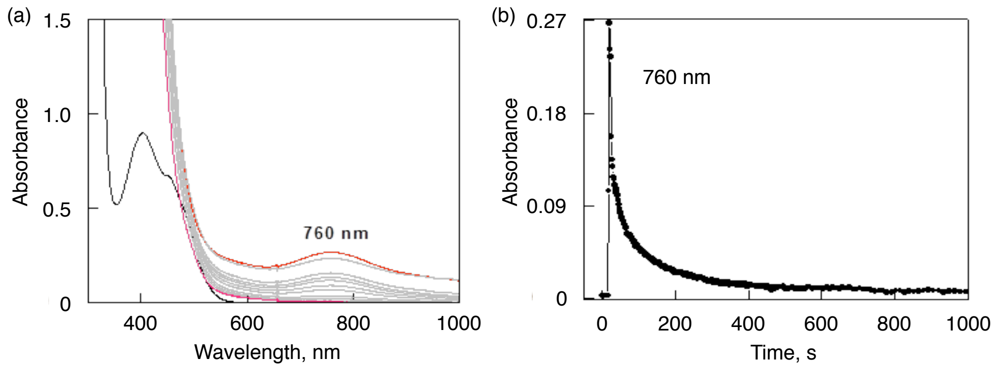

Figure 13. (a) UV-vis spectral changes observed in the water oxidation by CAN (0.10 M) in the presence of **1** (1.0 mM) in a non-buffered aqueous solution. (b) Time courses of the decay of absorption band at 760 nm due to $[Fe^{IV}(BQEN)(O)]^{2+}$ in the water oxidation by CAN (0.10 M) in the presence of **1** (1.0 mM).

To understand the role of $Fe^{IV}=O$ in the catalytic water oxidation by CAN, the relation between O_2 evolution and the formation and decay of $Fe^{IV}=O$ was investigated by comparing the time courses of the absorbance at 760 nm due to $Fe^{IV}=O$ and O_2 evolution as shown in Figure 14. When 4 equiv of CAN were added to a non-buffered aqueous solution of **1**, the absorption band at 760 nm assigned to $Fe^{IV}=O$ immediately appeared, and decreased gradually as the O_2 evolution occurred and then ceased. The O_2 yield was determined to be 24% in the first run. Upon second and third addition of 4 equiv of CAN, the absorption band at 760 nm due to $Fe^{IV}=O$ increased again immediately (Figure 14a), but each at initial absorbance was lower than that of previous run because of the ligand dissociation due to the gradual pH decrease in each time. The initial pH was 5.4 and decreased to 2.1, to 1.8, and then to 1.7 at the end of the first, second, and third runs, respectively. The yields of O_2 evolved at the second and third runs were 28% and 18%, respectively, which may be caused by two opposite factors, such as the higher oxidizing ability of CAN and increasing ligand dissociation at lower pH (Figures 6 and 8). The prohibition of the ligand dissociation from the iron complex was confirmed by the rapid formation of the $Fe^{IV}=O$ complex, because the decay of absorbance at 760 nm due to $Fe^{IV}=O$ was much slower than the ligand dissociation by the addition of an acid (Figure 10). The formation of $Fe^{IV}=O$ prevented ligand

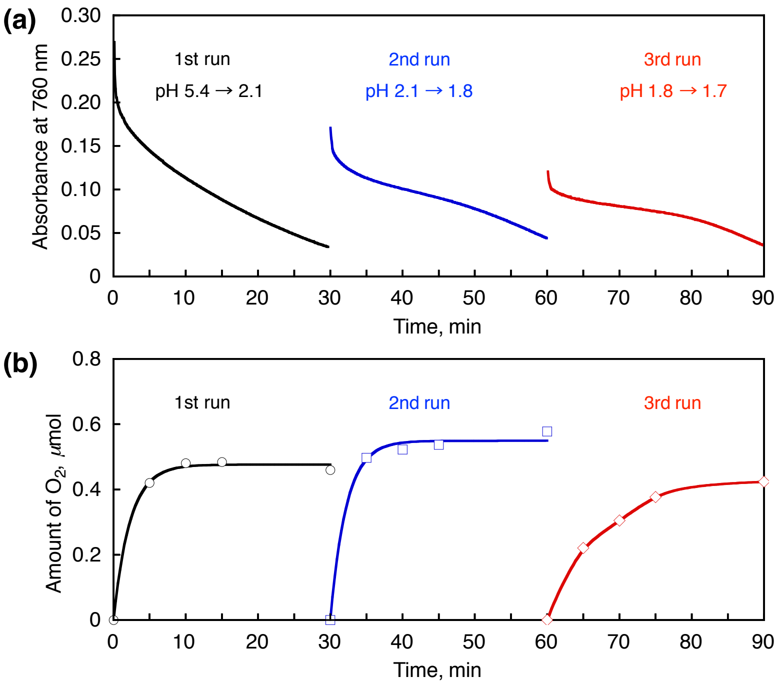

Figure 14. (a) Time courses of the absorbance at 760 nm in the water oxidation by addition of 4 equiv of CAN (4.0 mM) to **1** (1.0 mM) in a non-buffered aqueous solution (2.0 mL, first run, black line), and further additions of CAN (4.0 mM) to the resulting solution for the second run (blue line), and the third run (red line). (b) Time courses of O_2 evolution quantified by GC in those reactions.

dissociation, however, the Fe^{IV}=O decomposed during the reaction in a similar way to the decomposition of Fe^{II} complexes under acidic conditions.

When the stoichiometric reaction of CAN with **1** was performed in the presence of 0.10 M HNO_3 in water (pH 1.2), neither O_2 evolution nor the absorption band at 760 nm due to Fe^{IV}=O was observed because of the complete ligand dissociation from **1** (Figure 15). These results indicate that the catalytic water oxidation by CAN with **1** occurs via formation of Fe^{IV}=O.

Mechanistic Insight into Water Oxidation by 1 and CAN. In order to gain mechanistic insight into the O-O bond formation in the catalytic water oxidation by CAN with **1**, the oxygen exchange in $[Fe^{IV}(BQEN)(^{16}O)]^{2+}$ with $H_2{}^{18}O$ (98% ^{18}O-enriched) was further examined by GC-MS (Figure 16). First the reaction of **1** with two equiv of CAN was performed in $H_2{}^{16}O$ to produce $Fe^{IV}{=}^{16}O$ and then two equiv of CAN in $H_2{}^{18}O$ were added to the resulting solution to detect the isotopes of evolved O_2.

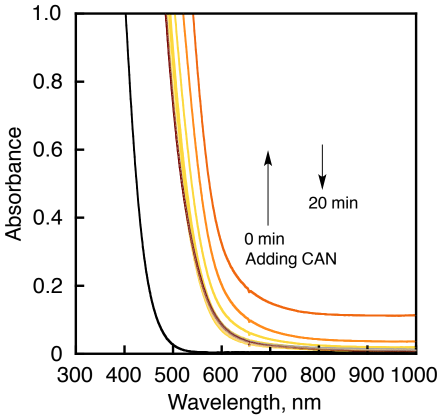

Figure 15. UV-vis spectral changes of an aqueous solution containing CAN (0.10 M), **1** (1.0 mM) and HNO_3 (0.10 M).

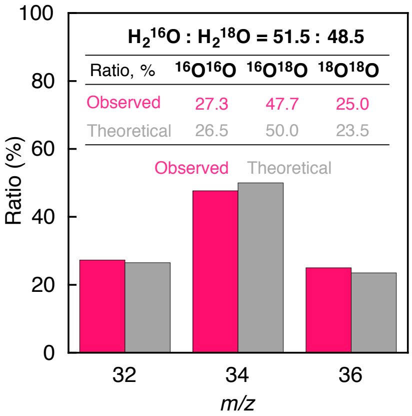

Figure 16. Comparison of relative abundance of ^{18}O-labeled and unlabeled oxygen evolved during the stoichiometric oxidation of $H_2{}^{18}O$-enriched water (48.5% $H_2{}^{18}O$) by addition of 2 equiv of CAN to **1** (2.0 μmol) in $H_2{}^{16}O$ followed by the addition of $H_2{}^{18}O$ and additional 2 equiv of CAN.

The evolved O_2 was detected by GC-MS, which revealed that the isotope ratio of $^{16}O^{16}O$: $^{18}O^{16}O$: $^{18}O^{18}O$ was 27.3 : 47.7 : 25.0 (Figure 16), which agrees with the theoretical ratio (26.5 : 50.0 : 23.5) calculated by assuming that the oxygen exchange between $[Fe^{IV}(BQEN)(^{16}O)]^{2+}$ and $H_2{}^{18}O$ is much faster than the oxygen evolution under the reaction conditions. If the oxygen exchange between $[Fe^{IV}(BQEN)(^{16}O)]^{2+}$ and $H_2{}^{18}O$ is much slower than the oxygen evolution, no $^{18}O^{18}O$ would be evolved. Thus, the oxygen exchange between $[Fe^{IV}(BQEN)(^{16}O)]^{2+}$ and $H_2{}^{18}O$ (48.5%) occurs rapidly via $[Fe^{IV}(BQEN)(^{16}OH)(^{18}OH)]$ following coordination of $H_2{}^{18}O$ to produce the same amount of $[Fe^{IV}(BQEN)(^{16}O)]^{2+}$ and $[Fe^{IV}(BQEN)(^{18}O)]^{2+}$ as indicated in Figure 5b (Scheme 1b and c). Both $[Fe^{IV}(BQEN)(^{16}O)]^{2+}$ and $[Fe^{IV}(BQEN)(^{18}O)]^{2+}$ are further oxidized with CAN in $H_2{}^{16}O$ (51.5%) and $H_2{}^{18}O$ (48.5%) as solvent to produce O_2 with the theoretical isotope ratio of $^{16}O^{16}O$: $^{18}O^{16}O$: $^{18}O^{18}O$ = 26.5 : 50.0 : 23.5 (Scheme 1a–d).

Scheme 1. Proposed Mechanism of Oxygen Exchange in $Fe^{IV}(^{16}O)$ with $H_2{}^{18}O$ in Relation with the Mechanism of the O-O Bond Formation in the Catalytic Water Oxidation by CAN with 1

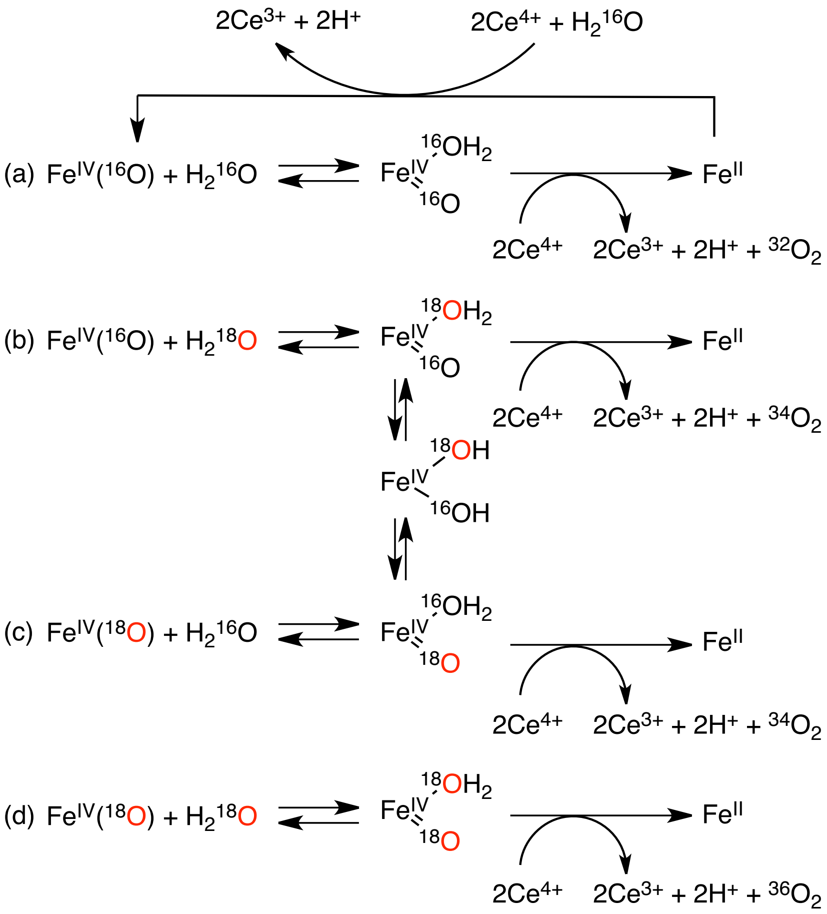

The formation of O-O bond in $[Fe^{IV}(BQEN)(O)(OH_2)]^{2+}$ may be a key step, though it would be difficult to distinguish whether O-O bond is formed by intramolecular interaction between the Fe^{IV}=O and Fe^{IV}–OH groups or the nucleophilic attack by water to Fe^{IV}=O from the labeling experiments. If H_2O_2 is produced from the O-O bond formation, it will be oxidized by 2 equiv of CAN to evolve O_2. Thus, we have investigated the H_2O_2 oxidation by CAN to confirm the rate-determining step in the water oxidation by CAN. When 2 equiv of CAN were added to H_2O_2 in an aqueous solution containing HNO_3 (0.10 M), the absorbance at 420 nm assigned to CAN completely disappeared within 20 s accompanied by O_2 evolution (Figure 17). The O_2 yield for the H_2O_2 oxidation reached 55% at 60 s and 90% at 300 s according to the stoichiometric reaction of eq 2. This result suggests that O_2 was evolved rapidly when H_2O_2 was oxidized by 2 equiv of CAN. The subsequent oxidation of H_2O_2 would also be taken place in the iron metal center during the catalytic water oxidation. Thus, H_2O_2 cannot be involved in the rate-determining step for the four-electron oxidation of H_2O. The rate-determining step of the water oxidation by CAN may be the O-O bond formation in the oxidation of $[Fe^{IV}(BQEN)(O)(OH_2)]^{2+}$ by CAN (see Scheme 1). The oxidation of $[Fe^{IV}(BQEN)(O)(OH_2)]^{2+}$ by CAN may produce the Fe^{V} species as suggested by Costas, Fillol and coworkers.[32] In this study, only $[Fe^{IV}(BQEN)(O)(OH_2)]^{2+}$ was observed during the water oxidation, although the formation of the Fe^{V} species cannot be excluded in the mechanism of water oxidation.

$$H_2O_2 + 2Ce^{IV} \rightarrow O_2 + 2Ce^{III} + 2H^+ \qquad (2)$$

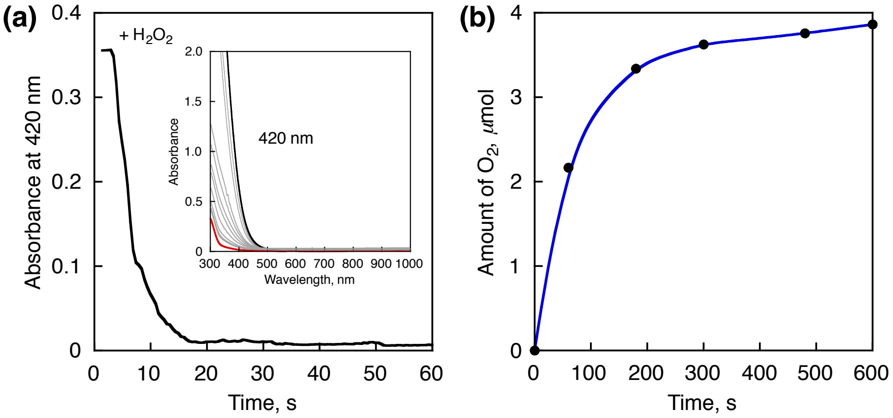

Figure 17. (a) Time course of the decay of CAN monitored at 420 nm in the reaction of H_2O_2 (2.0 mM) with CAN (4.0 mM) in the presence of HNO_3 (0.10 M) in an aqueous solution (2.0 mL). Insert shows the UV-vis spectral changes of the reaction solution. (b) Time course of O_2 evolution for H_2O_2 oxidation quantified by GC during the reaction of H_2O_2 (2.0 mM) with CAN (4.0 mM) in the presence of HNO_3 (0.10 M) in a non-buffered aqueous solution (2.0 mL).

Light-Driven Water Oxidation by Iron Hydroxides Derived from 1. Under basic conditions, CAN is not a suitable oxidant for water oxidation, because hydrolysis of CAN occurs and reduces its oxidation power.[37] Thus, we examined the light-driven water oxidation under basic conditions using $[Ru(bpy)_3]^{2+}$ and $S_2O_8^{2-}$ as a photosensitizer and a sacrificial electron accepter, respectively. The catalytic cycle of the light-driven water oxidation is shown in Scheme 2. Photoinduced electron transfer from $[Ru(bpy)_3]^{2+*}$ (where * denotes the excited state) to $S_2O_8^{2-}$ occurs to produce $[Ru(bpy)_3]^{3+}$, which can oxidize water in the presence of a water oxidation catalyst to evolve O_2. The light-driven water oxidation was performed in a borate buffer solution (0.10 M, 2.0 mL, initial pH 8.0, 8.5, or 9.0) containing **1** (5.0 μM), $Na_2S_2O_8$ (5.0 mM), and $[Ru(bpy)_3]SO_4$ (0.25 mM). The light-driven water oxidation reaction was started by irradiating the solution with a Xe lamp (500 W) through a transmitting glass filter ($\lambda >$ 420 nm) with vigorous stirring at room temperature. Time courses of O_2 evolution at different initial pHs are shown in Figure 18a. The evolution of O_2 was not observed in the absence of **1** under the reaction conditions. The amount of O_2 obtained after 20 min photoirradiation at initial pH 9.0 (2.6 μmol, TON = 259) was larger than those at initial pH 8.5 (2.4 μmol, TON = 238) and 8.0 (0.67 μmol, TON = 67). The stoichiometric amount of O_2 evolution is 5.0 μmol in the present reaction systems based on the stoichiometry of eq 3, where $Na_2S_2O_8$ acts as a two-electron acceptor.[42] A high O_2 yield

$$2H_2O + 2Na_2S_2O_8 \rightarrow O_2 + 4H^+ + 4Na^+ + 4SO_4^{2-} \tag{3}$$

(52%) was obtained at initial pH 9.0. DLS measurements were performed to investigate the formation of nanoparticles in the reaction solution, since it has been reported that iron oxides formed during the reaction catalyze light-driven water oxidation by $S_2O_8^{2-}$.[33] Nanoparticles were detected by the DLS measurements as shown in Figure 19. Figure 18b shows the time courses of average size of particles formed in the solution. Formation of nanoparticles even at the initial stage of photoirradiation indicates that

Scheme 2. Catalytic Cycle of Light-Driven Water Oxidation with $Na_2S_2O_8$ and $[Ru(bpy)_3]^{2+}$ Using an Iron-Based Catalyst

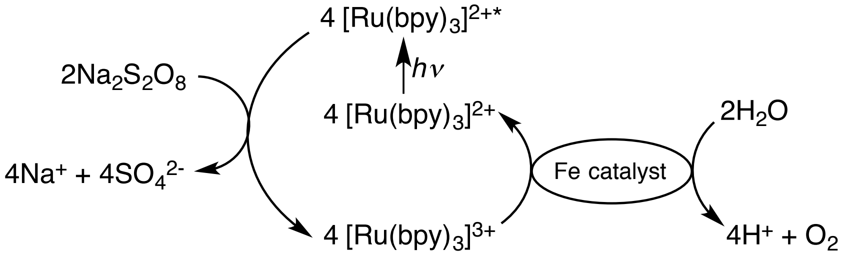

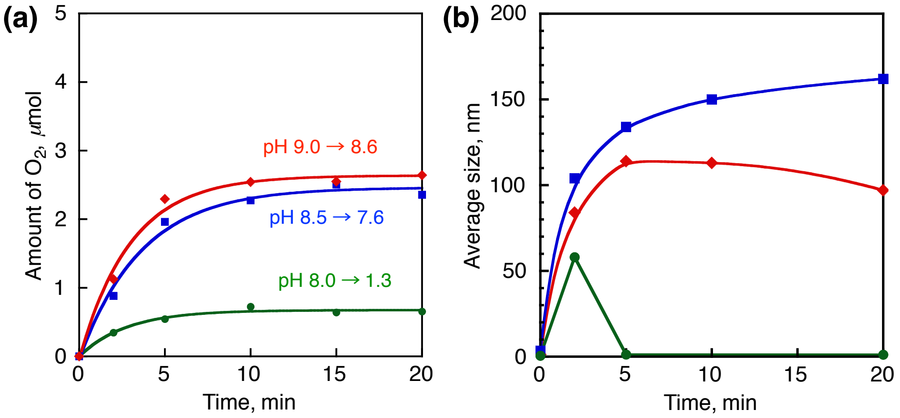

Figure 18. Time courses of O_2 evolution under photoirradiation ($\lambda > 420$ nm) of a borate buffer solution (0.10 M, 2.0 mL) containing $Na_2S_2O_8$ (5.0 mM), $[Ru(bpy)_3]SO_4$ (0.25 mM), and **1** (5.0 μM) at different initial pH conditions (green circles: pH 8.0, blue squares: pH 8.5, red rhombi: pH 9.0). (b) Time courses of average particle size formed in the photocatalytic reaction. See Figure 19 for particle size distribution determined by dynamic light scattering (DLS) measurements.

nanoparticles derived from **1** act as a true catalyst in the light-driven water oxidation. In fact, the titration of sodium hydroxide to **1** monitored by UV-vis spectra demonstrated that the ligand of **1** was dissociated to release Fe^{2+} ions under basic condition (Figure 20a). As a result, nanoparticles derived from Fe^{2+} ions released from **1** by the ligand dissociation under the basic conditions act as the true catalyst in the light-driven water oxidation. When the concentration of **1** was increased to 1.0 mM, the ligand oxidation to CO_2 was also observed under the basic conditions (Figure 20b). Nanoparticles also formed during the light-driven water oxidation with **2** at initial pH 9.0 (Figure 21).

When the initial pH was 9.0, the final pH after the reaction slightly decreased to 8.6 (red line in Figure 18a) and the size of nanoparticles increased with the photoirradiation time to reach the size of 100 nm but slightly decreased as the pH decreased (red line in

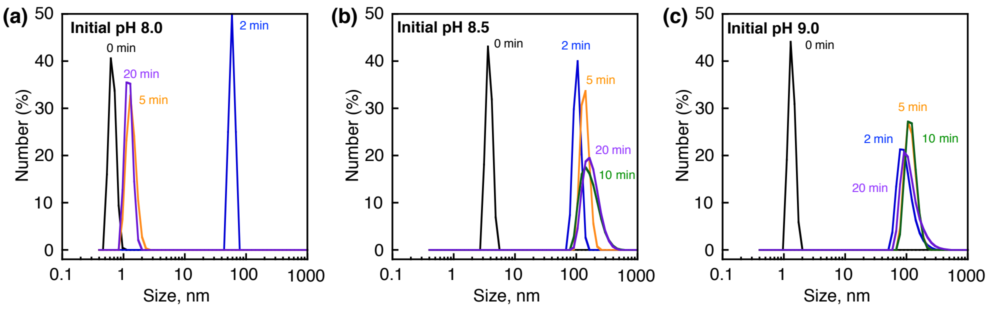

Figure 19. Particle size distribution determined by DLS measurements at initial pH (a) 8.0, (b) 8.5, and (c) 9.0 in borate buffer solutions containing **1** (5.0 μM), $Na_2S_2O_8$ (5.0 mM) and $[Ru(bpy)_3]SO_4$ (0.25mM) at the irradiation times of 2.0 min (blue line), 5.0 min (orange line), 10 min (green line), and 20 min (purple line). The black line shows the particle size distribution in the absence of **1** at 0 min.

Figure 18b). When the initial pH was 8.5, the final pH decreased to 7.6 (blue line in Figure 18a) and the size of nanoparticles increased with the photoirradiation time. In the case of the initial pH 8.0, the final pH decreased significantly to 1.3 (green line in Figure 18a) and the nanoparticles formed initially disappeared at pH 1.3 (green line in Figure 18b). Under such an acidic condition, the O_2 yield decreased significantly as compared with those obtained under basic conditions.

When a phosphate buffer solution (50 mM, pH 8.0) was employed for the

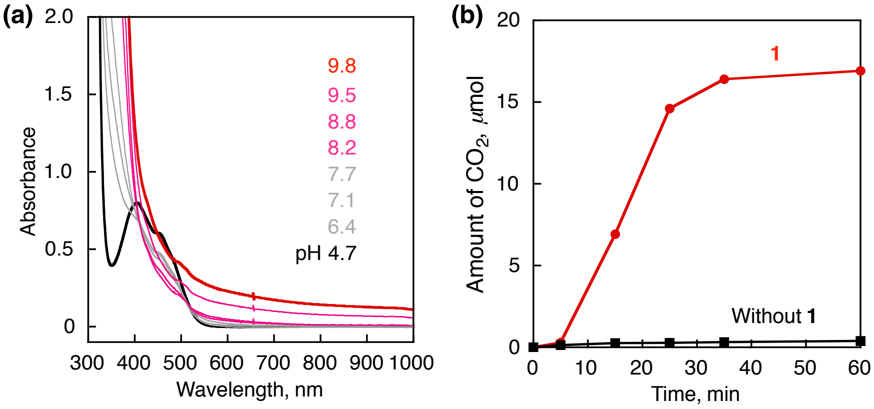

Figure 20. (a) UV-vis spectral changes observed for the titration of a non-buffered aqueous solution (2.0 mL) containing **1** (1.0 mM) with NaOH. (b) Time courses of CO_2 evolution under photoirradiation ($\lambda >$ 420 nm) of a borate buffer solution (0.10 M, 2.0 mL) containing $Na_2S_2O_8$ (25 mM) and $[Ru(bpy)_3]SO_4$ (0.25 mM) in the absence (black squares) and presence of **1** (1.0 mM, red cycles). The CO_2 evolution was quantified by GC.

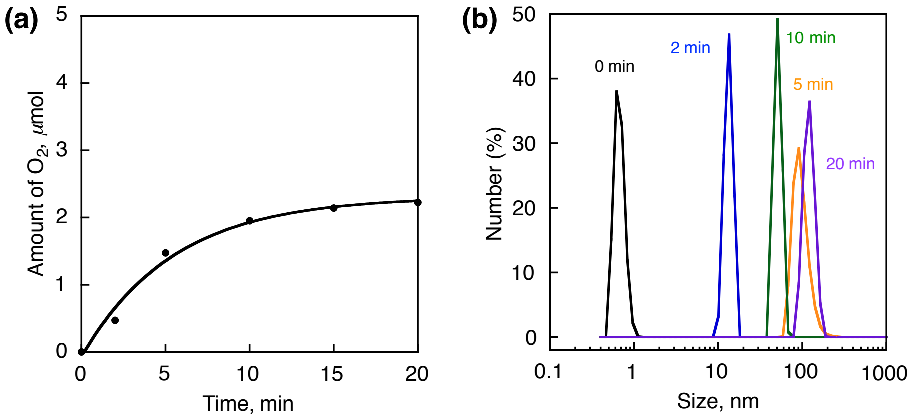

Figure 21. (a) Time course of O_2 evolution under photoirradiation (λ > 420 nm) of a borate buffer solution (0.10 M, 2.0 mL, initial pH 9.0) containing $Na_2S_2O_8$ (5.0 mM), $[Ru(bpy)_3]SO_4$ (0.25 mM), and **2** (5.0 μM). (b) Particle size distribution determined by DLS measurements at initial pH 9.0 in a borate buffer solution containing **2** (5.0 μM), $Na_2S_2O_8$ (5.0 mM) and $[Ru(bpy)_3]SO_4$ (0.25mM) at the irradiation times of 2.0 min (blue line), 5.0 min (orange line), 10 min (green line), and 20 min (purple line). The black line shows the particle size distribution in the absence of **2** at 0 min.

light-driven water oxidation, no O_2 evolution was observed by GC. In the phosphate buffer solution, dissolved Fe^{2+} ions were precipitated by phosphate anions.[33] The nanoparticles formed after the light-driven water oxidation by $S_2O_8^{2-}$ with **1** at the initial pH 9.0 were isolated and they were found to be iron hydroxides by X-ray photoelectron spectroscopy (XPS) measurements (Figure 22) and transmission electron microscopy (TEM) measurements (Figure 23), because higher binding energy of O 1s observed in Figure 22 indicates formation of hydroxide species rather than the oxide species.[43] Thus, the true catalyst in the light-driven water oxidation by $S_2O_8^{2-}$ is iron hydroxide nanoparticles derived from **1** at the initial stage of the reaction.

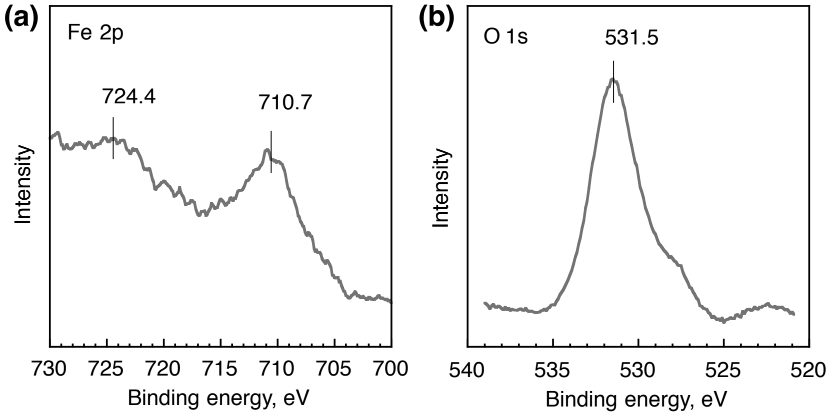

Figure 22. X-ray photoelectron spectra in the energy regions of (a) Fe 2p and (b) O 1s of the isolated particles formed in a borate buffer solution (100 mM, 2.0 mL) containing $Na_2S_2O_8$ (5.0 mM), $[Ru(bpy)_3]SO_4$ (0.25 mM), and **1** (1.0 mM). The binding energy of each element was corrected by the C 1s peak (284.6 eV) from the residual carbon.

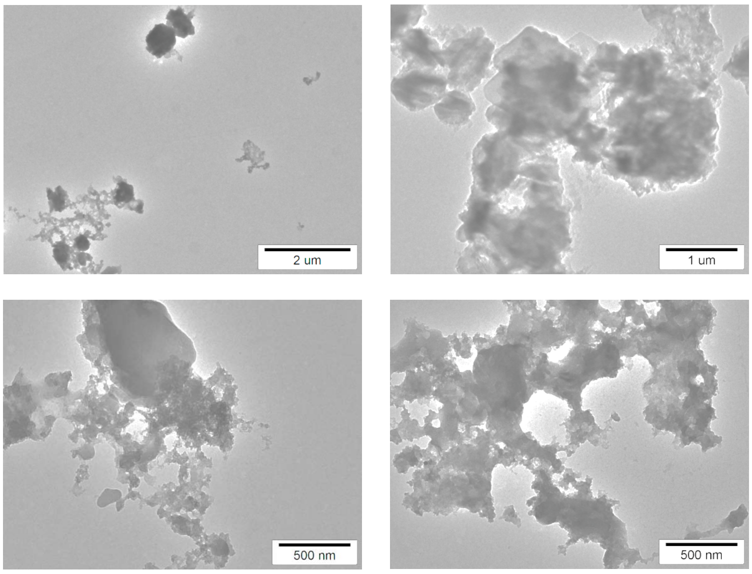

Figure 23. TEM images of the isolated particles formed in a borate buffer solution (0.10 M, 2.0 mL) containing $Na_2S_2O_8$ (5.0 mM), $[Ru(bpy)_3]SO_4$ (0.25 mM) and **1** (1.0 mM).

Conclusion

I have shown that the true catalysts that affect the water oxidation by iron complexes, **1** and **2**, are different in acidic and basic conditions, as shown in Scheme 3. The iron complexes act as homogeneous catalysts in the water oxidation by CAN under acidic conditions. The Fe^{IV}=O species formed by the two-electron oxidation of **1** and **2** by CAN in competition with the ligand dissociation under acidic conditions are involved in the catalytic water oxidation. The O-O bond formation may occur by the reaction of Fe^{IV}=O species with H_2O in the presence of two equiv of CAN or by the coupling of two Fe^{IV}=O species. The dissociated ligands are oxidized by CAN to yield CO_2, resulting in the decrease in the O_2 yield. In contrast to the homogeneous catalysis under acidic conditions, light-driven water oxidation using $[Ru(bpy)_3]^{2+}$ as a photosensitizer and $S_2O_8^{2-}$ as a sacrificial electron acceptor occurs under basic conditions, where **1** and **2** are converted to iron hydroxide nanoparticles that act as the true catalyst for the water oxidation. The iron complexes used here cannot act as efficient WOCs in their original forms, however, they provided an important mechanistic insight into actual form of molecular iron complexes in water oxidation. Although the intermediate on the surface of iron hydroxides in the photocatalytic system has yet to be identified, the present study provides valuable insights into the development of efficient water oxidation catalysts using earth-abundant iron at different pHs.

Scheme 3. Iron catalysts derived from a nonheme iron complex in catalytic water oxidation at different pHs

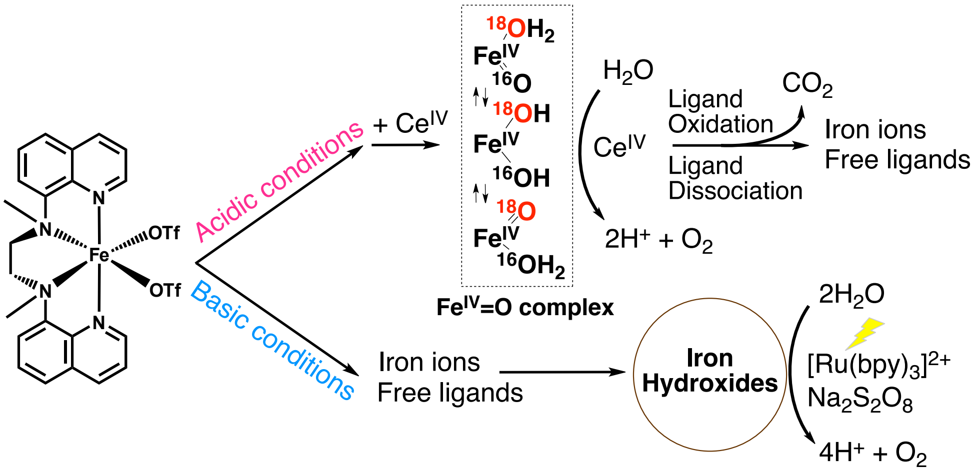

References

(1) (a) Nocera, D. G. *Acc. Chem. Res.* **2012**, *45*, 767. (b) Lewis, N. S.; Nocera, D. G. *Proc. Natl. Acad. Sci. U. S. A.* **2006**, *103*, 15729.

(2) (a) Eisenberg, R.; Gray, H. B. *Inorg. Chem.* **2008**, *47*, 1697. (b) Gray, H. B. *Nat. Chem.* **2009**, *1*, 7. (c) Muckerman, J. T.; Polyansky, D. E.; Wada, T.; Tanaka, K.; Fujita, E. *Inorg. Chem.* **2008**, *47*, 1787.

(3) (a) Duan, L.; Tong, L.; Xu, Y.; Sun, L. *Energy Environ. Sci.* **2011**, *4*, 3296. (b) Artero, V.; Chavarot-Kerlidou, M.; Fontecave, M. *Angew. Chem., Int. Ed.* **2011**, *50*, 7238.

(4) (a) Fukuzumi, S. *Phys. Chem. Chem. Phys*. **2008**, *10*, 2283. (b) Fukuzumi, S.; Ohkubo, K. *J. Mater. Chem*. **2012**, *22*, 4575. (c) Fukuzumi, S.; Yamada, Y. *J. Mater. Chem*. **2012**, *22*, 24284.

(5) (a) Concepcion, J. J.; Jurss, J. W.; Brennaman, M. K.; Hoertz, P. G.; Patrocinio, A. O. T.; Murakami Iha, N. Y.; Templeton, J. L.; Meyer, T. J. *Acc. Chem. Res.* **2009**, *42*, 1954. (b) Magnuson, A.; Anderlund, M.; Johansson, O.; Lindblad, P.; Lomoth, R.; Polivka, T.; Ott, S.; Stensjo, K.; Styring, S.; Sundstrom, V.; Hammarstrom, L. *Acc. Chem. Res.* **2009**, *42*, 1899.

(6) Fukuzumi, S.; Yamada, Y.; Suenobu, T.; Ohkubo, K.; Kotani, H. *Energy Environ. Sci.* **2011**, *4*, 2754.

(7) (a) Hetterscheid, D. G. H.; Reek, J. N. H. *Angew. Chem., Int. Ed.* **2012**, *51*, 9740. (b) Cao, R.; Lai, W.; Du, P. *Energy Environ. Sci.* **2012**, *5*, 8134. (c) Sala, X.; Romero, I.; Rodríguez, M.; Escriche, L.; Llobet, A. *Angew. Chem., Int. Ed.* **2009**, *48*, 2842.

(8) (a) Hurst, J. K.; Cape, J. L.; Clark, A. E.; Das, S.; Qin, C. Y. *Inorg. Chem.* **2008**, *47*, 1753. (b) Deng, Z. P.; Tseng, H. W.; Zong, R. F.; Wang, D.; Thummel, R. *Inorg. Chem.* **2008**, *47*, 1835.

(9) (a) Gersten, S. W.; Samuels, G. J.; Meyer, T. J. *J. Am. Chem. Soc.* **1982**, *104*, 4029. (b) Lebeau, E. L.; Adeyemi, S. A.; Meyer, T. J. *Inorg. Chem.* **1998**, *37*, 6476. (c) Concepcion, J. J.; Jurss, J. W.; Norris, M. R.; Chen, Z. F.; Templeton, J. L.; Meyer, T. J. *Inorg. Chem.* **2010**, *49*, 1277.

(10) (a) Harriman, A.; Pickering, I. J.; Thomas, J. M.; Christensen, P. A. *J. Chem. Soc., Faraday Trans. I* **1988**, *84*, 2795. (b) Jiao, F.; Frei, H. *Energy Environ. Sci.* **2010**, *3*, 1018. (c) Morris, N. D.; Mallouk, T. E. *J. Am. Chem. Soc.* **2002**, *124*, 11114.

(11) (a) Murakami, M.; Hong, D.; Suenobu, T.; Yamaguchi, S.; Ogura, T.; Fukuzumi, S. *J. Am. Chem. Soc.* **2011**, *133*, 11605. (b) Polyansky, D. E.; Muckerman, J. T.; Rochford, J.; Zong, R.; Thummel, R. P.; Fujita, E. *J. Am. Chem. Soc.* **2011**, *133*, 14649. (c) Boyer, J. L.; Polyansky, D. E.; Szalda, D. J.; Zong, R.; Thummel, R. P.; Fujita, E. *Angew. Chem., Int. Ed.* **2011**, *50*, 12600. (d) Kimoto, A.; Yamauchi, K.; Yoshida, M.; Masaoka, S.; Sakai, K.

Chem. Commun. **2012**, *48*, 239. (e) Kärkäs, M. D.; Åkermark, T.; Johnston, E. V.; Karim, S. R.; Laine, T. M.; Lee, B.-L.; Åkermark, T.; Privalov, T.; Åkermark, B. *Angew. Chem., Int. Ed.* **2012**, *51*, 11589.

(12) (a) Mola, J.; Mas-Marza, E.; Sala, X.; Romero, I.; Rodríguez, M.; Viñas, C.; Parella, T.; Llobet, A. *Angew. Chem., Int. Ed.* **2008**, *47*, 5830. (b) Bozoglian, F.; Romain, S.; Ertem, M. Z.; Todorova, T. K.; Sens, C.; Mola, J.; Rodríguez, M.; Romero, I.; Benet-Buchholz, J.; Fontrodona, X.; Cramer, C. J.; Gagliardi, L.; Llobet, A. *J. Am. Chem. Soc.* **2009**, *131*, 15176.

(13) (a) Geletii, Y. V.; Botar, B.; Koegerler, P.; Hillesheim, D. A.; Musaev, D. G.; Hill, C. L. *Angew. Chem., Int. Ed.* **2008**, *47*, 3896. (b) Geletii, Y. V.; Besson, C.; Hou, Y.; Yin, Q. S.; Musaev, D. G.; Quiñonero, D.; Cao, R.; Hardcastle, K. I.; Proust, A.; Kögerler, P.; Hill, C. L. *J. Am. Chem. Soc.* **2009**, *131*, 17360. (c) Sartorel, A.; Carraro, M.; Scorrano, G.; De Zorzi, R.; Geremia, S.; McDaniel, N. D.; Bernhard, S.; Bonchio, M. *J. Am. Chem. Soc.* **2008**, *130*, 5006.

(14) (a) Duan, L.; Bozoglian, F.; Mandal, S.; Stewart, B.; Privalov, T.; Llobet, A.; Sun, L. *Nat. Chem.* **2012**, *4*, 418. (b) Jiang, Y.; Li, F.; Zhang, B.; Li, X.; Wang, X.; Huang, F.; Sun, L. *Angew. Chem., Int. Ed.* **2013**, *52*, 3398. (c) Duan, L. L.; Xu, Y. H.; Zhang, P.; Wang, M.; Sun, L. C. *Inorg. Chem.* **2010**, *49*, 209. (d) Wang, L.; Duan, L.; Stewart, B.; Pu, M.; Liu, J.; Privalov, T.; Sun, L. *J. Am. Chem. Soc.* **2012**, *134*, 18868. (e) Xu, Y.; Fischer, A.; Duan, L.; Tong, L.; Gabrielsson, E.; Åkermark, B.; Sun, L. *Angew. Chem., Int. Ed.* **2010**, *49*, 8934.

(15) (a) Kaveevivitchai, N.; Chitta, R.; Zong, R.; El Ojaimi, M.; Thummel, R. P. *J. Am. Chem. Soc.* **2012**, *134*, 10721. (b) Natali, M.; Orlandi, M.; Berardi, S.; Campagna, S.; Bonchio, M.; Sartorel, A.; Scandola, F. *Inorg. Chem.* **2012**, *51*, 7324.

(16) (a) Francàs, L.; Sala, X.; Escudero-Adan, E.; Benet-Buchholz, J.; Escriche, L.; Llobet, A. *Inorg. Chem.* **2011**, *50*, 2771. (b) Radaram, B.; Ivie, J. A.; Singh, W. M.; Grudzien, R. M.; Reibenspies, J. H.; Webster, C. E.; Zhao, X. *Inorg. Chem.* **2011**, *50*, 10564.

(17) (a) Morris, N. D.; Suzuki, M.; Mallouk, T. E. *J. Phys. Chem. A* **2004**, *108*, 9115. (b) Yagi, M.; Tomita, E.; Sakita, S.; Kuwabara, T.; Nagai, K. *J. Phys. Chem. B* **2005**, *109*, 21489. (c) Hoertz, P. G.; Kim, Y. I.; Youngblood, W. J.; Mallouk, T. E. *J. Phys. Chem. B* **2007**, *111*, 6845.

(18) (a) McDaniel, N. D.; Coughlin, F. J.; Tinker, L. L.; Bernhard, S. *J. Am. Chem. Soc.* **2008**, *130*, 210. (b) Blakemore, J. D.; Schley, N. D.; Balcells, D.; Hull, J. F.; Olack, G. W.; Incarvito, C. D.; Eisenstein, O.; Brudvig, G. W.; Crabtree, R. H. *J. Am. Chem. Soc.* **2010**, *132*, 16017. (c) Lalrempuia, R.; McDaniel, N. D.; Muller-Bunz, H.; Bernhard, S.; Albrecht, M. *Angew. Chem., Int. Ed.* **2010**, *49*, 9765.

(19) (a) Savini, A.; Bellachioma, G.; Ciancaleoni, G.; Zuccaccia, C.; Zuccaccia, D.; Macchioni, A. *Chem. Commun.* **2010**, *46*, 9218. (b) Savini, A.; Bellachioma, G.; Bolano, S.; Rocchigiani, L.; Zuccaccia, C.; Zuccaccia, D.; Macchioni, A. *ChemSuschem* **2012**, *5*, 1415. (c) Wang, C.; Wang, J.-L.; Lin, W. *J. Am. Chem. Soc.* **2012**, *134*, 19895.

(20) (a) Hong, D.; Murakami, M.; Yamada, Y.; Fukuzumi, S. *Energy Environ. Sci.* **2012**, *5*, 5708. (b) Hintermair, U.; Hashmi, S. M.; Elimelech, M.; Crabtree, R. H. *J. Am. Chem. Soc.* **2012**, *134*, 9785. (c) Zuccaccia, C.; Bellachioma, G.; Bolano, S.; Rocchigiani, L.; Savini, A.; Macchioni, A. *Eur. J. Inorg. Chem.* **2012**, 1462. (d) Grotjahn, D. B.; Brown, D. B.; Martin, J. K.; Marelius, D. C.; Abadjian, M.-C.; Tran, H. N.; Kalyuzhny, G.; Vecchio, K. S.; Specht, Z. G.; Cortes-Llamas, S. A.; Miranda-Soto, V.; van Niekerk, C.; Moore, C. E.; Rheingold, A. L. *J. Am. Chem. Soc.* **2011**, *133*, 19024.

(21) (a) Kanan, M. W.; Nocera, D. G. *Science* **2008**, *321*, 1072. (b) Stracke, J. J.; Finke, R. G. *J. Am. Chem. Soc.* **2011**, *133*, 14872. (c) Gerken, J. B.; McAlpin, J. G.; Chen, J. Y. C.; Rigsby, M. L.; Casey, W. H.; Britt, R. D.; Stahl, S. S. *J. Am. Chem. Soc.* **2011**, *133*, 14431. (d) McAlpin, J. G.; Surendranath, Y.; Dincă, M.; Stich, T. A.; Stoian, S. A.; Casey, W. H.; Nocera, D. G.; Britt, R. D. *J. Am. Chem. Soc.* **2010**, *132*, 6882.

(22) (a) Yin, Q. S.; Tan, J. M.; Besson, C.; Geletii, Y. V.; Musaev, D. G.; Kuznetsov, A. E.; Luo, Z.; Hardcastle, K. I.; Hill, C. L. *Science* **2010**, *328*, 342. (b) Natali, M.; Berardi, S.; Sartorel, A.; Bonchio, M.; Campagna, S.; Scandola, F. *Chem. Commun.* **2012**, *48*, 8808. (c) Huang, Z.; Luo, Z.; Geletii, Y. V.; Vickers, J. W.; Yin, Q.; Wu, D.; Hou, Y.; Ding, Y.; Song, J.; Musaev, D. G.; Hill, C. L.; Lian, T. *J. Am. Chem. Soc.* **2011**, *133*, 2068. (d) Tanaka, S.; Annaka, M.; Sakai, K. *Chem. Commun.* **2012**, *48*, 1653.

(23) (a) Jiao, F.; Frei, H. *Angew. Chem., Int. Ed.* **2009**, *48*, 1841. (b) Wee, T.-L.; Sherman, B. D.; Gust, D.; Moore, A. L.; Moore, T. A.; Liu, Y.; Scaiano, J. C. *J. Am. Chem. Soc.* **2011**, *133*, 16742.

(24) Hong, D.; Jung, J.; Park, J.; Yamada, Y.; Suenobu, T.; Lee, Y.-M.; Nam, W.; Fukuzumi, S. *Energy Environ. Sci.* **2012**, *5*, 7606.

(25) (a) Barnett, S. M.; Goldberg, K. I.; Mayer, J. M. *Nat. Chem.* **2012**, *4*, 498. (b) Zhang, M.-T.; Chen, Z.; Kang, P.; Meyer, T. J. *J. Am. Chem. Soc.* **2013**, *135*, 2048.

(26) (a) Yagi, M.; Narita, K. *J. Am. Chem. Soc.* **2004**, *126*, 8084. (b) Jiao, F.; Frei, H. *Chem. Commun.* **2010**, *46*, 2920. (c) Najafpour, M. M. *Chem. Commun.* **2011**, *47*, 11724.

(27) (a) Gao, Y.; Crabtree, R. H.; Brudvig, G. W. *Inorg. Chem.* **2012**, *51*, 4043. (b) Dismukes, G. C.; Brimblecombe, R.; Kolling, D. R. J.; Bond, A. M.; Swiegers, G. F.; Spiccia, L. *Inorg. Chem.* **2009**, *48*, 7269.

(28) Najafpour, M. M.; Moghaddam, A. N. *Dalton Trans.* **2012**, *41*, 10292.

(29) (a) Kim, T. V.; Elizarova, G. L.; Parmon, V. N. *React. Kinet. Catal. Lett.* **1984**, *26*, 57. (b) Hong, D.; Yamada, Y.; Nagatomi, T.; Takai, Y.; Fukuzumi, S. *J. Am. Chem. Soc.* **2012**,

134, 19572. (c) Ellis, W. C.; McDaniel, N. D.; Bernhard, S.; Collins, T. J. *J. Am. Chem. Soc.* **2010**, *132*, 10990. (d) Kundu, S.; Matito, E.; Walleck, S.; Pfaff, F. F.; Heims, F.; Rábay, B.; Luis, J. M.; Company, A.; Braun, B.; Glaser, T.; Ray, K. *Chem.–Eur. J.* **2012**, *18*, 2787. (e) Hoffert, W. A.; Mock, M. T.; Appel, A. M.; Yang, J. Y. *Eur. J. Inorg. Chem.* **2013**, in press. DOI: 10.1002/ejic.201201499. (f) Codolà, Z.; Garcia-Bosch, I.; Acuña-Parés, F.; Prat, I.; Luis, J. M.; Costas, M.; Lloret-Fillol, J. *Chem.–Eur. J.* **2013**, *19*, 8042.

(30) (a) Sun, C.-L.; Li, B.-J.; Shi, Z.-J. *Chem. Rev*. **2011**, *111*, 1293. (b) Chow, T. W.-S.; Chen, G.-Q.; Liu, Y.; Zhou, C.-Y.; Che, C.-M. *Pure Appl. Chem*. **2012**, *84*, 1685. (c) Talsi, E. P.; Bryliakov, K. P. *Coord. Chem. Rev*. **2012**, *256*, 1418. (d) Sun, X.; Li, J.; Huang, X.; Sun, C. *Curr. Inorg. Chem*. **2012**, *2*, 64.

(31) (a) Allpress, C. J.; Grubel, K.; Szajna-Fuller, E.; Arif, A. M.; Berreau, L. M. *J. Am. Chem. Soc*. **2013**, *135*, 659. (b) Bugg, T. D. H.; Ramaswamy, S. *Curr. Opin. Chem. Biol*. **2008**, *12*, 134. (c) Kim, Y. J.; Feng, X.; Lippard, S. J. *Inorg. Chem*. **2007**, *46*, 6099.

(32) Fillol, J. L.; Codolà, Z.; Garcia-Bosch, I.; Gómez, L.; Pla, J. J.; Costas, M. *Nat. Chem.* **2011**, *3*, 807.

(33) Chen, G.; Chen, L.; Ng, S.-M.; Man, W.-L.; Lau, T.-C. *Angew. Chem., Int. Ed.* **2013**, *52*, 1789.

(34) (a) Artero, V.; Fonteacave, M. *Chem. Soc. Rev.* **2013**, *42*, 2338. (b) Fukuzumi, S.; Hong, D. *Eur. J. Inorg. Chem.* in press. DOI: 10.1002/ejic.201300684.

(35) Hagen, K. S. *Inorg. Chem*. **2000**, *39*, 5867.

(36) (a) England, J.; Britovsek, G. J. P.; Rabadia, N.; White, A. J. P. *Inorg. Chem*. **2007**, *46*, 3752. (b) Hong, S.; Lee, Y.-M.; Cho, K.-B.; Sundaravel, K.; Cho, J.; Kim, M. J.; Shin, W.; Nam, W. *J. Am. Chem. Soc.* **2011**, *133*, 11876.

(37) Wadsworth, E.; Duke, F. R.; Goetz, C. A. *Anal. Chem.* **1957**, *29*, 1824.

(38) (a) Baalousha, M.; Manciulea, A.; Cumberland, S.; Kendall, K.; Lead, J. R. *Environ. Toxicol. Chem*. **2008**, *27*, 1875. (b) Mandel, K.; Szczerba, W.; Thünemann, A. F.; Riesemeier, H.; Girod, M.; Sextl, G. *J. Nanopart. Res*. **2012**, *14*, 1066.

(39) Lee, Y.-M.; Dhuri, S. N.; Sawant, S. C.; Cho, J.; Kubo, M.; Ogura, T.; Fukuzumi, S.; Nam, W. *Angew. Chem., Int. Ed.* **2009**, *48*, 1803.

(40) Yoon, J.; Wilson, S. A.; Jang, Y. K.; Seo, M. S.; Nehru, K.; Hedman, B.; Hodgson, K. O.; Bill, E.; Solomon, E. I.; Nam, W. *Angew. Chem., Int. Ed.* **2009**, *48*, 1257.

(41) Measurements of ESI-MS spectra required the presence of MeCN. $[Fe^{III}(BQEN)(^{16}OH)(OTf)]^+$ and $[Fe^{III}(BQEN)(^{18}OH)(OTf)]^+$ were detected by ESI-MS spectroscopy in the reaction of **1** (1.0 mM) with CAN (2.0 mM) in $H_2{}^{16}O$/MeCN (1:4 v/v) and $H_2{}^{18}O$/MeCN (1:4 v/v), respectively (Figure S5 in SI). The formation of $[Fe^{IV}(BQEN)(O)]^{2+}$ by CAN may be unstable under the ESI-MS measurements.

(42) Kaledin, A. L.; Huang, Z.; Geletii, Y. V.; Lian, T.; Hill, C. L.; Musaev, D. G. *J. Phys. Chem. A* **2010**, *114*, 73.

(43) (a) Yamada, Y.; Yano, K.; Xu, Q. A.; Fukuzumi, S. *J. Phys. Chem. C* **2010**, *114*, 16456. (b) Mcintyre, N. S.; Zetaruk, D. G. *Anal. Chem.* **1977**, *49*, 1521. (c) Mathew, T.; Shiju, N. R.; Sreekumar, K.; Rao, B. S.; Gopinath, C. S. *J. Catal.* **2002**, *210*, 405.

Supporting Information for Chapter 3

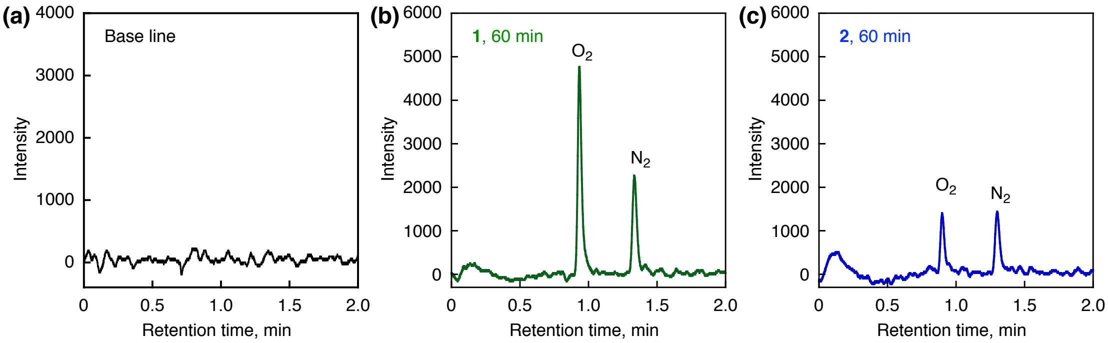

Figure S1. GC charts of (a) a base line and the gas evolved at 60 min in the catalytic water oxidation with (b) **1** (12.5 μM) and (c) **2** (12.5 μM) by CAN (125 mM) in a non-buffered aqueous solution (2.0 mL).

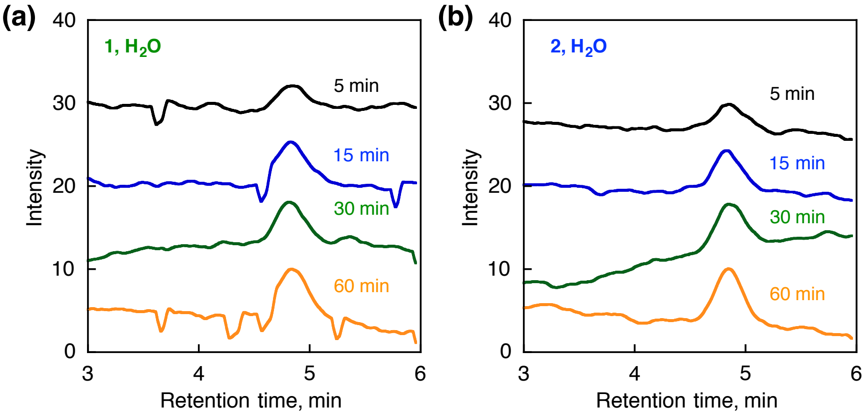

Figure S2. GC charts of CO_2 evolution in the catalytic water oxidation with (a) **1** (12.5 μM) and (b) **2** (12.5 μM) by CAN (125 mM) in a non-buffered aqueous solution (2.0 mL).

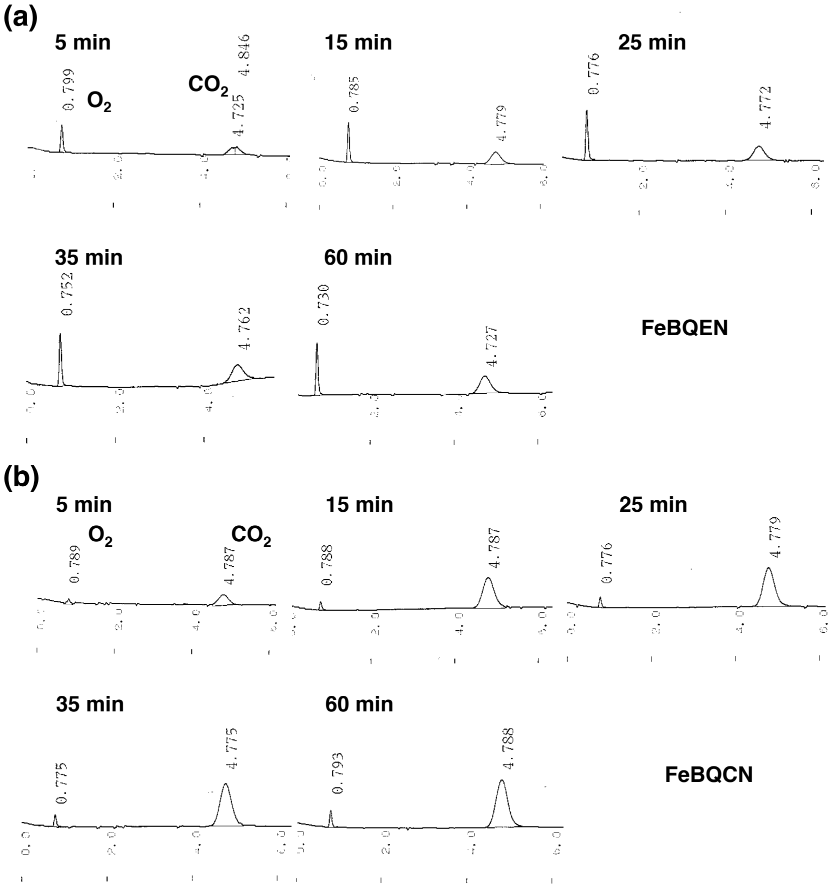

Figure S3. GC charts of CO_2 evolution observed with (a) **1** (1.0 mM) and (b) **2** (1.0 mM) in the catalytic reactions by CAN (0.10 M) in a non-buffered aqueous solution (2.0 mL).

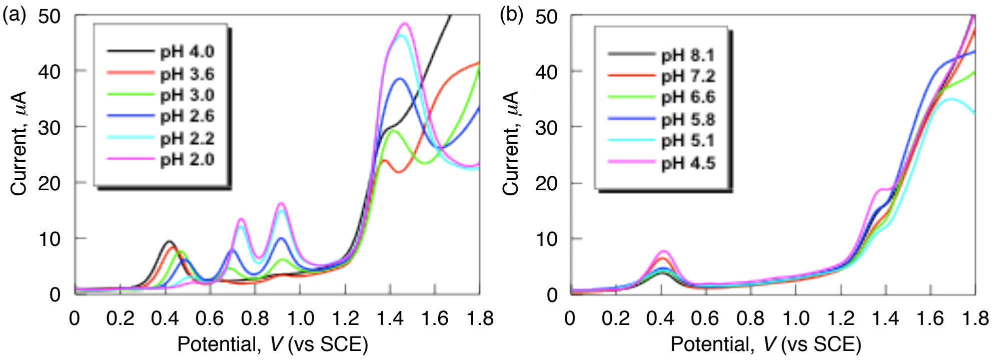

Figure S4. Differential pulse voltammetry (DPV) of an aqueous solution containing **1** (0.50 mM) and $NaNO_3$ (0.10 M) in different pH ranges: (a) from 2.0 to 4.0 and (b) from 4.5 to 8.1 (conditions: amplitude = 50 mV; pulse period = 0.2 s).

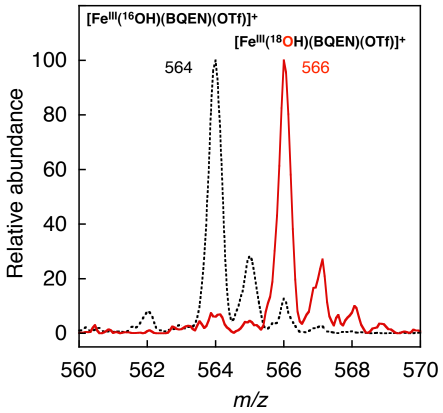

Figure S5. ESI-MS spectra of the solutions obtained in the reaction of **1** (1.0 mM) with CAN (2.0 mM) in $H_2{}^{16}O$/MeCN [1:4 (v/v), black dots] and $H_2{}^{18}O$/MeCN [1:4 (v/v), red line]. The peaks at m/z 564.0 and 566.0 correspond to $[Fe^{III}(BQEN)(^{16}OH)(OTf)]^+$ and $[Fe^{III}(BQEN)(^{18}OH)(OTf)]^+$ (calcd *m/z* = 564.1 and 566.1, respectively).

Chapter 4

Catalytic Mechanism of Water Oxidation with Single-Site Ruthenium-Heteropolytungstate Complexes

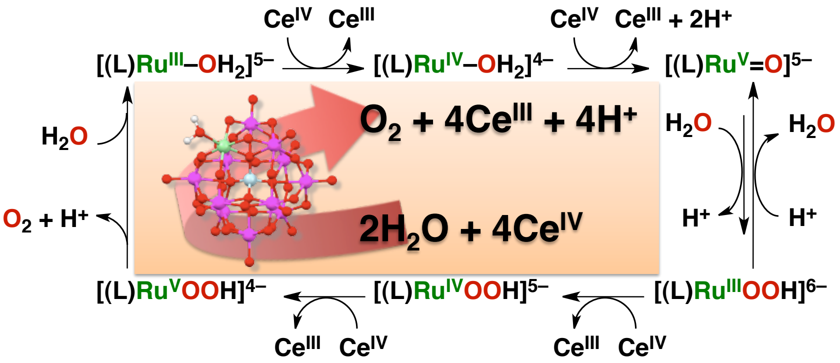

Abstract: Catalytic water oxidation to generate oxygen was achieved using all-inorganic mononuclear ruthenium complexes bearing Keggin-type lacunary heteropolytungstate, $[Ru^{III}(H_2O)SiW_{11}O_{39}]^{5-}$ (**1**) and $[Ru^{III}(H_2O)GeW_{11}O_{39}]^{5-}$ (**2**) as catalysts with $(NH_4)_2[Ce^{IV}(NO_3)_6]$ (CAN) as a one-electron oxidant in water. The oxygen atoms of evolved oxygen come from water as confirmed by isotope-labeled experiments. Cyclic voltammetric measurements of **1** and **2** at various pHs indicate that both complexes **1** and **2** exhibit three one-electron redox couples based on ruthenium center. The Pourbaix diagrams (plots of $E_{1/2}$ vs pH) support that the Ru(III) complexes are oxidized to the Ru(V)-oxo complexes with CAN. The Ru(V)-oxo complex derived from **1** was detected by UV-visible absorption, EPR, and resonance Raman measurements in situ as an active species during the water oxidation reaction. This indicates that the Ru(V)-oxo complex is involved in the rate-determining step of the catalytic cycle of water oxidation. The overall catalytic mechanism of water oxidation was revealed based on the kinetic analysis and detection of the catalytic intermediates. The complex **2** exhibited the higher catalytic activity for the water oxidation with CAN than complex **1**.

Introduction

Effective and sustained catalysts for water oxidation are absolutely imperative to achieve the conversion of sunlight into clean and accumulable chemical energy by artificial photosynthesis as typified by sunlight-driven water splitting into hydrogen and oxygen (eqs 1, 2).[1] Thus, extensive efforts have so far been devoted to the development of water oxidation catalysts (WOCs) over the past three decades.[2–4]

$$2H_2O \rightarrow O_2 + 4H^+ + 4e^- \quad (1)$$

$$4H^+ + 4e^- \rightarrow H_2 \quad (2)$$

WOCs can be classified into heterogeneous[2] and homogeneous[3–4] types. Heterogeneous WOCs are generally robust and easy to fabricate, providing potential applications. However, the difficulty to identify the catalytically active species of heterogeneous catalysts has precluded to clarify the catalytic mechanism of water oxidation.[2,5] In contrast to heterogeneous catalysts, homogeneous catalysts provide the better opportunity to study the catalytic mechanism of water oxidation, which has yet to be clarified though.

The first homogeneous WOC reported by Meyer et al.[6–8] is *cis*,*cis*-$[(bpy)_2(H_2O)Ru^{III}ORu^{III}(H_2O)(bpy)_2]^{4+}$ (bpy = 2,2'-bipyridine), so-called "blue dimer". To date, several bimetallic Ru[9–19] and Mn[20,21] WOCs have been documented, and the multinuclear structure similar to that in the oxygen evolving complex (OEC) in Photosystem II[22] was regarded to be essential for mediating four-electron process of water oxidation. However, a number of mononuclear Ru[23–34] and Ir[35,36] complexes have also been reported as efficient WOCs. Although the catalytic mechanisms of multinuclear WOCs as the functional model of OEC have attracted considerable attention, there are a few detailed mechanistic studies on binuclear Ru complexes due presumably to the complexity of multinuclear catalysis.[7,11,16,37] Mononuclear WOCs may be more suitable to elucidate the catalytic mechanism of water oxidation because of their simple structure. However, all the single-site Ru complexes reported so far contain organic ligands,[23–34] and oxidation of the organic ligands under the water oxidation conditions would make it difficult to obtain mechanistic insight into the catalytic water oxidation. In order to avoid the oxidative damage of WOCs, the adoption of inorganic ligands, which is stable under water oxidation conditions, is suitable as demonstrated by a tetraruthenium complex with silicodecatungstate $[\{Ru_4O_4(OH)_2(H_2O)_4\}(\gamma\text{-}SiW_{10}O_{36})_2]^{10-}$, which acts a robust water oxidation catalyst with one-electron oxidants such as diammonium cerium (IV) nitrate,

$(NH_4)_2[Ce^{IV}(NO_3)_6]$ (CAN) and $[Ru(bpy)_3]^{3+}$ (bpy = 2,2'-bipyridine).[38–41] A tetracobalt complex with phosphononatungstate $[Co_4(H_2O)_2(PW_9O_{34})_2]^{10-}$ was also reported to be capable of oxidizing water with $[Ru^{III}(bpy)_3]^{3+}$.[42,43] However, the catalytic mechanism of water oxidation with those all-inorganic tetranuclear complexes has yet to be clarified, and there has so far been no report on all-inorganic single-site WOCs.

In Chapter 4, I report that single-site ruthenium complexes with heteroundecatungstate, $[Ru^{III}(H_2O)SiW_{11}O_{39}]^{5-}$ (**1**)[44] and $[Ru^{III}(H_2O)GeW_{11}O_{39}]^{5-}$ (**2**) (Chart 1) act as robust water oxidation catalysts with CAN. The catalytic mechanism of water oxidation with **1** and **2** was revealed by electrochemical and spectroscopic measurements as well as by the kinetic analysis. The comparison of the catalytic activity between **1** and **2** for water oxidation with CAN provides a valuable insight into the further improvement of the catalytic activity for water oxidation.

Chart 1. Structure of Polyanions 1 and 2[44] (Ru: Light Green; W: Purple; O: Red; H: White; Si: Light Blue; Ge: Deep Blue)

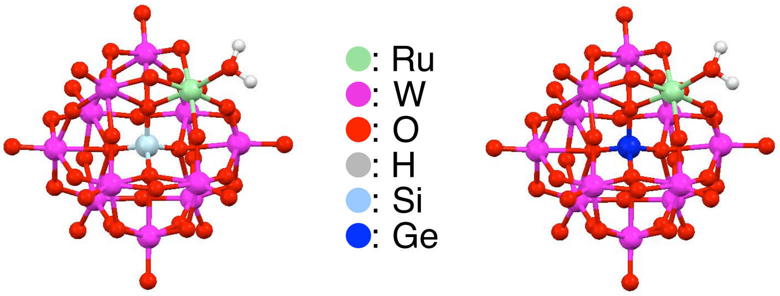

$[Ru^{III}(H_2O)SiW_{11}O_{39}]^{5-}$ (1) **$[Ru^{III}(H_2O)GeW_{11}O_{39}]^{5-}$ (2)**

Experimental Section

Materials. $Cs_5[Ru^{III}(H_2O)SiW_{11}O_{39}]$ (Cs_5•**1**) and $Cs_5[Ru^{III}(H_2O)GeW_{11}O_{39}]$ (Cs_5•**2**) were prepared according to the literature procedures and characterized by IR, UV-visible spectroscopic and electrochemical measurements.[44] Commercially available reagents: sodium sulfate (Na_2SO_4), phosphoric acid (H_3PO_4), boric acid (H_3BO_4), acetic acid (CH_3COOH), nitric acid (HNO_3), diluted nitric acid (1.0 M and 0.1 M HNO_3), diammonium cerium (IV) nitrate ($(NH_4)_2[Ce^{IV}(NO_3)_6]$, CAN), diammonium cerium (III) nitrate ($(NH_4)_2[Ce^{III}(NO_3)_5]$) (Wako Pure Chemical Industries.), D_2O (99.9% D), $H_2{}^{18}O$ (97% ^{18}O) (Cambridge Isotope Laboratories) were used without further purification.

General Methods. Purification of water (18.2 MΩ cm) was performed with a Milli-Q system (Millipore, Direct-Q 3 UV). UV-visible absorption spectra were recorded using a Hewlett Packard 8453 diode array spectrophotometer with a quartz cuvette (the light path length = 1 cm). The pH values of a solution were determined by a pH meter (TOA, HM-20J) equipped with a pH combination electrode (TOA, GST-5725C). The pH meter was calibrated relative to standard phthalate (pH 4.0) and phosphate (pH 6.9) buffer solutions prior to each use.

TGA Analysis. The number of crystal water in **1** and **2** were determined to be 6 and 8, respectively, based on the results of TGA analysis recorded on an SII TG/DTA 7200 instrument. The samples (~5 mg) were heated from 25 to 300 °C with a ramp rate of 2 °C min^{-1}. The number of crystal water contained in the sample was evaluated from the weight loss by heating the sample.

Catalytic Oxygen Evolution. The yield of oxygen was determined with a Shimadzu GC-17A gas chromatograph {Ar carrier, a capillary column with molecular sieves (Agilent Technologies, 19095P-MS0, 30 m × 0.53 mm) at 313 K} equipped with a thermal conductivity detector. An aliquot (100 μL) of a deaerated 0.1 M HNO_3 aqueous solution containing **1** (6.0×10^{-7} mol) was injected into a deaerated 0.1 M HNO_3 aqueous solution (2 mL) containing CAN (1.2×10^{-5} mol) in the reaction vessel (4.9 mL) with a magnetic stirrer. At every 10 minutes, 100 μL of gas in headspace of the reaction vessel was taken using a gas-tight syringe and analyzed by GC. The total amount of evolved oxygen was determined based on the calibration curve prepared for various concentrations of oxygen in argon gas.

Isotope-Labeled Experiment. The ratio of $^{16}O_2$, $^{16}O^{18}O$, and $^{18}O_2$ was determined based on the intensity of mass spectrum (m/z = 32, 34, and 36) obtained on a Shimadzu GC-17A gas chromatograph {He carrier, TC-FFAP column (GL Science, 1010-15242) at 313 K} equipped with a mass spectrometer (Shimadzu, QP-5000). An aliquot (100 μL) of a deaerated $H_2{}^{18}O$ solution (83.8% ^{18}O) containing **1** (3.0×10^{-7} mol) and HNO_3 (0.1 M) was injected to into 1 mL of a deaerated $H_2{}^{18}O$ solution (83.8% ^{18}O) containing CAN (6.0×10^{-6} mol) and HNO_3 (0.1 M) in the reaction vessel (2 mL). The air in the headspace of sealed reaction vessel was replaced by He before the reaction by bubbling He gas through syringe. After 1 hour, 50 μL of gas in headspace of the reaction vessel was taken using a gas-tight syringe and analyzed by GC-MS.

Determination of pK_a Values. The spectroscopic titrations were performed to determine the pK_a values of **1** and **2** in a 0.1 M Britton-Robinson buffer ([CH_3COOH] = 0.1 M, [H_3PO_4] = 0.1 M, [H_3BO_4] = 0.1 M) at 298 K. A small amount of 0.36–3.6 M NaOH aqueous solutions was added to a 0.1 M Britton-Robinson buffer solution containing **1** (5.0×10^{-4} M) or **2** (5.0×10^{-4} M). The absorption spectra of **1** and **2** were changed with an increase in pH and the plot of absorbance at particular wavelengths (λ = 440 nm for **1**, λ = 430 nm for **2**) vs pH was fitted by eq 3, where A_0 is the absorbance

$$A = A_0 + K_a(A_\infty - A_0)/(K_a + 10^{-pH}) \qquad (3)$$

of the aqua complex, and A_∞ is the absorbance of the hydroxo complex. The pK_a value was determined from the fitting curve as the pH value when the absorbance was the average value of A_0 and A_∞. Derivation of eq 3 is described in Supporting Information.

Spectral Titration. The UV-visible spectroscopic titration was performed with a spectrophotometer. UV-visible spectra were taken after every addition of a 0.1 M HNO_3 aqueous solution (20 μL) containing CAN (6.0×10^{-3} M) to a 0.1 M HNO_3 aqueous solution (2 mL) containing 1 (3.0×10^{-4} M). The absorbances at λ = 380 and 550 nm were plotted against the ratio of [CAN] to [**1**].

Electrochemical Measurements. Cyclic voltammetry (CV) was performed on an ALS 630B electrochemical analyzer using a glassy carbon electrode as a working electrode, a saturated calomel electrode (SCE) as a reference electrode, and Pt wire as an auxiliary electrode. Cyclic voltammograms and differential pulse voltammograms of **1** (2.0×10^{-3} M) and **2** (2.0×10^{-3} M) were obtained in 0.1 M Britton-Robinson buffer solutions in the range of $1.5 < pH < 8.0$ and in 0.1 M Na_2SO_4 aqueous solutions in the range of $0 < pH < 1.5$. The pH of a solution was changed by using 0.36~3.6 M NaOH aqueous solutions and HNO_3 (69 %).

Electron Paramagnetic Resonance (EPR) Measurements. The EPR cell (3.0 mm i.d.) containing a deaerated 0.1 M HNO_3 aqueous solution (0.5 mL) of **1** (1.0×10^{-3} M) or **2** (1.0×10^{-3} M) was maintained at 77 K in a liquid-nitrogen dewar. The remaining gas in headspace of the EPR cell was removed under vacuum, then the EPR cell was cooled to 4 K with use of liquid helium in the EPR cavity and EPR spectrum was taken on a JEOL JEX-REIXE spectrometer under nonsaturating microwave power conditions. The magnitude of the modulation was chosen to optimize the resolution and the signal-to-noise (*S*/*N*) ratio of the observed spectra. The *g* values were calibrated using Mn^{2+} marker. The EPR spectrum of oxidized **1** was obtained as follows. A deaerated 0.1 M HNO_3 aqueous solution (0.5 mL) of **1** (1.0×10^{-3} M) and a deaerated 0.1 M HNO_3 aqueous solution (10 μL) of CAN were mixed in an EPR cell. After a few seconds, the EPR cell was cooled to 77 K in a liquid-nitrogen Dewar and the remaining gas in headspace of the EPR cell was removed under vacuum. The EPR spectrum of the mixture was measured after cooling the EPR cell down at 4 K or 77 K. The EPR spectrum of oxidized **2** was measured in the same manner as **1**.

Resonance Raman (rR) Measurements. rR spectra were measured using a λ =

442 nm line of a HeCd laser (Kinmon, IK4401R-D). The laser power at the sample point was 10 mW. The sample solution was in an NMR tube and spun with a spinning cell device designed to minimize off-center deviation during rotation. Raman scattered light was collected at 135° with a pair of fused quartz lenses, *f*-matched to a 1.0 m spectrograph (Ritsu Oyo Kogaku, MC-1000DG) which was equipped with a holographic grating (2400 grooves mm^{-1}) and a liquid nitrogen-cooled CCD detector. A depolarizer was used to scramble the polarization of collected light and thus eliminate intensity artifacts created by polarization-dependent grating reflectivity. The spectra were calibrated using the standard Raman spectra of acetone and indene. An aliquot (10 μL) of an $H_2{}^{16}O$ or $H_2{}^{18}O$ solution of CAN (1.5×10^{-6} mol) was added to a 500 μL $H_2{}^{16}O$ or $H_2{}^{18}O$ solution of **1** (5.0×10^{-7} mol) and **2** (5.0×10^{-7} mol). Formation of a precipitate was observed immediately after mixing two solutions of **1** (or **2**) and CAN. The precipitate was removed with a membrane filter and the filtrate was transferred to a quartz NMR tube, then the NMR tube was supplied for rR measurement.

Kinetic Measurements. All kinetic experiments were performed using a spectrophotometer with 1 cm cell at 298 K. The absorbance at $\lambda = 420$ nm assignable to CAN was monitored during water-oxidation reaction under various conditions. Each of initial reaction rate was obtained on the basis of the decay rate of absorbance at $\lambda = 420$ nm.

Results and Discussion

Catalytic Water Oxidation. The catalytic water oxidation was investigated by an addition of 20 equiv of Ce^{IV} to aqueous solution containing **1** (3.0×10^{-4} M) and 0.1 M HNO_3, and the evolution of oxygen was confirmed by gas-chromatographic analysis (see Experimental Section and Figure 1). The loss of Ce^{IV} was monitored by photodiode array UV-visible spectrophotometer ($\lambda = 400$ nm) and the amount of evolved O_2 was determined by gas chromatography. The result of a typical experiment is shown as the time profiles of the decay of Ce^{IV} and the evolution of O_2 in Figure 2a. The decrease in the concentration of CAN in the solution virtually coincides with the O_2 evolution (Figure 2b), and 2.7 μmol of oxygen was finally produced from 12 μmol of CAN. The efficiency of oxygen evolution is approximately 90 % based on the initial amount of oxidant, indicating that nearly stoichiometric water oxidation by Ce^{IV} occurred with **1**, i.e., 4 equivalents of Ce^{IV} is consumed for 1 equivalent of O_2 evolution based on eq 1.TONs of oxygen evolution catalyzed by **1** and **2** reaches up to 20 and 50, respectively.

The oxygen evolution was not observed upon additions of $RuCl_3{\bullet}3H_2O$, $Ru(acac)_3$,

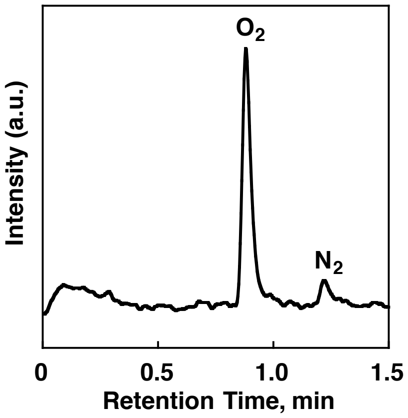

Figure 1. GC chart of the gas in the headspace of sealed reaction vessel (4.9 mL) taken at 50 min after mixing **1** (3.0×10^{-4} M) and CAN (6.0×10^{-3} M) in an aqueous solution containing 0.10 M HNO_3 at 298 K.

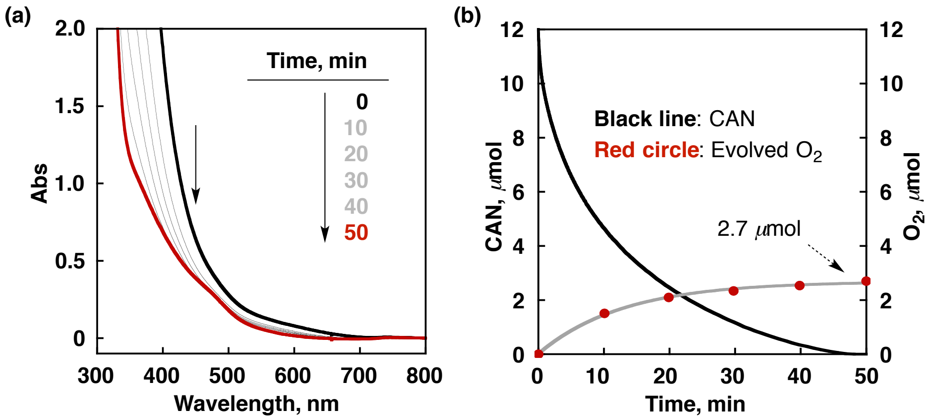

Figure 2. (a) UV-vis spectral changes in the course of the reaction of **1** (3.0×10^{-4} M) with CAN (6.0×10^{-3} M) in 0.1 M HNO_3 at 298 K. (b) Time course of the amount of evolved oxygen (red circle) and CAN (black line) in the reaction of **1** (3.0×10^{-4} M) with CAN (6.0×10^{-3} M) in 0.1 M HNO_3 at 298 K.

and $K_8[SiW_{11}O_{39}]$ instead of **1** to an aqueous solution containing CAN and 0.1 M HNO_3. The addition of **2** to the same aqueous solution led to more efficient oxygen evolution as compared with **1**. Thus, it should be noted that only **1** and **2** were able to act as a water oxidation catalyst with CAN, and the ruthenium sources and the ruthenium-free ligand of **1** had no effect on the catalysis.

I conducted GC-MS analysis of oxygen evolved during water oxidation using $H_2{}^{18}O$ to clarify the oxygen source of evolved oxygen. The evolved oxygen in the oxidation of water with CAN in $H_2{}^{18}O$-enriched aqueous solution (83.8% ^{18}O) containing **1** and 0.1 M HNO_3 was analyzed by GC–MS (Figure 3). In the mass spectrum, the molecular ion peak at $m/z = 36$ assignable to $^{18}O_2$ exhibited the largest intensity among the molecular ion peaks at $m/z = 32$, 34, and 36 (Table 1). The relative abundance of oxygen isotopes, which were determined from the intensities of those three molecular ion peaks, is listed in Table 2. The theoretical ratio of oxygen isotopes in Table 2 was calculated by assuming that both oxygen atoms of oxygen come only from water. The observed ratios agree well with the calculated ratios, indicating that evolved oxygen comes exclusively from water.

Redox Properties of 1 and 2. In order to get insight into the catalytically active species for water oxidation with CAN, I have examined the comprehensive redox and acid-base properties of **1** and **2** by electrochemical and pK_a measurements. The

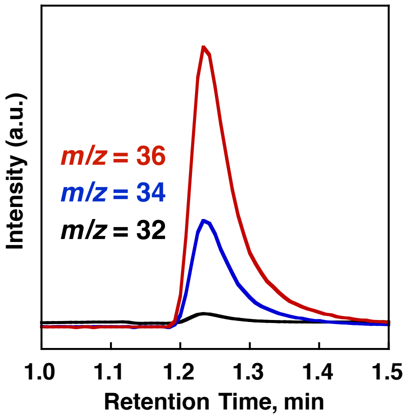

Figure 3. GC-MS charts of the gas in the headspace of sealed reaction vessel taken at 60 min after mixing **1** (3.0×10^{-4} M) and CAN (6.0×10^{-3} M) in an aqueous solution containing 0.10 M HNO_3 (85% $H_2{}^{18}O$) at 298 K.

Table 1. Intensity of Molecular Ion Peaks at *m*/*z* = 32, 34, and 36 and Relative Abundance of Oxygen Isotopes

m/*z*	intensity	relative abundance, %
32	6469	3.4
34	49864	26.7
36	130771	69.9

Table 2. Observed and Theoretical Relative Abundances of ^{18}O-Labeled and Unlabeled Oxygen Evolved during the Oxidation of $H_2{}^{18}O$-Enriched Water (83.8% $H_2{}^{18}O$) Catalyzed by 1 (3.0×10^{-4} M) with CAN (6.0×10^{-3} M) in 0.1 M HNO_3 at 298 K

	relative abundance, %		
	$^{16}O_2$	$^{16}O^{18}O$	$^{18}O_2$
observed	3.4	26.7	69.9
theoretical[a]	2.6	27.2	70.2

[a] Theoretical values were calculated by assuming that evolved oxygen comes only from water.

electrochemical behavior and the pK_a values of **1** and **2** were studied in a broad pH range. The aqua complexes **1** and **2** are converted to the corresponding hydroxo complexes, i.e., (L)Ru^{III}-OH (L = $[SiW_{11}O_{39}]^{8-}$ for **1** or $[GeW_{11}O_{39}]^{8-}$ for **2**) by increasing pH as shown in Figure 2. The pK_a values of the aqua complexes of **1** and **2** are determined by fitting eq 3 (Experimental Section) to the data of UV-visible spectroscopic titration in Figure 4 to be 6.4 and 6.2, respectively.

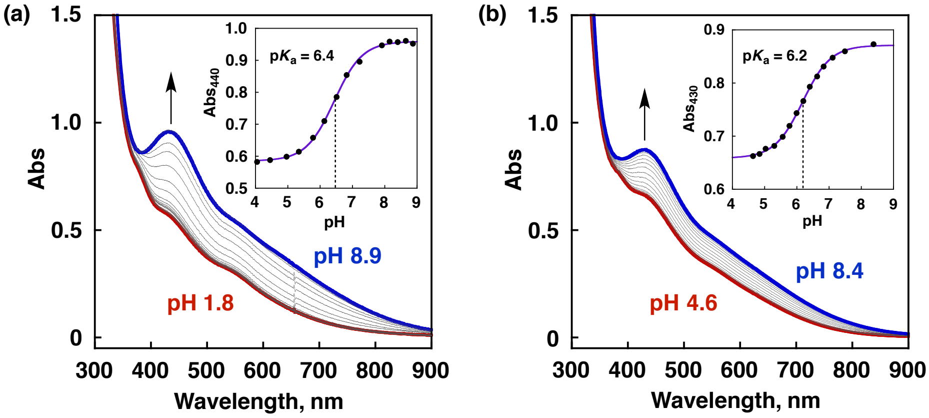

Figure 4. Absorption spectral changes in the course of titration of (a) **1** (5.0×10^{-4} M) and (b) **2** (5.0×10^{-4} M) with NaOH aqueous solution in 0.1 M Britton-Robinson buffer at 298 K. Inset: Plot of the absorbance at $\lambda = 440$ nm for **1** and $\lambda = 430$ nm for **2**) vs pH.

Cyclic voltammograms of **1** and **2** depending on pH were measured in the range of $0 < pH < 8$ (Figure 5).[45] Both **1** and **2** undergo three one-electron oxidation processes, each of which exhibited ca 90 mV of a peak separation at a sweep rate of 0.1 V s^{-1}, indicating that three one-electron redox couples are chemically reversible. The first one-electron reduction process starting from the Ru(III) complexes is ascribed to the Ru(III)/Ru(II) redox couple, whereas the first and second one-electron oxidation processes are ascribed to the Ru(IV)/Ru(III) and Ru(V)/Ru(IV) redox couples, respectively. The three one-electron redox potentials are shifted to a positive direction with decreasing pH (Figure 5).[46]

Figure 6 illustrates the Pourbaix diagrams ($E_{1/2}$ vs pH)[47] for **1** and **2** in the range of $0 < pH < 8$ in water. When $E_{1/2}$ is independent of pH, no proton is coupled in the one-electron redox process.[44a,48] On the other hand, when $E_{1/2}$ decreases with increasing pH with a slope of 59 and 118 mV, one and two protons are coupled with the one-electron redox process, respectively.[47] Thus, all the species depending on the $E_{1/2}$ and pH values can be identified as shown in Figure 4. For example, the (L)Ru^{III}-OH_2 (L = $[SiW_{11}O_{39}]^{8-}$ for **1** or $[GeW_{11}O_{39}]^{8-}$ for **2**) complex is oxidized to the (L)Ru^{IV}-OH_2 complex at pH 1 at an applied potential between 0.62 and 0.90 V (vs SCE) without

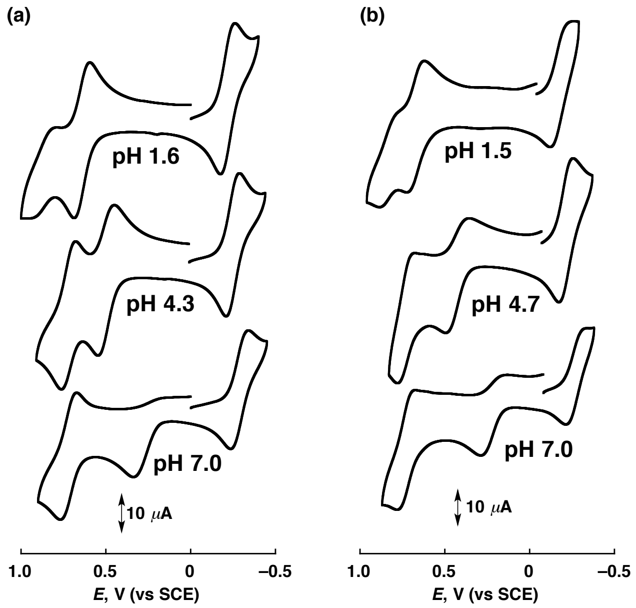

Figure 5. Cyclic voltammograms of (a) $[Ru^{III}SiW_{11}O_{39}]^{5-}$ (**1**, 2.0 × 10^{-3} M), and (b) $[Ru^{III}GeW_{11}O_{39}]^{5-}$ (**2**, 2.0 × 10^{-3} M) depending on pH with a scan rate of 0.1 V s^{-1} in 0.1 M Britton-Robinson buffer at 298 K. The pH of the solution was adjusted by NaOH aqueous solution.

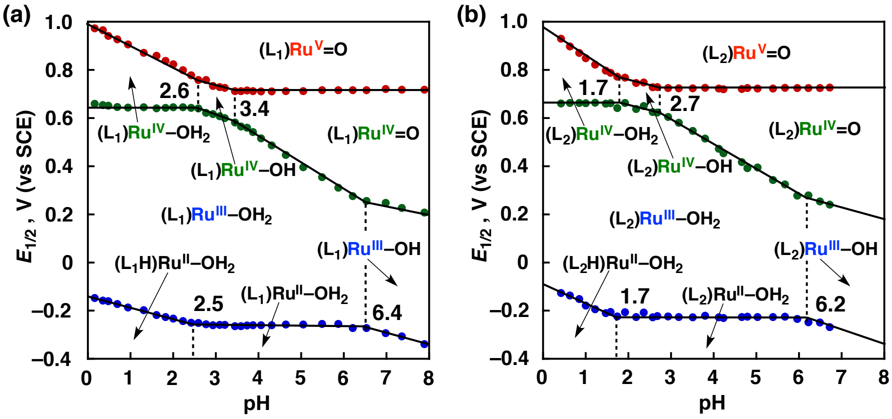

Figure 6. Pourbaix diagrams for (a) **1** and (b) **2**. The blue, green, and red points correspond to the Ru(III)/Ru(II), Ru(IV)/Ru(III), and Ru(V)/Ru(IV) redox potentials, respectively. All the four pK_a values are shown by the vertical dashed lines. L1 and L2 denote the ligand of **1** and **2**, respectively.

losing proton when the $E_{1/2}$ value remains constant with the change in pH around 1. In contrast, the $(L)Ru^{IV}$-OH_2 complex is oxidized to the $(L)Ru^V{=}O$ complex at pH 1 at an applied potential above 0.90 V with removal of two protons, when the $E_{1/2}$ value decreases with increasing pH from 1 with a slope of 118 mV. Thus, **1** and **2** are expected to be oxidized by CAN ($E_{1/2}$ = 1.21 V vs SCE at pH 1.0,[34b] and $E_{1/2}$ = 1.61 V vs NHE (= 1.34 V vs SCE) at lower pH with 0.5–5 M HNO_3)[34c] to the $(L)Ru^V{=}O$ complexes of **1** and **2**, respectively. The complexes **1** and **2** are not stable at pH higher than 8.

All the four pK_a values of **2** (6.2 for $[Ru^{III}(H_2O)GeW_{11}O_{39}]^{5-}$, 1.7 for $[Ru^{II}(H_2O)HGeW_{11}O_{39}]^{5-}$, 2.7 for $[Ru^{IV}(H_2O)GeW_{11}O_{39}]^{4-}$, and 1.7 for $[Ru^{IV}(OH)GeW_{11}O_{39}]^{5-}$) are smaller than the corresponding values of **1** (6.4 for $[Ru^{III}(H_2O)SiW_{11}O_{39}]^{5-}$, 2.5 for $[Ru^{II}(H_2O)HSiW_{11}O_{39}]^{5-}$, 3.4 for $[Ru^{IV}(H_2O)SiW_{11}O_{39}]^{4-}$, and 2.6 for $[Ru^{IV}(OH)SiW_{11}O_{39}]^{5-}$). This indicates that the ruthenium site and the ligand of **2** are more difficult to be protonated due to the electron-withdrawing effect of germanium, core-atom of the ligand, because of the larger electronegativity of germanium (2.01) than silicon (1.90).[49] The more electronegative Ge than Si withdraws electron at higher degree from the framework of polytungstate anion, which causes the lower basicity of the heteropolytungstate anion. The weaker coordination of the heteropolytungstate anion resulted in the higher acidity of the Ru metal center, which induces the higher acidity of the coordinated aqua ligand with lower pK_a.

Spectroscopic Redox Titrations. The UV-visible spectral titration of **1** with CAN in an acidic medium showed that the oxidation of **1** led to the formation of corresponding Ru(IV) and Ru(V) complexes as shown in Figure 7. The formation of respective Ru(IV) and Ru(V) species were observed with the isosbestic points ($\lambda = 500$ nm for first one-electron oxidation, $\lambda = 358$, 500 nm for second one-electron oxidation) by adding stoichiometric equivalents of CAN to aqueous solution containing **1** (3.0×10^{-4} M) and 0.1 M HNO_3. According to the Pourbaix diagram for **1** in Figure 6a, the respective Ru(IV) and Ru(V) species in the range of $0 < pH < 2.6$ can be assigned to $[Ru^{IV}(H_2O)SiW_{11}O_{39}]^{4-}$ and $[Ru^{V}(O)SiW_{11}O_{39}]^{5-}$. The first and second electron-transfer processes between **1** and CAN are thermodynamically favorable due to the high reduction potential of Ce(IV)/Ce(III), which is 1.61 V vs NHE (1.34 V vs SCE).[34c]

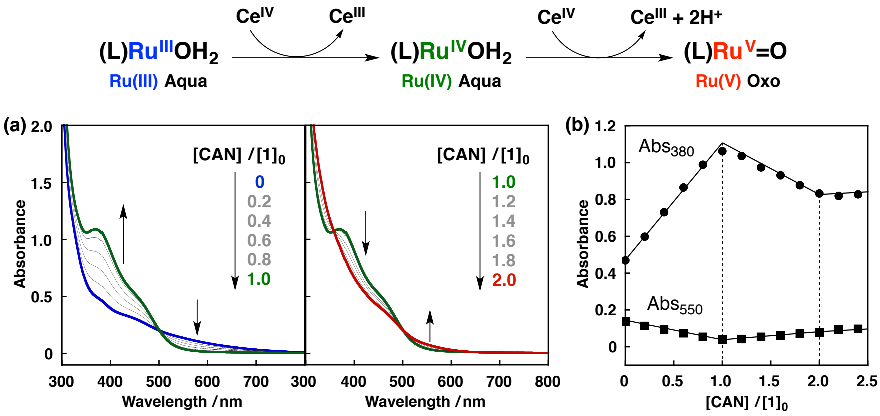

Figure 7. (a) UV–visible spectral changes of **1** upon addition of CAN in 0.1 M HNO_3 at 298 K. The initial concentration of **1**, $[\mathbf{1}]_0$ was 3.0×10^{-4} M. Each spectrum was monitored after every addition of 0.2 equivalent of CAN. (b) Plots of the absorbance at $\lambda = 380$ (circles) and 550 nm (squares) relative to the ratio of [CAN] to $[\mathbf{1}]_0$.

Because the oxidation potentials of $[\mathrm{Ru^{III}(H_2O)SiW_{11}O_{39}}]^{5-}$ and $[\mathrm{Ru^{IV}(H_2O)SiW_{11}O_{39}}]^{4-}$ at pH 1.0 were determined to be 0.64 and 0.91 V, respectively, the reduction potential of CAN is high enough to oxidize these complexes under the catalytic conditions. The driving forces of the first and second electron-transfer processes are estimated to be 0.57 and 0.30 eV, respectively. Thus, the first and second electron-transfer oxidation processes are expected to proceed at the diffusion-limited rate. Actually, the rates of electron-transfer oxidation of **1** and **2** with CAN were too fast to be determined even by using a stopped-flow method. This indicates that the electron-transfer rate constant is larger than 10^6 $\mathrm{M^{-1}\ s^{-1}}$.[50]

In cryogenic EPR measurements at 4 K, **1** exhibited a two-axis anisotropic signal with $g_\perp = 2.4$ and $g_{//} = 2.0$ (Figure 8a). The spin state of **1** can be assigned to $S = 1/2$ and the oxidation number of ruthenium in **1** is III judging from the $g_\perp$ value higher than 2.3.[51] The addition of 2 equivalents of CAN to the solution of **1** resulted in a sharp two-axis anisotropic signal at $g_\perp = 2.1$ and $g_{//} = 1.9$ (Figure 8b) at 77 K. This indicates that the spin state of **1** under catalytic conditions is also $S = 1/2$. The anisotropic EPR signal at $g_\perp = 2.1$ and $g_{//} = 1.9$~2.0 is not characteristic of the $\mathrm{Ru^{III}}$ species but the $\mathrm{Ru^V{=}O}$ species as reported in the literature.[51,52] On the other hand, the EPR signal due to $\mathrm{Ce^{III}}$ ion observable at 4 K (Figure 9) was not observed at 77 K due to the strong spin–orbit coupling and the short relaxation time of the $4f^1$ state above 30 K.[53] Thus, these EPR results together with rR spectral data (*vide infra*) rationalize the steady state formation of $[\mathrm{(L)Ru^V{=}O}]^{5-}$ of **1** in the catalytic cycle. In the case of **2**, the EPR spectra of **2** and its oxidized species showed similar tendency as those of complex **1** (Figure 10).

The characterization of the catalytically active species derived from **1** for water

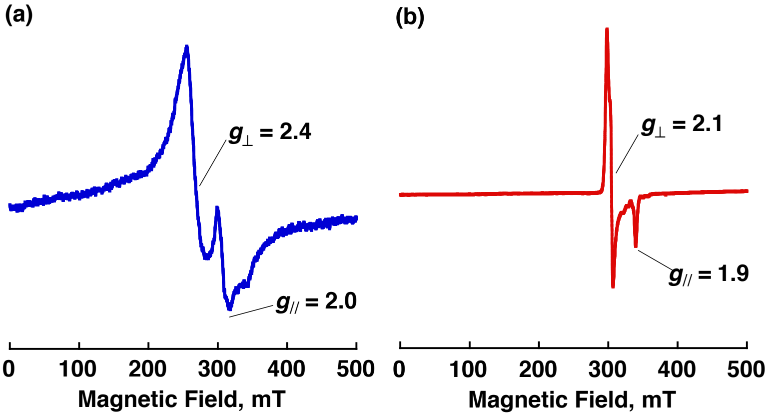

Figure 8. (a) X-band EPR spectrum of **1** (1.0 mM) measured at 4 K in a frozen 0.1 M $\mathrm{HNO_3}$ solution. (b) X-band EPR spectrum of **1** (1.0 mM) observed upon addition of 2 equivalents of CAN to a 0.10 M $\mathrm{HNO_3}$ solution measured at 77 K. The scale in longitudinal axis of (b) is 15 times larger than that of (a).

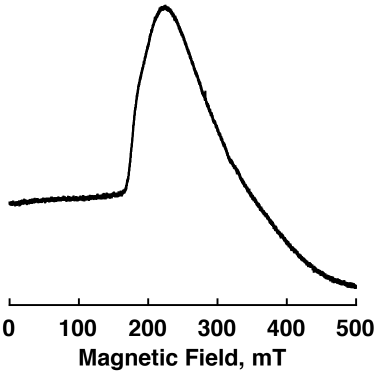

Figure 9. X-band EPR spectrum of $(NH_4)_2[Ce^{III}(NO_3)_5]$ (5.0×10^{-3} M) in a frozen aqueous solution containing 0.10 M HNO_3 at 4 K.

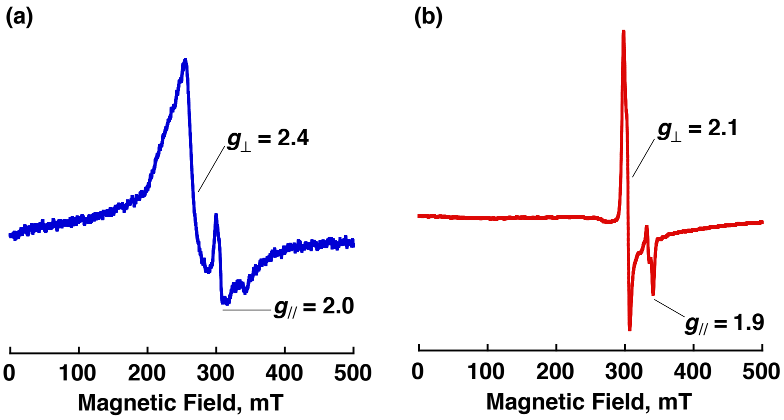

Figure 10. (a) X-band EPR spectrum of **2** (1.0×10^{-3} M) in a frozen aqueous solution containing 0.10 M HNO_3 at 4 K. (b) X-band EPR spectrum of **2** (1.0×10^{-3} M) upon addition of CAN (2.0×10^{-3} M) in a frozen aqueous solution containing 0.10 M HNO_3 at 77 K.

oxidation was also performed by the resonance Raman (rR) measurements. Figure 11 shows the result of the rR measurements of oxidized **1** produced by the addition of CAN (3 equiv, 3.0×10^{-3} M) in water with excitation at λ = 442 nm. The Raman scattering at 800 cm^{-1} was observed and this was shifted to 785 cm^{-1} when $H_2{}^{18}O$ was employed as a solvent. Similar Raman bands were observed for oxidized **2** with CAN (Figure 12). The rR band appearing at 800 cm^{-1} is assignable to the typical Ru^V=O species as identified in the previous papers.[54,55] In comparison with other Ru=O complexes together with the results of the redox titration and the EPR spectrum, this band is assigned to the stretching of Ru(V)-oxo double bond (Ru^V=O) of $[Ru^V(O)SiW_{11}O_{39}]^{5-}$. The smaller isotopic shift (15 cm^{-1}) than the theoretical value for the ^{18}O substitution in a Ru=O harmonic oscillator ($\Delta\nu$ = 40 cm^{-1}) may result from the binding of Ce(IV) to the oxo complex as suggested by the literature.[55]

The UV-visible spectrum of **1** observed during the catalytic oxidation with CAN in

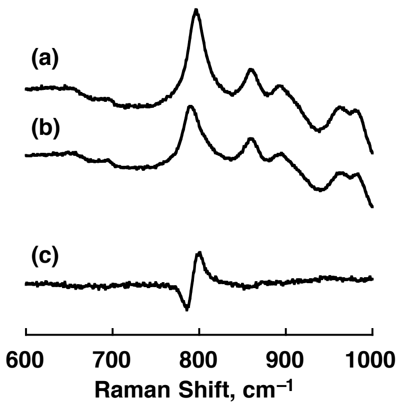

Figure 11. (a) Resonance Raman spectrum of $[Ru^{V}(^{16}O)SiW_{11}O_{39}]^{5-}$ generated in the reaction of $[Ru^{III}(H_2{}^{16}O)SiW_{11}O_{39}]^{5-}$ with CAN in $H_2{}^{16}O$ solution at room temperature with an excitation wavelength of λ = 442 nm. (b) Resonance Raman spectrum of $[Ru^{V}(^{18}O)SiW_{11}O_{39}]^{5-}$ generated in the reaction of $[Ru^{III}(H_2{}^{18}O)SiW_{11}O_{39}]^{5-}$ with CAN in $H_2{}^{18}O$ solution at room temperature with an excitation wavelength of λ = 442 nm. (c) Difference spectrum between (a) and (b).

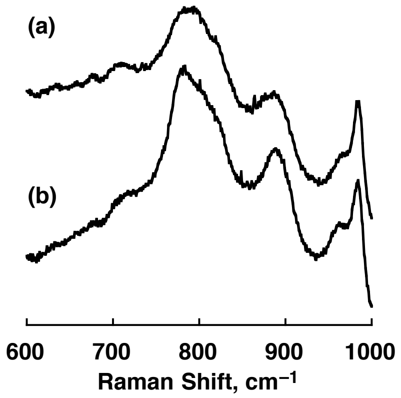

Figure 12. (a) Resonance Raman spectrum of $[Ru^{V}(^{16}O)GeW_{11}O_{39}]^{5-}$ generated in the reaction of $[Ru^{III}(H_2{}^{16}O)GeW_{11}O_{39}]^{5-}$ with CAN in an $H_2{}^{16}O$ solution at room temperature with an excitation wavelength of λ = 442 nm. (b) Resonance Raman spectrum of $[Ru^{V}(^{18}O)GeW_{11}O_{39}]^{5-}$ generated in the reaction of $[Ru^{III}(H_2{}^{18}O)GeW_{11}O_{39}]^{5-}$ with CAN in an $H_2{}^{18}O$ solution at room temperature with an excitation wavelength of λ = 442 nm.

an aqueous solution containing 0.1 M HNO_3 (Figure 13) agrees well with the spectrum of $[Ru^{V}(O)SiW_{11}O_{39}]^{5-}$ in Figure 7a. Because the formation of $[Ru^{V}(O)SiW_{11}O_{39}]^{5-}$ by the electron-transfer oxidation of **1** with CAN is very fast (vide supra), the Ru^{V}=O complex remains the catalytically active species for the water oxidation. The more detailed mechanistic insight is provided by the kinetic analysis (*vide infra*).

Kinetics and Catalytic Mechanism. Kinetic studies on the catalytic oxidation of water by CAN with **1** and **2** were conducted with an excess amount of CAN in acidic media to clarify the catalytic mechanism. The rates of water oxidation were determined from the decay rates of CAN, which agree with the rates of oxygen evolution (see

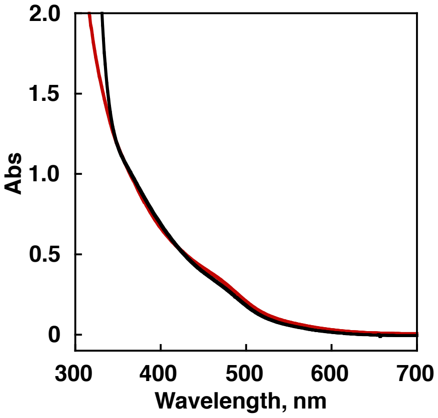

Figure 13. UV-vis absorption spectrum of **1** (3.0×10^{-4} M) during water oxidation (black) and that of $[Ru^V(O)SiW_{11}O_{39}]^{5-}$ (3.0×10^{-4} M) obtained by the titration with CAN as shown in Figure 7a (red).

Figure 2b). The decay rate of CAN was determined by monitoring the decay of absorbance at λ = 400 and 420 nm due to CAN using a photodiode array UV-visible spectrophotometer (see Experimental Section). The initial rates of water oxidation (R_i) were used to analyze the kinetics under catalytic turnover conditions to avoid the effect of decomposition of **1** and **2** under strongly acidic conditions.

The initial rates of water oxidation were investigated with various concentrations of **1** and **2** in an aqueous solution containing 100 equivalents of CAN and 0.55 M HNO_3.[56] The relatively high concentration of HNO_3, i.e., 0.55 M was employed because the solubility of catalyst **2** was limited in the presence of CAN at higher pH in the presence of 0.1 M HNO_3 due to the counter cation exchange. The rate law is determined to be first order with respect to the concentrations of **1** and **2** as shown in Figure 14a and 14b, respectively. If two Ru^V=O molecules, i.e., two $[Ru^V(O)SiW_{11}O_{39}]^{5-}$ for **1** or two $[Ru^V(O)GeW_{11}O_{39}]^{5-}$ for **2**, are involved for O-O bond formation in O_2 evolution, the rate law would be second order with respect to the catalyst concentration. Thus, the most likely reaction pathway for the O-O bond formation may be the reaction of the Ru^V=O complex with water to produce the Ru^{III}-OOH complex.[23,24] The water oxidation rate slightly increases with increasing pH (Figure 14c) and it also increases with increasing concentration of CAN to approach a constant value (Figure 14d). If the reaction of the Ru^V=O complex with water is solely the rate-determining step for the water oxidation, the water oxidation rate would be constant with change in pH or concentrations of CAN, because the formation of the Ru^V=O complex by the electron-transfer oxidation of **1** with CAN occurs at the diffusion-limited rate (*vide supra*). The saturation behaviors of the water oxidation rate with increasing pH and concentration of CAN indicate that the subsequent oxidation of the Ru^{III}-OOH complex by CAN competes with the back reaction from the Ru^{III}-OOH complex, which

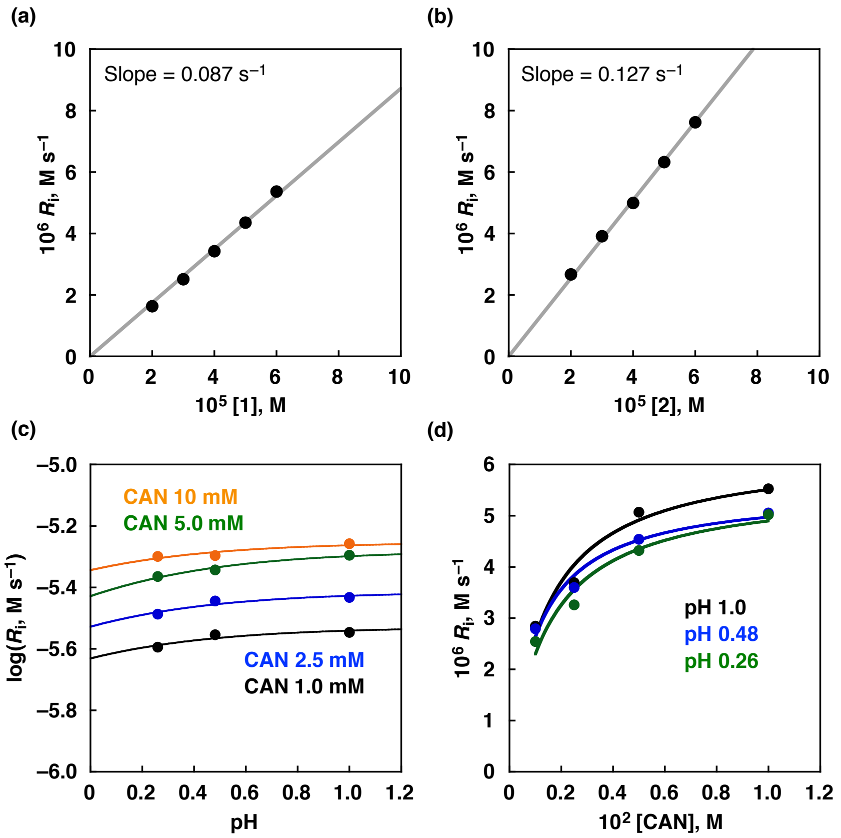

Figure 14. (a) Dependence of the initial rate (R_i) on [**1**] in the water oxidation catalyzed by **1** with CAN (100 equivalents, (2.0–6.0) × 10^{-3} M) in 0.55 M HNO_3 at 298 K. (b) Dependence of R_i on [**2**] in the water oxidation catalyzed by **2** with CAN (100 equivalents, (2.0–6.0) × 10^{-3} M) in 0.55 M HNO_3 at 298 K. (c) Dependence of logR_i on pH in the water oxidation catalyzed by **1** (5.0 × 10^{-5} M) with CAN ((0.10–1.0) × 10^{-2} M) in 0.10 ~ 0.55 M HNO_3 at 298 K. (d) Dependence of R_i on [CAN] in the water oxidation catalyzed by **1** (5.0 × 10^{-5} M) with CAN ((0.10–1.0) × 10^{-2} M) in 0.10 ~ 0.55 M HNO_3 at 298 K.

undergoes the O-O bond cleavage to regenerate the Ru^V=O complex as shown in Scheme 1. The driving force of dissociation of H^+ and O_2 from $[(L)Ru^V\text{-}OOH]^{4-}$ could be attributed to the deprotonation coupled with the oxidation of the peroxo ligand (O_2^{2-}) with high valent Ru^V. This may be the reason why the deprotonation occurs in such a highly acidic medium.

According to Scheme 1, the water oxidation rate (R_i) is given by eq 4, where k_w is

$$R_i = k_w k_{et}[Ru^V{=}O][H_2O][CAN]/(k_{-w}[H^+] + k_{et}[CAN]) \quad (4)$$

the rate constant of the reaction of the Ru^V=O complex with H_2O to produce the Ru^{III}-OOH complex, k_{et} is the rate constant of electron transfer from the Ru^{III}-OOH complex to CAN and k_{-w} is the rate constant of the back reaction from the Ru^{III}-OOH complex with H^+ to regenerate the Ru^V=O complex. Equation 4 agrees with

Scheme 1. Proposed Catalytic Mechanism of Water Oxidation by CAN with the Ru Complexes

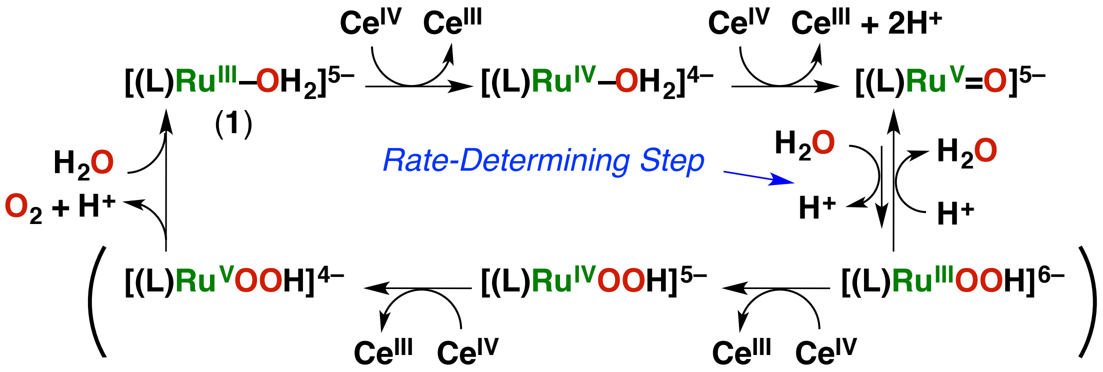

experimental observations in Figure 14: the first order dependence on the catalyst concentration that corresponds to [Ru^V=O], the saturation dependence on pH and the CAN concentration. Thus, the catalytic water oxidation by CAN with the Ru^{III}-OH_2 complex (**1** and **2**) proceeds via the Ru^V=O complex, which is immediately formed by the fast two-electron oxidation of the Ru^{III}-OH_2 complex coupled with deprotonation. The reaction of the Ru^V=O complex with H_2O to produce the Ru^{III}-OOH complex is the rate-determining step, but the electron transfer oxidation of the Ru^{III}-OOH by CAN leading to the oxygen evolution competes with the back reaction from the Ru^{III}-OOH complex with H^+ to regenerate the Ru^V=O complex. Because the further oxidation of the Ru^{III}OOH complex may be fast (not the rate-determining step), the Ru^{IV}OOH intermediate in Scheme 1 is putative.

It should be noted that the rate of **2** (Figure 14b) is 1.5 times higher than that of **1** (Figure 14a). The higher catalytic activity of **2** may result from the electron-withdrawing effect of germanium (core atom of the ligand), which are reflected by the smaller pK_a values of **2** as compared with **1** (*vide supra*).[57] Thus, the present study provides a valuable insight into the further improvement of the catalytic activity for water oxidation.

Conclusions

In this study, catalytic water oxidation was demonstrated using two types of all-inorganic mononuclear ruthenium complexes, **1** and **2**. TONs of oxygen evolution catalyzed **1** and **2** reaches up to 20 and 50, respectively. The origin of evolved oxygen was revealed to be water by ^{18}O isotope-labeling experiments in $H_2{}^{18}O$, where $^{18}O^{18}O$ was mainly obtained by measuring GC-MS. The intermediate Ru^V=O complex of **1** was detected by a characteristic anisotropic EPR signal at $g_{\perp} = 2.1$ and $g_{//} = 1.9$ at 77 K and a resonance Raman peaks which show the significant isotopic shift when the measurement has been done in $H_2{}^{18}O$. The (L)Ru^V=O complex is the two-electron oxidized species of **1** and **2** assignable to an active intermediate for oxidizing water in the rate-determining step of whole catalytic cycle to give (L)Ru^{III}OOH via the O–O bond formation step, where the reverse O–O bond cleavage process might be in competition with the follow-up two electron oxidation processes to generate oxygen. Actually the rate-determining equilibrium between (L)Ru^V=O and (L)Ru^{III}OOH was confirmed by the observation of saturated dependence of the oxygen evolution rate on pH and the concentration of CAN. When the catalytic activity of **1** was compared with that of **2**, the improvement of the catalytic activity was made possible by changing core-atom of the heteropolytungstate ligand from Si to Ge.

References

(1) (a) Lewis, N. S.; Nocera, D. G. *Proc. Natl. Acad. Sci.* **2006**, *103*, 15729. (b) Fukuzumi, S. *Phys. Chem. Chem. Phys.* **2008**, *10*, 2283. (c) Gray, H. B. *Nat. Chem.* **2009**, *1*, 7. (d) Hurst, J. K. *Science* **2010**, *328*, 315.

(2) (a) Youngblood, W. J.; Lee, S.-H. A.; Maeda, K.; Mallouk, T. E. *Acc. Chem. Res.* **2009**, *42*, 1966. (b) Kanan, M. W.; Surendranath, Y.; Nocera, D. G. *Chem. Soc. Rev.* **2009**, *38*, 109.

(3) (a) Rüttinger, W.; Dismukes, G. C. *Chem. Rev.* **1997**, *97*, 1. (b) Yagi, M.; Kaneko, M. *Chem. Rev.* **2001**, *101*, 21.

(4) (a) Hurst, J. K. *Coord. Chem. Rev.* **2005**, *249*, 313. (b) Cady, C. W.; Crabtree, R. H.; Brudvig, G. W. *Coord. Chem. Rev.* **2008**, *252*, 444. (c) Sala, X.; Romero, I.; Rodríguez, M.; Escriche, L.; Llobet, A. *Angew. Chem., Int. Ed.* **2009**, *48*, 2842. (d) Dismukes, G. C.; Brimblecombe, R.; Felton, G. A. N.; Pryadun, R. S.; Sheats, J. E.; Spiccia, L.; Swiegers, G. F. *Acc. Chem. Res.* **2009**, *42*, 1935. (e) Concepcion, J. J.; Jurss, J. W.; Brennaman, M. K.; Hoertz, P. G.; Patrocinio, A. O. T.; Murakami Iha, N. Y.; Templeton, J. L.; Meyer, T. J. *Acc. Chem. Res.* **2009**, *42*, 1954.

(5) Sala, X.; Ertem, M. Z.; Vigara, L.; Todorova, T. K.; Chen, W.; Rocha, R. C.; Aquilante, F.; Cramer, C. J.; Gagliardi, L.; Llobet, A. *Angew. Chem., Int. Ed.* **2010**, *49*, 7745.

(6) (a) Gersten, S. W.; Samuels, G. J.; Meyer, T. J. *J. Am. Chem. Soc.* **1982**, *104*, 4029. (b) Gilbert, J. A.; Eggleston, D. S.; Murphy, W. R.; Geselowitz, D. A.; Gersten, S. W.; Hodgson, D. J.; Meyer, T. J. *J. Am. Chem. Soc.* **1985**, *107*, 3855. (c) Geselowitz, D.; Meyer, T. J. *Inorg. Chem.* **1990**, *29*, 3894.

(7) (a) Chronister, C. W.; Binstead, R. A.; Ni, J.; Meyer, T. J. *Inorg. Chem.* **1997**, *36*, 3814. (b) Binstead, R. A.; Chronister, C. W.; Ni, J.; Hartshorn, C. M.; Meyer, T. *J. Am. Chem. Soc.* **2000**, *122*, 8464. (c) Liu, F.; Concepcion, J. J.; Jurss, J. W.; Cardolaccia, T.; Templeton, J. L.; Meyer, T. J. *Inorg. Chem.* **2008**, *47*, 1727.

(8) (a) Concepcion, J. J.; Jurss, J. W.; Templeton, J. L.; Meyer, T. J. *Proc. Natl. Acad. Sci.* **2008**, *105*, 17632. (b) Jurss, J. W.; Concepcion, J. C.; Norris, M. R.; Templeton, J. L.; Meyer, T. J. *Inorg. Chem.* **2010**, *49*, 3980.

(9) Nagoshi, K.; Yagi, M.; Kaneko, M. *Bull. Chem. Soc. Jpn.* **2000**, *73*, 2193.

(10) Sens, C.; Romero, I.; Rodríguez, M.; Llobet, A.; Parella, T.; Benet-Buchholz, J. *J. Am. Chem. Soc.* **2004**, *126*, 7798.

(11) (a) Romain, S.; Bozoglian, F.; Sala, X.; Llobet, A. *J. Am. Chem. Soc.* **2009**, *131*, 2768. (b) Bozoglian, F.; Romain, S.; Ertem, M. Z.; Todorova, T. K.; Sens, C.; Mola, J.; Rodríguez, M.; Romero, I.; Benet-Buchholz, J.; Fontrodona, X.; Cramer, C. J.; Gagliardi, L.; Llobet, A. *J. Am. Chem. Soc.* **2009**, *131*, 15176.

(12) (a) Mola, J.; Mas-Marza, E.; Sala, X.; Romero, I.; Rodríguez, M.; Viñas, C.; Parella, T.; Llobet, A. *Angew. Chem., Int. Ed.* **2008**, *47*, 5830. (b) Francàs, L.; Sala, X.; Benet-Buchholz, J.; Escriche, L.; Llobet, A. *ChemSusChem* **2009**, *2*, 321.

(13) Zong, R.; Thummel, R. P. *J. Am. Chem. Soc.* **2005**, *127*, 12802.

(14) (a) Xu, Y.; Åkermark, T.; Gyollai, V.; Zou, D.; Eriksson, L.; Duan, L.; Zhang, R.; Åkermark, B.; Sun, L. *Inorg. Chem.* **2009**, *48*, 2717. (b) Xu, Y.; Duan, L.; Tong, L.; Åkermark, B.; Sun, L. *Chem. Commun.* **2010**, *46*, 6506.

(15) Wasylenko, D. J.; Ganesamoorthy, C.; Koivisto, B. D.; Berlinguette, C. P. *Eur. J. Inorg. Chem.* **2010**, *2010*, 3135.

(16) Wang, L.-P.; Wu, Q.; Van Voorhis, T. *Inorg. Chem.* **2010**, *49*, 4543.

(17) (a) Wada, T.; Tsuge, K.; Tanaka, K. *Angew. Chem., Int. Ed.* **2000**, *39*, 1479. (b) Muckerman, J. T.; Polyansky, D. E.; Wada, T.; Tanaka, K.; Fujita, E. *Inorg. Chem.* **2008**, *47*, 1787.

(18) Wada, T.; Muckerman, J. T.; Fujita, E.; Tanaka, K. *Dalton Trans.* **2011**, *40*, 2225.

(19) (a) Cape, J. L.; Hurst, J. K. *J. Am. Chem. Soc.* **2007**, *130*, 827. (b) Cape, J. L.; Siems, W. F.; Hurst, J. K. *Inorg. Chem.* **2009**, *48*, 8729.

(20) (a) Limburg, J.; Vrettos, J. S.; Liable-Sands, L. M.; Rheingold, A. L.; Crabtree, R. H.; Brudvig, G. W. *Science* **1999**, *283*, 1524. (b) Limburg, J.; Vrettos, J. S.; Chen, H.; de Paula, J. C.; Crabtree, R. H.; Brudvig, G. W. *J. Am. Chem. Soc.* **2000**, *123*, 423.

(21) Shimazaki, Y.; Nagano, T.; Takesue, H.; Ye, B.-H.; Tani, F.; Naruta, Y. *Angew. Chem., Int. Ed.* **2004**, *43*, 98.

(22) (a) Ferreira, K. N.; Iverson, T. M.; Maghlaoui, K.; Barber, J.; Iwata, S. *Science* **2004**, *303*, 1831. (b) Loll, B.; Kern, J.; Saenger, W.; Zouni, A.; Biesiadka, J. *Nature* **2005**, *438*, 1040.

(c) Yano, J.; Kern, J.; Sauer, K.; Latimer, M. J.; Pushkar, Y.; Biesiadka, J.; Loll, B.; Saenger, W.; Messinger, J.; Zouni, A.; Yachandra, V. K. *Science* **2006**, *314*, 821. (d) Umena, Y.; Kawakami, K.; Shen, J.-R.; Kamiya, N. *Nature* **2011**, *473*, 55.

(23) (a) Concepcion, J. J.; Jurss, J. W.; Templeton, J. L.; Meyer, T. J. *J. Am. Chem. Soc.* **2008**, *130*, 16462. (b) Concepcion, J. J.; Jurss, J. W.; Norris, M. R.; Chen, Z.; Templeton, J. L.; Meyer, T. J. *Inorg. Chem.* **2010**, *49*, 1277.

(24) Concepcion, J. J.; Tsai, M.-K.; Muckerman, J. T.; Meyer, T. J. *J. Am. Chem. Soc.* **2010**, *132*, 1545.

(25) (a) Chen, Z.; Concepcion, J. J.; Jurss, J. W.; Meyer, T. J. *J. Am. Chem. Soc.* **2009**, *131*, 15580. (b) Concepcion, J. J.; Jurss, J. W.; Hoertz, P. G.; Meyer, T. J. *Angew. Chem., Int. Ed.* **2009**, *48*, 9473. (c) Chen, Z.; Concepcion, J. J.; Hull, J. F.; Hoertz, P. G.; Meyer, T. J. *Dalton Trans.* **2010**, *39*, 6950.

(26) (a) Chen, Z.; Concepcion, J. J.; Luo, H.; Hull, J. F.; Paul, A.; Meyer, T. J. *J. Am. Chem. Soc.* **2010**, *132*, 17670. (b) Chen, Z.; Concepcion, J. J.; Hu, X.; Yang, W.; Hoertz, P. G.; Meyer, T. J. *Proc. Natl. Acad. Sci.* **2010**, *107*, 7225.

(27) (a) Tseng, H.-W.; Zong, R.; Muckerman, J. T.; Thummel, R. *Inorg. Chem.* **2008**, *47*, 11763. (b) Zhang, G.; Zong, R.; Tseng, H.-W.; Thummel, R. P. *Inorg. Chem.* **2008**, *47*, 990.

(28) (a) Duan, L.; Fischer, A.; Xu, Y.; Sun, L. *J. Am. Chem. Soc.* **2009**, *131*, 10397. (b) Nyhlén, J.; Duan, L.; Åkermark, B.; Sun, L.; Privalov, T. *Angew. Chem., Int. Ed.* **2010**, *49*, 1773. (c) Tong, L.; Duan, L.; Xu, Y.; Privalov, T.; Sun, L. *Angew. Chem., Int. Ed.* **2011**, *50*, 445.

(29) (a) Duan, L.; Xu, Y.; Gorlov, M.; Tong, L.; Andersson, S.; Sun, L. *Chem.–Eur. J.* **2010**, *16*, 4659. (b) Li, L.; Duan, L.; Xu, Y.; Gorlov, M.; Hagfeldt, A.; Sun, L. *Chem. Commun.* **2010**, *46*, 7307.

(30) Roeser, S.; Farràs, P.; Bozoglian, F.; Martínez-Belmonte, M.; Benet-Buchholz, J.; Llobet, A. *ChemSusChem* **2011**, *4*, 197.

(31) Duan, L.; Xu, Y.; Tong, L.; Sun, L. *ChemSusChem* **2011**, *4*, 238.

(32) (a) Masaoka, S.; Sakai, K. *Chem. Lett.* **2009**, *38*, 182. (b) Yoshida, M.; Masaoka, S.; Sakai, K. *Chem. Lett.* **2009**, *38*, 702. (c) Yoshida, M.; Masaoka, S.; Abe, J.; Sakai, K. *Chem. Asian J.* **2010**, *5*, 2369.

(33) Kiyota, J.; Yokoyama, J.; Yoshida, M.; Masaoka, S.; Sakai, K. *Chem. Lett.* **2010**, *39*, 1146.

(34) (a) Wasylenko, D. J.; Ganesamoorthy, C.; Koivisto, B. D.; Henderson, M. A.; Berlinguette, C. P. *Inorg. Chem.* **2010**, *49*, 2202. (b) Wasylenko, D. J.; Ganesamoorthy, C.; Henderson, M. A.; Koivisto, B. D.; Osthoff, H. D.; Berlinguette, C. P. *J. Am. Chem. Soc.* **2010**, *132*, 16094. (c) Wadsworth, E.; Duke, F. R.; Goetz, C. A. *Anal. Chem.* **1957**, *29*, 1824.

(35) (a) McDaniel, N. D.; Coughlin, F. J.; Tinker, L. L.; Bernhard, S. *J. Am. Chem. Soc.* **2008**, *130*, 210. (b) Lalrempuia, R.; McDaniel, N. D.; Müller-Bunz, H.; Bernhard, S.; Albrecht, M. *Angew. Chem., Int. Ed.* **2010**, *49*, 9765.

(36) (a) Hull, J. F.; Balcells, D.; Blakemore, J. D.; Incarvito, C. D.; Eisenstein, O.; Brudvig, G. W.; Crabtree, R. H. *J. Am. Chem. Soc.* **2009**, *131*, 8730. (b) Blakemore, J. D.; Schley, N. D.; Balcells, D.; Hull, J. F.; Olack, G. W.; Incarvito, C. D.; Eisenstein, O.; Brudvig, G. W.; Crabtree, R. H. *J. Am. Chem. Soc.* **2010**, *132*, 16017.

(37) (a) Yang, X.; Baik, M.-H. *J. Am. Chem. Soc.* **2006**, *128*, 7476. (b) Yang, X.; Baik, M.-H. *J. Am. Chem. Soc.* **2008**, *130*, 16231.

(38) (a) Geletii, Y. V.; Botar, B.; Kögerler, P.; Hillesheim, D. A.; Musaev, D. G.; Hill, C. L. *Angew. Chem., Int. Ed.* **2008**, *47*, 3896. (b) Geletii, Y. V.; Besson, C.; Hou, Y.; Yin, Q.; Musaev, D. G.; Quiñonero, D.; Cao, R.; Hardcastle, K. I.; Proust, A.; Kögerler, P.; Hill, C. L. *J. Am. Chem. Soc.* **2009**, *131*, 17360. (c) Kuznetsov, A. E.; Geletii, Y. V.; Hill, C. L.; Morokuma, K.; Musaev, D. G. *J. Am. Chem. Soc.* **2009**, *131*, 6844. (d) Quiñonero, D.; Kaledin, A. L.; Kuznetsov, A. E.; Geletii, Y. V.; Besson, C.; Hill, C. L.; Musaev, D. G. *J. Phys. Chem. A* **2009**, *114*, 535.

(39) (a) Sartorel, A.; Carraro, M.; Scorrano, G.; Zorzi, R. D.; Geremia, S.; McDaniel, N. D.; Bernhard, S.; Bonchio, M. *J. Am. Chem. Soc.* **2008**, *130*, 5006. (b) Sartorel, A.; Miró, P.; Salvadori, E.; Romain, S.; Carraro, M.; Scorrano, G.; Valentin, M. D.; Llobet, A.; Bo, C.; Bonchio, M. *J. Am. Chem. Soc.* **2009**, *131*, 16051.

(40) (a) Geletii, Y. V.; Huang, Z.; Hou, Y.; Musaev, D. G.; Lian, T.; Hill, C. L. *J. Am. Chem. Soc.* **2009**, *131*, 7522. (b) Besson, C.; Huang, Z.; Geletii, Y. V.; Lense, S.; Hardcastle, K. I.; Musaev, D. G.; Lian, T.; Proust, A.; Hill, C. L. *Chem. Commun.* **2010**, *46*, 2784.

(41) (a) Orlandi, M.; Argazzi, R.; Sartorel, A.; Carraro, M.; Scorrano, G.; Bonchio, M.; Scandola, F. *Chem. Commun.* **2010**, *46*, 3152. (b) Puntoriero, F.; La Ganga, G.; Sartorel, A.; Carraro, M.; Scorrano, G.; Bonchio, M.; Campagna, S. *Chem. Commun.* **2010**, *46*, 4725. (c) Toma, F. M. et al. *Nat. Chem.* **2010**, *2*, 826.

(42) (a) Yin, Q.; Tan, J. M.; Besson, C.; Geletii, Y. V.; Musaev, D. G.; Kuznetsov, A. E.; Luo, Z.; Hardcastle, K. I.; Hill, C. L. *Science* **2010**, *328*, 342. (b) Huang, Z.; Luo, Z.; Geletii, Y. V.; Vickers, J. W.; Yin, Q.; Wu, D.; Hou, Y.; Ding, Y.; Song, J.; Musaev, D. G.; Hill, C. L.; Lian, T. *J. Am. Chem. Soc.* **2011**, *133*, 2068.

(43) For the cobalt-based water oxidation catalysts see: (a) Kanan, M. W.; Nocera, D. G. *Science* **2008**, *321*, 1072. (b) Surendranath, Y.; Dincă M.; Nocera, D. G. *J. Am. Chem. Soc.* **2009**, *131*, 2615. (c) Kanan, M. W.; Yano, J.; Surendranath, Y.; Dincă, M.; Yachandra, V. K.; Nocera, D. G. *J. Am. Chem. Soc.* **2010**, *132*, 13692. (d) McAlpin, J. G.; Surendranath, Y.; Dincă, M.; Stich, T. A.; Stoian, S. A.; Casey, W. H.; Nocera, D. G.; Britt, R. D. *J. Am. Chem. Soc.* **2010**, *132*, 6882.

(44) (a) Sadakane, M.; Higashijima, M. *Dalton Trans.* **2003**, 659. (b) Sadakane, M.; Tsukuma, D.; Dickman, M. H.; Bassil, B.; Kortz, U.; Higashijima, M.; Ueda, W. *Dalton Trans.* **2006**, 4271.

(45) The pH dependence of **1** with more limited pH region was reported in ref 44a.

(46) No observation of catalytic currents at the highest anodic peak in Figure 3 is consistent with the rate-determining step in Scheme 1, which is not the oxidation of the catalyst. The anodic scan from the potential higher than 1.1 V vs SCE with slow scan rate (50 mV s^{-1}) resulted in the catalytic current for the water oxidation, which increases with increasing the concentration of the catalyst (see Figure S1 in Supporting Information).

(47) Pourbaix, M. *Atlas of Electrochemical Equilibria in Aqueous Solutions*, NACE: Houston, 1966.

(48) Dobson, J. C.; Meyer, T. J. *Inorg. Chem.* **1988**, *27*, 3283.

(49) (a) Mullay, J. *J. Am. Chem. Soc.* **1984**, *106*, 5842. (b) Allen, L. C. *J. Am. Chem. Soc.* **1989**, *111*, 9003.

(50) The lower limit of the time scale of stopped-flow measurements is about 10 ms due to the mixing of two solutions. When the reactive species decays obeying the first-order kinetics and its half-life period is longer than 10 ms, the first-order rate constant must be less than ca. 10^2 s^{-1} for the determination of the rate constant using a stopped-flow apparatus. As the concentration of catalyst **1** must be higher than ca 10^{-4} M because of the detectable limit of the absorbance change (ΔA ~ ca. 0.1), the second-order rate constant must be lower than 10^6 M^{-1} s^{-1} (= 10^2 s^{-1} / 10^{-4} M) for the accurate determination of the rate constant.

(51) (a) Medhi, O. K.; Agarwala, U. *Inorg. Chem.* **1980**, *19*, 1381. (b) Taqui Khan, M. M.; Srinivas, D.; Kureshy, R. I.; Khan, N. H. *Inorg. Chem.* **1990**, *29*, 2320. (c) Besson, C.; Mirebeau, J.-H.; Renaudineau, S.; Roland, S.; Blanchard, S.; Vezin, H.; Courillon, C.; Proust, A. *Inorg. Chem.* **2011**, *50*, 2501. (d) Sukanya, D.; Raja, D. S.; Bhuvanesh, N. S. P.; Natarajan, K. *Polyhedron* **2011**, *30*, 1108. (e) Mondal, B.; Chakraborty, S.; Munshi, P.; Walawalkar, M. G.; Lahiri, G. K. *J. Chem. Soc., Dalton Trans.* **2000***,* 2327.

(52) (a) Dengel, A. C.; Griffith, W. P.; O'Mahoney, C. A.; Williams, D. J. *J. Chem. Soc., Chem. Commun.,* **1989**, 1720. (b) Dengel, A. C.; Griffith, W. P. *Inorg. Chem.* **1991**, *30,* 869. (c) Neumann, R.; Abu-Gnim, C. *J. Am. Chem. Soc.*, **1990**, *112*, 6025. (d) Lahootun, V.; Besson, C.; Villanneau, R.; Villain, F.; Chamoreau, L.-M.; Boubekeur, K.; Blanchard, S.; Thouvenot, R.; Proust, A. *J. Am. Chem. Soc.* **2007**, *129*, 7127. (e) Kuan, S. L.; Tay, E. P. L.; Leong, W. K.; Goh, L. Y.; Lin, C. Y.; Gill, P. M. W.; Webster, R. D. *Organometallics* **2006**, *25*, 6134.

(53) Sidorenko, A. V.; Rodnyĭ, P. A.; Guillot-Noel, O.; Gourier, D.; van Eijk, C. W. E. *Phys. Solid State* **2003**, *45*, 1676.

(54) Hunt, J. K.; Zhou, J.; Lei, Y. *Inorg. Chem.* **1992**, *31*, 1010.

(55) Yamada, H.; Hurst, J. K. *J. Am. Chem. Soc.* **2000**, *122*, 5303.

(56) The effect of ionic strength was examined by the addition of 0.5 M $NaNO_3$ to the solution of 0.1 M HNO_3 (pH 1) and it was confirmed that neither the rate constant nor pH of the solution was affected by the ionic strength.

(57) The more electronegative Ge withdraws electron at higher degree than Si from the framework of polytungstate anion, which causes the lower basicity of the heteropolytungstate anion. The weaker coordination of the heteropolytungstate anion resulted in the higher acidity of the Ru metal center, which induces the higher acidity of the coordinated aqua ligand with lower pK_a as well as the higher electrophilicity of the Ru metal center appropriate for the rate-determining nucleophilic attack of a water molecule to the Ru center.

Supporting Information for Chapter 3

Derivation of eq 3:

In the acid dissociation equilibrium:

$\mathbf{B\text{-}H} \leftrightarrow \mathbf{B}^- + \mathbf{H}^+$ ($\mathbf{B\text{-}H}$: $\mathbf{(L)Ru^{III}\text{-}OH_2}$, $\mathbf{B}^-$: $\mathbf{(L)Ru^{III}\text{-}OH}$)

The **eq 3** was derived according to the following procedure, where A: Observed absorbance, A_0: Initial absorbance of **B-H** at $\lambda = 440$ nm for 1 and $\lambda = 430$ nm for 2, A_∞: Final absorbance of $\mathbf{B}^-$ at $\lambda = 440$ nm for 1 and $\lambda = 430$ nm for 2, K_a: Acid dissociation constant, $[\mathbf{B\text{-}H}]_0$: Initial concentration of **B-H**, α: Ratio of $[\mathbf{B}^-]$ to $[\mathbf{B\text{-}H}]_0$.

$[\mathbf{B\text{-}H}]_0 = [\mathbf{B\text{-}H}] + [\mathbf{B}^-]$

$[\mathbf{B}^-] = \alpha[\mathbf{B\text{-}H}]_0$ (1)

$\therefore\ [\mathbf{B\text{-}H}] = (1 - \alpha)[\mathbf{B\text{-}H}]_0$ (2)

$A = (1 - \alpha)A_0 + \alpha A_\infty$

$\therefore\ A = A_0 + \alpha(A_\infty - A_0)$ (3)

$K_a = [\mathbf{B}^-][\mathbf{H}^+]/[\mathbf{B\text{-}H}]$ (4)

$\mathrm{pH} = -\log[\mathbf{H}^+]$

$\therefore\ [\mathbf{H}^+] = 10^{-\mathrm{pH}}$ (5)

(1), (2), (4) … $K_a = \alpha[\mathbf{H}^+]/(1 - \alpha)$

$\therefore\ \alpha = K_a/(K_a + [\mathbf{H}^+])$ (6)

(5), (6) … $\alpha = K_a/(K_a + 10^{-\mathrm{pH}})$ (7)

(3), (7) … $A = A_0 + K_a(A_\infty - A_0)/(K_a + 10^{-\mathrm{pH}})$ **eq 3**

Complete list of ref 41c:

(41) (c) Toma, F. M.; Sartorel, A.; Iurlo, M.; Carraro, M.; Parisse, P.; Maccato, C.; Rapino, S.; Gonzalez, B. R.; Amenitsch, H.; Da Ros, T.; Casalis, L.; Goldoni, A.; Marcaccio, M.; Scorrano, G.; Scoles, G.; Paolucci, F.; Prato, M.; Bonchio, M. *Nat. Chem.* **2010**, *2*, 826.

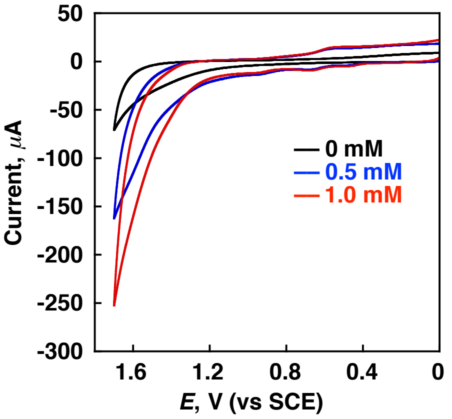

Figure S1. Cyclic voltammograms measured in the absence (black line) and presence of $[Ru^{III}SiW_{11}O_{39}]^{5-}$ [**1**: 5.0×10^{-4} M (blue line) and 1.0×10^{-3} M (red line)] at a sweep rate of 50 mV s^{-1} in a 0.1 M HNO_3 solution at 298 K.

Chapter 5

$LaCoO_3$ Acting as an Efficient and Robust Catalyst for Photocatalytic Water Oxidation with Persulfate

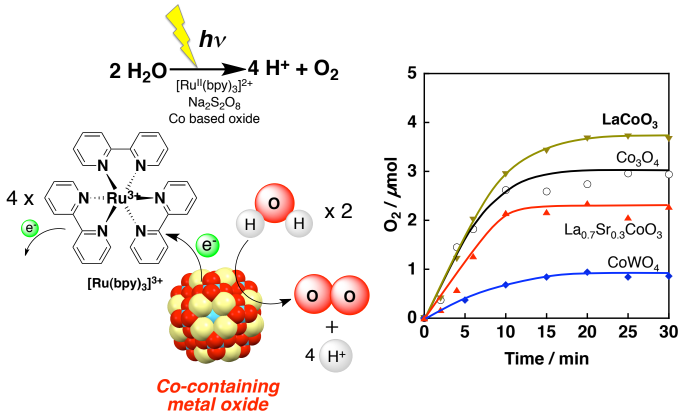

Abstract: Cobalt-containing metal oxides [perovskite ($LaCoO_3$, $NdCoO_3$, $YCoO_3$, $La_{0.7}Sr_{0.3}CoO_3$), spinel (Co_3O_4) and wolframite ($CoWO_4$)] have been examined as catalysts for photocatalytic water oxidation with $Na_2S_2O_8$ and $[Ru(bpy)_3]^{2+}$ as an electron acceptor and a photosensitizer, respectively. Catalysts with perovskite structure exhibited higher catalytic activity as compared with the catalysts with spinel and wolframite structure. $LaCoO_3$, which stabilizes Co(III) species in the perovskite structure, exhibited the highest catalytic activity in the photocatalytic water oxidation compared with $CoWO_4$, Co_3O_4 and $La_{0.7}Sr_{0.3}CoO_3$, which contain Co(II) or Co(IV) species in the matrixes. The high catalytic reactivity of $LaCoO_3$ possessing perovskite structure was maintained in $NdCoO_3$ and $YCoO_3$, which exclusively contain Co(III) species. Thus, the catalytic activity of Co ions can be controlled by the additional metal ions, which leads to develop highly reactive and robust catalysts for the photocatalytic water oxidation.

Introduction

Artificial photosynthesis is a chemical process producing fuels directly by utilizing solar energy for sustainable development.[1–11] For realizing the artificial photosynthesis, an efficient catalyst oxidizing water to extract electrons is strongly demanded.[12–14] Extensive efforts have been devoted to catalysts development in water oxidation with various types of materials including metal complexes and metal oxides.[15–26] In metal complexes, the first successful example was the blue dimer, which contains binuclear ruthenium ions connected with two water molecules.[27–29] Additionally, manganese and iridium-containing complexes and metal oxides have been also reported as active catalysts.[30]

So far, cobalt-based catalysts have been also regarded as promising candidates, because of the highest oxidation potential of cobalt ions among naturally abundant metal ions.[31–47] For example, oxygen evolution by thermal or photocatalytic water oxidation has been observed from an aqueous buffer solution containing a tetranuclear cobalt-based polyoxometalate complex of $[\mathrm{Co^{II}}_4(\mathrm{H_2O})_2(\alpha\text{-}\mathrm{PW_9O_{34}})_2]^{10-}$.[48,49] Such a homogeneous catalyst, however, has recently been reported to be converted to a more reactive heterogeneous CoO_x.[50] In fact, Co_3O_4 and Co phosphate (CoPi) have been reported as active catalysts in electrocatalytic and photocatalytic water oxidation.[51–56] During the electrodeposition of CoPi on a substrate, the formation of high valent Co^{IV} species from Co^{II} species has been recently confirmed by EPR.[57] These cobalt-containing catalysts are more active compared with those composed of other first-row transition metals,[31] however, further improvement in the catalytic activity and stability is certainly necessary for realizing the artificial photosynthesis.

In natural systems, a manganese oxide cluster together with a calcium ion acts as the water oxidation catalyst.[58–60] As a role of the calcium ion, regulation of the redox properties of the manganese cluster has been proposed from studies on metal ion-coupled electron-transfer reactions.[61–67] Introduction of non-redox active metal ions to cobalt oxides may improve the catalytic activity of cobalt oxides for water oxidation. However, the effects of addition of non-redox active metal ions to cobalt oxides on the activity of the photocatalytic water oxidation have yet to be examined.

In Chapter 5, I report the catalytic activity of a series of metal oxides containing cobalt with various valences and non-redox active metal ions in the photocatalytic oxidation of water with persulfate ($Na_2S_2O_4$) and $[Ru(bpy)_3]^{2+}$ (bpy = 2,2’-bipyridine) as an oxidant and a photosensitizer, respectively. First, the catalytic activities were compared among perovskite $LaCoO_3$ that contains Co^{III} and La^{3+}, wolframite $CoWO_4$ that composed of Co^{II} and W^{VI} and spinel Co_3O_4 consisting of two Co^{III} and one Co^{II}

ions. The catalytic activity of perovskite $La_{0.7}Sr_{0.3}CoO_3$, in which La^{3+} is partially replaced by Sr^{2+}, was also investigated to clarify the effect of valence of ions in A-site of perovskite on the catalytic property of $LaCoO_3$. Then, La^{3+} of perovskite $LaCoO_3$ was fully replaced by other trivalent metal ions (Nd^{3+} and Y^{3+}) to compare the catalytic activity.

Experimental Section

Materials. All chemicals used for synthesizing Co-containing catalysts were obtained from a chemical company and used without further purification. Purified water was provided by a Millipore Milli-Q water purification system where the electronic conductance was 18.2 MΩ cm. $LaCoO_3$, $La_{0.7}Sr_{0.3}CoO_3$, $CoWO_4$, Co_3O_4, $YCoO_3$ and $SrCoO_3$ were synthesized by following reported methods.[67–71]

Synthesis of $LaCoO_3$.[67] To an aqueous solution (0.40 mL) containing lanthanum nitrate hexahydrate (1.0 mmol, 0.43 g) and cobalt nitrate hexahydrate (1.0 mmol, 0.29 g) was added acetic acid (1.0 mmol, 0.058 mL) with magnetic stirring at 333 K for 5 min. Then, citric acid (1.0 mmol, 0.19 g) was slowly added to the solution at the temperature and the solution was heated to 373 K with maintaining the temperature for 2 h to form gel. The obtained gel was calcined in air at 873 K for 4 h.

Synthesis of $La_{0.7}Sr_{0.3}CoO_3$.[68] To an aqueous solution (2.0 mL) containing lanthanum nitrate hexahydrate (0.35 mmol, 0.15 g), strontium nitrate (0.15 mmol, 32 mg) and cobalt nitrate hexahydrate (0.50 mmol, 0.15 g) was added urea (4.5 mmol, 270 mg) with magnetically stirring at 358 K. After 2 h stirring, the solution changed into viscous slurry. The slurry was further dried in an oven at 393 K for 8 h. At last, the resulting solid was calcined in air at 973 K for 5 h.

Synthesis of $CoWO_4$.[69] Sodium tungstate 2-hydrate (7.0 mmol, 2.1 g) was dissolved to water (60 mL) and sodium dodecyl sulphate (14 mmol, 4.0 g) was added slowly to it with vigorous stirring. When the solution clarified, an aqueous solution (30 mL) of cobalt nitrate hexahydrate (7.0 mmol, 1.7 g) was added to the above solution under continuous stirring. The obtained suspension transferred to a Teflon cup with inner volume of 100 mL. The Teflon cup was sealed in a stainless steal jacket and heated to 453 K for 12 h. The obtained particles were collected by filtration and washed with pure water three times and dried at 338 K for several hours.

Synthesis of Co_3O_4.[70] An aqueous ammonia solution (25%, 7.3 mL) was slowly added to an aqueous solution of cobalt acetate (80 mM, 73 mL) with vigorous stirring by a magnetic stirrer. After 20 min of stirring, the obtained pale pink slurry was transferred to a Teflon cup with an inner volume of 140 mL. The Teflon cup was sealed in a stainless steel jacket and heated to 423 K in an oven for 3 h. The obtained particles were collected by filtration and washed with pure water three times and dried at 338 K for several hours.

Synthesis of $NdCoO_3$. To an aqueous solution (0.40 mL) containing neodymium nitrate hexahydrate (1.0 mmol, 0.44 g) and cobalt nitrate hexahydrate (1.0 mmol, 0.29 g) was added acetic acid (1.0 mmol, 0.058 mL) with magnetically stirring at 333 K for 5 min. Then, citric acid (1.0 mmol, 0.19 g) was slowly added to the solution at the temperature and the solution was heated to 373 K with maintaining the temperature for 2 h to form gel. The obtained gel was calcined in air at 873 K for 4 h.

Synthesis of $YCoO_3$.[71] To an aqueous solution (10 mL) of yttrium nitrate hexahydrate (1.0 mmol, 380 mg) and cobalt nitrate hexahydrate (1.0 mmol, 0.29 g) was added an aqueous solution (10 mL) of citric acid (1.0 mmol, 0.19 g) with magnetically stirring. The mixtures were slowly heated up to dryness at 363 K for 6 h. The products were annealed in air at 573 K, and a black powder was obtained. After grinding and compressing into pellets, these were calcined in air at 1173 K (a heating rate of 100 K h^{-1}).

Synthesis of $SrCoO_3$. To an aqueous solution (2.0 mL) of strontium nitrate (1.0 mmol, 0.21 g) and cobalt nitrate hexahydrate (1.0 mmol, 0.29 g) was added citric acid (4.0 mmol, 0.77 g) with magnetically stirring. The mixtures were evaporated at 333 K for 8 h. Then the obtained viscous material was subsequently dried at 353 K for 8 h. The resulting pink spongy and friable material was powdered and was kept at 423 k for 8 h. The obtained solid was calcined in air at 1173 K for 5 h. (a heating rate of 10 K min^{-1}). (ref: Khazaei, M.; Malekzadeh, A.; Amimi, F.; Mortazavi, Y.; Khodadadi, A. *Cryst. Res. Technol.* **2010**, *45*, 1064.)

Catalyst Characterization. Transmission electron microscope images of nanoparticles, which were mounted on a copper microgrid coated with elastic carbon, were observed by a JEOL JEM 2100 operating at 200 keV. Powder X-ray diffraction patterns were recorded by a Rigaku Ultima IV. Incident X-ray radiation was produced by a Cu X-ray tube, operating at 40 kV and 40 mA with Cu $K\alpha$ radiation of 1.54 Å. The scanning rate was 2 °/min from 20° to 80° in 2θ. X-ray photoelectron spectra were measured by a Kratos Axis 165x with a 165 mm hemispherical electron energy analyzer. The incident radiation was Mg $K\alpha$ X-rays (1253.6 eV) at 200 W. Each sample was attached on a stainless stage with a double-sided carbon scotch tape. The binding energy of each element was corrected by C 1s peak (248.6 eV) from residual carbon. Nitrogen adsorption-desorption at 77 K was performed with a Belsorp-mini (BEL Japan, Inc.) within a relative pressure range from 0.01 to 101.3 kPa. A sample mass of about 100 mg was used for adsorption analysis after pretreatment at 473 K for 30 min under vacuum conditions and kept in N_2 atmosphere until N_2-adsorption measurements. The sample was exposed to a mixed gas of He and N_2 with a programmed ratio and adsorbed amount of N_2 was calculated from the change of pressure in a cell after reaching the equilibrium (at least 5 min). EPR spectra were measured at 77K with a JEOL X-band spectrometer (JES-RE1XE). A certain amount of each sample was introduced to a quartz tube (1 mm, i.d.) in a solid state. The EPR spectra were recorded under non-saturating microwave power conditions. The magnitude of the modulation was chosen to optimize the resolution and the signal-to-noise (*S*/*N*) ratio of the observed spectra. The *g* values were calibrated with an Mn^{2+} marker.

Catalysis measurements and quantum yield determination. Photocatalytic oxygen evolution was performed as follows. A Co-containing catalyst (0.025–0.50 g L^{-1}) was added to a phosphate buffer solution (pH 7.0, 2.0 mL) containing $Na_2S_2O_8$ (5.0 mM) and $[Ru(bpy)_3](ClO_4)_2$ (0.25 mM) flushed with Ar gas. The solution was then irradiated with a xenon lamp (Ushio Optical, Model X SX-UID 500X AMQ) through a color filter glass (Asahi Techno Glass) transmitting $\lambda > 420$ nm at room temperature. Evolved oxygen gas in a headspace was quantified by a Shimadzu GC-17A gas chromatograph [Ar carrier, a capillary column with molecular sieves (Agilent Technologies, 19095PMS0, 30 m×0.53 mm) at 313 K] equipped with a thermal conductivity detector.

A quantum yield of photon to O_2 evolution was determined for the reaction system with $LaCoO_3$ under the conditions. A square quartz cuvette (10 mm i.d.), which contained a phosphate buffer solution (50 mM, pH 7.0, 2.0 mL) of $LaCoO_3$ (0.025 g L^{-1}), $Na_2S_2O_8$ (5 mM) and $[Ru(bpy)_3](ClO_4)_2$ (0.25 mM), was irradiated with monochromatized light of $\lambda = 450$ nm from a Shimadzu RF-5300PC fluorescence spectrophotometer. The total number of incident photons were measured by a standard method using an actinometer (potassium ferrioxalate, $K_3[Fe^{III}(C_2O_4)]_3$) in an aqueous solution at room temperature where photon flux was determined to be 3.67×10^{-8} einstein s^{-1}. The evolved oxygen in a headspace of the cuvette was quantified by gas chromatography.

Results and Discussion

Characterization of Co-Containing Metal Oxides. $LaCoO_3$, $CoWO_4$, Co_3O_4 and $La_{0.7}Sr_{0.3}CoO_3$ were prepared by reported methods with modifications.[67–71] The obtained nanoparticles were characterized by TEM, XPS, EPR, XRD and N_2 adsorption measurements. Figure 1 shows the TEM images and X-ray diffraction spectra of the nanoparticles. The sizes of $LaCoO_3$, $CoWO_4$, Co_3O_4 and $La_{0.7}Sr_{0.3}CoO_3$ were about 60 nm, 20 nm, 15 nm and 70 nm, respectively. The BET surface areas determined by N_2 adsorption measurements at 77 K were 13 $m^2\ g^{-1}$ for $LaCoO_3$, 44 $m^2\ g^{-1}$ for $CoWO_4$, 37 $m^2\ g^{-1}$ for Co_3O_4 and 13 $m^2\ g^{-1}$ for $La_{0.7}Sr_{0.3}CoO_3$. The perovskite structure of $LaCoO_3$ and $La_{0.7}Sr_{0.3}CoO_3$, spinel structure of Co_3O_4 and wolframite-type structure of $CoWO_4$ were confirmed by their XRD patterns as shown in Figure 1e to 1h. The spectrum pattern of each catalyst agreed with the pattern in the literature.[72,73] The valences of Co species in $LaCoO_3$, $CoWO_4$ and Co_3O_4 were confirmed by XPS measurements for the energy region of Co 2p as shown in Fig. 2a. Strong satellite peaks, which are characteristic for Co^{2+} species, appeared around 787 eV and 804 eV for $CoWO_4$ (Figure 2a, blue).[69] Very weak satellite peaks for Co_3O_4 indicated the presence of cobalt(II) ions in Co_3O_4 as shown in Figure 2a (black). No satellite peak for $LaCoO_3$ assures that

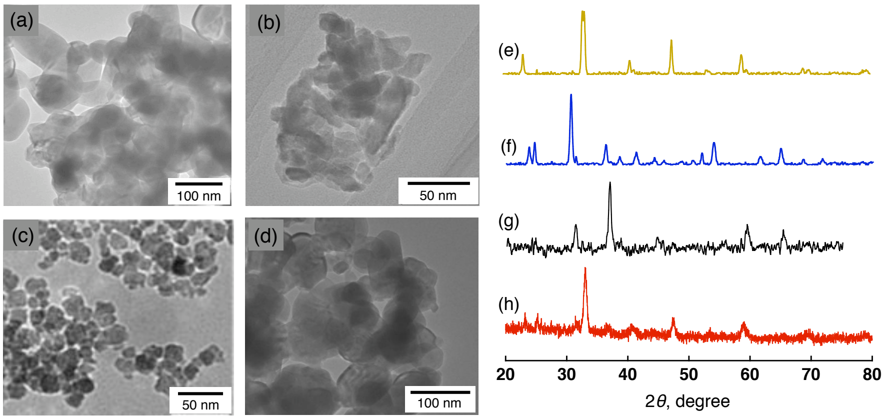

Figure 1. TEM images and powder X-ray diffraction patterns of (a), (e) $LaCoO_3$, (b), (f) $CoWO_4$, (c), (g) Co_3O_4 and (d), (h) $La_{0.7}Sr_{0.3}CoO_3$.

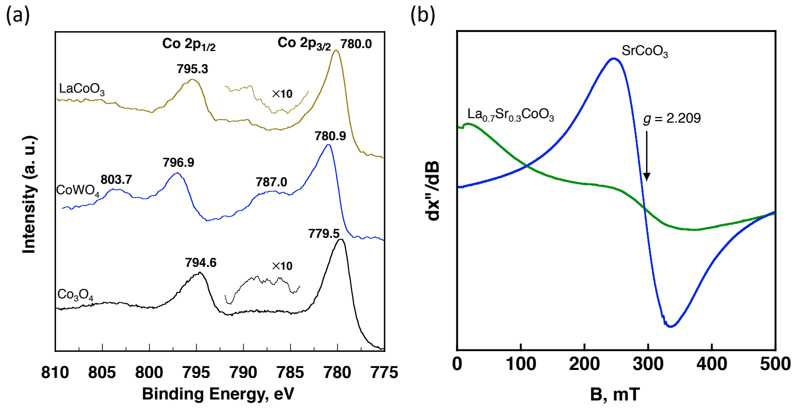

Figure 2. (a) X-ray photoelectron spectra in the region of Co $2p_{3/2}$ and Co $2p_{1/2}$ peaks of $LaCoO_3$ (brown), $CoWO_4$ (blue) and Co_3O_4 (black). (b) EPR spectrum of $La_{0.7}Sr_{0.3}CoO_3$ (green) measured at 77 K compared with that of $SrCoO_3$ (blue).

$LaCoO_3$ exclusively contains Co^{III} ions. The inclusion of Co^{IV} ions in $La_{0.7}Sr_{0.3}CoO_3$ was confirmed by the comparison of EPR spectrum with $SrCoO_3$, which contains cobalt(IV) species exclusively, as shown in Figure 2b (blue). A characteristic peak derived from cobalt(IV) species at $g = 2.209$ was observed for $La_{0.7}Sr_{0.3}CoO_3$ (Figure 2b, green).[74]

Catalytic Behaviors of Co-Containing Metal Oxides for Photocatalytic Water Oxidation. The photocatalytic cycle of water oxidation with a two-electron oxidant ($Na_2S_2O_8$) and a photosensitizer ($[Ru(bpy)_3]^{2+}$) using Co-containing metal oxide catalysts is shown in Scheme 1. Photoinduced electron transfer from the excited state of $[Ru(bpy)_3]^{2+}$ ($[Ru(bpy)_3]^{2+*}$: * denotes the excited state) to $S_2O_8^{2-}$ affords $[Ru(bpy)_3]^{3+}$, SO_4^{2-} and $SO_4^{\bullet-}$. The produced $SO_4^{\bullet-}$ is known to be a very strong oxidant [$E^0(SO_4^{\bullet-}/SO_4^{2-}) = 2.6$ V],[75] which can oxidize another $[Ru(bpy)_3]^{2+}$ to produce two equiv of $[Ru(bpy)_3]^{3+}$ in the overall photoinduced process. $[Ru(bpy)_3]^{3+}$ can oxidized water to evolve O_2 with Co-containing metal oxide catalysts.[76]

Scheme 1. Photocatalytic cycle of water oxidation with $Na_2S_2O_8$ and $[Ru(bpy)_3]^{2+}$

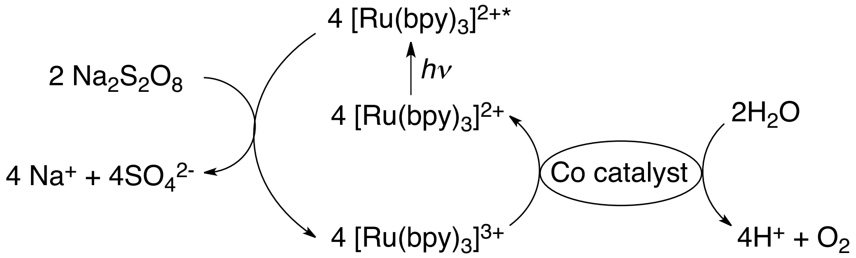

The catalytic activity of Co-containing metal oxide catalysts was examined in the thermal oxidation of water with $[Ru(bpy)_3]^{3+}$ prior to photocatalytic reaction. To a phosphate buffer solution (50 mM, pH 7.0) of $[Ru(bpy)_3]^{3+}$ (0.20 mM, 2.0 mL) in a quartz cuvette (1.0 cm path length), a small aliquot (50 μL) of an aqueous buffer solution (pH 7.0) containing a catalyst ($LaCoO_3$ or $La_{0.7}Sr_{0.3}CoO_3$, 63 mg L^{-1}) was added at 298 K. As indicated in Figure 3a (black), the concentration of $[Ru(bpy)_3]^{3+}$ decreased even in the absence of catalyst, however, the absorption decay was much faster in the presence of $LaCoO_3$ (brown) and $La_{0.7}Sr_{0.3}CoO_3$ (red). The faster decay observed for $LaCoO_3$ and $La_{0.7}Sr_{0.3}CoO_3$ compared with no catalyst conditions indicates that $LaCoO_3$ and $La_{0.7}Sr_{0.3}CoO_3$ can act as water oxidation catalyst.

Figure 3b depicts time courses of evolved O_2 with each Co-containing metal oxide catalyst under photocatalytic reaction conditions. A Co-containing metal oxide catalyst (0.50 mg) was added to a phosphate buffer solution (50 mM, pH 7.0, 2.0 mL) containing $Na_2S_2O_8$ (5.0 mM) and $[Ru(bpy)_3](ClO_4)_2$ (0.25 mM) with vigorous

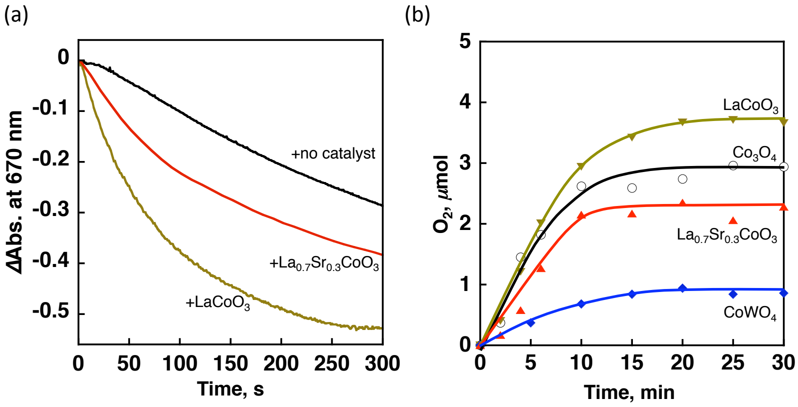

Figure 3. (a) Time courses of absorbance decay at 670 nm due to $[Ru(bpy)_3]^{3+}$ (pH 7.0, 0.20 mM) in the absence and presence of water oxidation catalysts (63 mg L^{-1}, black, none; blue, $La_{0.7}Sr_{0.3}CoO_3$; red, $LaCoO_3$) at 298 K. (b) Time courses of O_2 evolution under visible light irradiation (Xe lamp, $\lambda > 420$ nm) of a phosphate buffer solution (50 mM, 2 mL, pH 7.0) containing $[Ru(bpy)_3]^{2+}$ (0.25 mM), $Na_2S_2O_8$ (5 mM) with a Co-containing catalyst [0.25 g L^{-1}, Co_3O_4 (black), $LaCoO_3$ (brown), $La_{0.7}Sr_{0.3}CoO_3$ (red) and $CoWO_4$ (blue)].

magnetic stirring at room temperature. Then, the water oxidation reaction was started by photoirradiation of the reaction solution ($\lambda > 420$ nm). The evolved oxygen in a headspace of a reaction vial was quantified by a gas chromatograph at each reaction time. When no catalyst was added to the reaction solution, no oxygen evolution was observed in 30 min. When a catalyst was added to the reaction solution, oxygen evolution was observed and the catalyst amount of 0.25 g L^{-1} is the optimum conditions to provide the highest oxygen yield for the Co-containing metal oxide catalysts (Figure 4a–c and Table 1). As described above, $Na_2S_2O_8$ acts as a two-electron oxidant, thus, two moles of $Na_2S_2O_8$ are consumed for evolving 1 mole of O_2.[48] In the present reaction system, the stoichiometric amount of evolved oxygen would be 5 μmol.

The photocatalytic water oxidation with $LaCoO_3$, $CoWO_4$, Co_3O_4 and $La_{0.7}Sr_{0.3}CoO_3$ afforded the oxygen yields of 74%, 19%, 59% and 47%, respectively. The obtained oxygen yields were always lower than 100%, because of competitive oxidation of the bpy ligand of $[Ru(bpy)_3]^{2+}$.[77] The highest oxygen yield obtained with $LaCoO_3$ (74%) is higher than the reported value for the photocatalytic oxidation of water with $Na_2S_2O_8$ and $[Ru(bpy)_3]^{2+}$ using a tetracobalt polyoxometalate, $[Co_4(H_2O)_2(\alpha\text{-}PW_9O_{34})_2]^{10-}$, (45%) at pH 8.0.[48]

An apparent turnover frequency normalized by a catalyst surface area of O_2 evolution was calculated from the slope of the time course in the first 6 min after photoirradiation. The BET surface area, oxygen evolution rate (R_{O2}), the apparent TOF and O_2 yield in the photocatalytic water oxidation with various Co-containing metal oxides are listed in Table 2. The catalytic activity of heterogeneous catalysts is usually compared in terms

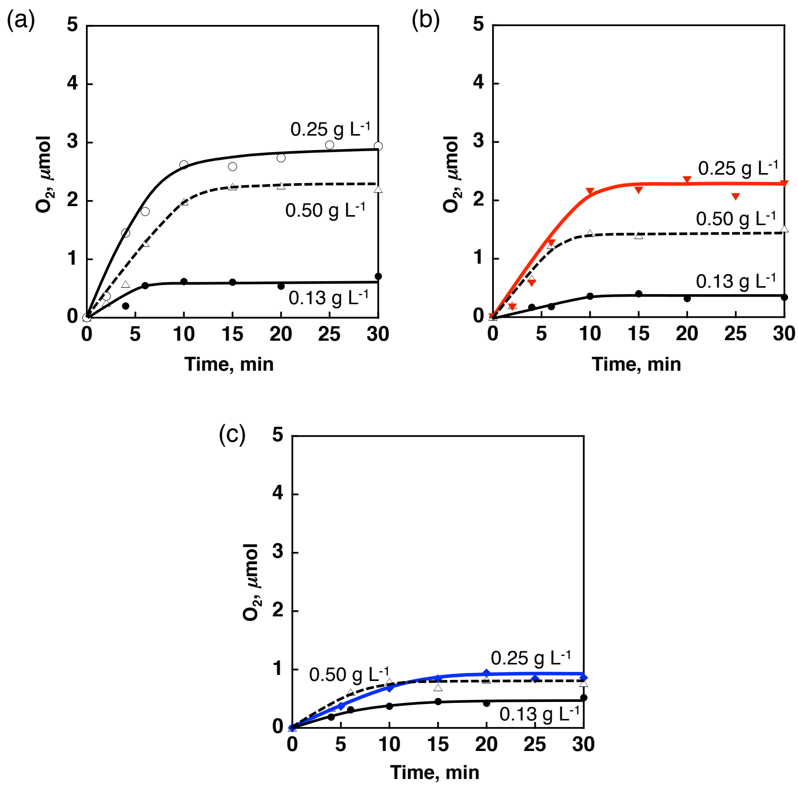

Figure 4. Time courses of oxygen evolution in the photocatalytic water oxidation with $[Ru(bpy)_3](ClO_4)_2$ (0.25 mM), $Na_2S_2O_8$ (5.0 mM) and different concentrations (0.13 g L^{-1}, 0.25 g L^{-1} and 0.50 g L^{-1}) of cobalt-based oxides (a) Co_3O_4, (b) $La_{0.7}Sr_{0.3}CoO_3$ and (c) $CoWO_4$. [photoirradiation ($\lambda >$ 420 nm) of a phosphate buffer solution (2.0 mL) at pH 7]. The apparent TOF values are tabulated in Table 1.

of the specific activity normalized by the surface area. The largest apparent TOF value of 0.89 μmol s^{-1} m^{-2} was obtained with $LaCoO_3$. The other apparent TOF values were 0.67 μmol s^{-1} m^{-2} with $La_{0.7}Sr_{0.3}CoO_3$, 0.27 μmol s^{-1} m^{-2} with Co_3O_4 and 0.056 μmol s^{-1} m^{-2} with CoWO4. These results clearly indicate that perovskite $LaCoO_3$ containing La^{3+} and Co^{III} ions is more active in the photocatalytic water oxidation than wolframite $CoWO_4$ containing solely W^{6+} and Co^{II} ions, spinel Co_3O_4 and $La_{0.7}Sr_{0.3}CoO_3$ which contains Sr^{2+} and Co^{IV} species in perovskite structure.

Electrocatalytic water oxidation has been previously reported with perovskite catalysts $LaCoO_3$ and $La_{0.6}Sr_{0.4}CoO_3$ under pH 14 conditions where $La_{0.6}Sr_{0.4}CoO_3$ provided smaller Arrhenius activation energy (18.1 kcal mol^{-1}) than $LaCoO_3$ for oxygen evolution (19.5 kcal mol^{-1}).[78] Direct comparison of water oxidation activities under different reaction conditions is difficult, however, the difference in the catalytic behavior may be ascribed to mainly the different pH conditions. The oxidation of hydroxide anion instead of water oxidation proceeded at pH 14.[78,79]

A quantum yield of photon to O_2 evolution was determined for the reaction system with $LaCoO_3$ under the conditions of pH 7.0 by visible light irradiation (λ = 450 nm). All of the incident photons are captured by $[Ru(bpy)_3]^{2+}$ in the reaction solution due to the large extinction coefficient ($\varepsilon_{450} = 1.4 \times 10^4$ M^{-1} cm^{-1}) and high concentration of $[Ru(bpy)_3]^{2+}$ (0.25 mM). Because one photon absorption by $[Ru(bpy)_3]^{2+}$ in the presence of $S_2O_8^{2-}$ produces two equiv. of $[Ru(bpy)_3]^{3+}$,[48] the quantum yield (ϕ) was determined by eq 1. By using eq 1, the quantum yield of O_2 evolution with $LaCoO_3$ was

Table 1. BET Surface Area, Oxygen Evolution Rate (R_{O2}), Apparent Turnover Frequency (TOF) and O_2 Yield in the Photocatalytic Water Oxidation with Various Cobalt-Containing Metal Oxide Catalysts in Different Concentrations

catalyst	concentration ($g\ L^{-1}$)	BET ($m^2\ g^{-1}$)	R_{O2}[a] ($\mu mol\ s^{-1}$)	R_{O2}[b] ($\mu mol\ s^{-1}\ g^{-1}$)	Apparent TOF[c] ($\mu mol\ s^{-1}\ m^{-2}$)	O_2 yield[d] (%)
$LaCoO_3$	0.13	13	0.0032	13	0.66	31
$LaCoO_3$	0.25	13	0.0056	11	0.89	74
$LaCoO_3$	0.50	13	0.0064	6.4	1.37	78
$CoWO_4$	0.13	44	0.00086	3.5	0.079	10
$CoWO_4$	0.25	44	0.0012	2.5	0.056	19
$CoWO_4$	0.50	44	0.0017	1.7	0.039	17
Co_3O_4	0.13	37	0.0015	6.1	0.16	14
Co_3O_4	0.25	37	0.0051	10	0.27	59
Co_3O_4	0.50	37	0.0036	3.6	0.10	45
$La_{0.7}Sr_{0.3}CoO_3$	0.13	13	0.00049	1.9	0.15	8
$La_{0.7}Sr_{0.3}CoO_3$	0.25	13	0.0035	7.1	0.55	47
$La_{0.7}Sr_{0.3}CoO_3$	0.50	13	0.0034	3.4	0.27	30
$NdCoO_3$	0.13	11	0.0018	7.1	0.67	17
$NdCoO_3$	0.25	11	0.0046	9.2	0.87	59
$NdCoO_3$	0.50	11	0.0033	3.3	0.31	30
$YCoO_3$	0.13	4.5	0.00069	2.8	0.62	6
$YCoO_3$	0.25	4.5	0.0018	3.6	0.80	24
$YCoO_3$	0.50	4.5	0.00053	0.5	0.12	7

[a] O_2 Evolution rate in the first 6 min after photoirradiation (λ > 420 nm) of an aqueous buffer solution (pH 7.0, 2.0 mL) containing Co-based oxide, $Na_2S_2O_8$ (5.0 mM) and $[Ru(bpy)_3]^{2+}$ (0.20 mM). [b] O_2 Evolution rate normalized by catalyst weight. [c] apparent TOF values normalized by the catalyst surface area. [d] Two times of amount of evolved O_2 divided by the initial amount of $Na_2S_2O_8$.

Table 2. BET Surface Area, Oxygen Evolution Rate (R_{O2}), Apparent Turnover Frequency (TOF) and O_2 Yield Obtained with Cobalt-Containing Catalysts in the Photocatalytic Water Oxidation

catalyst	BET ($m^2\ g^{-1}$)	R_{O2}[a] ($\mu mol\ s^{-1}\ g^{-1}$)	apparent TOF[b] ($\mu mol\ s^{-1}\ m^{-2}$)	O_2 yield[c] (%)
$LaCoO_3$	13	11	0.89	74
$CoWO_4$	44	2.5	0.056	19
Co_3O_4	37	10	0.27	59
$La_{0.7}Sr_{0.3}CoO_3$	13	7.1	0.67	47
$NdCoO_3$	11	9.2	0.87	59
$YCoO_3$	4.5	3.6	0.80	24

[a] O_2 evolution rate normalized by catalyst weight in the first 6 min after photoirradiation ($\lambda > 420$ nm) of an aqueous buffer solution (pH 7.0, 2 mL) containing a Co-containing metal oxide catalyst (0.25 g L^{-1}), $Na_2S_2O_8$ (5.0 mM) and $[Ru(bpy)_3]^{2+}$ (0.20 mM). [b] Turnover frequency normalized by a catalyst surface area for O_2 evolution. [c] Two times of amount of evolved O_2 divided by the initial amount of $Na_2S_2O_8$.

$$\phi = 2 \times (\text{No. of evolved O2})/(\text{No. of absorbed photons}) \tag{1}$$

determined to be 0.16.

In general, an advantage of heterogeneous catalysts can be found in robustness compared with homogeneous catalysts. After 1st reaction, catalytic powder of $LaCoO_3$ (0.25 g L^{-1}) was separated by centrifugation and added to a phosphate buffer solution (pH 7.0, 2.0 mL) containing $Na_2S_2O_8$ (5.0 mM) and $[Ru(bpy)_3](ClO_4)_2$ (0.25 mM) with photoirradiation ($\lambda > 420$ nm). Figure 5a shows time courses of oxygen evolution with $LaCoO_3$ for repetitive uses. The apparent TOF for O_2 evolution were determined to be 0.89 μmol s^{-1} m^{-2}, 0.93 μmol s^{-1} m^{-2} and 0.97 μmol s^{-1} m^{-2} with oxygen yields of 74%, 78% and 64% for 1st, 2nd and 3rd cycles, respectively. Even though it looks that the catalyst was deactivated at 3rd cycle, it may be ascribed to loss of the catalyst particles during the recovering process, because the apparent TOF value was maintained to be the same for the 3rd cycle as the 1st and 2nd cycles.

The catalytic activity of $LaCoO_3$ in the photocatalytic water oxidation with $Na_2S_2O_8$ was also examined under various pH conditions. Figure 5b shows time courses of O_2 evolution by photoirradiation ($\lambda > 420$ nm) of a phosphate buffer solution (2.0 mL, pH 6.0, 7.0 or 8.0) containing $Na_2S_2O_8$ (5.0 mM) and $[Ru(bpy)_3](ClO_4)_2$ (0.25 mM) with $LaCoO_3$ (0.25 g L^{-1}). When the pH was decreased from 7 to 6, the oxygen yield dropped to 52% with the smaller apparent TOF value of 0.61 μmol s^{-1} m^{-2}. When pH was increased from 7 to 8, both oxygen yield and the apparent TOF are improved to

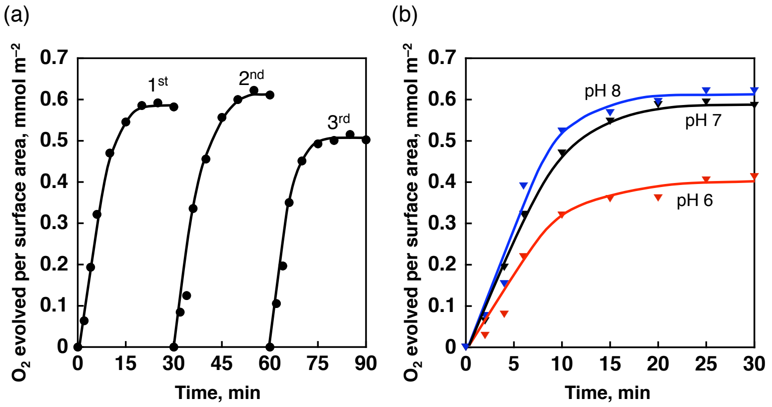

Figure 5. (a) Time courses of O_2 evolution normalized by a catalyst surface area in repetitive examinations of $LaCoO_3$ (0.25 g L^{-1}) for the photocatalytic water oxidation [$Na_2S_2O_8$ (5.0 mM) and $[Ru(bpy)_3](ClO_4)_2$ (0.25 mM) under photoirradiation ($\lambda > 420$ nm) of a phosphate buffer solution (pH 7.0, 2.0 mL) at 298 K]. (b) Time courses of O_2 evolution normalized by a catalyst surface area in the photocatalytic water oxidation with $LaCoO_3$ under various pH conditions (pH 6.0, 7.0 and 8.0) at 298 K.

78% and 1.08 μmol s^{-1} m^{-2}, respectively. Even though the reactions were performed in buffer solutions, pH values of the solutions have changed from 6.0 to 3.7, 7.0 to 6.8 and 8.0 to 7.3. The water oxidation is thermodynamically favorable under the conditions of higher pH, therefore, the lower O_2 yield obtained at pH 6.0 may be resulted from the lowering pH during the reaction.

In order to optimize the reaction conditions for $LaCoO_3$, the concentration effect of each component on O_2 evolution rates has been investigated as shown in Figure 6. When the concentration of $[Ru(bpy)_3]^{2+}$ was increased from 0.25 mM to 0.50 mM (Fig. 6a, black to blue), the apparent TOF of O_2 evolution determined from the slope for the first 6 min increased from 0.89 μmol s^{-1} m^{-2} to 1.37 μmol s^{-1} m^{-2} with similar O_2 yields of 74% and 76%. On the other hand, a decrease in the concentration of $[Ru(bpy)_3]^{2+}$ to 0.13 mM (Figure 6a, red) resulted in a decrease in the apparent TOF value to 0.66 μmol s^{-1} m^{-2} with a lower O_2 yield of 59%. When the concentration of $Na_2S_2O_8$ was increased from 5.0 mM to 10 mM (Figure 6b), the apparent TOF value increased to 1.43 μmol s^{-1} m^{-2} with the O_2 yield of 70%. A decrease in $Na_2S_2O_8$ concentration to 2.5 mM also resulted in a decrease in the apparent TOF to 0.63 μmol s^{-1} m^{-2} with a slightly higher O_2 yield of 79%.

On the contrary, the concentration of $LaCoO_3$ has quite different influence as compared with those of $[Ru(bpy)_3]^{2+}$ and $Na_2S_2O_8$. Even when the amount of $LaCoO_3$ was doubled from 0.25 g L^{-1} to 0.50 g L^{-1}, no obvious difference was observed in the O_2 evolution rate (Figure 6c). Because the apparent TOF values were calculated based on the surface area of a used catalyst, the apparent TOF for the system using a large amount of $LaCoO_3$ (0.50 g L^{-1}) became smaller value (0.55 μmol s^{-1} m^{-2}). When the

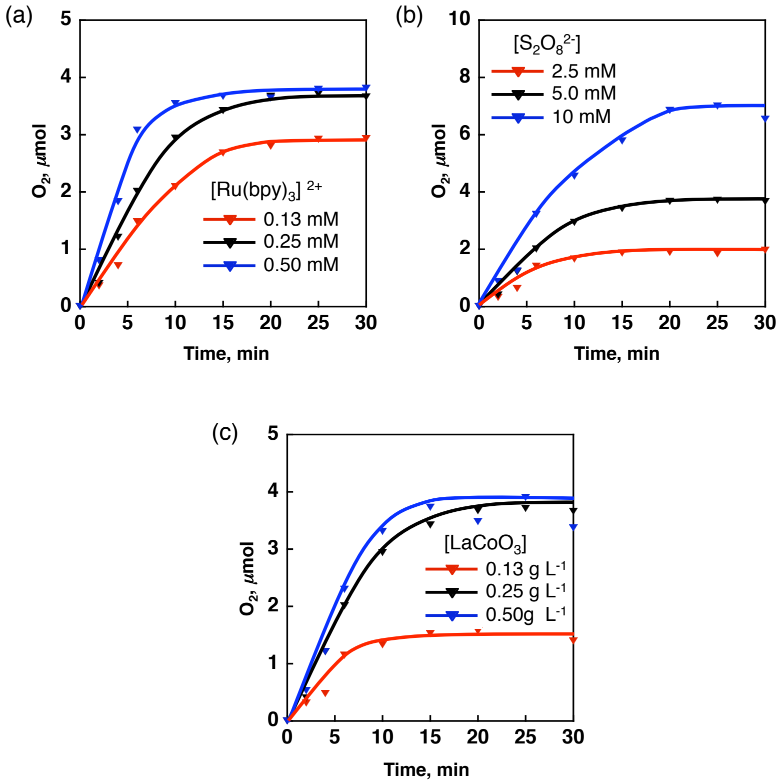

Figure 6. Time courses of oxygen evolution in the photocatalytic water oxidation with different concentrations of $[Ru(bpy)_3](ClO_4)_2$, $Na_2S_2O_8$ and $LaCoO_3$. (a) $[Ru(bpy)_3](ClO_4)_2$ (0.125 mM, red; 0.25 mM, black and 0.50 mM, blue), $Na_2S_2O_8$ (5.0 mM) and $LaCoO_3$ (0.25 g L^{-1}), (b) $Na_2S_2O_8$ (2.5 mM, red; 5.0 mM, black and 10 mM, blue), $[Ru(bpy)_3](ClO_4)_2$ (0.25 mM) and $LaCoO_3$ (0.25 g L^{-1}) and (c) $LaCoO_3$ (0.13 g L^{-1}, red; 0.25 g L^{-1}, black and 0.50 g L^{-1}, blue), $[Ru(bpy)_3](ClO_4)_2$ (0.25 mM) and $Na_2S_2O_8$ (5.0 mM) [photoirradiation ($\lambda > 420$ nm) of a phosphate buffer solution (2.0 mL) at pH 7]. The apparent TOF values are tabulated in Table 1.

amount of $LaCoO_3$ was reduced to 0.13 g L^{-1}, the apparent TOF slightly increased to 1.02 μmol s^{-1} m^{-2} (Figure 6c and Table 2). Thus, these experiments suggest that high concentrations of $[Ru(bpy)_3]^{2+}$ and $Na_2S_2O_8$ with a small amount of $LaCoO_3$ catalyst provide a high apparent TOF for the photocatalytic O_2 evolution. The photocatalytic water oxidation using high concentrations of $[Ru(bpy)_3]^{2+}$ and $Na_2S_2O_8$ with smaller amounts of the $LaCoO_3$ catalyst has been examined to maximize the apparent TOF value for O_2 evolution (Figure 7). When the concentrations of $[Ru(bpy)_3]^{2+}$ and $Na_2S_2O_8$ were increased to 0.5 mM and 10 mM and the catalyst amount was reduced to 0.050 g L^{-1}, the apparent TOF value becomes as high as 3.1 μmol s^{-1} m^{-2} with a lower O_2 yield of 22%. The further reduction of the catalyst concentration to 0.025 g L^{-1} resulted in the apparent TOF value of 4.1 μmol s^{-1} m^{-2} with the O_2 yield of 14%. The apparent TOF value of 4.1 μmol s^{-1} m^{-2} is more than 5 times higher than the highest apparent TOF value of 0.74 μmol s^{-1} m^{-2} ever reported for photocatalytic water oxidation with

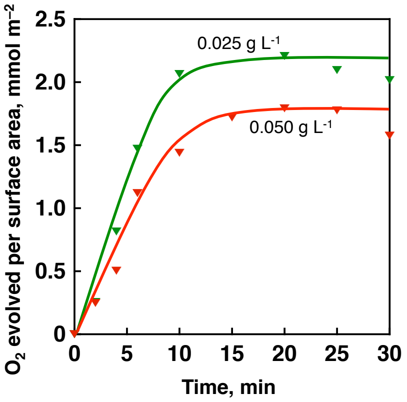

Figure 7. Time courses of oxygen evolution normalized by a catalyst surface area in the photocatalytic water oxidation with different concentrations of $LaCoO_3$. ($LaCoO_3$ (0.050 g L^{-1}, red and 0.025 g L^{-1}, green), $[Ru(bpy)_3](ClO_4)_2$ (0.25 mM) and $Na_2S_2O_8$ (5.0 mM) [photoirradiation (λ > 420 nm) of a phosphate buffer solution (2.0 mL) at pH 7]).

Co_3O_4.[80] In addition, the apparent TOF value of 4.1 μmol s^{-1} m^{-2} was beyond the highest apparent TOF value of 0.97 μmol s^{-1} m^{-2} reported for Mn_2O_3 among oxides with first-row transition metal ions under non-basic conditions.[80]

Co_3O_4 nanoparticles encapsulated in mesoporous silica have previously been reported to have TOF values for the photocatalytic water oxidation between 6.0×10^{-4} and 1.0×10^{-2} s^{-1} under conditions of around pH 5.8.[80] Under the electrocatalytic conditions at room temperature, Co_3O_4 has been reported to exhibit TOF values in the range between 8×10^{-4} and 6×10^{-3} s^{-1} at pH 14.[80] In more basic solutions of pH 14.7, much higher TOF value of 0.12 s^{-1} has also been reported for 5.9 nm Co_3O_4.[81] When the number of Co ions on the surface of Co3O4 was estimated from the BET surface area, the Co_3O_4 particles employed herein showed slightly higher but a comparable TOF of 1.3×10^{-2} s^{-1} under the conditions of pH 7.

In order to confirm the importance of additional ions, a series of perovskite catalysts were prepared by isomorphous substitution of the trivalent cation of La^{3+} in $LaCoO_3$ with Nd^{3+} and Y^{3+}. The perovskite structures of synthesized $NdCoO_3$ and $YCoO_3$ were confirmed by XRD as shown in Figure 8. BET surface areas of $NdCoO_3$ and $YCoO_3$ were 11 and 4.5 m^2 g^{-1}, respectively. The photocatalytic water oxidation was conducted with $NdCoO_3$ or $YCoO_3$ (0.25 g L^{-1}) for an aqueous buffer solution (pH 7.0, 2.0 mL) containing $Na_2S_2O_8$ (5.0 mM) and $[Ru(bpy)_3](ClO_4)_2$ (0.25 mM). The optimum concentrations of $NdCoO_3$ and $YCoO_3$ for high TOF values and O_2 yields were also 0.25 g L^{-1} as indicated in Figure 9.

Figure 10 shows time profiles of O_2 evolution normalized by catalyst surface area in the photocatalytic water oxidation with $LaCoO_3$, $NdCoO_3$ and $YCoO_3$. The O_2 yields with $NdCoO_3$ and $YCoO_3$ were 59% and 24%, which are lower than the yield of 74%

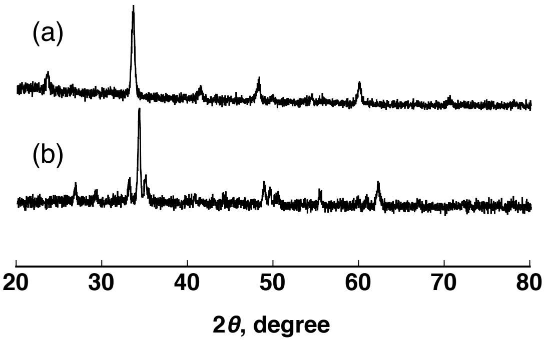

Figure 8. Powder X-ray diffraction patterns of (a) $NdCoO_3$ and (b) $YCoO_3$.

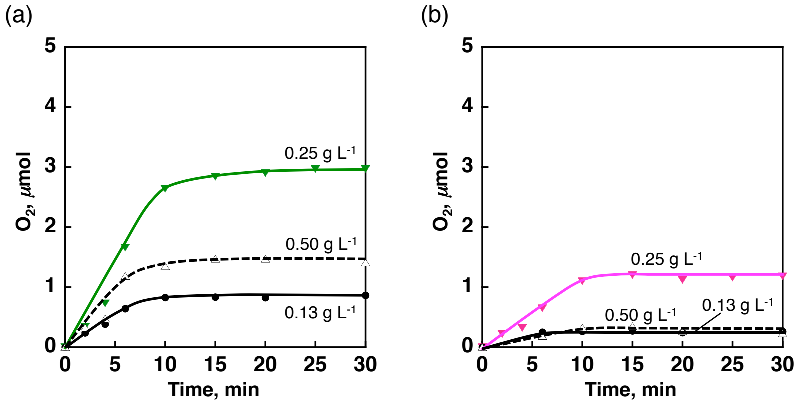

Figure 9. Time courses of oxygen evolution in the photocatalytic water oxidation with $[Ru(bpy)_3](ClO_4)_2$ (0.25 mM), $Na_2S_2O_8$ (5.0 mM) and different concentrations (0.13 g L^{-1}, 0.25 g L^{-1} and 0.50 g L^{-1}, green) of a cobalt-based catalyst (a) $NdCoO_3$ and (b) $YCoO_3$. [photoirradiation (λ > 420 nm) of a phosphate buffer solution (2.0 mL) at pH 7]).

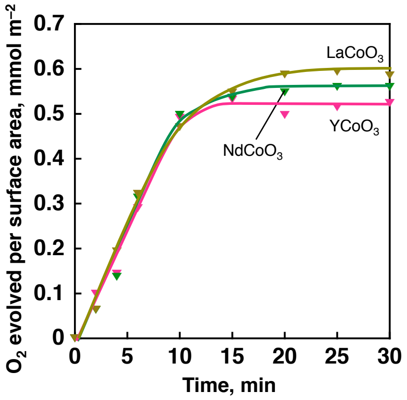

Figure 10. Time courses of oxygen evolution normalized by a catalyst surface area in the photocatalytic water oxidation with $Na_2S_2O_8$ (5.0 mM) and $[Ru(bpy)_3](ClO_4)_2$ (0.25 mM) using perovskites (0.25 g L^{-1}, $LaCoO_3$, brown; $NdCoO_3$, green and $YCoO_3$, pink) under photoirradiation (λ > 420 nm) of a phosphate buffer solution (2.0 mL) at pH 7.0.

with $LaCoO_3$. However, the apparent TOF values of $LaCoO_3$, $NdCoO_3$ and $YCoO_3$ were quite similar to each other: 0.89 μmol s^{-1} m^{-2}, 0.87 μmol s^{-1} m^{-2} and 0.80 μmol s^{-1} m^{-2} as summarized in Table 2. Thus, perovskite containing non-redox active trivalent ions and Co ions act as highly active starting catalysts in the photocatalytic water oxidation.

Conclusions

In conclusion, we have shown that the catalytic activity of Co-containing metal oxides depends on the additional metal ions, which are not redox active, in the photocatalytic water oxidation with $Na_2S_2O_8$ and $[Ru(bpy)_3]^{2+}$. $LaCoO_3$ exhibited the highest catalytic activity compared with other Co-containing catalysts of $CoWO_4$ and Co_3O_4. The partial replacement of La^{3+} with Sr^{2+} allowing the formation of Co^{IV} species in Co-containing perovskite led to decrease in catalytic activity. On the other hand, the high catalytic activity of $LaCoO_3$ was maintained by the replacement of La^{3+} with Nd^{3+} or Y^{3+}, $NdCoO_3$ and $YCoO_3$. The trivalent metal ions enhance the oxidation activity of Co^{IV} species, which should be formed during the water oxidation, by stabilizing Co^{III} state. Thus, the property of the additional metal ions affects the catalytic activity of Co-containing catalyst and is important for developing highly reactive and robust catalysts for the photocatalytic water oxidation.

References

(1) Kiwi, J.; Kalyanasundaram, K.; Grätzel, M. *Struct. Bonding* **1982**, *49*, 37.

(2) H. B. Gray and A. W. Maverick, *Science*, 1981, **214**, 1201.

(3) Esswein, A. J.; Nocera, D. G. *Chem. Rev.* **2007**, *107*, 4022.

(4) Fukuzumi, S. *Phys. Chem. Chem. Phys.* **2008**, *10*, 2283.

(5) Fukuzumi, S. *Eur. J. Inorg. Chem*. **2008**, 1351.

(6) Wang, M.; Na, Y.; Gorlov, M.; Sun, L. *Dalton Trans*. **2009**, 6458.

(7) Tinker, L. L.; McDaniel, N. D.; Bernhard, S. *J. Mater. Chem.* **2009**, *19*, 3328.

(8) Amao, Y. *ChemCatChem* **2011**, *3*, 458.

(9) Guldi, D. M.; Sgobba, V. *Chem. Commun*. **2011**, *47*, 606.

(10) Fukuzumi, S.; Yamada, Y.; Suenobu, T.; Ohkubo, K.; Kotani, H. *Energy Environ. Sci.* **2011**, *4*, 2754.

(11) Yamada, Y.; Miyahigashi, T.; Kotani, H.; Ohkubo, K.; Fukuzumi, S. *J. Am. Chem. Soc.* **2011**, *133*, 16136.

(12) Lewis, N. S.; Nocera, D. G. *Proc. Natl. Acad. Sci. U. S. A.* **2006**, *103*, 15729.

(13) Gray, H. B. *Nat. Chem.* **2009**, *1*, 7.

(14) Hurst, J. K. *Science* **2010**, *328*, 315.

(15) Cook, T. R.; Dogutan, D. K.; Reece, S. Y.; Surendranath, Y.; Teets, T. S.; Nocera, D. G.; *Chem. Rev.* **2010**, *110*, 6474.

(16) Eisenberg, R.; Gray, H. B. *Inorg. Chem.* **2008**, *47*, 1697.

(17) Concepcion, J. J.; Jurss, J. W.; Brennaman, M. K.; Hoertz, P. G.; Patrocinio, A. O. T.; Murakami Iha, N. Y.; Templeton, J. L.; Meyer, T. J. *Acc. Chem. Res.* **2009**, *42*, 1954.

(18) Jiao, F.; Frei, H. *Energy Environ. Sci.* **2010**, *3*, 1018.

(19) Dismukes, G. C.; Brimblecombe, R.; Felton, G. A. N.; Pryadun, R. S.; Sheats, J. E.; Spiccia, L.; Swiegers, G. F. *Acc. Chem. Res.* **2009**, *42*, 1935.

(20) Youngblood, W. J.; Lee, S.-H. A.; Maeda, K.; Mallouk, T. E. *Acc. Chem. Res.* **2009**, *42*, 1966.

(21) Xu, Y.; Fischer, A.; Duan, L.; Tong, L.; Gabrielsson, E.; Åkermark, B.; Sun, L. *Angew. Chem., Int. Ed.* **2010**, *49*, 8934.

(22) Xu, Y. H.; Duan, L. L.; Tong, L. P.; Åkermark, B.; Sun, L. C. *Chem. Commun.* **2010**, *46*, 6506.

(23) Duan, L. L.; Xu, Y. H.; Zhang, P.; Wang, M.; Sun, L. C. *Inorg. Chem.* **2010**, *49*, 209.

(24) Polyansky, D. E.; Muckerman, J. T.; Rochford, J.; Zong, R.; Thummel, R. P.; Fujita, E. *J. Am. Chem. Soc.* **2011**, *133*, 14649.

(25) Blakemore, J. D.; Schley, N. D.; Balcells, D.; Hull, J. F.; Olack, G. W.; Incarvito, C. D.; Eisenstein, O.; Brudvig, G. W.; Crabtree, R. H. *J. Am. Chem. Soc.* **2010**, *132*, 16017.

(26) Murakami, M.; Hong, D.; Suenobu, T.; Yamaguchi, S.; Ogura, T.; Fukuzumi, S. *J. Am. Chem. Soc.* **2011**, *133*, 11605.

(27) Gersten, S. W.; Samuels, G. J.; Meyer, T. J. *J. Am. Chem. Soc.* **1982**, *104*, 4029.

(28) Concepcion, J. J.; Tsai, M. K.; Muckerman, J. T.; Meyer, T. J. *J. Am. Chem. Soc.* **2010**, *132*, 1545.

(29) Concepcion, J. J.; Jurss, J. W.; Norris, M. R.; Chen, Z. F.; Templeton, J. L.; Meyer, T. J. *Inorg. Chem.* **2010**, *49*, 1277.

(30) Yamazaki, H.; Shouji, A.; Kajita, M.; Yagi, M. *Coord. Chem. Rev.* **2010**, *254*, 2483.

(31) Artero, V.; Chavarot-Kerlidou, M.; Fontecave, M. *Angew. Chem. Int. Ed.* **2011**, *50*, 7238.

(32) Dau, H.; Limberg, C.; Reier, T.; Risch, M.; Roggan, S.; Strasser, P. *ChemCatChem* **2010**, *2*, 724.

(33) Barroso, M.; Cowan, A. J.; Pendlebury, S. R.; Graetzel, M.; Klug, D. R.; Durrant, J. R. *J. Am. Chem. Soc.* **2011**, *133*, 14868.

(34) Chou, N. H.; Ross, P. N.; Bell. A. T.; Tilley, T. D. *ChemSusChem* **2011**, *4*, 1566.

(35) Dogutan, D. K.; McGuire, Jr. R.; Nocera, D. G. *J. Am. Chem. Soc.* **2011**, *133*, 9178.

(36) Esswein, A. J.; Surendranath, Y.; Reece, S. Y.; Nocera, D. G. *Energy Environ. Sci.* **2011**, *4*, 499.

(37) Gerken, J. B.; McAlpin, J. G.; Chen, J. Y. C.; Rigsby, M. L.; Casey, W. H.; Britt, R. D.; Stahl, S. S. *J. Am. Chem. Soc.* **2011**, *133*, 14431.

(38) Lieb, D.; Zahl, A.; Wilson, E. F.; Streb, C.; Nye, L. C.; Meyer, K.; Ivanovic-Burmazovic, I. *Inorg. Chem.* **2011**, *50*, 9053.

(39) Mattioli, G.; Risch, M.; Bonapasta, A. A.; Dau H.; Guidoni, L. *Phys. Chem. Chem. Phys.* **2011**, *13*, 15437.

(40) McAlpin, J. G.; Stich, T. A.; Ohlin, C. A.; Surendranath, Y.; Nocera, D. G.; Casey, W. H.; Britt, R. D. *J. Am. Chem. Soc.* **2011**, *133*, 15444.

(41) McDonald, K. J.; Choi, K.-S. *Chem. Mater.* **2011**, *23*, 1686.

(42) Pijpers, J. J. H.; Winkler, M. T.; Surendranath, Y.; Buonassisi, T.; Nocera, D. G. *Proc. Nat. Acad. Sci. U. S. A.* **2011**, *108*, 10056.

(43) Shevchenko, D.; Anderlund, M. F.; Thapper, A.; Styring, S. *Energy Environ. Sci.* **2011**, *4*, 1284.

(44) Symes, M. D.; Surendranath, Y.; Lutterman, D. A.; Nocera, D. G. *J. Am. Chem. Soc.* **2011**, *133*, 5174.

(45) Wang, L.-P.; Van Voorhis, T. *J. Phys. Chem. Lett.* **2011**, *2*, 2200.

(46) Wasylenko, D. J.; Ganesamoorthy, C.; Borau-Garcia, J.; Berlinguette, C. P.; *Chem. Commun.* **2011**, *47*, 4249.

(47) Young, E. R.; Costi, R.; Paydavosi, S.; Nocera, D. G.; Bulovic, V.; *Energy Environ. Sci.* **2011**, *4*, 2058.

(48) Huang, Z.; Luo, Z.; Geletii, Y. V.; Vickers, J. W.; Yin, Q.; Wu, D.; Hou, Y.; Ding, Y.; Song, J.; Musaev, D. G.; D. G.; Hill, D. G.; Lian, T. *J. Am. Chem. Soc.* **2011**, *133*, 2068.

(49) Yin, Q.; Tan, J. M.; Besson, C.; Geletii, Y. V.; Musaev, D. G.; Kuznetsov, A. E.; Luo, Z.; Hardcastle, K. I.; Hill, C. L. *Science* **2010**, *328*, 342.

(50) Stracke, J. J.; Finke, R. G. *J. Am. Chem. Soc.* **2011**, *133*, 14872.

(51) Kanan, M. W.; Nocera, D. G. *Science* **2008**, *321*, 1072.

(52) Kanan, M. W.; Surendranath, Y.; Nocera, D. G. *Chem. Soc. Rev.* **2009**, *38*, 109.

(53) Kanan, M. W.; Yano, J.; Surendranath, Y.; Dincă, M.; Yachandra, V. K.; Nocera, D. G. *J. Am. Chem. Soc.* **2010**, *132*, 13692.

(54) Surendranath, Y.; Kanan, M. W.; Nocera, D. G. *J. Am. Chem. Soc.* **2010**, *132*, 16501.

(55) Zhong, D. K.; Cornuz, M.; Sivula, K.; Grätzel, M.; Gamelin, D. R. *Energy Environ. Sci.* **2011**, *4*, 1759.

(56) Zhong, D. K.; Gamelin, D. R. *J. Am. Chem. Soc.* **2010**, *132*, 4202.

(57) McAlpin, J. G.; Surendranath, Y.; Dincă, M.; Stich, T. A.; Stoian, S. A.; Casey, W. H.; Nocera, D. G.; Britt, R. D. *J. Am. Chem. Soc.* **2010**, *132*, 6882.

(58) Amunts, A.; Drory, O.; Nelson, N. *Nature* **2007**, *447*, 58.

(59) Umena, Y.; Kawakami, K.; Shen, J.-R.; Kamiya, N. *Nature* **2011**, *473*, 55.

(60) Kanady, J. S.; Tsui, E. Y.; Day, M. W.; Agapie, T. *Science* **2011**, *333*, 733.

(61) Fukuzumi, S.; Morimoto, Y.; Kotani, H.; Naumov, P.; Lee, Y. M.; Nam, W. *Nature Chem.* **2010**, *2*, 756.

(62) Morimoto, Y.; Kotani, H.; Park, J.; Lee, Y. M.; Nam, W.; Fukuzumi, S. *J. Am. Chem. Soc.* **2011**, *133*, 403.

(63) Park, J.; Morimoto, Y.; Lee, Y.-M.; Nam W.; Fukuzumi, S. *J. Am. Chem. Soc.* **2011**, *133*, 5236.

(64) Park, J.; Morimoto, Y.; Lee, Y.-M.; Nam, W.; Fukuzumi, S. *Inorg. Chem.* **2011**, *50*, 11612.

(65) Fukuzumi, S. *Prog. Inorg. Chem*. **2009**, *56*, 49.

(66) Fukuzumi, S.; Ohkubo, K. *Coord. Chem. Rev*. **2010**, *254*, 372.

(67) Ghasdi, M.; Alamdari, H. *Sens. Actuators, B* **2010**, *148*, 478.

(68) Gao, Z.; Wang, R. *Appl. Catal. B* **2010**, *98,* 147.

(69) Song, X. C.; Yang, E.; Ma, R.; Chen, H. F.; Zhao, Y. *J. Nanopart. Res.* **2007**, *10*, 709.

(70) Dong, Y. M.; He, K.; Yin, L.; Zhang, A. M. *Nanotechnology* **2007**, *18*, 435602.

(71) Buassi-Monroy, O. S.; Luhrs, C. C.; Chávez-Chávez, A.; Michel, C. R. *Mater. Lett.* **2004**, *58*, 716.

(72) Yamada, Y.; Yano, K.; Xu, Q.; Fukuzumi, S. *J. Phys. Chem. C* **2010**, *114*, 16456.

(73) Mathew, T.; Shiju, N. R.; Sreekumar, K.; Rao, B. S.; Gopinath, C. S. *J. Catal.* **2002**, *210*, 405.

(74) Phan, T. L.; Bau, L. V.; Khiem, N. V.; Phuc, N. X.; Yu, S. C. *Phys. Stat. Sol. (b)* **2005**, *242*, 1522.

(75) Eberson, L. *Electron Transfer Reactions in Organic Chemistr*y; Springer-Verlag, Berlin, **1987**.

(76) Harriman, A.; Pickering, I. J.; Thomas, J. M.; Christensen, P. A. *J. Chem. Soc., Faraday Trans. 1* **1988**, *84*, 2795.

(77) White, H. S.; Becker, W. G.; Bard, A. J. *J. Phys. Chem.* **1984**, *88*, 1840.

(78) Bockris, J. O. M.; Otagawa, T. *J. Phys. Chem.* **1983**, *87*, 2960.

(79) Bockris, J. O. M.; Otagawa, T. *J. Electrochem. Soc.* **1984**, *131*, 290.

(80) Jiao, F.; Frei, H. *Angew. Chem*., *Int. Ed.* **2009**, *48*, 1841.

(81) Esswein, A. J.; McMurdo, M. J.; Ross, P. N.; Bell, A. T.; Tilley, T. D. *J. Phys. Chem. C* **2009**, *113*, 15068.

Chapter 6

Catalysis of Nickel Ferrite for Photocatalytic Water Oxidation Using $[Ru(bpy)_3]^{2+}$ and $S_2O_8^{2-}$

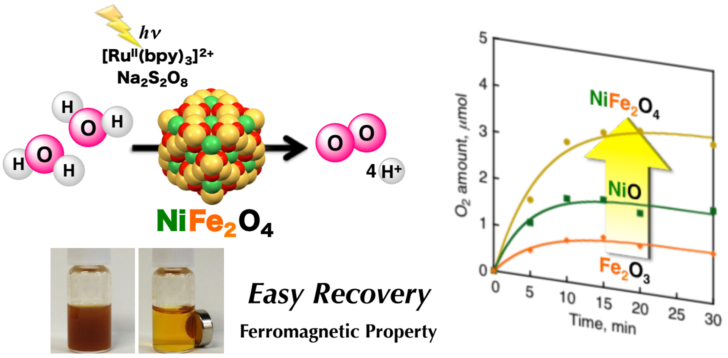

Abstract: Single or mixed oxides of iron and nickel have been examined as catalysts in photocatalytic water oxidation using $[Ru(bpy)_3]^{2+}$ and $S_2O_8^{2-}$ as a photosensitizer and a sacrificial oxidant, respectively. The catalytic activity of nickel ferrite ($NiFe_2O_4$) is comparable to that of a catalyst containing Ir, Ru or Co in terms of O_2 yield and O_2 evolution rate under ambient reaction conditions. $NiFe_2O_4$ also possesses robustness and ferromagnetic properties, which are beneficial for easy recovery from the solution after reaction. Water oxidation catalysis achieved by a composite of earth-abundant elements will contribute to a new approach to the design catalysts for artificial photosynthesis.

Introduction

Artificial photosynthesis directly converting solar energy into chemical energy is one of the most promising systems to realize a sustainable energy cycle.[1–7] The artificial-photosynthesis systems are composed of at least three functional units; a catalyst for water oxidation ($2H_2O \rightarrow O_2 + 4H^+ + 4e^-$) to extract electrons and protons, a catalyst for reduction of protons or other chemicals to produce fuels, and light-harvesting and charge-separation molecules for solar energy harvesting and utilization.[7] In order to construct truly sustainable systems, the use of noble or minor metals should be avoided from each unit. Recently photocatalytic hydrogen evolution has been achieved with Ni nanoparticles instead of Pt nanoparticles[8] and a long-lived charge-separated state can be established with a donor-acceptor linked dyad including no metal ions.[9] On the other hand, developing efficient water oxidation catalysts (WOCs) with earth abundant elements still remains as the most challenging for artificial photosynthesis.[10]

Most of WOCs reported previously contain precious metals of iridium and ruthenium as active species.[11–26] Previous screening of various metal oxides suggested that cobalt oxides showed relatively high activity among non-precious metals.[21,22] Thus, much effort has been devoted to improve catalytic activity of cobalt oxide by various methods. A distinguished example is the use of cobalt phosphate, which exhibits high catalytic activity in the electrocatalytic water oxidation.[3] Homogeneous cobalt complexes have also been used as a precursor for providing WOCs, which include organic residues derived from organic ligands during the photocatalytic water oxidation reaction.[23] Additionally, doping of trivalent metal ions such as La^{3+} to cobalt oxides has been reported to improve catalytic activity of cobalt oxides for photocatalytic water oxidation using $[Ru(bpy)_3]^{2+}$ (bpy = 2,2'-bipyridine) and $S_2O_8^{2-}$ as a photosensitizer and a sacrificial oxidant, respectively.[24] However, doping of foreign metal ions to iron oxides, which are much more earth-abundant than cobalt oxides, has yet to be reported in the photocatalytic water oxidation.

In Chapter 6, I report a highly active and robust catalyst composed of iron-based oxide doped with foreign elements for the photocatalytic water oxidation. Before doping foreign metal ions to iron oxide, catalysis of Fe_3O_4 containing Fe^{2+} and Fe^{3+} ions was compared with that of Fe_2O_3, which is known as the most stable form under ambient conditions,[21] because Fe_3O_4 is isostructural to Co_3O_4 which shows high activity in the photocatalytic water oxidation.[22] Then, Fe^{2+} ion of Fe_3O_4 was replaced by another divalent metal ion of Ni, Mg or Mn to improve the activity and robustness of the catalyst under water-oxidation conditions. From the catalysis comparisons of MFe_2O_4

(M = Mg, Mn, Fe or Ni) in terms of an O_2 evolution rate and an O_2 yield, nickel ferrite ($NiFe_2O_4$), which has been often used for organic oxidation reactions,[27] has exhibited the highest activity for the photocatalytic water oxidation. The O_2 yields obtained with $NiFe_2O_4$ are comparable to those of Co_3O_4. Additionally, ferromagnetic properties of $NiFe_2O_4$ are quite beneficial to be recovered by a magnet without any loss from a solution after reaction. The superior catalysis of $NiFe_2O_4$ shown in the photocatalytic water oxidation was also found in electrochemical water oxidation. The surface conditions of $NiFe_2O_4$ after the photocatalytic water oxidation were investigated by X-ray photoelectron spectroscopy. A highly active and robust WOC in the photocatalytic system composed of only earth abundant elements of Fe and Ni has been disclosed in this study for the first time.

Experimental Section

Materials. All chemicals used for synthesis were obtained from a chemical company and used without further purification. Nickel(II) acetate tetrahydrate, nickel(II) chloride hexahydrate, cobalt(II) acetate tetrahydrate, iron(III) chloride hexahydrate, iron(II) sulfate heptahydrate, $Na_2S_2O_8$ and ethylene glycol (EG) were purchased from Wako Pure chemicals. Polyacrylamide (PAM) and Ag_2SO_4 were obtained from Sigma-Aldrich Co. $[Ru(bpy)_3]Cl_2$ was obtained from Tokyo Chemical Industry Co., Ltd. $[Ru(bpy)_3]SO_4$ was synthesized by adding one equivalent of Ag_2SO_4 to an aqueous solution of $[Ru(bpy)_3]Cl_2$. Purified water was provided by a Millipore Milli-Q water purification system where the electronic conductance was 18.2 MΩ cm. $NiFe_2O_4$, NiO, Fe_2O_3, Fe_3O_4, Co_3O_4, $MnFe_2O_4$ and $MgFe_2O_4$ were synthesized by following reported methods.

Synthesis of $NiFe_2O_4$. To an aqueous solution (24 mL) containing $NiCl_2 \cdot 6H_2O$ (2.0 mmol, 0.46 g) and $Fe(NO_3)_3 \cdot 9H_2O$ (4.0 mmol, 1.62 g) was added KOH solution (2.0 M, 24 mL) with magnetic stirring in room temperature (RT). The mixture was then transferred into a Teflon-lined stainless-steel autoclave of 140 mL capacity. The sealed tank was heated to and maintained at 160 ºC for 10 h in an oven and cooled to RT. The resulting brown precipitates were collected by filtration and washed with water and ethanol for more than 3 times, and finally dried in an oven at 60 ºC for 10 h.

Synthesis of NiO. To an aqueous solution (24 mL) containing $Ni(CH_3COO)_2 \cdot 4H_2O$ (5.0 mmol, 1.24 g) was added ethylene glycol (EG) (24 mL) with magnetic stirring to form a homogeneous in RT. The mixture was then transferred into a Teflon-lined stainless-steel autoclave of 140 mL capacity. The sealed tank was heated to and maintained at 200 ºC for 3.0 h in an oven and cooled to RT. The resulting emerald green precipitates [$Ni(OH)_2$] were collected by filtration and washed with water and ethanol for several times, and dried in a vacuum. NiO was prepared by calcination of the obtained $Ni(OH)_2$ in an oven at 300 ºC in air for 3.0 h. (ref: Yang, L.-X.; Zhu, Y.-J.; Tong, H.; Liang, Z.-H.; Li, L.; Zhang, L. *J. Solid State Chem.* **2007**, *180*, 2095.)

Synthesis of Fe_2O_3. To an aqueous solution (30 mL) containing $FeSO_4·7H_2O$ (1.0 M) was added NaOH (6.0 M) drop wisely to pH ~11 with magnetic stirring in RT. The mixtures were stirred vigorously for 1.5 h with bubbling air. The products were collected by filtration and washed with water several times, dried at 65 ºC.

Synthesis of Fe_3O_4. To an aqueous solution (40 mL) containing $FeCl_3·6H_2O$ (2.0 mmol, 0.54 g) and sodium citrate (4.0 mmol, 1.176 g) was added ammonia (25%, 0.50 mL) and polyacrylamide (PAM) (0.30 g) with vigorous magnetic stirring in RT. The mixtures were stirred vigorously for 0.50 h and then transferred into a Teflon-lined stainless-steel autoclave of 140 mL capacity. The sealed tank was heated to and maintained at 200 °C for 12 h and cooled to RT. The solid product was collected by magnetic filtration and washed several times with deionized water and ethanol. The final product was dried in an oven at 100 °C for 10 h.

Synthesis of Co_3O_4. An aqueous solution of cobalt acetate (80 mM, 73 mL) was slowly added to an aqueous ammonia solution (25%, 7.3 mL) with vigorous stirring by a magnetic stirrer. After 20 min stirring, the obtained pale pink slurry was transferred to a Teflon-lined stainless-steel autoclave of 140 mL capacity. The sealed tank was heated to and maintained at 350 ºC for 3.0 h in an oven and cooled to RT. The obtained particles were collected by filtration and washed with water for several times and dried at 65 ºC for several hours.

Synthesis of $MnFe_2O_4$. NaOH (3.0 g) was slowly added to an aqueous solution (40 mL) containing $FeSO_4·7H_2O$ (5.0 mmol, 1.11 g) and $MnCl_2·4H_2O$ (2.5 mmol, 0.40 g) at RT with magnetic stirring. The mixture was stirred vigorously for 30 min and then transferred into a Teflon-lined stainless-steel autoclave of 140 mL capacity. The sealed tank was heated to and maintained at 200 °C for 5 h and cooled to RT. The solid product was collected by a magnet and washed several times with deionized water and ethanol respectively. The final product was dried at 100 ºC for 6 h.

Synthesis of $MgFe_2O_4$. $FeCl_3·6H_2O$ (5.0 mmol, 1.25 g) and $MgSO_4$ (2.5 mmol, 0.30 g) were dissolved in ethylene glycol (40 ml), then CH_3COONa (3.6 g) and polyethylene glycol (1.0 g) were added to the solution. The mixture was stirred vigorously for 0.50 h and then transferred into a Teflon-lined stainless-steel autoclave of 140 mL capacity. The sealed tank was heated to and maintained at 200 °C for 12 h and cooled to RT. The puce product was separated by centrifugation, washed several times with ethanol and finally dried at 60 ºC for 6 h.

X-Ray Diffraction. X-ray diffraction patterns were recorded by a Rigaku Ultima IV. Incident X-ray radiation was produced by Cu X-ray tube, operating at 40 kV and 40 mA with Cu $K\alpha$ radiation of 1.54 Å. The scanning rate was 2 ° $\min^{-1}$ from 10° to 80° in 2θ.

N_2 Adsorption for BET Surface Area Determination. Nitrogen adsorption-desorption at 77 K was performed with a Belsorp-mini (BEL Japan, Inc.) within a relative pressure range from 0.01 to 101.3 kPa. A sample mass of ~100 mg was used for adsorption analysis after pretreatment at 120 ºC for ~1.0 h under vacuum conditions and kept in N_2 atmosphere until N_2-adsorption measurements. The sample was exposed to a mixed gas of He and N_2 with a programmed ratio and adsorbed amount of N_2 was calculated from the change of pressure in a cell after reaching the equilibrium (at least 5 min).

X-ray Photoelectron Spectra. X-ray photoelectron spectra (XPS) were measured by a ULVAC-PHI ESCA5600. The incident radiation was Mg $K\alpha$ X-ray (1253.6 eV) at 400 W and a charge neutralizer was turned on for acquisition. $NiFe_2O_4$ used for 1st run were collected by magnetic centrifugation and dried in vacuo. Iron and nickel oxides foil were prepared by calcinating each metal foils at 400 ºC for 2 h. The particles of $NiFe_2O_4$ before and after reaction were pressed on each copper foil and fixed on a stainless stage together with iron and nickel metals/oxides foil. The binding energy of each element was corrected by C 1s peak (284.8 eV) from residual carbon.

Transmission Electron Microscope (TEM). Transmission electron microscope (TEM) images of nanoparticles, which were mounted on a copper microgrid coated with elastic carbon, were observed by a JEOL JEM-2100 operating at 200 keV.

Photocatalytic Water Oxidation. Photocatalytic oxygen evolution was performed as follows. A iron- or nickel-based catalyst (0.050–1.0 g L^{-1}) was added to a phosphate buffer solution (50 mM, pH 8.0, 2.0 mL) containing $Na_2S_2O_8$ (5.0 mM) and $[Ru(bpy)_3]SO_4$ (0.25 mM) flushed with Ar gas. The solution was then irradiated with a xenon lamp (Ushio Optical, Model X SX-UID 500X AMQ) through a color filter glass (Asahi Techno Glass) transmitting $\lambda > 420$ nm at room temperature. Evolved oxygen gas in a headspace was quantified by a Shimadzu GC-17A gas chromatograph [Ar carrier, a capillary column with molecular sieves (Agilent Technologies, 19095PMS0, 30 m × 0.53 mm) at 40 ºC] equipped with a thermal conductivity detector.

Electrochemical Water Oxidation. Electrochemical water oxidation was performed on an ALS 630B electrochemical analyzer using a carbon paste electrode modified with 5% of a metal oxide catalyst as a working electrode, a saturated calomel reference electrode (SCE) and a Pt wire as a counter electrode. Linear sweep voltammograms were recorded by applying the voltage from 0 V to 1.5 V to the working electrode in a phosphate buffer (50 mM, pH 8.0) at room temperature with a scanning rate of 100 mV s^{-1}.

Results and Discussion

The photocatalytic water oxidation was performed in a phosphate buffer solution (50 mM, pH 8.0, 2.0 mL) containing a metal-oxide catalyst, $Na_2S_2O_8$ (5.0 mM) as a two-electron oxidant and $[Ru(bpy)_3]SO_4$ (0.25 mM) as a photosensitizer purged with Ar gas for 10 min in a vial (i.d. ~1 cm) sealed with a rubber septum. The reaction was started by irradiating the solution with a Xe lamp (500 W) through a transmitting glass filter (λ > 420 nm) with vigorous magnetic stirring at room temperature. The overall photocatalytic cycle of water oxidation with $Na_2S_2O_8$, $[Ru(bpy)_3]SO_4$ and a WOC is depicted in Scheme 1. Photoinduced electron transfer from the excited state of $[Ru(bpy)_3]^{2+}$ ($[Ru(bpy)_3]^{2+*}$; * denotes the excited state) to $S_2O_8^{2-}$ affords $[Ru(bpy)_3]^{3+}$, SO_4^{2-} and $SO_4^{\bullet-}$. The produced $SO_4^{\bullet-}$ is known to be a very strong oxidant [$E^0(SO_4^{\bullet-}/SO_4^{2-})$ = 2.6 V vs NHE], which can oxidize another $[Ru(bpy)_3]^{2+}$ to produce two equivalent of $[Ru(bpy)_3]^{3+}$ in the overall photoinduced process.[28] Finally $[Ru(bpy)_3]^{3+}$ can oxidized water to evolve O_2 with WOCs. However, the photosensitizer will be decomposed by nucleophilic attack of OH^- or water on $[Ru(bpy)_3]^{3+}$ under neutral or basic conditions in competition with electron transfer from WOCs to $[Ru(bpy)_3]^{3+}$, leading to low O_2 evolution yields.[26] Thus, highly active WOCs will improve the lifetime of the photosensitizer and O_2 yield. In order to confirm the effect of the crystal phase of iron oxides on catalytic activity for the photocatalytic water oxidation, Fe_2O_3 and Fe_3O_4 were synthesized by reported methods[29,30] and characterized by powder X-ray diffraction (XRD) measurements as shown in Figure 1a. Co_3O_4, which is known as an active WOC, was also synthesized and characterized by XRD to be used as a reference.[24] All XRD peaks were clearly indexed as the spinel structure for Fe_3O_4

Scheme 1. Cycle of Photocatalytic Water Oxidation with $Na_2S_2O_8$ and $[Ru(bpy)_3]^{2+}$ Using a Water Oxidation Catalyst

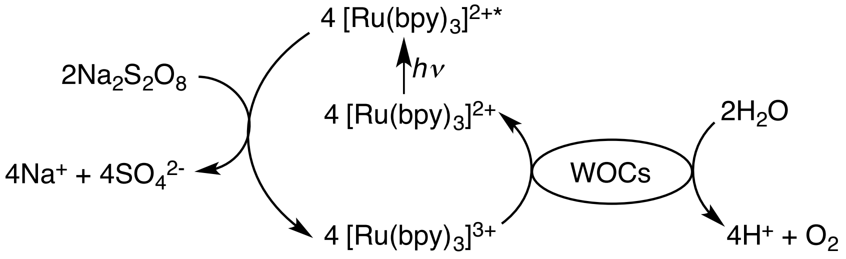

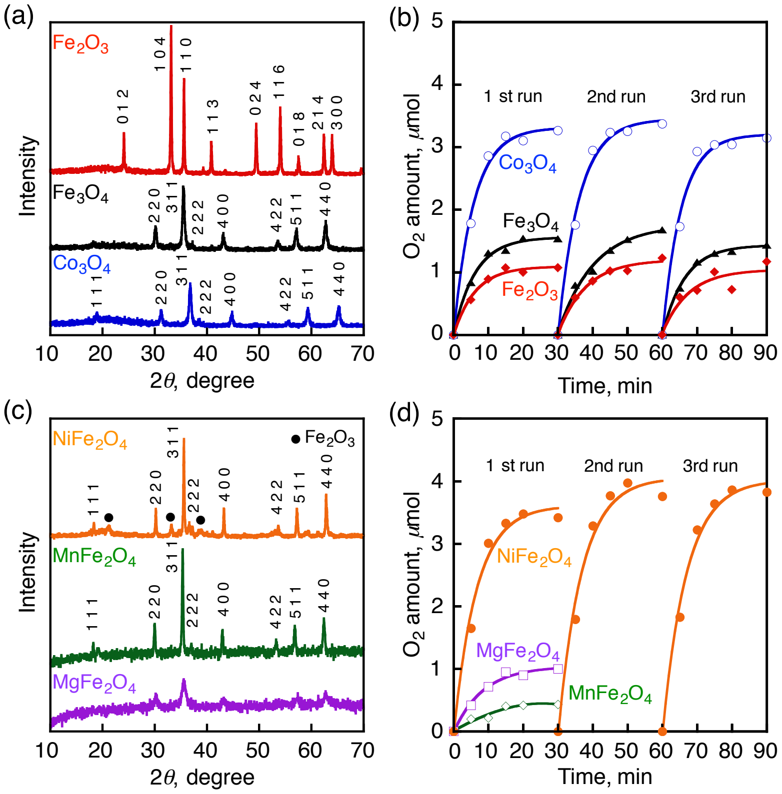

Figure 1. (a) Powder-XRD patterns of Fe_2O_3, Fe_3O_4 and Co_3O_4 catalysts. The number indicated in each peak is *hkl* index. (b) Time courses of O_2 evolution under photoirradiation (Xe lamp, $\lambda > 420$ nm) of a phosphate buffer solution (pH 8.0, 2.0 mL) containing $Na_2S_2O_8$ (5.0 mM) and $[Ru(bpy)_3]SO_4$ (0.25 mM) with Fe_2O_3, Fe_3O_4 or Co_3O_4 (0.50 g L^{-1}) at room temperature in three repetitive examinations. (c) Powder-XRD patterns of $NiFe_2O_4$, $MgFe_2O_4$ and $MnFe_2O_4$ catalysts. (d) Time courses of O_2 evolution with $NiFe_2O_4$, $MgFe_2O_4$ and $MnFe_2O_4$ catalysts in the same conditions with (b).

(magnetite) and Co_3O_4 or the corundum structure for Fe_2O_3 (hematite).

The time courses of O_2 evolution with metal oxides are shown in Figure 1b. Table 1 tabulates O_2 evolution rates (R_{O2}) and O_2 yields obtained with various metal oxides. No O_2 evolution was confirmed from a reaction solution without a catalyst. Because $Na_2S_2O_8$ is a two-electron accepter as described above, the stoichiometric amount of O_2 evolution is 5.0 μmol in the present reaction systems. A comparison between the reaction systems with iron oxides indicates that the amount of O_2 evolution obtained with Fe_3O_4 (1.5 μmol in 30 min photoirradiation) was larger than that of Fe_2O_3 (1.0 μmol in 30 min). Even when the concentration of Fe_3O_4 was reduced to half in the reaction solution, the same amount of O_2 evolution (1.5 μmol in 30 min) was achieved with a similar O_2 evolution rate (Figure 2). After the 1st run of the photocatalytic reaction, Fe_2O_3 was recovered from a reaction solution by centrifugation for further experiment and Fe_3O_4 was collected by a magnet due to its ferromagnetic properties. A fresh buffer solution containing $Na_2S_2O_8$ (5.0 mM) and $[Ru(bpy)_3]SO_4$ (0.25 mM) was

Table 1. O_2 Evolution Rates (R_{O2}) and O_2 Yields of WOCs in the Photocatalytic Water Oxidation

catalyst	$R_{O2}{}^{a}$ (μmol s^{-1} g^{-1})	O_2 yield^{b} (%)
$NiFe_2O_4$	5.3 ± 0.2	74 ± 4
NiO	3.0 ± 0.1	38 ± 2
Fe_2O_3	1.3 ± 0.1	21 ± 2
Fe_3O_4	1.9 ± 0.2	29 ± 3
Co_3O_4	4.8 ± 0.1	64 ± 3

[a] O_2 evolution rates are the average values of the repetitive examinations (3 times), which normalized by the catalyst weight in 10 min after photoirradiation ($\lambda > 420$ nm) of an aqueous buffer solution (pH 8.0, 2mL) containing a catalyst (0.50 g L^{-1}), $Na_2S_2O_8$ (5.0 mM) and $[Ru(bpy)_3]^{2+}$ (0.25 mM). [b] O_2 yield is the average value of three times repetitive examinations, which defined as twice the number of moles of O_2 per moles of $Na_2S_2O_8$.

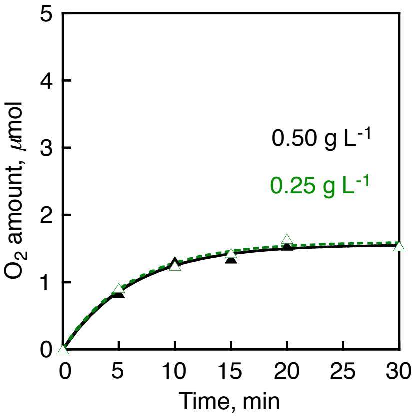

Figure 2. Time course of O_2 evolution under photoirradiation (Xe lamp, $\lambda > 420$ nm) with various concentrations of Fe_3O_4 [0.50 g L^{-1} (black, closed triangles), and 0.25 g L^{-1} (green, open triangles)] in an aqueous buffer solution (2.0 mL, pH 8.0) containing $[Ru(bpy)_3]^{2+}$ (0.25 mM) and $Na_2S_2O_8$ (5.0 mM).

added to the collected particles for the repetitive examination under photoirradiation. No significant changes of the total amount of O_2 evolution were observed at 2nd and 3rd run from the reaction solutions with these three catalysts. These results indicated that Fe_3O_4 acts as better WOC than Fe_2O_3 in the photocatalytic system. However, the catalysis of Fe_3O_4 is inferior to Co_3O_4 in terms of an O_2 evolution rate and an O_2 yield (i.e., O_2 evolution of 3.2 μmol with Co_3O_4 is more than double of that with Fe_3O_4).

In order to improve catalytic activity and robustness of iron-based oxides for photocatalytic water oxidation, Fe^{2+} ions, which are easily oxidized to Fe^{3+} under highly oxidizing conditions, in Fe_3O_4 were substituted to Ni^{2+}, Mg^{2+} and Mn^{2+} where the spinel structure is maintained. A series of spinel MFe_2O_4 (M = Ni, Mg and Mn) were synthesized by reported methods[31–33] and characterized by powder XRD measurements as shown in Figure 1c. The powder XRD measurements have evidenced that these three metal oxides have spinel structure. Figure 1d shows the time courses of O_2 evolution with $NiFe_2O_4$, $MgFe_2O_4$ and $MnFe_2O_4$ in the photocatalytic water oxidation. While the amounts of evolved O_2 from reaction solutions with $MgFe_2O_4$ (0.95 μmol) and $MnFe_2O_4$ (0.42 μmol) were smaller than that with Fe_3O_4 (1.5 μmol), the amount of O_2 evolution (3.7 μmol) from the reaction solution with $NiFe_2O_4$ was higher than that with Co_3O_4 (3.2 μmol). $NiFe_2O_4$ can be easily collected from a solution after the reaction because of its ferromagnetic properties (Figure 3). The high O_2 yield with $NiFe_2O_4$ was maintained even after 10th run in 5 h (Figure 4). The $NiFe_2O_4$ catalysts before and after the reaction were investigated by powder XRD and TEM measurements. No significant changes in both powder XRD pattern and morphology were observed on the $NiFe_2O_4$ catalysts (Figure 5 and 6). A small amount of Fe_2O_3 was contaminated in $NiFe_2O_4$, however, the highest catalytic activity of $NiFe_2O_4$ among the spinel MFe_2O_4 can be ascribed to the pure $NiFe_2O_4$, because the addition of Fe_2O_3 to NiO or Fe_3O_4 showed no significant improvement in the O_2 yields (Figure 7). The catalytic activity of a series of MFe_2O_4 was increased in the order of $M = Ni^{2+} > Fe^{2+} > Mg^{2+} > Mn^{2+}$. Catalytic activity of NiO for the photocatalytic water oxidation has been examined (Figure 8), however, the amount of O_2 evolution was around 1.9 μmol, which is only half of that with $NiFe_2O_4$. These results clearly indicate that $NiFe_2O_4$ is a highly active and robust catalyst for the photocatalytic water oxidation.

As the catalytic activity of heterogeneous catalysts is usually compared in terms of the activity normalized by the specific surface area, the apparent TOF was normalized by surface area. BET surface areas determined by N_2 adsorption measurements at 77 K were 48 m^2 g^{-1} for $NiFe_2O_4$, 45 m^2 g^{-1} for Fe_3O_4 and 34 m^2 g^{-1} for Co_3O_4 and 150 m^2 g^{-1} for NiO. The R_{O2} values calculated from the initial slope (10 min) of time courses

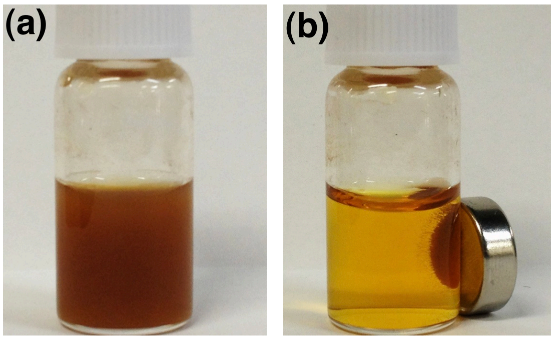

Figure 3. (a) $NiFe_2O_4$ is dispersed in a reaction solution. (b) $NiFe_2O_4$ is attracted to a magnet in the reaction solution.

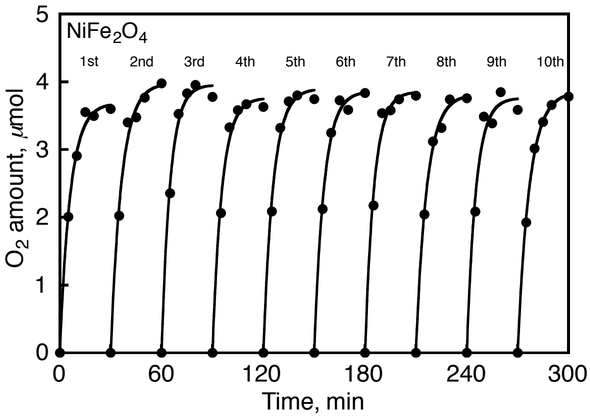

Figure 4. Time courses of O_2 evolution under photoirradiation (Xe lamp, $\lambda > 420$ nm) of a phosphate buffer solution (pH 8.0, 2.0 mL) containing $Na_2S_2O_8$ (5.0 mM) and $[Ru(bpy)_3]SO_4$ (0.25 mM) with $NiFe_2O_4$ (0.50 g L^{-1}) at room temperature in 10 repetitive examinations.

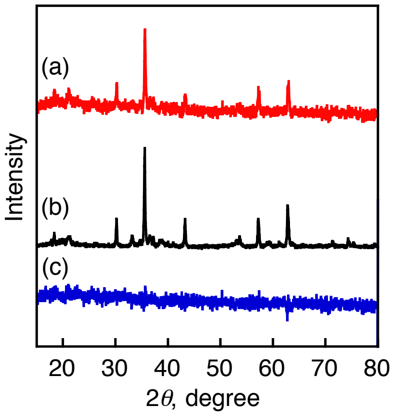

Figure 5. X-ray diffraction pattern of (a) $NiFe_2O_4$ after the catalytic reaction and (b) $NiFe_2O_4$ before the reaction. (c) Subtraction from spectrum (a) to spectrum (b). No peaks assignable to NiO or Fe_2O_3 were observed.

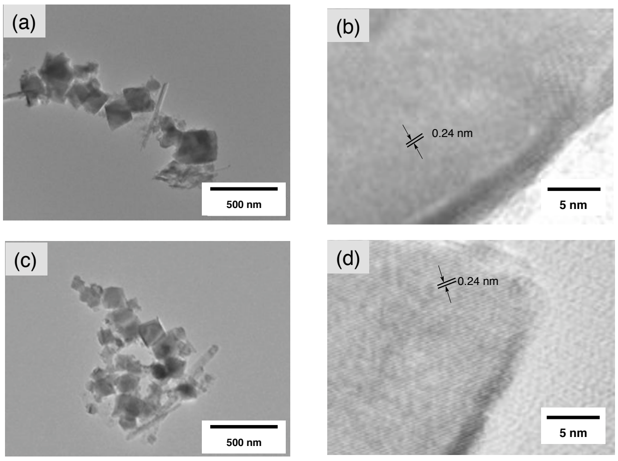

Figure 6. TEM images of (a, b) $NiFe_2O_4$ before the catalytic reaction and (c, d) $NiFe_2O_4$ after the reaction. No changes in morphology and lattice parameters were observed after the reaction.

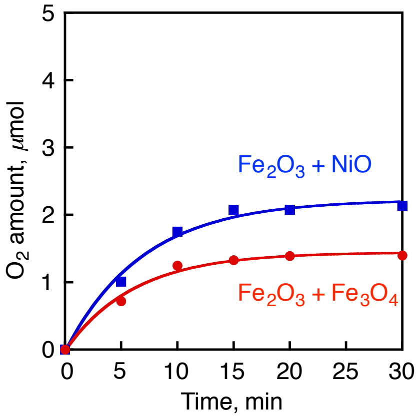

Figure 7. Time courses of O_2 evolution under photoirradiation (Xe lamp, $\lambda > 420$ nm) of a phosphate buffer solution (pH 8.0, 2.0 mL) containing $Na_2S_2O_8$ (5.0 mM) and $[Ru(bpy)_3]SO_4$ (0.25 mM) with the addition of Fe_2O_3 (0.25 g L^{-1}) to NiO (0.25 g L^{-1}) or Fe_3O_4 (0.25 g L^{-1}) at room temperature.

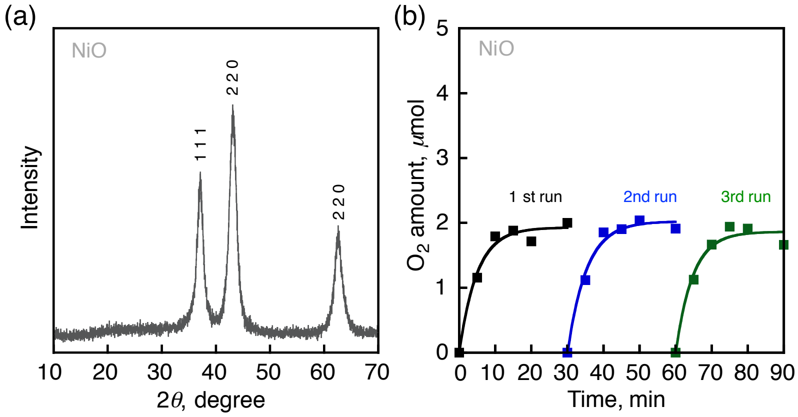

Figure 8. (a) Powder-XRD spectra of NiO catalysts. (b) Time courses of O_2 evolution under photoirradiation (Xe lamp, $\lambda > 420$ nm) of a phosphate buffer solution (pH 8.0, 2.0 mL) containing $Na_2S_2O_8$ (5.0 mM) and $[Ru(bpy)_3]SO_4$ (0.25 mM) with NiO (0.50 g L^{-1}) at room temperature in three repetitive examinations.

were divided by surface areas of catalysts in the reaction solution to determine the apparent TOF values. The apparent TOF value of 0.11 μmol s^{-1} m^{-2} obtained with $NiFe_2O_4$ was higher than those of Fe_3O_4 (0.042 μmol s^{-1} m^{-2}) and NiO (0.020 μmol s^{-1} m^{-2}). These results support that the high activity of $NiFe_2O_4$ is contributed by the composite effect of nickel and iron oxides. The apparent TOF value with $NiFe_2O_4$ is slightly smaller than that with Co_3O_4 (0.14 μmol s^{-1} m^{-2}). However, the O_2 yield obtained with $NiFe_2O_4$ (74%) was higher than that of Co_3O_4 (64%) by 10%. The O_2 yield with $NiFe_2O_4$ is also higher than those reported with catalysts containing precious metals such as IrO_2 particles (69%, pH 5.0)[21] and RuO_2 particles (22%, pH 5.0)[21], and abundant metals such as Mn_xO_y particles (55%, pH 5.8)[25] and comparable to that with $LaCoO_3$ particles (74%, pH 7.0).[24] Thus, $NiFe_2O_4$ composed of earth abundant metal ions is one of most active catalysts for the photocatalytic water oxidation.

Superior catalysis of $NiFe_2O_4$ for the photocatalytic water oxidation was scrutinized under electrocatalytic conditions. The electrochemical deposition of nickel or cobalt ion on the surface of hematite Fe_2O_3 has been previously reported to improve the catalysis of Fe_2O_3 for the electrochemical water oxidation.[34,35] Figure 9 shows cyclic voltammetry of water using a working electrode modified with a metal oxide catalyst in a buffer solution of pH 8.0. The anodic currents with $NiFe_2O_4$ started growing around 0.8 V (vs saturated calomel electrode: SCE) and reached more than 650 μA at 1.5 V, which is larger compared with those with iron-based oxides. The overpotential of $NiFe_2O_4$ (η = 0.43 V) for the electrochemical water oxidation is comparable to the reported overpotential of catalysts such as Co phosphate,[3] CoO_x[36] and Ni borate[37](Table 2). Around 0.8 V, a small redox couple assignable to the redox of Ni^{2+} species appears. A similar redox couple has been assigned to Ni^{2+}/Ni^{3+} for Ni oxide electrode formed on Ni metal in alkaline solution.[38] Recently, the oxidized nickel species under anodic potential is assigned to Ni^{4+} in nickel borate by X-ray absorption near edge structure spectra.[37] Further investigation is necessary to clarify the valence of active nickel species of $NiFe_2O_4$, however, the growing of oxidation peak started just after the oxidation peak assures that high valent nickel species is an active species for the water oxidation. The onset potentials for water oxidation with both Fe_2O_3 and Fe_3O_4 were observed around 1.1 V. The anodic currents with Fe_2O_3 and Fe_3O_4 at 1.5 V were as small as 190 μA and 290 μA. These results suggest that Ni^{2+} ions incorporated into iron oxide enhances the water oxidation ability of iron oxides, which is able to exhibit high activity for the photocatalytic water oxidation.

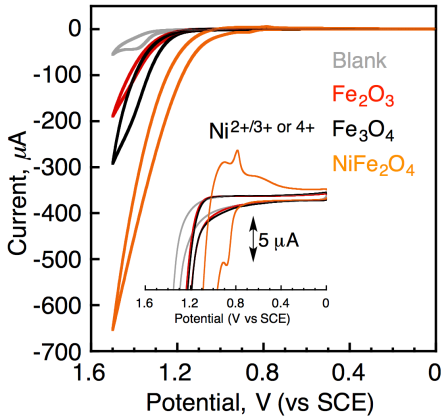

Figure 9. Cyclic voltammograms (CV) in a buffer solution (pH 8.0) with a carbon-paste working electrode (gray, A = 0.071 cm^2) containing 5% of $NiFe_2O_4$ (orange), Fe_3O_4 (black) or Fe_2O_3 (red), a Pt wire (counter electrode) and a standard calomel electrode (scan rate of 100 mV s^{-1}). Inset shows the initial range of the electrocatalytic current.

Table 2. Overpotential of Various Catalysts for Electrochemical Water Oxidation

catalyst	onset potential V (*vs* SCE)	pH	standard potential (V *vs* SCE)	overpotential (V)	ref.
$NiFe_2O_4$	0.95	8.0	0.52	0.43	this work
Co phosphate	0.99	7.0	0.58	0.41	3
CoO_x	1.01	8.0	0.52	0.49	36
Ni borate	0.89	9.2	0.45	0.44	37

A critical issue of a series of spinel compound under highly oxidizing conditions is oxidation of divalent metal species. The oxidation may lead to micro-phase separation and deactivation of catalysts. Magnetite of Fe_3O_4 has been reported to be oxidized to form Fe_2O_3 under highly oxidizing conditions.[39] NiO is rather stable, however, transformation to nonstoichiometric nickel oxide has been reported under highly oxidizing conditions.[40] Thus, confirmation of surface conditions of each component after water oxidation is necessary. The change in the surface conditions of $NiFe_2O_4$ before and after the photocatalytic reaction was observed by X-ray photoelectron spectroscopy (XPS). The XPS measurements were performed for the energy regions of Fe $2p_{3/2}$, Ni $2p_{3/2}$, O 1s, Ru 3d and C 1s, although no peak was observed in the Ru 3d region. The binding energy of each element was corrected by C 1s peak (284.8 eV) from residual carbon. Figure 10a displays the XPS spectra for Ni $2p_{3/2}$ peaks appeared at 854.8 eV with a weak satellite peak around 861 eV for $NiFe_2O_4$ samples before and after the reaction. The binding energies of these peaks indicate the Ni species in the samples are Ni^{2+} by comparison with peak positions of Ni $2p_{3/2}$ peaks of pure Ni metal and NiO peaks (Figure 11a). The similar ratio of peak strength between Ni $2p_{3/2}$ main peak and satellite peak for both samples supports that the surface conditions are the same even after the photocatalytic water oxidation performed under highly oxidizing conditions. Figure 10b displays the XPS spectrum for Fe $2p_{3/2}$ peaks appeared at 710.2 eV with a weak satellite peak at 723.7 eV for $NiFe_2O_4$ before the reaction and 710.6 eV with a weak satellite peak at 724.1 eV after the reaction. These peaks are assigned to Fe^{3+} by comparing with the Fe $2p_{3/2}$ peaks of Fe_2O_3 and Fe metal (Figure 11b). Although the main peak of Fe $2p_{3/2}$ from the sample after the reaction was slightly shifted to the direction of higher binding energy, the same separation between main peak and satellite peak in both samples and similarity of peak shapes including satellite peaks in the whole energy region between 700 an 730 eV strongly support no change in the valence state of Fe^{3+}. The absence of changes in the surface conditions of $NiFe_2O_4$ before and after the reaction was also supported by no shift of O 1s peak (Figure 10c).

Thus, $NiFe_2O_4$ is highly robust even during the photocatalytic water oxidation.

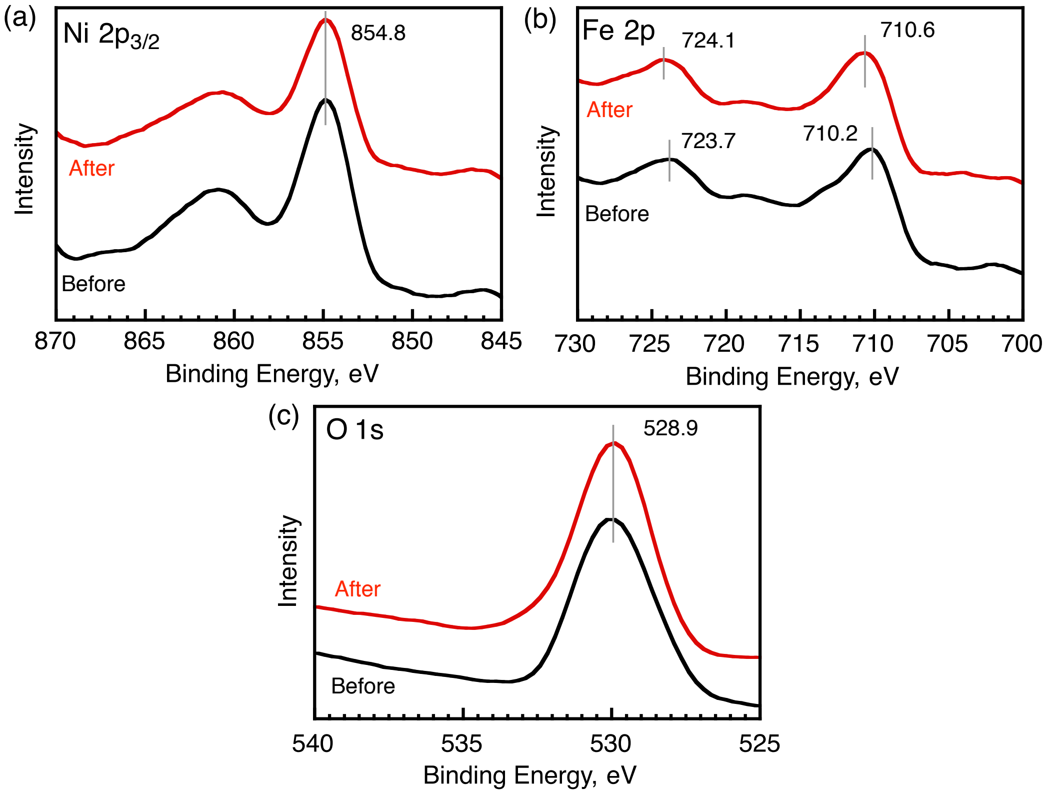

Figure 10. X-ray photoelectron spectra of $NiFe_2O_4$ before and after the reaction in the energy regions of (a) Ni $2p_{3/2}$, (b) Fe 2p and (c) O 1s of $NiFe_2O_4$ before and after the reaction.

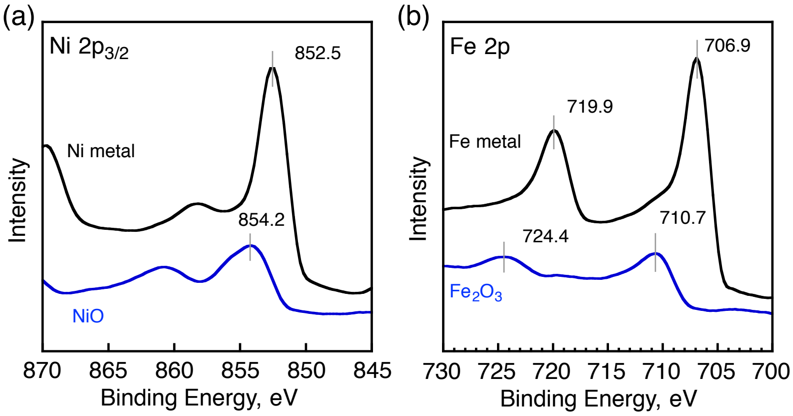

Figure 11. X-ray photoelectron spectra in the energy regions of (a) Ni $2p_{3/2}$ of a Ni metal foil (black) and NiO foil (blue) and (b) Fe 2p of Fe metal foil (black) and Fe_2O_3 foil (blue).

Conclusions

In summary, we have demonstrated the superior catalysis of $NiFe_2O_4$ composed of only earth-abundant metal ions toward the photocatalytic water oxidation for the first time. This catalyst possesses high catalytic activity as well as durability for the photocatalytic water oxidation with $Na_2S_2O_8$ and $[Ru(bpy)_3]^{2+}$ as evidenced by the maintenance of high O_2 yield after 10 times repetitive uses. The cyclic voltammetry for electrocatalytic water oxidation with $NiFe_2O_4$ suggests that high valent nickel species is the active species for the photocatalytic water oxidation. This indicates important implications for exploitation of efficient WOCs to expand widespread use of iron-based oxides for water oxidation.

References

(1) Lewis, N. S.; Nocera, D. G. *Proc. Natl. Acad. Sci. U. S. A.* **2006**, *103*, 15729.

(2) Eisenberg, R.; Gray, H. B. *Inorg. Chem.* **2008**, *47*, 1697.

(3) Kanan, M. W.; Nocera, D. G. *Science* **2008**, *321*, 1072.

(4) Youngblood, W. J.; Lee, S.-H. A.; Maeda, K.; Mallouk, T. E. *Acc. Chem. Res.* **2009**, *42*, 1966.

(5) Concepcion, J. J.; Jurss, J. W.; Brennaman, M. K.; Hoertz, P. G.; Patrocinio, A. O. T.; Murakami Iha, N. Y.; Templeton, J. L.; Meyer, T. J. *Acc. Chem. Res.* **2009**, *42*, 1954.

(6) Romain, S.; Vigara, L.; Llobet, A. *Acc. Chem. Res.* **2009**, *42*, 1944.

(7) Fukuzumi, S. *Eur. J. Inorg. Chem.*, **2008**, 1351.

(8) Yamada, Y.; Miyahigashi, T.; Kotani, H.; Ohkubo, K.; Fukuzumi, S. *Energy Environ. Sci.,* **2012**, *5*, 6111.

(9) (a) Fukuzumi, S.; Kotani, H.; Ohkubo, K.; Ogo, S.; Tkachenko, N. V.; Lemmetyinen, H. *J. Am. Chem. Soc*. **2004**, *126*, 1600. (b) Hoshino, M.; Uekusa, H.; Tomita, A.; Koshihara, S.; Sato, T.; Nozawa, S.; Adachi, S.; Ohkubo, K.; Kotani, H.; Fukuzumi, S. *J. Am. Chem. Soc.* **2012**, *134*, 4569. (c) Kotani, H.; Ohkubo K.; Fukuzumi, S. *Faraday Discuss*. **2012**, *155*, 89.

(10) Du, P.; Eisenberg, R. *Energy Environ. Sci.* **2012**, *5*, 6012.

(11) Najafpour, M. M.; Ehrenberg, T.; Wiechen, M.; Kurz, P. *Angew. Chem., Int. Ed.* **2010**, *49*, 2233.

(12) Fillol, J. L.; Codolà, Z.; Garcia-Bosch, I.; Gómez, L.; Pla, J. J.; Costas, M. *Nat. Chem.* **2011**, *3*, 807.

(13) Yin, Q. S.; Tan, J. M.; Besson, C.; Geletii, Y. V.; Musaev, D. G.; Kuznetsov, A. E.; Luo, Z.; Hardcastle, K. I.; Hill, C. L. *Science* **2010**, *328*, 342.

(14) Murakami, M.; Hong, D.; Suenobu, T.; Yamaguchi, S.; Ogura, T.; Fukuzumi, S. *J. Am. Chem. Soc.* **2011**, *133*, 11605.

(15) Poulsen, A. K.; Rompel, A.; McKenzie, C. J. *Angew. Chem., Int. Ed.* **2005**, *44*, 6916.

(16) Polyansky, D. E.; Muckerman, J. T.; Rochford, J.; Zong, R.; Thummel, R. P.; Fujita, E. *J. Am. Chem. Soc.* **2011**, *133*, 14649.

(17) Duan, L.; Bozoglian, F.; Mandal, S.; Stewart, B.; Privalov, T.; Llobet, A.; Sun, L. *Nat. Chem.* **2012**, *4*, 418.

(18) Fukuzumi, S.; Kato, S.; Suenobu, T. *Phys. Chem. Chem. Phys.* **2011**, *13*, 17960.

(19) Kaveevivitchai, N.; Chitta, R.; Zong, R.; El Ojaimi, M.; Thummel, R. P. *J. Am. Chem. Soc.* **2012**, *134*, 10721.

(20) Hong, D.; Murakami, M.; Yamada, Y.; Fukuzumi, S. *Energy Environ. Sci.* **2012**, *5*, 5708.

(21) Harriman, A.; Pickering, I. J.; Thomas, J. M.; Christensen, P. A. *J. Chem. Soc., Faraday Trans. I* **1988**, *84*, 2795.

(22) Jiao, F.; Frei, H. *Energy Environ. Sci.* **2010**, *3*, 1018.

(23) Hong, D.; Jung, J.; Park, J.; Yamada, Y.; Suenobu, T.; Lee, Y.-M.; Nam, W.; Fukuzumi, S. *Energy Environ. Sci.* **2012**, *5*, 7606.

(24) Yamada, Y.; Yano, K.; Hong, D.; Fukuzumi, S. *Phys. Chem. Chem. Phys.* **2012**, *14*, 5753.

(25) Jiao, F.; Frei, H. *Chem. Commun.* **2010***, 46, 2920.*

(26) Morris, N. D.; Mallouk, T. E. *J. Am. Chem. Soc.* **2002**, *124*, 11114.

(27) (a) Fouad, O. A.; Abdel, H. K. S.; Rashad, M. M. *Top. Catal.* **2008**, *47*, 61; (b) Miki, J.; Asanuma, M.; Tachibana, Y.; Shikada, T. *J. Catal.* **1995**, *151*, 323; (c) Turek, W.; Strzezik, J.; Krowiak, A. *React. Kinet. Mech. Cat.* **2012**, *107*, 115.

(28) Kaledin, A. L.; Huang, Z.; Geletii, Y. V.; Lian, T.; Hill, C. L.; Musaev, D. G. *J. Phys. Chem. A* **2010**, *114*, 73.

(29) Elizarova, G. L.; Matvienko, L. G.; Parmon, V. N. *J. Mol. Catal.* **1987**, *43*, 171.

(30) Wang, L.; Li, J.; Jiang, Q.; Zhao, L. *Dalton Trans.* **2012**, *41*, 4544.

(31) Cheng, Y.; Zheng, Y.; Wang, Y.; Bao, F.; Qin, Y. *J. Solid State Chem.* **2005**, *178*, 2394.

(32) Deng, H.; Chen, H.; Li, H. *Mater. Chem. Phys.* **2007**, *101*, 509.

(33) Wang, L.; Li, J.; Wang, Y.; Zhao, L.; Jiang, Q. *Chem. Eng. J.* **2012**, *181-182*, 72.

(34) (a) Liao, P.; Keith, J. A.; Carter, E. A. *J. Am. Chem. Soc.* **2012**, *134*, 13296; (b) Landon, J.; Demeter, E.; Inoglu, N.; Keturakis, C.; Wachs, I. E.; Vasic, R.; Frenkel, A. I.; Kitchin, J. R. *ACS Catal.* **2012**, *2*, 1793.

(35) Liu, Y.; Yu, Y.-X.; Zhang, W.-D. *Electrochim. Acta* **2012**, *59*, 121.

(36) Stracke, J. J.; Finke, R. G. *J. Am. Chem. Soc.* **2011**, *133*, 14872.

(37) Bediako, D. K.; Lassalle-Kaiser, B.; Surendranath, Y.; Yano, J.; Yachandra, V. K.; Nocera, D. G. *J. Am. Chem. Soc.* **2012**, *134*, 6801.

(38) Lyons, M. E. G.; Brandon, M. P. *Int. J. Electrochem. Sci.*, **2007**, *3*, 1386.

(39) Tang, J.; Myers, M.; Bosnick, K. A.; Brus L. E. *J. Phys. Chem. B***, 2003**, *107,* 7501.

(40) Greenwood, N. N.; Earnshaw, A. *Chemistry of the Elements* (2nd ed.). Butterworth–Heinemann (1997).

Chapter 7

Catalytic Activity of $NiMnO_3$ for Visible Light-Driven and Electrochemical Water Oxidation

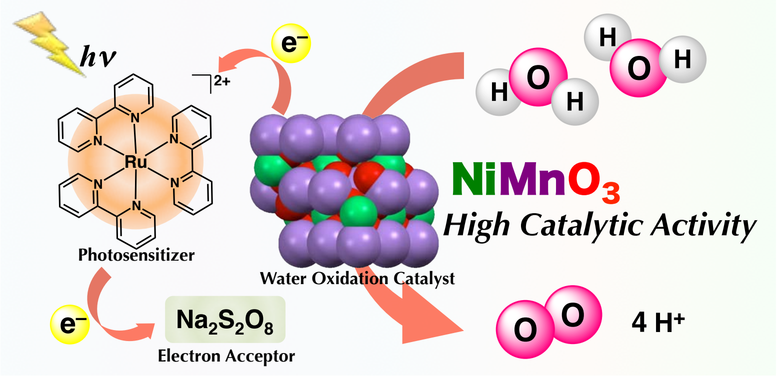

Abstract: $NiMnO_3$ was found to be an efficient catalyst for light-driven water oxidation using $[Ru(bpy)_3]^{2+}$ and $S_2O_8^{2-}$ as a photosensitiser and a sacrificial oxidant, respectively. $NiMnO_3$ exhibited remarkably high catalytic activity in comparison with manganese oxides and nickel oxide. For electrochemical water oxidation, the highest catalytic current was also obtained with $NiMnO_3$ among the manganese oxides.

Introduction

On the urgent demand of developing a sustainable energy cycle, artificial photosynthesis is a promising system, in which solar energy is directly converted to chemical energy.[1–4] Efficient water oxidation catalysts (WOCs) are essential to achieve artificial photosynthesis.[5–12] In nature, water oxidation is catalyzed by the manganese-oxo-calcium cluster (Mn_4CaO_5) in oxygen evolving center (OEC) of Photosystem II.[13] Thus, much attention has been paid to the development of homogeneous and heterogeneous WOCs containing manganese, which is an earth-abundant and environmentally-friendly element.[14–28] Heterogeneous manganese oxides, which are more robust than homogeneous catalysts under water oxidation conditions, have a significant merit for practical applications.

Manganese oxides prepared by a conventional method have been reported to exhibit lower activity than noble metal oxides such as iridium or ruthenium oxides.[20] To improve the catalytic activity of manganese oxides, various methods, such as structural controls of size, shape or phase, have been studied.[21–25] For examples, manganese oxide nanoparticles supported on mesoporous silica,[21] nanostructured α-MnO_2[22] and λ-MnO_2[23] have been reported to act as efficient catalysts for visible light-driven water oxidation using $[Ru(bpy)_3]^{2+}$ (bpy = 2,2’-bipyridine) as a photosensitiser and $S_2O_8^{2-}$ as a sacrificial oxidant. Similarly, manganese oxide nanoparticles dispersed in faujasite zeolite[24] and nano-sized manganese oxides[25] have been reported as efficient catalysts for thermal water oxidation by cerium(IV) ammonium nitrate (CAN).

Doping Ca^{2+} ions in manganese oxides is another method to improve catalytic activity of manganese oxides as observed in the manganese cluster in OEC. Ca^{2+} ion doped manganese oxides ($CaMn_2O_4$, $CaMnO_3$ and $Ca_2Mn_2O_8$) have been reported to enhance the catalytic activity of manganese oxides for water oxidation by CAN,[26–28] in which the Ca^{2+} ions have been proposed to activate H_2O molecules by polarization. Similarly, introduction of foreign metal ions to metal-oxide WOCs can also improve the catalytic activity for water oxidation. Indeed, doping of La^{3+} ion to cobalt oxides has improved the catalysis of cobalt oxide in the visible light-driven water oxidation.[29] Ni^{2+} ion doped iron oxides ($NiFe_2O_4$) has been reported to be a highly active and robust catalyst for the visible light-driven water oxidation despite the low activity of iron oxides for water oxidation.[30] However, doping effect of Ni^{2+} ion to manganese oxides has yet to be reported for the visible light-driven catalytic water oxidation.

In Chapter 7, I report a highly active and robust WOC catalysis of Ni^{2+} ion doped manganese oxide ($NiMnO_3$) for the visible light-driven water oxidation with $[Ru(bpy)_3]^{2+}$ as a photosensitiser and $S_2O_8^{2-}$ as a sacrificial oxidant. The catalytic activity of $NiMnO_3$ was compared with those of α-MnO_2, Mn_2O_3 and Mn_3O_4; the highest activity was obtained with $NiMnO_3$. Additionally, the ferromagnetic properties of $NiMnO_3$ are quite beneficial, enabling the catalyst to be recovered from the solution after the reaction using a magnet without any loss. The superior catalysis of $NiMnO_3$ shown in the visible light-driven water oxidation was also found in electrochemical water oxidation. The effective doping of Ni^{2+} ion was demonstrated in improving the catalytic reactivity of manganese oxides.

Experimental Section

Materials. All chemicals used for synthesis were obtained from a chemical company and used without further purification. Manganese(II) nitrate hexahydrate, Mn_2O_3 (mesh 325) and Mn_3O_4 (mesh 325) were purchased from Sigma-Aldrich Co. Nickel(II) nitrate hexahydrate, nickel(II) acetate tetrahydrate, cobalt(II) acetate, $Na_2S_2O_8$, $NaHCO_3$, ethylene glycol (EG), phosphate buffer powder (pH 7.0) and Ag_2SO_4 were obtained from Wako Pure Chemical Industries, Ltd. $[Ru(bpy)_3]Cl_2$ was obtained from Tokyo Chemical Industry Co., Ltd. $[Ru(bpy)_3]SO_4$ was synthesized by adding one equivalent of Ag_2SO_4 to an aqueous solution of $[Ru(bpy)_3]Cl_2$. Purified water was provided by a Millipore Milli-Q water purification system where the electronic conductance was 18.2 MΩ cm. $NiMnO_3$, α-MnO_2, NiO and Co_3O_4 were synthesized by following reported methods.

Synthesis of $NiMnO_3$ and α-MnO_2. An aqueous solution (10 mL) containing nickel(II) nitrate hexahydrate (2.5 mmol, 0.73 g) and manganese(II) nitrate hexahydrate (2.5 mmol, 0.72 g) was slowly added to $NaHCO_3$ aqueous solution (1.0 M, 50 mL) with magnetic stirring at room temperature (RT). The resulting precipitates were collected by centrifugation and washed with water and ethanol for several times, and finally dried *in vacuo*. The precursor was heated with a rate of 10 ºC/min up to 450 ºC in air, maintaining the temperature for 5 h, and finally rapid cooling to RT. α-MnO_2 was prepared by addition of an aqueous solution (10 mL) containing manganese(II) nitrate hexahydrate (5.0 mmol, 1.4 g) to $NaHCO_3$ aqueous solution (1.0 M, 50 mL) and followed by the same procedure of $NiMnO_3$.

Synthesis of NiO. Ethylene glycol (EG) (24 mL) was added to an aqueous solution (24 mL) containing nickel(II) acetate tetrahydrate (5.0 mmol, 1.24 g) with magnetic stirring at RT. The solution was then transferred into a Teflon-lined stainless-steel autoclave of 140 mL capacity. The sealed autoclave was heated to and maintained at 200 ºC for 3.0 h in an oven and cooled to RT. The resulting emerald green precipitates [$Ni(OH)_2$] were collected by filtration and washed with water and ethanol for several times, and dried *in vacuo*. NiO was prepared by calcination of the obtained $Ni(OH)_2$ in an oven at 300 ºC in air for 3.0 h.

Synthesis of Co_3O_4. An aqueous solution of cobalt(II) acetate (80 mM, 73 mL) was slowly added to an aqueous ammonia solution (25%, 7.3 mL) with vigorous stirring by a magnetic stirrer. After 20 min stirring, the obtained pale pink slurry was transferred to a Teflon-lined stainless-steel autoclave of 140 mL capacity. The sealed autoclave was heated to and maintained at 150 ºC for 3.0 h in an oven and cooled to RT. The obtained particles were collected by filtration and washed with water for several times and dried at 65 ºC for several hours.

Characterization of Catalysts. X-ray diffraction patterns were recorded by a Rigaku Ultima IV. Incident X-ray radiation was produced by Cu X-ray tube, operating at 40 kV and 40 mA with Cu $K\alpha$ radiation of 1.54 Å. The scanning rate was 2 °/min from 10° to 70° in 2θ. Scanning electron microscope images of metal oxides were observed by a FE-SEM (JSM-6701F) operating at 3.0 kV. X-ray fluorescence analysis was performed with a ZSX-100e (Rigaku). Nitrogen adsorption-desorption at 77 K was performed with a Belsorp-mini (BEL Japan, Inc.) within a relative pressure range from 0.01 to 101.3 kPa. A sample mass of ~200 mg was used for adsorption analysis after pretreatment at 150 ºC for ~3.0 h under vacuum conditions and kept in N_2 atmosphere until N_2-adsorption measurements. The sample was exposed to a gas mixture of He and N_2 with a programmed ratio and adsorbed amount of N_2 was calculated from the change of pressure in a cell after reaching the equilibrium (at least 5 min).

Light-Driven Water Oxidation. Light-driven water oxidation was performed as follows. A catalyst (0.10 or 0.50 g L^{-1}) was added to a phosphate buffer solution (50 mM, pH 7.0, 2.0 mL) containing $Na_2S_2O_8$ (5.0 mM) and $[Ru(bpy)_3]SO_4$ (0.25 mM) flushed with Ar gas. The solution was then irradiated with a xenon lamp (Ushio Optical, Model X SX-UID 500X AMQ) through a color filter glass (Asahi Techno Glass) transmitting $\lambda > 420$ nm at room temperature. Evolved oxygen gas in a headspace was quantified by a Shimadzu GC-17A gas chromatograph [Ar carrier, a capillary column with molecular sieves (Agilent Technologies, 19095PMS0, 30 m × 0.53 mm) at 313 K] equipped with a thermal conductivity detector.

Electrochemical Water Oxidation. Electrochemical water oxidation was performed on an ALS 630B electrochemical analyzer using a carbon paste electrode modified with 5% of a metal oxide catalyst as a working electrode, a saturated calomel reference electrode (SCE) and a Pt wire as a counter electrode. Cyclic voltammograms were recorded by applying the voltage from 0 V to 1.5 V to the working electrode in a phosphate buffer (50 mM, pH 7.0) at RT. with a scanning rate of 0.10 V s^{-1}.

Results and Discussions

$NiMnO_3$ was synthesized by a reported method[31] and characterized by powder X-ray diffraction (PXRD) measurements (Figure 1). Experimental details and the PXRD peaks with Millar indexes are described in Experimental Section and Figure 2 in Supporting Information, respectively. The same procedure was performed without a nickel ion source for synthesis of manganese oxides, which characterized to be α-MnO_2 by PXRD. Other manganese oxides (Mn_2O_3 and Mn_3O_4) were purchased from Aldrich. All the PXRD peaks were clearly indexed as the ilmenite structure for $NiMnO_3$, a hollandite structure for α-MnO_2, a bixbyite structure for Mn_2O_3 and a hausmannite structure for Mn_3O_4. Although the PXRD pattern of $NiMnO_3$ shows that a small amount of NiO was contaminated in $NiMnO_3$, X-ray fluorescence analysis of $NiMnO_3$ revealed that the molar ratio of Ni:Mn was 0.91:1.0. For comparison of the catalytic activity in the visible light-driven water oxidation, NiO and Co_3O_4 were synthesized by the reported methods,[32,33] because Co_3O_4 has been reported as the most active WOC among non-precious metal oxides. The structures of NiO and Co_3O_4 were confirmed by PXRD measurements as the rock-salt and spinel structures, respectively (Figure 3). The morphology of the metal oxides observed by scanning electron microscope (SEM) was shown in Figure 4 and Figure 5. $NiMnO_3$ and α-MnO_2 are spherical particles with a diameter of 1–2 μm as shown in Figure 4. Mn_2O_3 and Mn_3O_4 have an undefined shape with micron size (Figure 5). NiO exhibited architecture with flower-like morphology and Co_3O_4 was obtained as nanoparticles with a size around 20 nm.

The catalytic activity of the manganese oxides was examined in the visible light-driven water oxidation. The reaction was performed by the photoirradiation ($\lambda >$ 420 nm) of a buffer solution containing a manganese oxide catalyst, $Na_2S_2O_8$ as a

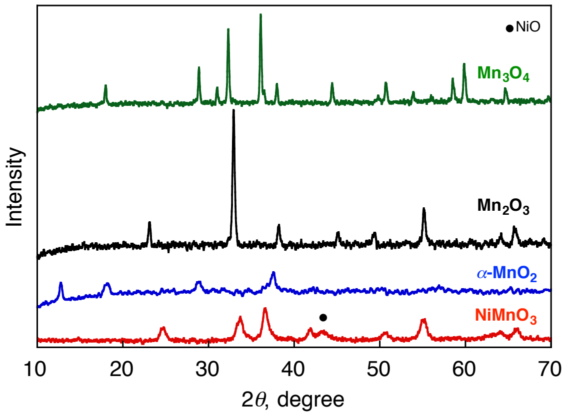

Figure 1. Powder XRD patterns of $NiMnO_3$, α-MnO_2, Mn_2O_3 and Mn_3O_4 (● denotes NiO pattern). The PXRD peaks with Millar indexes are shown in Figure 2.

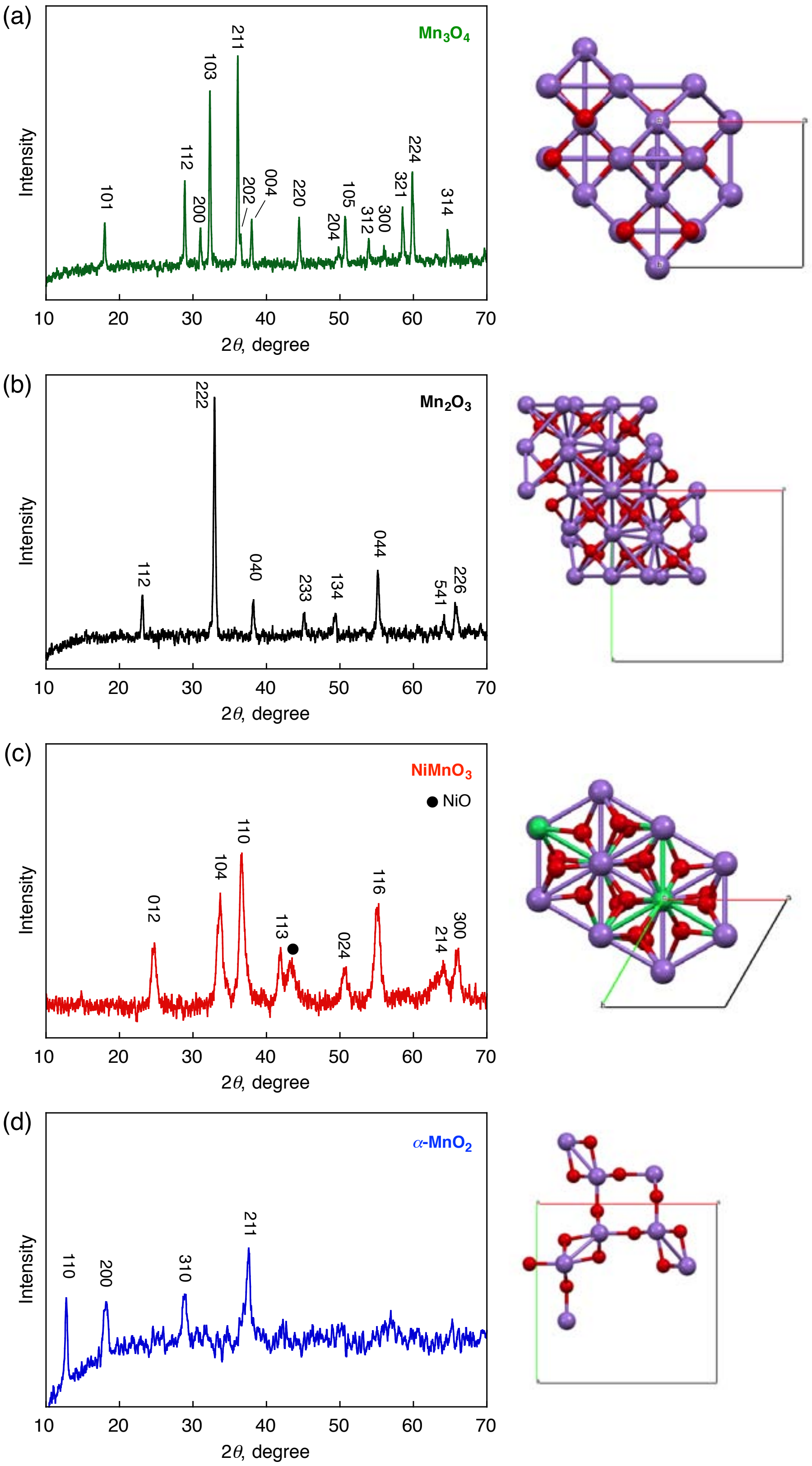

Figure 2. Powder XRD patterns of (a) Mn_3O_4, (b) Mn_2O_3 (c) $NiMnO_3$ and (d) α-MnO_2. The sizes of crystallites determined by using the Scherrer's equation were 33 nm for Mn_3O_4, 26 nm for Mn_2O_3, 8.8 nm for $NiMnO_3$ and 21 nm for α-MnO_2.

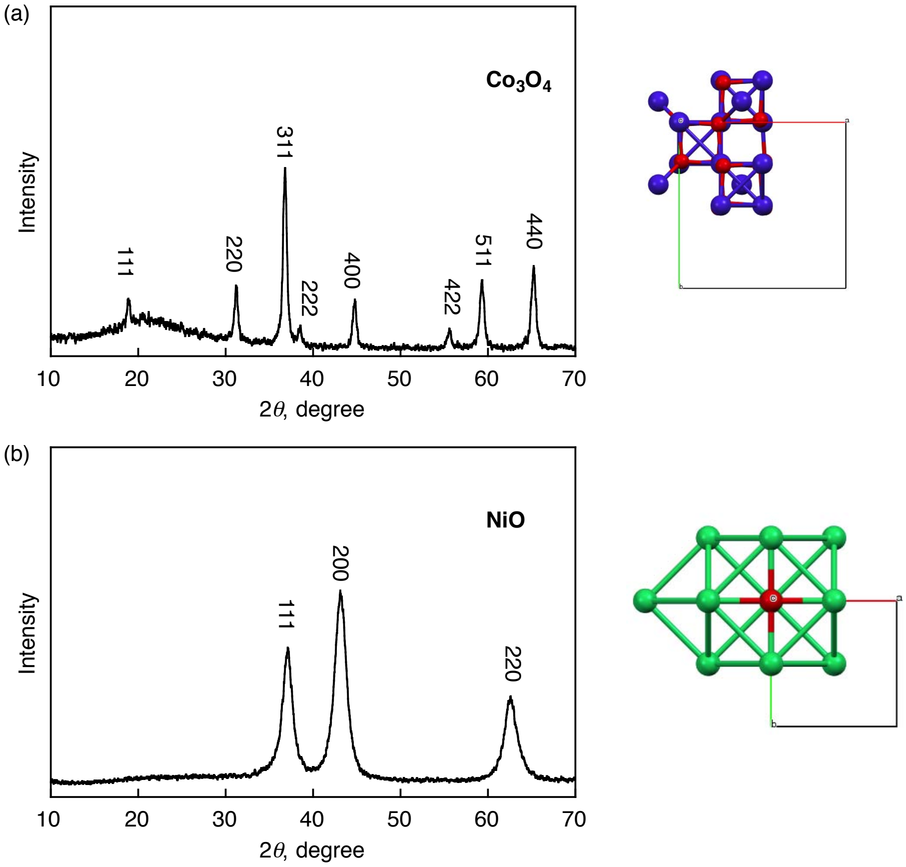

Figure 3. Powder XRD patterns of (a) Co_3O_4 and (b) NiO. The sizes of crystallites determined by using the Scherrer's equation were 15 nm for Co_3O_4 and 5.0 nm for NiO.

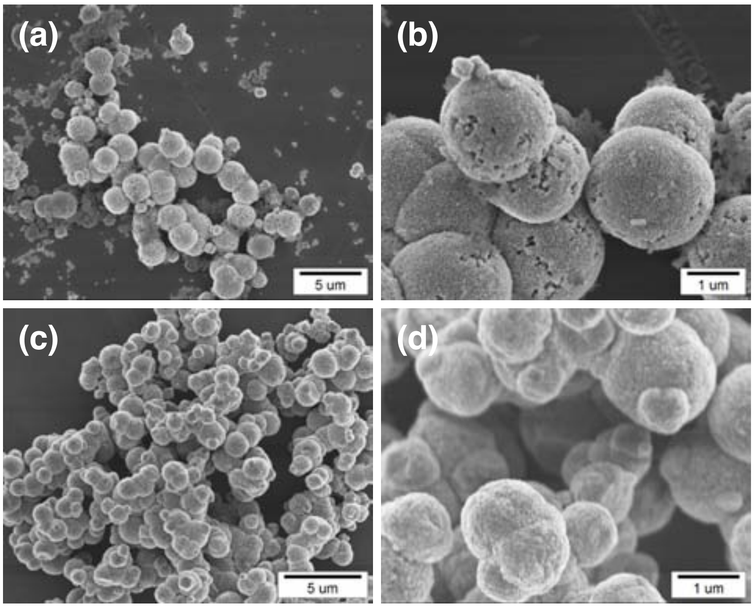

Figure 4. SEM images of (a and b) $NiMnO_3$ and (c and d) α-MnO_2

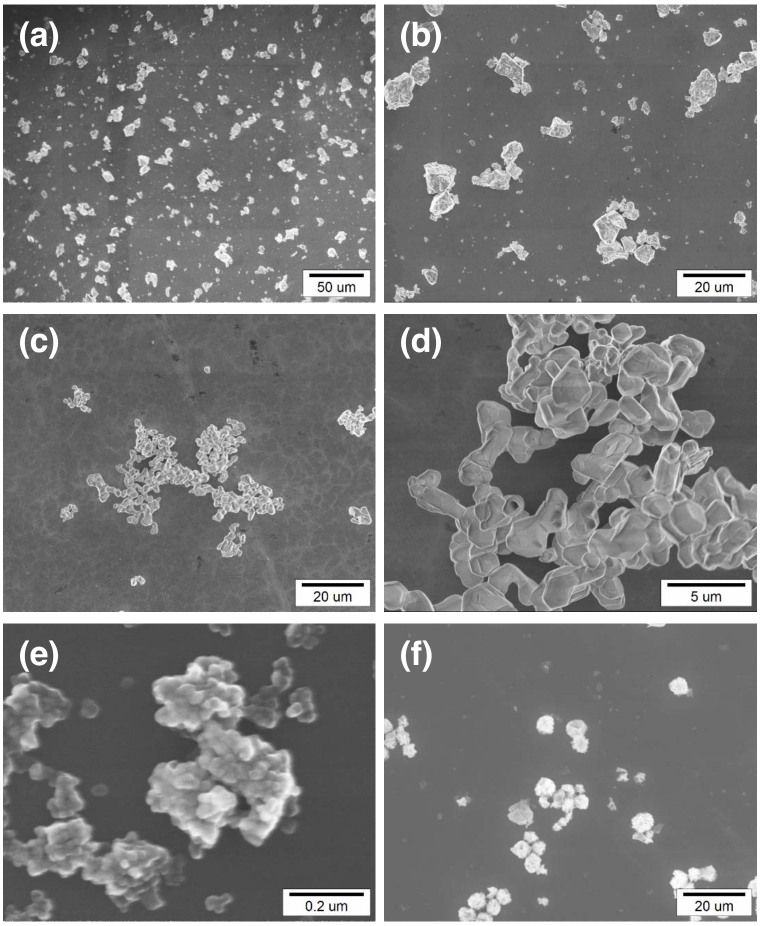

Figure 5. SEM images of (a and b) Mn_2O_3, (c and d) Mn_3O_4, (e) Co_3O_4 and (f) NiO.

two-electron oxidant, and $[Ru(bpy)_3]SO_4$ as a photosensitiser. The catalytic cycle of the visible light-driven water oxidation is shown in Scheme 1. Photoinduced electron transfer from $[Ru(bpy)_3]^{2+}$* (where * denotes the excited state) to $S_2O_8^{2-}$ occurs to produce $[Ru(bpy)_3]^{3+}$, which can oxidize water in the presence of a WOC to evolve O_2. However, self-quench and decomposition of the photosensitiser by a nucleophilic attack of OH^- or water on $[Ru(bpy)_3]^{3+}$, which competes with electron transfer from the WOC

Scheme 1. Catalytic Cycle of Visible Light-Driven Water Oxidation with $Na_2S_2O_8$ and $[Ru(bpy)_3]^{2+}$ Using Manganese Oxide Catalysts

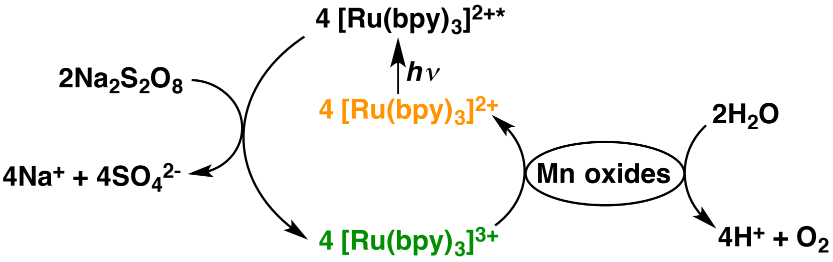

to $[Ru(bpy)_3]^{3+}$, can result in low O_2 evolution yields under neutral or basic conditions.[34] For increasing the O_2 evolution yield as well as improving the stability of the photosensitiser, highly active WOCs which can efficiently oxidize water and reduce $[Ru(bpy)_3]^{3+}$ should be developed.

The time courses of O_2 evolution with these manganese oxides are shown in Figure 6. The amount of O_2 evolution was quantified by gas chromatography. No O_2 evolution was observed from a reaction solution either without a catalyst or visible-light irradiation. The amount of O_2 evolution with $NiMnO_3$ obtained after 30 min photoirradiation was 2.6 μmol, which was remarkably larger than those obtained with α-MnO_2 (1.2 μmol), Mn_2O_3 (0.9 μmol) and Mn_3O_4 (0.2 μmol). Spinel Co_3O_4 known as an active WOC was also examined as a reference in the visible light-driven water oxidation as shown in Fig. 3. The amount of O_2 evolution with Co_3O_4 was 2.5 μmol, which was slightly lower than that of $NiMnO_3$. The amount of O_2 evolution with NiO was found to be 0.8 μmol, which is only one third of that with $NiMnO_3$. The stoichiometric amount of O_2 evolution is 5.0 μmol in the present reaction systems, because $Na_2S_2O_8$ is a two-electron acceptor. The O_2 yield with $NiMnO_3$ obtained after 30 min reached to 52%. A similar O_2 yield was also achieved under acidic conditions (pH 5.7). Non-stoichiometric amount of O_2 evolution may result from the self-quench and decomposition of photosensitiser. The O_2 evolution was gradually decreased as the time passes because of the consumption of $Na_2S_2O_8$ and partial decomposition of the photosensitizer. However, the O_2 evolution was recovered in repetitive experiments by adding fresh solutions to the collected catalyst as shown in Figure 7. After the first run of the photocatalytic reaction, $NiMnO_3$ was recovered from the reaction solution by

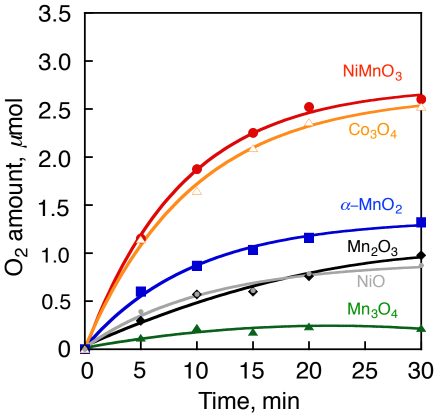

Figure 6. Time courses of O_2 evolution under visible light irradiation of (Xe lamp, $\lambda > 420$ nm) of a buffer solution (50 mM phosphate, 2.0 mL, pH 7.0) containing $[Ru(bpy)_3]^{2+}$ (0.25 mM), $Na_2S_2O_8$ (5.0 mM) and a catalyst (0.10 g L^{-1}) [$NiMnO_3$ (red cycles), α-MnO_2 (blue squares), Mn_3O_4 (green triangles), Mn_2O_3 (black diamonds), NiO (gray dots) or Co_3O_4 (yellow blank triangles)].

centrifugation for further experiments. A fresh buffer solution containing $Na_2S_2O_8$ (5.0 mM) and $[Ru(bpy)_3]SO_4$ (0.25 mM) was added to the collected particles for the repetitive examination under photoirradiation. The high catalytic activity of $NiMnO_3$ was maintained even after the 3rd run (Figure 7). These results clearly indicate that $NiMnO_3$ is a highly active and robust catalyst for the visible light-driven water oxidation.

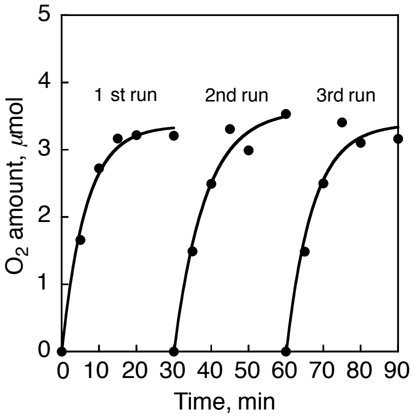

Figure 7. Time courses of O_2 evolution under visible light irradiation of (Xe lamp, $\lambda > 420$ nm) of a buffer solution (50 mM phosphate, 2.0 mL, pH 7.0) containing $[Ru(bpy)_3]^{2+}$ (0.25 mM), $Na_2S_2O_8$ (5.0 mM) and $NiMnO_3$ (0.50 g L^{-1}) in 3 repetitive examinations.

Table 1 summarizes catalytic reactivity obtained with the metal oxides. The O_2 evolution rate of $NiMnO_3$ was higher than those of manganese oxides and comparable to that of Co_3O_4. The catalytic activity of heterogeneous catalysts was also compared in terms of the activity normalized by a specific surface area. The apparent turnover frequencies (TOFs) were normalized by BET surface areas determined by N_2 adsorption measurements at 77 K (70 m^2 g^{-1} for $NiMnO_3$, 62 m^2 g^{-1} for α-MnO_2, 83 m^2 g^{-1} for Mn_2O_3, 76 m^2 g^{-1} for Mn_3O_4, 150 m^2 g^{-1} for NiO, and 34 m^2 g^{-1} for Co_3O_4). The apparent TOF of 0.27 μmol s^{-1} m^{-2} obtained with $NiMnO_3$ was obviously higher than those with α-MnO_2 (0.16 μmol s^{-1} m^{-2}), Mn_2O_3 (0.059 μmol s^{-1} m^{-2}) and Mn_3O_4 (0.026 μmol s^{-1} m^{-2}) and NiO (0.043 μmol s^{-1} m^{-2}). These results suggest that the improvement of catalytic activity of $NiMnO_3$ results from the composite effect of nickel and manganese oxides. The apparent TOF with $NiMnO_3$ was smaller than that with Co_3O_4 (0.56 μmol s^{-1} m^{-2}). However, the O_2 yield obtained with $NiMnO_3$ was slightly higher than that with Co_3O_4. The catalytic activity of $NiMnO_3$ was also compared with those of Mn-based catalysts. Among those Mn-based catalysts, $NiMnO_3$ exhibits the highest O_2 evolution rate, and the apparent TOF with $NiMnO_3$ is also comparable to the reported nanocrystalline Mn_2O_3[17].

Table 1. O_2 Evolution Rates, BET Surface Area and Apparent TOFs of WOCs in the Visible Light-Driven Water Oxidation

catalysts	O_2 evolution rate [a] (μmol s^{-1} g^{-1})	BET surface area [b] (m^2 g^{-1})	apparent TOF [c] (μmol s^{-1} m^{-2})	ref
$NiMnO_3$	19.2	70	0.27	this work
α-MnO_2	10.0	62	0.16	this work
Mn_2O_3	4.9	83	0.059	this work
Mn_3O_4	2.0	76	0.026	this work
Co_3O_4	19.0	34	0.56	this work
NiO	6.5	150	0.043	this work
Nanocrystalline Mn_2O_3	4.7[d]	16.3	0.29	17
Mn oxide/KIT-6	4.86[d]	-	-	21
α-MnO_2 nanowire	0.58[d]	47.3	0.012	22
λ-MnO_2	0.38[d,e]	20.0[f]	0.19	23

[a] O_2 evolution rates were normalized by the catalyst weight in 5 min after photoirradiation ($\lambda > 420$ nm) of an aqueous buffer solution (pH 8.0, 2 mL) containing a catalyst (0.10 g L^{-1}), $Na_2S_2O_8$ (5.0 mM) and $[Ru(bpy)_3]^{2+}$ (0.25 mM). [b] BET surface areas were determined by N_2 adsorption measurements at 77 K. [c] Apparent TOFs were normalized by BET surface area. [d] The values were calculated from the reported O_2 evolved rates based on the catalyst concentrations of 0.25 g L^{-1} for nanocrystalline Mn_2O_3 (pH 7), 0.30 g L^{-1} for Mn oxide/KIT-6 (pH 5.8), 1.2 g L^{-1} for α-MnO_2 nanowire (pH 7). [e] No description of catalyst concentration used for reactions (pH 5.8) in ref 23. [f] The value was reported in ref 22.

The catalysis of $NiMnO_3$ for the light-driven water oxidation was also scrutinized under electrocatalytic conditions. Figure 8 shows cyclic voltammograms (CVs) of water using a carbon paste electrode modified with a manganese oxide catalyst as a working electrode in a buffer solution (pH 7.0). The anodic currents with $NiMnO_3$ started growing at ~1.0 V (*vs*. SCE) and reached more than 200 μA at 1.5 V (*vs*. SCE), which is larger than those with manganese oxides. The onset potentials for water oxidation with both Mn_2O_3 and Mn_3O_4 were observed at ~1.1 V. The anodic currents with Mn_2O_3 and Mn_3O_4 at 1.5 V were as small as 60 and 70 μA, respectively. As α-MnO_2 has been reported to act as an electrostatic capacitor,[35] the current observed with α-MnO_2 at potentials lower than 1.0 V was not ascribed to water oxidation reactions. The anodic currents with α-MnO_2 at 1.5 V were still lower than that with $NiMnO_3$. The overpotential of $NiMnO_3$ for the electrochemical water oxidation (η = 0.42 V) is comparable to the reported overpotential of the catalysts such as cobalt phosphate,[36] nickel borate[37] and nickel ferrite[30] (Table 2). These results suggest that incorporation of Ni^{2+} ions enhances the electrocatalytic water oxidation reactivity of manganese oxides as the case of the visible light-driven catalytic water oxidation. The incorporation of Ni^{2+} ion to manganese oxides may enhance the oxidation power of a high valent Mn species, which are suggested as intermediates for water oxidation, resulting in the improvement of catalytic activity of $NiMnO_3$, although further mechanistic studies are required.

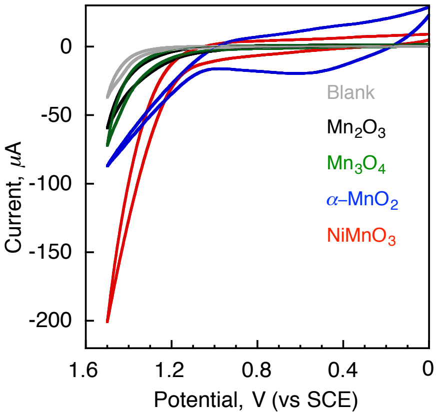

Figure 8. CVs in a buffer solution (pH 7.0) with a carbon paste-working electrode (A = 0.071 cm^2) containing no metal oxide (gray) and 5% of a catalyst [NiMnO3 (red), α-MnO_2 (blue), Mn_3O_4 (green) or Mn_2O_3 (black)] (standard calomel electrode; Pt wire counter electrode; scan rate 100 mV s^{-1}).

Table 2. Overpotential of Various Catalysts for Electrochemical Water Oxidation

catalyst	onset potential, (V *vs.* SCE)	pH	standard potential, (V *vs.* SCE)	overpotential, (V)	ref
$NiMnO_3$	1.0	7.0	0.58	0.42	this work
Co phosphate	0.99	7.0	0.58	0.41	36
Ni borate	0.89	9.2	0.45	0.44	37
Nickel ferrite	0.95	8.0	0.52	0.43	30

Conclusions

In summary, we have demonstrated excellent catalysis of visible light-driven and electrochemical water oxidation by Ni^{2+} ion doped manganese oxides, $NiMnO_3$. The high catalytic activity of $NiMnO_3$ can be ascribed to the composite effect of nickel and manganese oxides. This has important implications for the exploitation of efficient WOCs with bimetallic metal oxides of earth-abundant metals.

References

(1) Lewis, N. S.; Nocera, D. G. *Proc. Natl. Acad. Sci. U. S. A.* **2006**, *103*, 15729.

(2) Faunce, T. A.; Lubitz, W.; Rutherford, A. W.; MacFarlane, D.; Moore, G. F.; Yang, P.; Nocera, D. G.; Moore, T. A.; Gregory, D. H.; Fukuzumi, S.; Yoon, K. B.; Armstrong, F. A.; Wasielewski, M. R.; Styring, S. *Energy Environ. Sci.* **2013**, *6*, 695.

(3) Xu, J.; Li, Y.; Peng, S.; Lu, G.; Li, S. *Phys. Chem. Chem. Phys.* **2013**, *15*, 7657.

(4) Liu, X.; Li, Y.; Peng, S.; Lu, G.; Li, S. *Int. J. Hydrogen Energy* **2013**, *38*, 11709.

(5) Eisenberg, R.; Gray, H. B. *Inorg. Chem.* **2008**, *47*, 1697.

(6) Hong, D.; Murakami, M.; Yamada, Y.; Fukuzumi, S. *Energy Environ. Sci.* **2012**, *5*, 5708.

(7) Hong, D.; Jung, J.; Park, J.; Yamada, Y.; Suenobu, T.; Lee, Y.-M.; Nam, W.; Fukuzumi, S. *Energy Environ. Sci.* **2012**, *5*, 7606.

(8) Jiao, F.; Frei, H. *Energy Environ. Sci.* **2010**, *3*, 1018.

(9) Murakami, M.; Hong, D.; Suenobu, T.; Yamaguchi, S.; Ogura, T.; Fukuzumi, S. *J. Am. Chem. Soc.* **2011**, *133*, 11605.

(10) Fukuzumi, S.; Yamada, Y. *J. Mater. Chem.* **2012**, *22*, 24284.

(11) Morris, N. D.; Suzuki, M.; Mallouk, T. E. *J. Phys. Chem. A* **2004**, *108*, 9115.

(12) Yagi, M.; Toda, M.; Yamada, S.; Yamazaki, H. *Chem. Commun.* **2010**, *46*, 8594.

(13) Umena, Y.; Kawakami, K.; Shen, J.-R.; Kamiya, N. *Nature* **2011**, *473*, 55.

(14) Dismukes, G. C.; Brimblecombe, R.; Kolling, D. R. J.; Bond, A. M.; Swiegers, G. F.; Spiccia, L. *Inorg. Chem.* **2009**, *48*, 7269.

(15) Najafpour, M. M. *Chem. Commun.* **2011**, *47*, 11724.

(16) Yagi, M.; Narita, K. *J. Am. Chem. Soc.* **2004**, *126*, 8084.

(17) Robinson, D. M.; Go, Y. B.; Mui, M.; Gardner, G.; Zhang, Z.; Mastrogiovanni, D.; Garfunkel, E.; Li, J.; Greenblatt, M.; Dismukes, G. C. *J. Am. Chem. Soc.* **2013**, *135*, 3494.

(18) Shevela, D.; Koroidov, S.; Najafpour, M. M.; Messinger, J.; Kurz, P. *Chem.–Eur. J.* **2011**, *17*, 5415.

(19) Gao, Y.; Åkermark, T.; Liu, J. H.; Sun, L. C.; Åkermark, B. *J. Am. Chem. Soc.* **2009**, *131*, 8726.

(20) Harriman, A.; Pickering, I. J.; Thomas, J. M.; Christensen, P. A. *J. Chem. Soc., Faraday Trans. I* **1988**, *84*, 2795.

(21) Jiao, F.; Frei, H. *Chem. Commun.* **2010**, *46*, 2920.

(22) Boppana, V. B. R.; Jiao, F. *Chem. Commun.* **2011**, *47*, 8973.

(23) Robinson, D. M.; Go, Y. B.; Greenblatt, M.; Dismukes, G. C. *J. Am. Chem. Soc.* **2010**, *132*, 11467.

(24) Najafpour, M. M.; Pashaei, B. *Dalton Trans.* **2012**, *41*, 10156.

(25) Najafpour, M. M.; Rahimi, F.; Amini, M.; Nayeri, S.; Bagherzadeh, M. *Dalton Trans.* **2012**, *41*, 11026.

(26) Najafpour, M. M.; Ehrenberg, T.; Wiechen, M.; Kurz, P. *Angew. Chem., Int. Ed.* **2010**, *49*, 2233.

(27) Najafpour, M. M.; Pashaei, B.; Nayeri, S. *Dalton Trans.* **2012**, *41*, 4799.

(28) Najafpour, M. M.; Nayeri, S.; Pashaei, B. *Dalton Trans.* **2011**, *40*, 9374.

(29) Yamada, Y.; Yano, K.; Hong, D.; Fukuzumi, S. *Phys. Chem. Chem. Phys.* **2012**, *14*, 5753.

(30) Hong, D.; Yamada, Y.; Nagatomi, T.; Takai, Y.; Fukuzumi, S. *J. Am. Chem. Soc.* **2012**, *134*, 19572.

(31) Mehandjiev, D.; Naydenov, A.; Ivanov, G. *Appl. Catal., A* **2001**, *206*, 13.

(32) Yamada, Y.; Yano, K.; Xu, Q. A.; Fukuzumi, S. *J. Phys. Chem. C* **2010**, *114*, 16456.

(33) Yang, L.-X.; Zhu, Y.-J.; Tong, H.; Liang, Z.-H.; Li, L.; Zhang, L. *J. Solid State Chem.* **2007**, *180*, 2095.

(34) Morris, N. D.; Mallouk, T. E. *J. Am. Chem. Soc.* **2002**, *124*, 11114.

(35) Devaraj, S.; Munichandraiah, N. *J. Phys. Chem. C* **2008**, *112*, 4406.

(36) Kanan, M. W.; Nocera, D. G. *Science* **2008**, *321*, 1072.

(37) Bediako, D. K.; Lassalle-Kaiser, B.; Surendranath, Y.; Yano, J.; Yachandra, V. K.; Nocera, D. G. *J. Am. Chem. Soc.* **2012**, *134*, 6801.

Concluding Remarks

In the thesis, the author has revealed the catalytically active catalysts for water oxidation using homogeneous metal complexes with organic ligands in both thermal and light-driven water oxidation systems. The catalytic mechanism of water oxidation was investigated by using ruthenium complexes with inorganic ligands. The author has also developed efficient and robust heterogeneous WOCs based on earth-abundant metals. The results and finding in this work are summarized as follows (Chart 1):

Chart 1. Summary of this Thesis

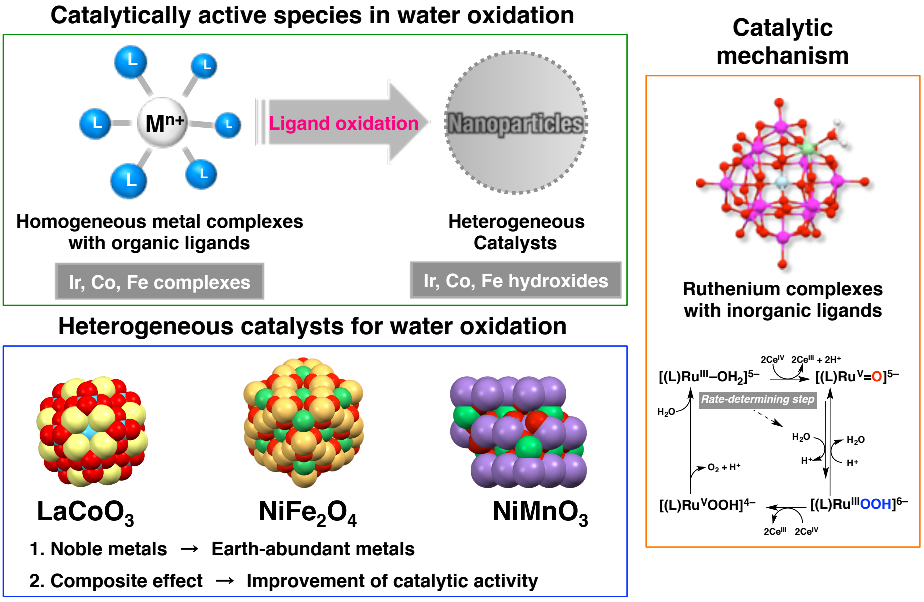

In Chapters 1 and 2, the author proved that the catalytically active species for water oxidation were not homogeneous molecular complexes but nanoparticles derived from mononuclear iridium and cobalt complexes with organic ligands in thermal and light-driven catalytic water oxidation systems, respectively.

In Chapter 3, catalytically active species for water oxidation in the presence of iron complexes possessing organic ligands were demonstrated to be changed depending on the pH conditions The iron complexes acted as homogeneous catalysts in the water oxidation by CAN under acidic conditions. In contrast to the homogeneous catalysis under acidic conditions, the iron complexes were converted to iron hydroxide nanoparticles that act as the actual catalyst for the light-driven water oxidation with $[Ru(bpy)_3]^{2+}$ and $S_2O_8^{2-}$.

Through Chapter 1–3, the author provides a valuable insight into how to choose the organic ligands of metal complexes for efficient and robust WOCs in the heterogeneous water oxidation systems using metal complexes as the catalyst precursors.

In Chapter 4, water oxidation by CAN was demonstrated with two types of all-inorganic mononuclear ruthenium complexes, which are suitable to elucidate the catalytic mechanism of water oxidation because of robust inorganic ligands against acidic and oxidative conditions. The rate-determining step involves in O-O bond formation by water nucleophilic attack to the Ru^V=O complex. The intermediate Ru^V=O complex was detected by a characteristic EPR signal and a resonance Raman peak.

In Chapter 5–7, the author has developed efficient and robust heterogeneous WOCs based on earth-abundant metals by introducing different metal ions into single metal oxides as observed in the $CaMn_4O_5$ cluster in OEC.

Throughout this study, valuable insights were given for the development of efficient WOCs. In particular, the identification of catalytically active species for water oxidation and the discovery of heterogeneous WOCs based on earth-abundant metals are important findings for development of artificial photosynthesis systems. In fact, an artificial photosynthesis system, in which hydrogen peroxide is produced from oxygen and water under photoirradiation, has been achieved by incorporating a heterogeneous WOC in this study (Chart 2). Despite low efficiency of hydrogen peroxides production, it may be expected to improve the efficiency in combination with semiconductor photocatalysts. Thus, this study provides valuable insights into both mechanism and application of catalytic water oxidation to realize artificial photosynthesis.

Chart 2. An Artificial Photosynthetic Cycle for Hydrogen Peroxide Production

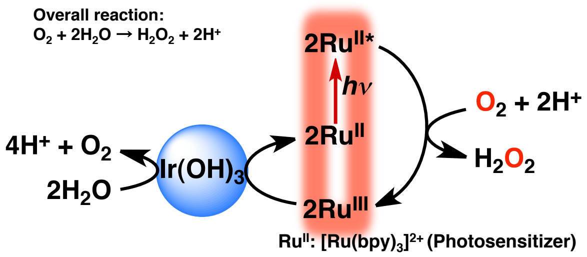

Publication List

Publications

1. Catalytic Mechanism of Water Oxidation with Single-Site Ruthenium-Heteropolytungstate Complexes
   Murakami, M.; Hong, D.; Suenobu, T.; Yamaguchi, S.; Ogura, T.; Fukuzumi, S.
   J. Am. Chem. Soc. **2011**, *133*, 11605.

2. Efficient Water Oxidation by Cerium Ammonium Nitrate with $[\mathrm{Ir^{III}(Cp^*)(4,4\text{-bishydroxy-}2,2\text{-bipyridine})(H_2O)}]^{2+}$ as a Precatalyst
   Hong, D.; Murakami, M.; Yamada, Y.; Fukuzumi, S.
   Energy Environ. Sci. **2012**, *5*, 5708.

3. Water-Soluble Mononuclear Cobalt Complexes with Organic Ligands Acting as Precatalysts for Efficient Photocatalytic Water Oxidation
   Hong, D.; Jung, J.; Park, J.; Yamada, Y.; Suenobu, T.; Lee, Y.-M.; Nam, W.; Fukuzumi, S.
   Energy Environ. Sci. **2012**, *5*, 7606.

4. $LaCoO_3$ Acting as an Efficient and Robust Catalyst for Photocatalytic Water Oxidation with Persulfate
   Yamada, Y.; Yano, K.; Hong, D.; Fukuzumi, S.
   Phys. Chem. Chem. Phys. **2012**, *14*, 5753.

5. Catalysis of Nickel Ferrite for Photocatalytic Water Oxidation Using $[Ru(bpy)_3]^{2+}$ and $S_2O_8^{2-}$
   Hong, D.; Yamada, Y.; Nagatomi, T.; Takai, Y.; Fukuzumi, S.
   J. Am. Chem. Soc. **2012**, *134*, 19572.

6. Water Oxidation Catalysis with Nonheme Iron Complexes under Acidic and Basic Conditions: Homogeneous or Heterogeneous?
   Hong, D; Mandal, S; Yamada, Y; Lee, Y.-M.; Nam, W.; Llobet, A; Fukuzumi, S.
   Inorg. Chem. **2013**, *52*, 9522.

7. Catalytic Activity of $NiMnO_3$ for Visible Light-Driven and Electrochemical Water Oxidation
   Hong, D.; Yamada, Y.; Nomura, A.; Fukuzumi, S.
   Phys. Chem. Chem. Phys. **2013**, *15*, 19125.

Perspectives

1. Homogeneous versus Heterogeneous Catalysts in Water Oxidation
   Fukuzumi, S.; Hong, D.
   Eur. J. Inorg. Chem. in press. (DOI: 10.1002/ejic.201300684)

2. Bioinspired Photocatalytic Water Reduction and Oxidation with Earth-Abundant Metal Catalysts
   Fukuzumi, S.; Hong, D.; Yamada, Y.
   J. Phys. Chem. Lett. **2013**, *4*, 3458.

Book

「人工光合成−システム構築に向けての最新技術動向と展望−」福住 俊一 監修
第 5 章「金属酸化物ナノ粒子による水の酸化触媒反応」
洪 達超、福住 俊一, CMC 出版, **2013**, pp.70-79.

Patent

「過酸化水素製造方法、過酸化水素製造用キットおよび燃料電池」
福住 俊一、末延 知義、加藤 慧、洪 達超
特願 2011-141280

Presentations at International Conferences

60th Anniversary Conference on Coordination Chemistry
"Mechanism of Catalytic Water Oxidation with Mononuclear Iridium Complexes"
○Hong, D; Fukuzumi, S.

The 7th Asian Photochemistry Conference
"Superior Catalysis of Nickel Ferrite for Photocatalytic Water Oxidation"
○Hong, D; Yamada, Y; Fukuzumi, S.

Award

錯体化学会第 63 回討論会　学生講演賞
「非ヘム単核鉄錯体を用いた水の酸化反応における反応活性種の同定」
○洪 達超、Sukanta Mandal、山田 裕介、Yong-Min Lee、Wonwoo Nam、Antoni Llobet、福住 俊一

Acknowledgements

The author would like to express his gratitude to Prof. Shunichi Fukuzumi and Dr. Yusuke Yamada for their kind guidance, invaluable suggestions, and encouragement throughout this study.

The author also would like to express his sincere thanks to Dr. Tomoyoshi Suenobu and Dr. Kei Ohkubo for their useful suggestion and kind help throughout this study.

The author is grateful to Prof. Wonwoo Nam, Dr. Yong-Min Lee, Prof. Antoni Llobet and Dr. Sukanta Mandal for their kind guidance, helpful comments, and valuable collaboration on the syntheses of cobalt and iron complexes, Dr. Satoru Yamaguchi and Prof. Takashi Ogura for their expertise in resonance Raman measurements, Dr. Takaharu Nagatomi and Prof. Yoshizo Takai for their expertise in XPS measurements, Dr. Norimitsu Tohnai for his kind advices for powder XRD measurements, and Research Center for Ultra-Precision Science & Technology for TEM measurements.

The author particularly appreciates Mr. Masato Murakami, Ms. Jiyun Park, Ms. Jieun Jung, Mr. Kentaro Yano and Mr. Akifumi Nomura for their contribution to a part of this study.

Thanks are also given to all members of the laboratory of Physical Chemistry for Life Science at Department of Material and Life Science, Graduate School of Engineering, Osaka University, for their help, valuable suggestions and friendship.

The author is deeply grateful to JSPS of the ministry of Education, Culture, Sports, Science and Technology, Japan for their support through scholarships.

Finally, the author would like to express his sincere appreciation for continuous encouragement and support given by his friends and his family; Mr. Yiqing Hong (his father), Mrs. Qiuyue Lü (his mother), Mr. Daqi Hong (his brother).

Dachao Hong

Department of Material and Life Science
Division of Advanced Science and Biotechnology
Graduate School of Engineering, Osaka University

Osaka Japan
January 2014